**ADVERTIMENT**. La consulta d'aquesta tesi queda condicionada a l'acceptació de les següents condicions d'ús: La difusió d'aquesta tesi per mitjà del servei TDX (www.tesisenxarxa.net) ha estat autoritzada pels titulars dels drets de propietat intel·lectual únicament per a usos privats emmarcats en activitats d'investigació i docència. No s'autoritza la seva reproducció amb finalitats de lucre ni la seva difusió i posada a disposició des d'un lloc aliè al servei TDX. No s'autoritza la presentació del seu contingut en una finestra o marc aliè a TDX (framing). Aquesta reserva de drets afecta tant al resum de presentació de la tesi com als seus continguts. En la utilització o cita de parts de la tesi és obligat indicar el nom de la persona autora.

**ADVERTENCIA**. La consulta de esta tesis queda condicionada a la aceptación de las siguientes condiciones de uso: La difusión de esta tesis por medio del servicio TDR (www.tesisenred.net) ha sido autorizada por los titulares de los derechos de propiedad intelectual únicamente para usos privados enmarcados en actividades de investigación y docencia. No se autoriza su reproducción con finalidades de lucro ni su difusión y puesta a disposición desde un sitio ajeno al servicio TDR. No se autoriza la presentación de su contenido en una ventana o marco ajeno a TDR (framing). Esta reserva de derechos afecta tanto al resumen de presentación de la tesis como a sus contenidos. En la utilización o cita de partes de la tesis es obligado indicar el nombre de la persona autora.

**WARNING**. On having consulted this thesis you're accepting the following use conditions: Spreading this thesis by the TDX (www.tesisenxarxa.net) service has been authorized by the titular of the intellectual property rights only for private uses placed in investigation and teaching activities. Reproduction with lucrative aims is not authorized neither its spreading and availability from a site foreign to the TDX service. Introducing its content in a window or frame foreign to the TDX service is not authorized (framing). This rights affect to the presentation summary of the thesis as well as to its contents. In the using or citation of parts of the thesis it's obliged to indicate the name of the author

UNIVERSITAT POLITÈCNICA
DE CATALUNYA
BARCELONATECH

# Design and Performance Evaluation of Millimeter-Wave Flat Lens Antennas for Communications, Radar and Imaging Applications

Author
**Marc Imbert i Villà**

Thesis Advisor
Prof. Jordi Romeu i Robert

A thesis submitted to the Universitat Politècnica de Catalunya (UPC) in
partial fulfillment of the requirements for the degree of
DOCTOR OF PHILOSOPHY

**Department of Signal**
**Theory and Communications**

Ph.D. program on Signal Theory and Communications
AntennaLab Research Group
Barcelona, July 2016

Marc Imbert i Villà

Design and Performance Evaluation of Millimeter-Wave Flat Lens Antennas for Communications, Radar and Imaging Applications

Ph.D. program on Signal Theory and Communications

This work was supported in part by the Spanish Inter-Ministerial Commission on Science and Technology (CICYT) under projects TEC2010-20841-C04-02, TEC2013-47360-C3-1-P and CONSOLIDER CSD2008-00068, and by the "Ministerio de Economía y Competitividad" through the FPI fellowship program.

**Curs acadèmic:** 2015/2016

# Acta de qualificació de tesi doctoral

Nom i cognoms
Marc Imbert i Villà

Programa de doctorat
Teoria del Senyal i Communicacions

Unitat estructural responsable del programa
Teoria del Senyal i Communicacions

## Resolució del Tribunal

Reunit el Tribunal designat a l'efecte, el doctorand / la doctoranda exposa el tema de la seva tesi doctoral titulada DESIGN AND PERFORMANCE EVALUATION OF MILLIMETER-WAVE FLAT LENS ANTENNAS FOR COMMUNICATIONS, RADAR AND IMAGING APPLICATIONS.

Acabada la lectura i després de donar resposta a les qüestions formulades pels membres titulars del tribunal, aquest atorga la qualificació:

☐ NO APTE ☐ APROVAT ☐ NOTABLE ☐ EXCEL·LENT

| | |
|---|---|
| (Nom, cognoms i signatura)<br>President/a | (Nom, cognoms i signatura)<br>Secretari/ària |

| | | |
|---|---|---|
| (Nom, cognoms i signatura)<br>Vocal | (Nom, cognoms i signatura)<br>Vocal | (Nom, cognoms i signatura)<br>Vocal |

______________________, _______ d'/de __________________ de _______________

El resultat de l’escrutini dels vots emesos pels membres titulars del tribunal, efectuat per l’Escola de Doctorat, a instància de la Comissió de Doctorat de la UPC, atorga la MENCIÓ CUM LAUDE:

☐ SÍ ☐ NO

| | |
|---|---|
| (Nom, cognoms i signatura)<br>President de la Comissió Permanent de l’Escola de Doctorat | (Nom, cognoms i signatura)<br>Secretari de la Comissió Permanent de l’Escola de Doctorat |

Barcelona, _______ d'/de ____________________ de _________

*Als meus estimats pares, Joaquim i Magda,*
*per haver-me donat tot el que un fill podria necessitar.*

*If you wish to find the secrets of the Universe,*
*think in terms of energy, frequency and vibration.*
Nikola Tesla (1856-1943)

# Preface and Acknowledgments

Dedicatòries i agraïments personals a la familia, professors, companys i amics.

The author wants to acknowledge the support of the following institutions:

- **MICINN** (Ministerio de Ciencia e Innovación) for providing financial support to part of the research performed in the frame of this thesis, under the projects TEC2010-20841-C04-02 (Design, Simulation and Measurement of Millimeter-Wave Antennas for Communications and Imaging), and TERASENSE-CONSOLIDER CSD 2008-00068.
- **MINECO** (Ministerio de Economía y Competitividad) for providing financial support under project TEC2013-47360-C3-1-P (Sistemas Radiantes en milimétricas y submilimétricas para radar, comunicaciones e imágenes), and for providing the Pre-Doctoral FPI fellowship (Ref. BES-2011-046870) during the research performed in the development of this thesis.

# Abstract

Over the last decades, the scientific community and the industry have focused their attention on different frequency bands that could satisfy the increasing bandwidth requirements of modern communications, radar and imaging systems. Given the large amount of bandwidth available, the millimeter-wave frequency band represents one of the most interesting candidates to allow such applications. In fact, different sub-bands of the millimeter-wave spectrum seem promising for future 5G communication systems, including the 28-30 GHz band, the 60 GHz band, and the E-band at 71-76 GHz, 81-86 GHz, and 92-95 GHz. This vast amount of bandwidth combined with the small system wavelength ($\lambda_{60GHz}$=5 mm) allows for the development of compact very high throughput (>1.5 Gbps) wireless communication systems. However, in accordance with the Friis transmission formula, for a fixed distance the path loss in free-space propagation is much higher at millimeter-wave frequencies than at lower microwave frequencies (e.g. the path loss at 60 GHz is 28 dB higher than at 2.45 GHz).

In consequence, millimeter-wave systems introduce a set of particular severe requirements from the antenna point of view in order to achieve specific performances. In this sense, high directive antennas are required to overcome the aforementioned extra path loss. Moreover, each particular application introduces additional requirements. For example, in very high throughput (VHT) wireless personal area networks (WPANs) communication systems at 60 GHz band beam-steering antennas are needed to deal with high user random mobility and human-body shadowing characteristic of indoor environments. Similarly, beam-steering capabilities are also needed in automotive radar applications at 77 GHz, since the determination of the exact position of an object is essential for most of the functions realized by the radar sensor. In the same way, beam-scanning, which is still commonly mechanically performed nowadays, is also needed in passive imaging systems at 94 GHz. Finally, from the integration perspective, the antennas must be small, low-profile, light weight and low-cost, in order to be successfully integrated in a commercial millimeter-wave wireless system.

For these reasons, many types of antenna structures have been considered to achieve high directivity and beam-steering capabilities for the aforementioned millimeter-wave communication, radar and imaging applications at 60, 77 and 94 GHz. The most part of the currently adopted solutions are based on the expensive, complex and bulky phased-array antenna concept. Actually, phased-array antenna systems can scan the beam at a fast rate. However, they require a complex integration of many expensive, lossy and bulky circuits, such as solid-state phase shifters and beam-forming networks.

In the present thesis, we contribute with a different approach to model, analyze, fabricate, and experimentally evaluate the performance of different alternatives, based on innovative inhomogeneous gradient-index dielectric flat lenses as a fundamental part of the switched-beam antenna array concept, instead on the current antenna designs at millimeter-wave frequencies existing in the literature.

Switched-beam arrays provide an interesting alternative to the common solutions based on phased-array antenna concept because they have a set of multiple fixed beams that can be easily selected individually, and the implementation is much easier. In this sense, this thesis is mainly devoted to study in depth and practically develop the fundamental part of this innovative switched-beam antenna array concept: novel inhomogeneous gradient-index dielectric flat lenses, which, despite their planar antenna profile configurations, allow full 2-D beam-scanning of high gain radiation beams.

First, we initially introduce the theoretical design and functioning principle of the flat lens-based switched-beam antenna array concept. In this novel antenna concept, the flat lens steers and enhances the radiation in a particular direction of the space. Only one radiating element of the array is selected for each operation mode. The focusing direction depends on the position of this single element of the array, which is selected and activated, allowing us to scan the high-gain radiation beam in both theta and phi directions of the space.

Then, the inhomogeneous flat lens antenna and its functioning principle are particularly introduced, providing the most fundamental design guidelines. A specific dielectric flat lens model is presented for millimeter-wave applications. This model is theoretically described, numerically simulated, practically fabricated and fully electromagnetically tested at 60 GHz WPAN frequency band for short-range communication systems, at 77 GHz for automotive radar applications, and at 94 GHz for passive imaging, radar and communication systems. It is demonstrated that this flat lens design leads to a low-profile antenna configuration, easy to manufacture and low-cost, in order to integrate the whole structure in a compact millimeter-wave wireless system showing very good electromagnetic performance.

Subsequently, the theoretical study and design of two alternatives of inhomogeneous ML (iML) to increase the maximum achievable gain, reduce the back-radiation level and the side-lobe levels (SLL), and enhance the bandwidth performance of the original dielectric flat lens are presented. We numerically evaluate and compare two different iML solutions with the aim to improve even more the performance of the original inhomogeneous flat lens design.

In the same way, in order to build the complete switched-beam array for the considered millimeter-wave applications, the radiating part of the structure is also studied, designed, fabricated, and experimentally tested. In this case, we propose a five by five planar array of slot and patch antennas to facilitate the integration in a low-profile antenna configuration for compact mobile devices. A total of 25 fixed high-gain beams can be selected, one by one, to scan in both theta and phi directions. However, the integration of the corresponding switching elements to individually select each one of the radiating elements of the array represents one of the biggest and more difficult technological challenges at millimeter-wave frequencies. These switch integration issues still have to be solved by the specific scientific community; therefore, an alternative solution is contemplated, studied and presented, to solve the problem directly from the antenna point of view: a switched-beam antenna array based on dielectric flat lenses with cylindrically distributed effective parameters. In consequence, a complete study of this innovative proposed antenna concept is carried out. Novel dielectric cylindrical lenses are introduced, studied, numerically simulated, fabricated and fully electromagnetic characterized at millimeter-wave frequencies.

With these kind of flat lenses, because of their cylindrically effective parameters distribution (i.e. effective gradient-index in one axis, constant-index in the other one), the beam-scanning can be performed by moving (or selecting) the position of the radiating element along the gradient-index axis, whereas the beam can be maintained invariant in the other direction, in which the effective parameters are maintained constant, despite changing the radiating element position in this particular axis. In this way, the beam-scanning can be achieved in the constant-index axis by means of a different technique, in order to reduce the switch elements needed, to finally perform a full 2-D scan in all the directions of the space. In this regard, a frequency-scanned stripline-fed transverse slot antenna array is designed in order to achieve beam-scanning in one single plane by sweeping the frequency. The combination of the two presented different antenna concepts (the cylindrical flat lens and the frequency-scanned array) allows the beam-steering capability in theta and phi directions in order to focus the radiation in a desired specific position of the space. The complete design of this new antenna concept is fabricated and fully electromagnetically characterized showing very good performance for the considered millimeter-wave applications and practically demonstrating the feasibility of the proposed antenna solution for compact commercial systems.

In addition, and because it represents a technological challenge to obtain a compact fully integrated antenna device at millimeter-wave frequencies with high-gain and beam-steering capabilities in both planes, an important part of this thesis is devoted to propose, study and evaluate a feasible solution, which could be practically easily implemented and commercially interesting. This main idea is constantly kept in mind through the different chapters. In this sense, low-temperature co-fired ceramics (LTCC) technology allows for the integration, layer by layer, of all the previously studied different parts in the whole switched-beam antenna array structure: from the array with its groundplanes, feeding lines and slots in different layers, to the flat lens, including the intermediate iML. It has been demonstrated the feasibility to integrate and manufacture in a single monolithic structure the whole antenna solution, leading to a compact low-profile configuration for commercial wireless devices in a low-cost technology.

Finally, in order to completely evaluate the performance of the designed novel inhomogeneous dielectric flat lenses, all the fabricated prototypes are also tested and compared to other antenna solutions in a real indoor environment for different transmitter-receiver communication scenarios, evaluating and analyzing their performance with wireless channel statistic parameters, such as power delay profile (PDP) and root mean square (RMS) delay spread, from a realistic point of view, confirming the potential applicability of the proposed antenna solution for future 5G wireless millimeter-wave communication systems and, in this way, concluding a complete transverse analysis, not only from the electromagnetic characterization point of view, but also from the real application perspective.

Furthermore, at the end of this document, additional contributions carried out during this PhD thesis are also briefly explained and summarized.

***Keywords:*** Dielectric Flat Lenses, Cylindrically Distributed Parameters Lens, Millimeter-Wave Antennas, WPAN, Automotive Radar Systems, Beam-Steering, Reconfigurable Antennas, Switched-Beam Array, Passive Imaging, power delay profile (PDP), root mean square (RMS) delay spread, low-temperature co-fired ceramics (LTCC) technology, 60 GHz band, 79 GHz band, 94 GHz band, 5G.

# Contents

1

## Chapter 1

# Introduction

*THIS chapter is devoted to describe the context, the scope, and the motivations that have led to the study carried out within this doctoral activity and the related main objectives to be fulfilled. The current state of the art is introduced, and the structure of this doctoral dissertation is also presented to point out specifically which are the main contributions of each chapter and how they are linked to the fundamental goals.*

Nowadays, wireless technologies have become one the fastest growing segments of the whole telecommunications industry and, almost without realizing it, they have evolved to be an essential part of our lives. Nevertheless, before the popularization of wireless technologies to the mainstream market for a commercial use, wireless communications were administrated and controlled by military, and for some specific industrial companies for their particular applications. However, during the last decades of the 20th Century, and the first decade of 21st, the increasing interest in wireless communications has been encouraged by the huge consumer demands, since the allocation of new radio spectrum bands carried out by the relevant authorities.

In this sense, one of the most important recently allocated frequency bands was the well-known industrial scientific and medical (ISM) band, which allows unlicensed applications around 2.45 GHz [1]. In fact, this band was originally instigated, in 1985, by Federal Communications Commission (FCC) of the United States, motivating the development of wireless local area networks (WLANs) and WPANs and, ultimately, providing the growth of wireless fidelity (Wi-Fi) and of a great part of the new wireless technologies that we currently use. However, the new user applications arising from these access technologies require, increasingly, larger data rates and this translates into the need of larger bandwidths according to the Shannon's capacity theorem. In consequence, there was an existing problem with the available spectrum allocated for unlicensed applications, which is of great importance for research and development purposes of future technologies.

For these reasons, the spectrum regulatory authorities foresaw the allocation of new frequency bands in order to allow the expansion of innovative high data rate applications, which require larger bandwidths. Hence, in February 14, 2002, the FCC adopted a First Report and Order that permits the operation of certain types of new products incorporating ultra-wide-band (UWB) technology for imaging, vehicular radar, and radiocommunication systems to operate as license-exempt in the frequency band from 3.1 to 10.6 GHz [2]. Afterward, in 2006, the Radio Communications Group of the International Telecommunications Union (ITU) allocated the same frequency band for UWB technologies [3] [4]. UWB devices can operate sharing the same spectrum band occupied by other existing communication technologies, such as Wi-Fi, limiting the power radiated. Consequently, UWB radio frequencies may coexist with other radio services using a large frequency band but, in contrast, with severe restricted power emissions that ultimately reduce the feasibility to achieve high data rate transmissions. Hopefully, in recent years, a very interesting alternative with a huge number of possibilities has appeared in wireless communication systems: the millimeter-wave frequency band.

## 1.1 Millimeter-Wave Frequency Band

The propagation characteristics of millimeter-waves make them appropriate for a numerous different applications. Actually, millimeter-wave technology is probably one of the most interesting challenges for the radio-frequency (RF) engineers over the next years in many areas, such as antenna design, propagation, and communication protocols for high data rate wireless applications. As it is illustrated in Fig. 1.1, the millimeter-wave band comprises frequencies of operation between 30 and 300 GHz (this corresponds to a wavelength range, in free-space propagation conditions, from 1 to 10 mm). Sometimes, the millimeter-wave frequency band is also called Extremely High Frequency (EHF).

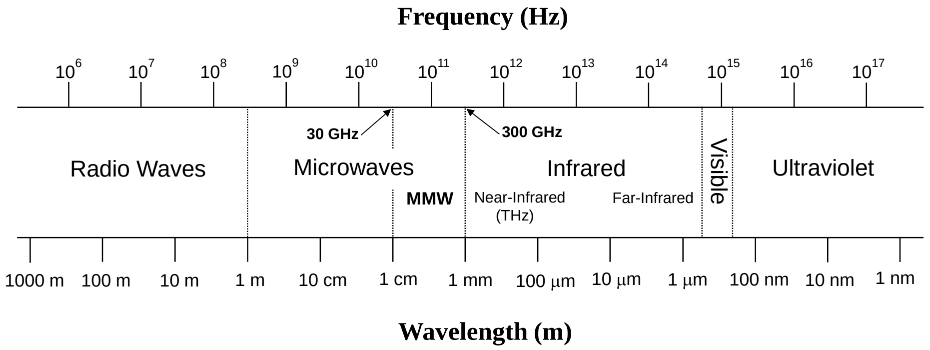

**Figure 1.1:** Electromagnetic spectrum from Radio Waves to Ultraviolet

## 1.2 Millimeter-Wave Technologies and Applications

The millimeter-wave frequency band is an emerging opportunity for industrial and commercial applications but, since many years ago, it has been widely known for military applications, mainly in development of radar [5]. Nevertheless, the recent improvements in the fabrication and integration processes, together with the allocation of new unlicensed frequency bands by the regulatory authorities, have led the growth of millimeter-wave technologies in the industrial and commercial sectors. In fact, there are several millimeter-wave civil applications that already exist for some specific purposes. Among these, we have to mention applications for radio astronomy observation, remote sensing, millimeter-wave scanners, and high resolution radars. For example, we can find satellite communication systems operating in some parts of the Ka band (26.5 to 40 GHz), novel wireless personal area networks at the recently allocated unlicensed 60 GHz band, and automotive radar applications, passive imaging, and communication systems at W band (75 to 110 GHz).

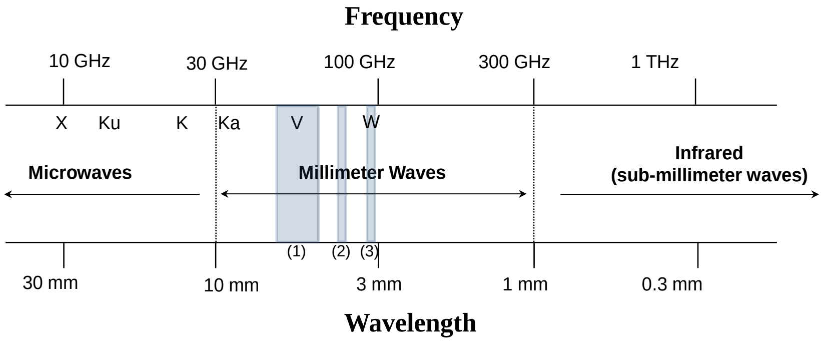

**Figure 1.2:** Millimeter-wave spectrum and identification of different sub-bands for the considered applications: (1) WPAN around 60 GHz (section 1.2.1), (2) automotive radar at 79 GHz (section 1.2.2) and (3) passive imaging at 94 GHz (section 1.2.3)

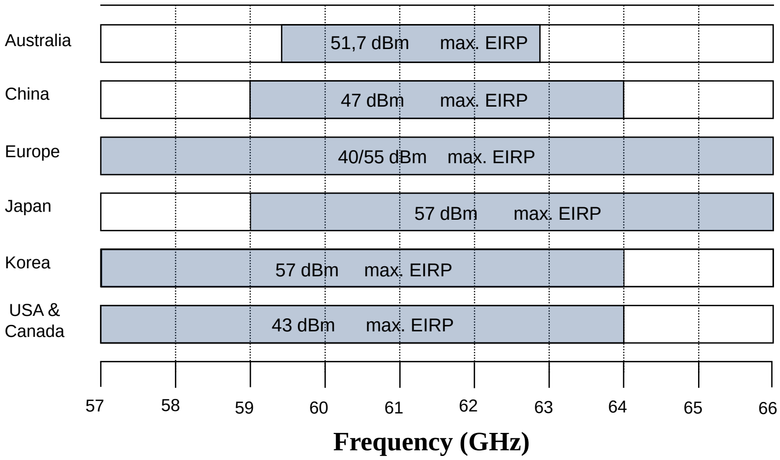

**Figure 1.3:** Unlicensed spectrum around 60 GHz band in different regions and maximum equivalent isotropic radiated power (EIRP)

### 1.2.1 60 GHz Wireless Communication Systems

The future broadband wireless communication systems will have the need for more bandwidth in order to satisfy the increasing demands to achieve higher data rates. Therefore, over the last decades, the scientific community and the industry have focused their attention on different frequency bands that could satisfy these increasing bandwidth requirements of modern communications systems. In this sense, there are multiple reasons to consider the 60 GHz frequency band the most prospective alternative to allow the future high-speed wireless communication systems. First of all, as it is illustrated in Fig. 1.2, a huge amount of spectrum around 60 GHz was available and seemed to be the perfect choice and the best option in order to allow the operating frequency band for high data rate applications.

Hence, in 2001, the FCC of the United States proposed the allocation of 7 GHz of spectrum surrounding the 60 GHz operating frequency band specifically for unlicensed applications [6]. This was the beginning of several such initiatives carried out by relevant authorities of different countries worldwide. Substantial efforts have been accomplished in order to achieve an international agreement between United States and Canada, Europe, Asia, and Australia, but still remain different regulations in each region [7] (see Fig. 1.3). The international table of frequency allocations of the ITU, which is contained in Article 5 of the Radio Regulations (Volume 1), specifies some frequency bands that may be made available for ISM applications (Radio Regulation 5.150 and, in particular for the 60 GHz band, Radio Regulation 5.138 [1]). Immediately, as occurred in 1985 with the allocation of 2.45 GHz unlicensed ISM band, a new great interest emerged from academic and industrial communities with the aim to solve many technological challenges to achieve high data rate communications, mainly for WPANss and WLANS, due to the particular propagation characteristics of the electromagnetic waves in the 60 GHz frequency band (determinated by specific atmospheric attenuation due to water vapor and oxygen absorption, as can be seen in Fig. 1.4). Therefore, this supposes a great challenge in delivering a multi-gigabit

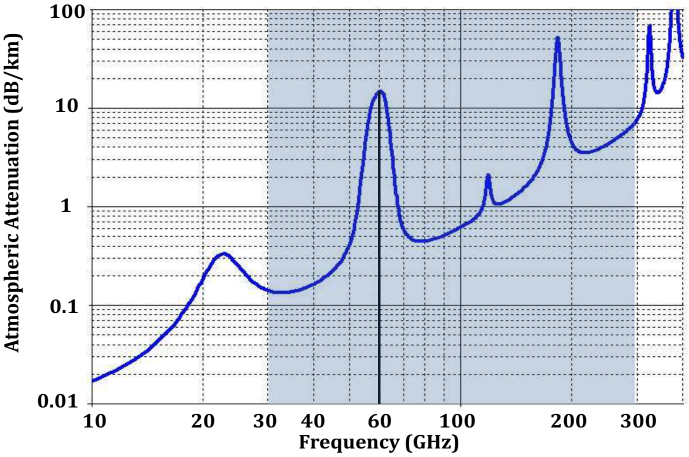

**Figure 1.4:** Specific atmospheric attenuation around 60 GHz band at sea level

wireless communications and makes 60 GHz a promising candidate for indoor, but also for outdoor applications employing high directional antennas pointing directly one to each other en clear line-of-sight (LOS) conditions. These high additional propagation losses seem to be a disadvantage; however, they can confine the 60 GHz operation within a short-range (about 10 meters) in an indoor environment (e.g. WPAN or even WLAN applications). Hence, the interference levels in 60 GHz band are less harmful than in systems located in the highly overcrowded 2.45 GHz ISM band. Additionally, higher frequency reuse can also be achieved per indoor environment, thus allowing a very high throughput network. This short-range scenario (see Fig. 1.5) also represents highly secure operating conditions due to inner networks are not reachable from the outdoors, a few meters away.

**Figure 1.5:** Typical application scenario for HD video streaming in a 60 GHz WPAN indoor environment (image taken from ITU-R Report M.2227 [8]

In this sense, the engineering community is currently doing great efforts for 60 GHz standardization. Current technical standard activities include IEEE 802.15.3c [9], IEEE 802.11ad [10] (supported by WiGig Alliance [11]), WirelessHD [12], and European computer manufacturers association (ECMA) 387 [13]. These different standards define very high throughput short-range (up to 10-15 meters) communications scenarios in indoor environments.

Moreover, although the 60 GHz band has been typically related to indoor communication systems due to the specific gaseous atmospheric attenuation around this frequency band, which limits the transmission range as it has been explained, recently, the Federal Communications Commission (FCC) of the United States proposed a change in the radio regulation to increase the effective radiated power limits from 40 to 82 dBm [14], thus motivating also great interest in developing outdoor communications for unlicensed backhaul applications. Therefore, new types of antennas will be absolutely necessary in future millimeter-wave communication systems at 60 GHz, not only in indoor but also outdoor situations.

Additionally, it is also clear that the millimeter-wave frequency band will play a key role in fifth generation (5G) wireless cellular networks [15–17]. Four different frequency bands around 28, 38, 60, and 73 GHz have recently been considered in the millimeter-wave region as perfect alternatives for future 5G mobile communication systems in both indoor and outdoor environments [14, 17]. Therefore, the vast amount of bandwidth available at 60 GHz will also allow the development of high data rate transmission systems for future 5G cellular networks in indoor and outdoor environments, which will increase even more the interest in this specific part of the electromagnetic spectrum.

### 1.2.2 79 GHz Automotive Radar Systems

Automotive radars have been available since 1999, both in the frequency range around 24 GHz as well as 76.5 GHz, with a the new frequency band around 79 GHz (from 77 to 81 GHz, already allocated in Europe) [18] [19], intended for medium and short-range sensors. Automotive radar sensors provide information about other vehicles and the road surroundings with respect to distance (range), speed, and, depending on the specific

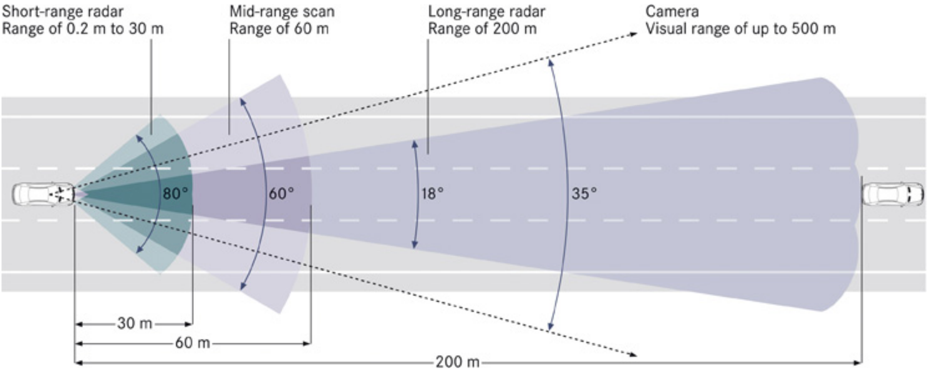

**Figure 1.6:** Automotive short-range, mid-range and long-range radar applications.

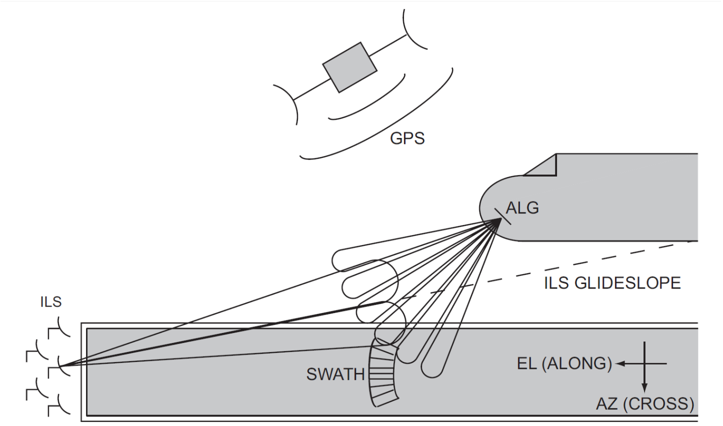

**Figure 1.7:** High resolution millimeter-wave imaging radar at 94 GHz for autonomous landing guidance (ALG) [20].

configuration, angle (cross range). Range is determined by measurement of the flight time of the electromagnetic wave from the radar to a target and back while relative speed is determined evaluating the Doppler frequency shift. The angular or cross range observation depends on the sensor application and is determined by its antenna arrangement. In an early stage, when automotive sensors were used solely in comfort functions supporting the automatic speed control by keeping a safe distance to the preceding vehicle, a few (switched) narrow antenna beams were sufficient to monitor the own and adjacent lanes on a highway. Today, automotive sensors increasingly are employed for safety purposes both for highway (i.e. long-range), as well as for dense urban (i.e. short-range) traffic scenarios, leading to the necessity of much more sophisticated antenna and overall system concepts.

### 1.2.3 94 GHz Passive Imaging, Radar and Communication Systems

The 94 GHz frequency band (from 92 to 95 GHz) was allocated by the FCC of the United States for imaging, indoor communications, radar, and some particular defense applications [21] in 2003, taking advantage of the low-absorption atmospheric window around this specific band. In this sense, the use of millimeter-waves in imaging systems at 94 GHz has become very common over the last years due to the benefits of these frequency bands as non-ionizing electromagnetic field, together with their capacity to penetrate dielectric bodies, and the small wavelength which allow high levels of resolution. Due to these reasons, different techniques are attractive for non-invasive imaging applications [22], such as security and defense applications in order to detect concealed weapons [23], or even in medical applications (e.g. for cancer breast detection) [24]. Moreover, since the FCC also allowed the use of the frequencies between 92 and 95 GHz for unlicensed indoor communication applications [21], and the European Telecommunications Standards Institute (ETSI) was invited to follow this indication, the possibility of avoiding requesting licenses has been a strong incentive to the widespread implementation of millimeter-wave body area networks (BAN) communication systems around 94 GHz [25]. Finally, this frequency band has been also reserved for radar applications, including aircraft landing systems [26] (see Fig. 1.7), and collision-avoidance sensors for adaptive cruise control (ACC) systems in automotive radar applications at 94 GHz [27], since the small wavelength of this high frequency of operation allows very high-resolution of various scenes.

## 1.3 State-of-the-art

Many types of antenna structures have been considered for short-range 60 GHz WPAN communication applications, for automotive radar systems at 79 GHz, and for passive imaging, radar, and communications at 94 GHz. In the next subsections, we will briefly review the current state of the art in antennas field for the specified millimeter-wave technologies around this three frequency sub-bands.

### 1.3.1 Antenna Solutions for Communication Systems at 60 GHz

As it has been explained, the large amount of bandwidth available combined with the small system wavelength could allow for the development of compact very high throughput (>1.5 Gbps) data rate short-range WPAN communication systems around 60 GHz band (from 57 to 64 GHz in the United States, and up to 66 GHz in Europe [7]). However, in accordance with Friis transmission formula, at millimeter-wave frequencies the path loss in free-space propagation is considerably higher than at lower microwave frequencies (for example, the attenuation is up to 28 dB higher at 60 GHz compared to at 2.45 GHz, for a fixed transmission distance). This represents one of the most significant challenges to overcome at millimeter-wave frequencies. Therefore, in order to achieve high data rate communications for WPANs and future 5G broadband wireless networks around 60 GHz band, it is essential to dispose of high-directive antennas. Additionally, antennas with certain beam-steering capabilities are also desirable in order to facilitate the reconfiguration of the radiation beam in situations of transmission blockage between mobile devices under line-of-sight (LOS), obstructed-line-of-sight (OLOS), or even in non-line-of-sight (NLOS) [28]. In fact, the recent IEEE 802.15.3c-2009 standard [9], which defines the physical (PHY) and medium access (MAC) layers specifications for the high-rate WPANs at 60 GHz band, suggests four levels in the beam-forming protocol to improve the range of communicating devices: quasi-omni-directional patterns, sectors (second level resolution patterns to cover a relatively broad area of multi-beams), fine beams, and high-resolution (HRS) beams; in this case, HRS beams are specifically needed to increase the antenna gain for supporting high data rate transmissions [9]. Therefore, high-gain beam-steerable antennas will be absolutely necessary for high-speed WPANs, as well as for future 5G millimeter-wave systems. Finally, from the commercial perspective, the antennas must be small, light-weight, low-cost, and low-profile in order to be successfully integrated in a compact millimeter-wave wireless system.

In this respect, many types of antenna structures have been proposed for WPAN 60 GHz band communication systems [29, 30]. Typical antenna solutions for millimeter-wave systems include reflectors, lenses, and horn antennas, which have achieved the highest level of development for high gain applications. Although these antenna alternatives provide high gain and beam-steering capabilities, in most of the cases, they have not been

**Table 1.1:** Summary of AoC from the literature for 60 GHz communication systems.

| Planar antenna type | Max. Gain (dB) | Literature reference |
|---|---|---|
| Dipole Antenna | 3.6 dB | [32] |
| Yagi Antenna | -10 dB | [33] |
| Triangular Monopole Antenna | -9.4 dB | [34] |
| Rectangular DRA | 3.2 dB | [35] |
| Planar Inverted-F Antenna | -19 dB | [31] |
| Quasi-Yagi Antenna | -12.5 dB | [31] |
| Dipole Antenna | -7.3 dB | [36] |
| Yagi Antenna | -3.5 dB | [36] |
| Rhombic Antenna | -0.2 dB | [36] |

suitable for commercial and consumer 60 GHz systems for the moment because they are expensive, bulky, heavy, and more importantly, they cannot be integrated with solid-state devices. Thus, most of the literature reported for millimeter-wave communication devices is focused in printed antennas (e.g. microstrip patch or dipole arrays). Printed antennas have many attractive properties such as low-profile, light-weight, and compact structure, which facilitate an easier fabrication and integration with solid-state devices. Hence, they seem suitable for commercial 60 GHz radios.

Recently, two main philosophies have been contemplated at millimeter-wave frequencies for the integration of the antenna together with the front-end: antenna-on-chip (AoC) and antenna-in-package (AiP) [31]. In the AoC solution, the antenna structure is fully embedded in the same chip substrate, fundamentally in silicon-based technologies while, on the other hand, in the AiP solution, the antenna elements are placed in the package surrounding the chip which encloses the rest of the electronics.

#### 1.3.1.1 On-Chip Antennas

On-chip integrated antennas simplify considerably the integration and packaging thanks to the absence of millimeter-wave signal outside the transceiver chip; they lead to a larger transceiver chip, but a smaller packaged module [37]. Their radiation performances are generally poor, between 0 and 2 dB maximum gain, even negative gain values, because the radiation losses are extremely large due to substrate absorption and conductive currents. However, the removal of all connections between RF circuits and the antenna offers substantial cost reduction and flexibility in circuit design for low-cost consumer electronics. Nowadays it is very difficult to justify on-chip antennas for low-power 60 GHz consumer devices due to high losses and low gains in the absence of compensating structures such as dielectric lenses [30]. In fact, typical on-chip antennas reported in the literature have only 10% efficiency values and negative gain. However, if very high gain antenna structures can be designed and fabricated on chip in sub-millimeter sizes (e.g., by using frequency selective surfaces [38] or highly directional antennas such as Yagi or rhombic antennas [36]), then the benefits of extreme cost reduction and improved design flexibility may outweigh the use of more efficient off-chip antennas that require more expensive and complex manufacturing processes. On-chip antennas have been reported for a large range of frequencies. Table 1.1 provides an overview of some of the results that

**Table 1.2:** Summary of AiP from the literature for 60 GHz communication systems.

| Planar antenna type & process | Max. Gain (dB) | Lit. reference |
|---|---|---|
| 16 patch antennas - grid array | 5 dB/element | [41] |
| 16 patch antennas - liquid-crystal polymer | 2 dB/element | [41] |
| Slot antenna - LTCC | 11 dB | [42] |
| Yagi - LTCC & grid array | 6 dB | [43] |
| Yagi - LTCC & cavity grid | 6 dB | [44] |
| 4 x 4 patch - LTCC | 16.8 dB | [45] |
| 4 elem. patch array - Thin film subs. | 7 dB | [46] |

have been reported in the literature for AoC at 60 GHz band for short-range WPAN applications.

The best on-chip antenna gains for single antennas around millimeter-wave frequencies have relied on the placement of dielectric lenses below or above the antenna (sometimes called a resonator). This technique has the effect of reducing energy lost to substrate modes [35, 39, 40]. Substrate modes allow waves of certain frequencies to propagate through the bulk silicon substrate, based on the material properties and physical dimensions of the chip. A dielectric lens above the antenna reduces the difference in the dielectric constants above and below the antenna (without the lens above the antenna, the dielectric constant below the antenna is that of the silicon substrate, while that above is of air). This lens has the effect of increasing the radiation intensity of the antenna out from the substrate, thus reducing the energy lost into the structure. The lens above the antenna should be made of a material with a dielectric constant equal to or larger than that of the substrate that supports the antenna [30].

#### 1.3.1.2 In-Package Antennas

On the other hand, in-package antennas can currently achieve much higher efficiencies than on-chip antennas due to their distance from the lossy chip silicon substrate. However, this technology is more expensive than the previously commented and involves advanced fabrication and interconnection technologies to accommodate millimeter-wave signals. Popular package technologies include Teflon ($\epsilon_r$=2.2), LTCC materials ($\epsilon_r$=5.9-7.7), fused silica ($\epsilon_r$=3.8), and liquid crystal polymer (LCP) ($\epsilon_r$=3.1). In general the best gain bandwidth product will be obtained using materials with low dielectric constants [29]. However, there are many challenges in using in-package antenna solutions [47], including a shift in the frequency response of the antennas due to the presence of surrounding packaging materials, difficulty in meeting mechanical and electrical reliability requirements, antenna interference from heat sinks, and possibly the high expense of packaging processes.

Table 1.1 summarizes some literature reports for 60 GHz in-package antennas. In this sense, advanced packaging technologies provide the possibility of integrating antennas and other millimeter-wave components in more flexible ways than on a single chip. This depends on the type of interconnects used in the package. Popular interconnect technologies include flip chip connections [48], which facilitate stacked structures and coupling connections that can reach higher frequencies than standard wire bonding [42]. Other

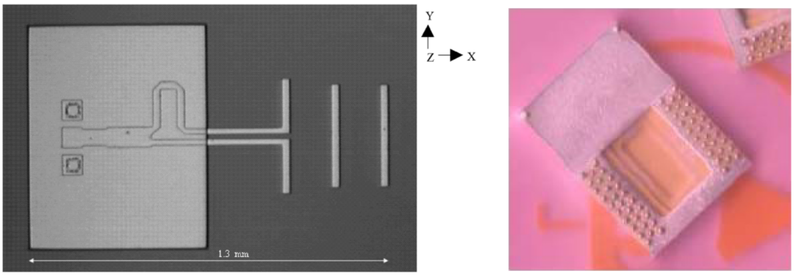

**Figure 1.8:** Yagi antenna-in-package (AiP) (left) [44], and quasi-Yagi antenna-on-chip (AoC) [31] (right).

techniques such as coupling inter-connections can be performed in many forms, being designed using capacitive connections between different components in the same package. This technique could be very useful for integrating multiple chips and antennas into a single package [30]. As a example, in Fig. 1.8, two different fabricated prototypes of Yagi AiP [44] and AoC [31] philosophies are shown.

### 1.3.2 Antenna Solutions for Automotive Radar Systems at 79 GHz

During the last years the aim for further developments has been to make radar available for safety functions like adaptive cruise control (ACC), forward collision alert, rear traffic crossing alert, or blind spot detection. Thus, sensors have to look into all directions around the vehicle with differently defined scanning and distance relations. As a consequence, a much wider field of view compared to ACC is required, resulting in some kind of imaging of the scenery in front of the sensor. Thus, much more effort has been put to the design of novel antenna concepts, partly in combination with modified overall sensor arrangements, including multi-beam antennas, scanning antennas, switched-beam antenna concepts, and beam-forming approaches with multiple transmit and receive antennas.

The choice and design of the respective sensor antennas are determined also by the requirement for high gain, low loss and beam-steering capabilities, combined with small size and depth for vehicle integration, the stated above challenges by the millimeter-wave frequency range, and a great cost pressure for this commercial application. Consequently, planar antennas are dominating in the lower frequency range of automotive radar around 24 GHz, while lens and reflector antennas had been the first choice at 79 GHz. For example, in far range applications at 79 GHz frequency band, typical antenna beamwidths required are in the range of 3º-4º, resulting in antenna apertures from 60 to 100 mm, which lead to gain values of around 30 dB [49].

With increasing requirements towards a much more detailed observation of the scenery in front or around the vehicle, multi-beam antennas or scanning antennas have been designed, and solutions based on digital beam-forming with a number of integrated antennas are in use or under development nowadays.

#### 1.3.2.1 Reflector and Lens Antennas

First antennas for automotive radar applications at 79 GHz were realized as lens antennas [50], or parabolic refector antennas [49], due to the aforementioned high gain and narrow beamwidths requirements. As the sensor depth is of great concern due to the limited space for integration into the vehicle surface, folded configurations of such antennas have been developed [51, 52]. In [53], the lens or curved reflectors have been replaced by a planar reflectarray printed structure which, at the same time, can perform focusing of an incident spherical wave and twist the polarization. Common rectangular printed patch antennas are the typical reflecting elements in a reflectarray. This type of antenna with three discrete beams (generated by three different feed locations) has been implemented into the second generation of Mercedes-Benz radars, and this principle is also used in the third generation sensors.

Lens and reflector antennas are very interesting because they typically exhibit very low losses, advantageous in combination with millimeter-wave semiconductor elements for power generation of quite moderate level, but usually they require a non-negligible depth of a few centimeters because their bulky structure. In this sense, there are not flat lenses reported in the literature (!) for automotive radar applications around 79 GHz and thus, planar antennas have been gaining more interest for their facility in the integration on the vehicle structure.

#### 1.3.2.2 Planar Antennas

The most common type of planar antennas is based on microstrip [54,55]. Single antenna elements can be half-wavelength resonators (dipoles or patch antennas) or the open end of a microstrip stub. These elements can be combined in series and/or parallel arrangements to form antenna arrays with the required overall antenna diagram. Typically, microstrip antennas exhibit bandwidths in the range of 1-2%, increasing with the use of lower dielectric permittivity substrates and substrate thicknesses. However, the later leads to an increased radiation also of the feeding network and to the excitation of surface waves. A way out of this may be feeding the patch from the backside via a slot in the ground plane. Single-patch antennas can be used as feeding elements for a lens antenna [50], or arrays of microstrip patches can be used directly as automotive antennas [56–59]. For larger antenna arrays, feeding network losses may pose a limit for antenna size.

An alternative approach to planar antennas is based on dielectric guides, exhibiting lower loss compared to microstrip solutions. To form an antenna, a dielectric guide typically is loaded with periodic perturbations where part of the guided power is radiated, and the fields superpose to form the overall far field radiation diagram [49].

A final antenna type to be mentioned in this section is the waveguide slotted array. It typically consists of a metal waveguide with longitudinal or transverse slots [60]. Once again, radiation contributions from a high number of slots add constructively in phase to form the desired radiation pattern. For an easy and low-cost fabrication of such arrays, a substrate integrated waveguide (SIW) can be realized within a dielectric substrate where the side walls are formed by rows of vias [61, 62].

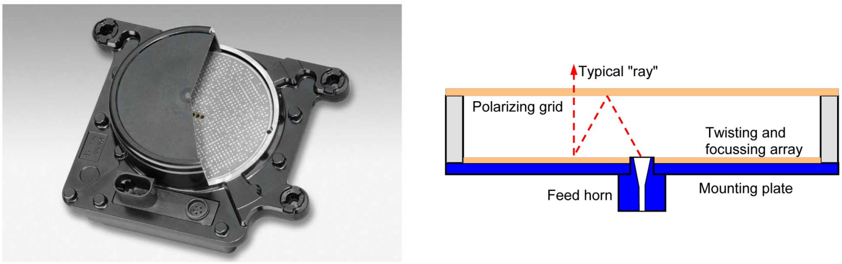

**Figure 1.9:** Cross section (right) and photograph (right) of a folded reflectarray antenna (90 mm in diameter) for automotive radar applications at 76.5 GHz [49].

#### 1.3.2.3 Phased-Array Antennas

Phased-array antennas can provide high gains and beam-steering capabilities. However, they require a complex integration of many expensive, lossy and bulky circuits such as solid-state phase shifters and beam-forming networks. And this could be more difficult at millimeter-wave frequencies. An alternative is to use several antenna elements or sub-arrays and either switch these successively to a receiver or transmitter, or connect them to multiple transmit–receive circuits, easily done with recent Monolithic Microwave Integrated Circuits (MMICs) [57]. With an appropriate digital beam-forming processing different radiation diagrams and beam shapes can be adjusted simultaneously, thus being able to measure the scenery in front of a car with high precision [51,63,64]. However, this is still an expensive antenna solution from any point of view.

#### 1.3.2.4 Additional Considerations on Automotive Radar Antennas

Finally, it is important to consider and stress that the whole structure of the antenna and the radar sensor has to be protected by a suitable package in the vehicle structure. The radome, the cover in front of the antenna, must be transparent to the electromagnetic waves in the respective frequency range, leading to an optimized thickness for the used plastic materials in the order of multiples of half a guide wavelength within the material. This optimized thickness only is perfect for one angle of radiation. For all other angles there is a performance degradation due to multiple-reflections. In Fig. 1.9, an example of typical reflectarray application for automotive radar sensors is shown.

### 1.3.3 Antenna Solutions for Radar, Imaging and Communications at 94 GHz

In the same way as it has been described for the previously considered applications at the two presented lower frequency bands , high-gain antennas with beam-steering capabilities are also needed in passive imaging, radar, and communication systems around 94 GHz band (from 92 to 95 GHz) [21]. Focusing our attention specifically to imaging systems, since radar and communications systems at 94 GHz have similar issues to be solved as in the previous radar and communication systems at described frequency bands, it is necessary to mention that for recent imaging applications is preferred to control electronically the beam-scanning of the radiation beams [65], instead of using mechanically front fed antenna systems to provide the required scan profile, as it is still performed, for example, in most of the imaging systems nowadays.

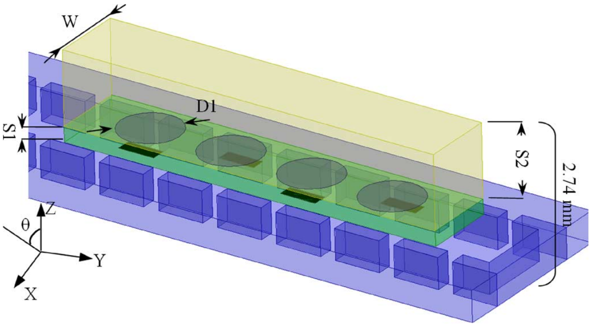

**Figure 1.10:** 94 GHz substrate integrated waveguide (SIW) antenna array layout introduced in [70].

One important factor that determines the imaging system resolution comes from the setup configuration. In general, precise profile reconstruction requires range (depth) and cross-range (angular position) information. Under the assumption of mechanically fixed transmitter and receiver in a monostatic configuration, range information is provided by the radar system bandwidth. Cross-range information can be achieved either by using fixed-beam antennas and placing the object-under-test on top of a rotary platform, or by means of beam scanning systems. Sometimes, rotation of the object-under-test is not possible, thus leaving beam-scanning methods as the only way to gather cross-range information, which is given by the knowledge of the beam steering angle [66]. Therefore, beam-steering has to be controlled by means of complex mechanical or electronic systems, which may become prohibitive at millimeter-wave frequency bands [65].

In this sense, at 94 GHz, the common adopted antenna solution for electronically beam-scanning imaging systems is based on the phased-array concept, with their beam-forming and electronic beam-steering capabilities of high gain radiation beams (e.g. a W-band scalable phased array for imaging and communications [67]). Nevertheless, as it has been mentioned before, this solution involves a complex integration of many phase-shifters and lossy beam-forming networks, which finally lead to a bulky structure [67], when compact and planar antenna solution is needed.

Several planar antennas in LTCC technology and printed circuit board (PCB) processes have been reported for the considered applications in the 94 GHz band [68]. For example, a wideband stacked 4 by 4 patch antenna array fed by Wilkinson power dividers on LTCC substrate achieved a maximum realized gain of up to 14.2 dB in [69]; a circular patch array fed by a SIW, which offers up to 18.8 dB gain [70]; or a dielectric-loaded antipodal linearly tapered slot antenna array of 4 elements, which delivers 19 dB gain [71]. However, despite their planar implementation, they result in a bulky volume due to complicated feeding networks and sophisticated realization issues (e.g. see Fig. 1.10 [70]), suffering from low radiation efficiencies.

Microstrip grid antenna and mesh arrays have received a great attention in recent years for 94 GHz applications [68, 72]. However, despite the acceptable provided gain values around 13-14 dB, the beam-steering capabilities are very limited, or in the worst case, not allowed.

## 1.4 Motivation

As it has been stated during the previous sections, in recent years, the scientific community and the industry have focused their attention on different frequency bands that could satisfy the increasing bandwidth requirements of modern communication, radar, and imaging systems. Given the large amount of bandwidth available, the millimeter-wave frequency band represents one of the most interesting candidates. In fact, different sub-bands of the millimeter-wave spectrum seem promising for future 5G communication systems, including the 28-30 GHz band, the 60 GHz band, and the E-band at 71-76 GHz, 81-86 GHz, and 92-95 GHz. This large amount of bandwidth combined with the small system wavelength allow for the development of compact very high throughput (>1.5 Gbps) wireless communication systems, very accurate long-range automotive radar applications, or fast scanning millimeter-wave imaging systems. However, in accordance with the Friis transmission formula, for a fixed distance, the path loss in free-space propagation is much higher at millimeter-wave frequencies than at lower microwave frequencies (e.g. the path loss at 60 GHz is 21 dB higher than at 5 GHz). In consequence, millimeter-wave systems introduce a set of particular requirements from the antenna point of view in order to achieve specific performances. In this sense, high directive antennas are required to overcome the aforementioned extra path loss. Moreover, each particular application introduces additional requirements. For example, in very high throughput 60 GHz band (from 57 to 64 GHz in the Unites States) wireless personal area networks (WPANs) beam-steering antennas are needed to deal with high user random mobility and human-body shadowing characteristic of indoor environments. Similarly, beam-steering capabilities are also needed in automotive radar applications at 79 GHz band (from 77 to 81 GHz, already allocated in Europe), since the determination of the exact position of an object is essential for most of the functions realized by the radar sensor, which has to look into all directions around the vehicle in adaptive cruise control, blind spot detection, or collision avoidance functions for future medium and short-range radar applications. In the same way, high-gain antennas with beam-steering capabilities are also needed in passive imaging, radar, and communication systems around 94 GHz band (from 92 to 95 GHz), in which it is preferred to control electronically the beam-scanning of the radiation beam, instead of using mechanically front fed antenna systems to provide the required scan profile. Finally, the antennas must be small, low-profile, light weight and low-cost, in order to be successfully integrated in a commercial millimeter-wave wireless system.

Therefore, although many types of antenna structures have been described for the considered millimeter-wave applications around 60, 79 and 94 GHz bands, the most common antenna solution in order to achieve high-gain and beam-steering capabilities in both theta and phi directions of the space is still traditionally based on the complex phased array antenna concept. Phased-array antenna systems can scan at a fast rate. However, they require a complex integration of many expensive, lossy and bulky circuits, such as solid-state phase shifters and beam-forming networks. Due to their high gain and wide bandwidth, aperture antennas, such as profiled lenses, are commonly used at millimeter-wave frequencies for communications, radar, and imaging applications. However, either their planar implementations allow only one-dimension (1-D) beam-steering, instead of 2-D, or their traditional shaped configurations, with the required 2-D beam-scanning capabilities, result in a bulky antenna structure difficult to integrate in a compact millimeter-wave commercial system.

For these exhaustively explained reasons, in the present thesis, we will contribute with a different approach to model, analyze, fabricate, and experimentally evaluate the performance of different alternatives, based on inhomogeneous dielectric flat lenses as a fundamental part of the switched-beam antenna array concept, instead on the current antenna designs existing in the literature at millimeter-wave frequencies, in order to solve the specific problems associated to the antennas at this high frequency band.

## 1.5 Objectives of the Thesis

The main objective of this doctoral thesis is the study, development, and assessment of the performance of innovative antenna solutions in order to improve the existing architectures at millimeter-wave frequencies, conveniently solving the problems related specifically to short-range high data rate communication systems at 60 GHz WPAN band, including future 5G millimeter-wave systems, automotive radar sensors at 79 GHz band, and communications, radar, and imaging systems at 94 GHz. The specific goals pursued in this work focus on defining an alternative antenna architecture able to achieve a full reconfigurable 2-D beam-scanning of high gain radiation beams at millimeter-wave frequencies. These goals are based on a transversal study, which encompasses theoretical investigations, numerical analysis, new fabrication strategies, performance evaluation, and full experimental assessment of the new antenna architectures in real application environment. A detailed enumeration of the partial objectives of the thesis can be summarized as follow:

- Perform a theoretical study, and propose novel antenna architectures and topologies to solve the specific problems associated to the electromagnetic propagation at millimeter-wave frequencies in order to achieve full beam-steering capability of high gain radiation beams. The new introduced antenna solutions must preserve a planar antenna structure, easy to manufacture, with broadband operation behavior, low-cost, high-efficiency, small overall size, and lightweight in order to be fully integrated in a compact millimeter-wave wireless commercial system.
- Perform an exhaustive numerical analysis of the new proposed antenna architectures to support the theoretical studies.
- Explore different fabrication alternatives for the new proposed antenna architectures, finally proposing an specific methodology and recommendations for future mass production.
- Completely experimentally evaluate the performance of the introduced novel antenna solutions, fully characterizing their behavior for the considered millimeter-wave applications.
- Finally, execute an experimental assessment of the proposed antenna architectures, comparing their performance to other existing antennas solutions in a real indoor environment, evaluating and analyzing their efficiency with wireless channel statistic parameters, from a realistic point of view, to confirm the potential applicability of the proposed antenna solution for future wireless millimeter-wave communication systems and, in this way, concluding a complete transverse analysis, not only from the electromagnetic characterization point of view, but also from the real application perspective.

Furthermore, the collaboration with researchers of different international institutions is also an additional objective. In this sense, during this doctoral work, we extended our collaboration with researches of the following Universities:

- University of California at Irvine
- Universitat Politècnica de València
- Universidad Politécnica de Cartagena
- Utah State University

## 1.6 Outline and Organization of the Document

This doctoral dissertation is organized in nine chapters, including this first chapter, which introduces the framework and reviews the current state of the art to establish the basis of the subsequent sections. Additional information is also distributed in three appendices at the end of the thesis. The main contents of each chapter is summarized as follows:

- **Chapter 2** addresses the design of an inhomogeneous gradient-index dielectric flat lens. First, the flat lens antenna concept and its functioning principle are introduced, providing the most fundamental design guidelines. Then, a specific dielectric flat lens model is presented for millimeter-wave applications. This model is theoretically described, numerically simulated, practically fabricated, and fully electromagnetically tested. This lens represents the fundamental part of the switched-beam antenna array concept, which it is also introduced at the end of the section.
- **Chapter 3** is specifically devoted to the design of a matching to increase the maximum achievable gain, reduce the back-radiation level, and enhance the bandwidth performance of a dielectric flat lens antenna for millimeter-wave applications. The performance of the original inhomogeneous gradient-index dielectric flat lens is compared to the performance of the lens with an inhomogeneous matching layer, and to the performance of the lens with a novel multiple-stacked inhomogeneous matching layer design.
- **Chapter 4** is intended to give an alternative solution to reduce the number of switching elements needed to perform a full 2-D beam-scanning of high gain radiation beams. A new switched-beam antenna array concept based on an inhomogeneous dielectric flat lens with a cylindrical effective parameter distribution is introduced. With this cylindrical parameters distribution, the beam-scanning can be performed in one plane by moving (or selecting) the position of a radiating single element along the gradient-index axis, whereas the beam can be maintained invariant in the other direction, despite changing the radiating element position. In this way, the beam-scanning can be achieved in the constant-index axis of the lens by means of a different technique, a frequency-scanned slot antenna array, in order to reduce the switching elements needed in the proposed complete switched-beam antenna array structure, to finally perform the scan of the high-gain radiation beam in both theta and phi dimensions of the space.
- **Chapter 5** addresses the design of a frequency-scanned stripline-fed transverse slot antenna array. Taking advantage of the huge amount of bandwidth allocated at

60 GHz frequency band for communication applications, a linear array of transverse slot antennas fed by a meandering stripline structure is designed to achieve beam-steering in one single plane by sweeping the carrier frequency, in order to be placed together with the presented cylindrically distributed parameters dielectric flat lens to obtain a full 2-D scanning capability.

- **Chapter 6** is devoted to study the potential fabrication of the designed inhomogeneous perforated flat lenses in low-temperature co-fired ceramics (LTCC) technology. This technology allows processing different layers separately, preserving a planar profile, thus making possible the integration of the dielectric flat lenses together with the designed arrays in different substrate layers, which are later stacked together, laminated, and co-fired (sintering process), in order to build a single monolithic structure.
- **Chapter 7** is intended to describe the final design, numerical simulation, practical fabrication, and experimental evaluation of the complete switched-beam antenna (SWBA) array structure performance based on both presented inhomogeneous dielectric flat lens with its effective parameters cylindrically distributed and frequency-scanned slot antenna (FSSA) array. The full SWBA array architecture is finally introduced to realize not only a one-dimensional (1-D) beam scanning, but a two-dimensional (2-D) beam scanning of high-gain radiation beams, reducing the switching elements needed in a compact millimeter-wave antenna solution, preserving a planar antenna profile, easy to integrate in a single monolithic structure with LTCC technology.
- In **Chapter 8** the performance of three inhomogeneous perforated lenses is experimentally evaluated and compared to a single omni-directional antenna and to a 10-element uniform linear array (ULA) of omni-directional antennas in real 60 GHz WPAN indoor line-of-sight (LOS) and obstructed-LOS environments, obtaining interesting and promising remarkable results in terms of measured received power and root mean square (RMS) delay spread, confirming the potential applicability of the proposed antenna solution for future 5G wireless millimeter-wave communication systems.
- **Chapter 9** presents the main conclusions and contributions of this doctoral thesis, as well as some insights of eventual continuations of the present research.

Furthermore, at the end of this document, additional contributions carried out during this thesis are also briefly explained and summarized.

# 2

## Chapter 2

# Inhomogeneous Dielectric Flat Lens Principles and Design

*The design of an inhomogeneous gradient-index dielectric flat lens is the central topic of this section. First, the flat lens antenna concept and its functioning principle are introduced, providing the most fundamental design guidelines. Then, a specific dielectric flat lens model is presented for millimeter-wave applications. This model is theoretically described, numerically simulated, practically fabricated, and fully electromagnetically tested at 60* GHz *WPAN frequency band for short-range communication systems, at 79* GHz *for automotive radar applications, and at 94* GHz *for passive imaging systems. This lens represents the fundamental part of the switched-beam antenna array concept, which it is also introduced at the end of this section.*

## 2.1 Introduction

At millimeter-wave frequencies, in order to achieve high data rate wireless communications, to determine the exact position of a target with a radar system, or to perform an adaptive scanning with an imaging technique, it is essential to dispose of high-directive antennas with certain beam-steering capabilities. In consequence, to provide an alternative solution to the aforementioned issues related to antennas and electromagnetic propagation at these high frequencies, we introduce a new switched-beam array antenna concept based on a innovative inhomogeneous gradient-index dielectric flat lens, which steers and enhances the radiation in a particular direction.

Switched-beam arrays provide an interesting alternative because they have a set of multiple fixed beams that can be easily selected individually, and the implementation is much easier, cheaper, and less bulky than the solutions based on the phased-array antenna concept, which is the traditional alternative to achieve high-gain and beam-scanning capabilities at millimeter-wave frequencies [30].

The proposed antenna concept is depicted in Fig. 2.1. It consist of a planar array of radiating elements placed at focal distance from the lens, which performs the radiation improvement. In this antenna concept only one element of the array is selected by the switch (SW) for each operation mode. The low-gain radiation pattern of the individually selected radiating element of the array is steered and enhanced by the lens into a high-gain radiation pattern pointing in a particular direction. This focusing direction depends on the position of the selected element.

The introduced antenna solution is very attractive because represents an innovative alternative to the existing antenna configurations at millimeter-wave frequencies to achieve a two dimensional (2-D) beam-scanning of high-gain radiation beams, while keeping at the same time a flat antenna profile, much thinner than conventional existing shaped lenses, leading to a low-profile, light weight and low-cost antenna solution, in order to be successfully integrated in a commercial wireless system.

In the following sections, the fundamental part of this proposed structure, i.e. the inhomogeneous gradient-index dielectric flat lens, is described and exhaustively numerically evaluated for a practical prototype fabrication and full experimental verification.

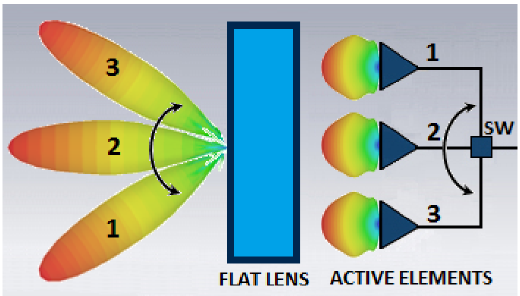

**Figure 2.1:** Switched-beam array antenna concept based on a dielectric flat lens.

## 2.2 Dielectric Flat Lens Concept Description

A lens is a three-dimensional structure, through which electromagnetic waves can pass, possessing an index of refraction that may be a function of position and a shape that is chosen so as to control the exiting aperture illumination (Institute of Electrical and Electronics Engineers (IEEE) [73]). Therefore, fundamentally, it is used to control and manipulate the electromagnetic radiation to obtain specific performances. In this sense, any lens can be seen a Fourier transforming device.

Multiple varieties of lenses have been considered in the literature; both homogeneous and inhomogeneous. Homogeneous material lens designs are reported in various shapes, such as cylinders, spheres, ellipsoids, hemispheres, or even hyper or hypo-hemispheres [74]. However, despite several efforts dedicated to reduce the size of dielectric lens antennas [75], they still remain bulky, especially at millimeter-wave frequencies for high data rate communication applications [76]. On the other side, the electromagnetic behavior of inhomogeneous dielectric lens [77] has been documented by extensive studies from the 1950s, but a planar implementation of this type of lenses to allow 2-D beam-scanning at millimeter-wave frequencies is still needed.

In this sense, many types of inhomogeneous (multi-material or gradient-index) lenses have been proposed in the literature for millimeter-wave applications [78–84]. Fresnel zone plate lenses [78] have been widely used to correct the phase of the feeding antenna. However, this correction is performed only at some discrete locations, leading to an inherently narrowband behavior. Luneburg lenses [79, 80, 82], Maxwell fish-eye [81, 82], Eaton or Eaton-Lippmann lenses [83], and Nomura-Takaku lenses [84], are interesting solutions of spherical or hemispherical gradient-index lenses because of their very good performance at millimeter-wave frequencies. However, their planar implementations allow only one-dimension (1-D) beam-steering, instead of 2-D. Therefore, a novel inhomogeneous gradient-index dielectric flat lens design is introduced in order to achieve the desired 2-D beam-steering of high-gain radiation beams at millimeter-wave frequencies, preserving a planar antenna structure. With the purpose of designing the dielectric flat lens, the principle of field transformation (FT) described in [85, 86] is followed, instead of the transformation optics (TO) approach.

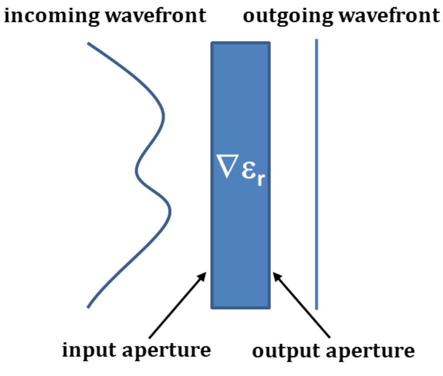

**Figure 2.2:** Field transformation principle.

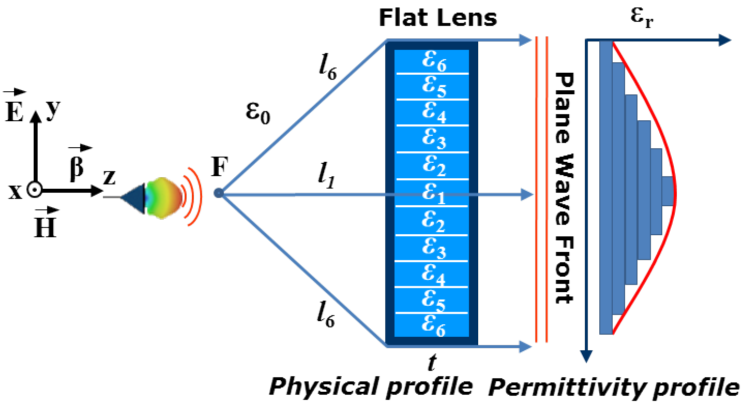

**Figure 2.3:** Dielectric flat lens functioning principle.

With this methodology, the range of the constitutive material parameters and their 3-D distribution in the lens can be selected, thus ensuring the practical viability of the design, offering flexibility in controlling the fields traversing through the lens from the input to the output in order to obtain a specific desired field distribution at the output of the lens [86]. We simply need to specify the desired field distribution at the output of the aperture and determine the parameters of the medium placed in between (i.e. the lens), to transform the field distribution at the input aperture, as it is shown in Fig. 2.2. This performance can be accomplished in many cases by tracing rays through the inhomogeneous medium (i.e. the lens) that we are trying to synthesize [86].

## 2.3 Dielectric Flat Lens Functioning Principle and Design

The design parameters of the lens are its center operating frequency ($f = 60\,\text{GHz}$), its focal length ($F$), the thickness ($t$) and the maximum achievable gain. In this sense, gain values greater than 14 dB, or even 20 dB are required to ensure acceptable system performance and range around 60 GHz, as it has been reported in [76,87]. Therefore, we determine the lens diameter dimensions by using the classical formulation for an aperture antenna, which states that the maximum achievable gain is given by,

$$G_{max} = \epsilon \frac{4\pi}{\lambda_0^2} Ap \tag{2.1}$$

where the maximum achievable gain ($G_{max}$) depends on the effective aperture size of the antenna ($A_p$), on the free-space wavelength ($\lambda_0$), and on the aperture efficiency ($\epsilon$). If we neglect the edge effects, the spill-over, and other loss-related effects, and considering the electric field perfectly uniform in phase and amplitude across the whole lens aperture, which means that the aperture efficiency is 1, or close to this value, the maximum achievable gain with a circular aperture of 25 mm in diameter would be 23.9 dB at 60 GHz. However, it is very difficult to obtain such ideal situation, and aperture ef-

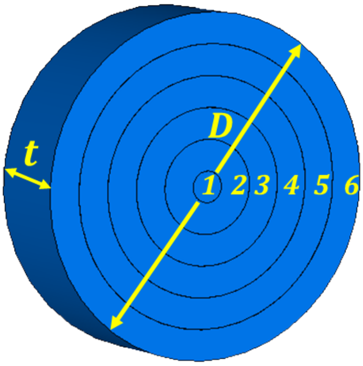

**Figure 2.4:** Dielectric flat lens model discretization.

ficiencies between 60 and 70% are more realistic approximations, which finally decrease the maximum gain. Then, we fixed the lens diameter value in 25 mm ($5\lambda_{60GHz}$), which represents a good trade-off between the maximum aperture dimensions in order to achieve the smallest design as possible, and the gain needed for the aforementioned applications at millimeter-wave frequencies. In the same way, we fixed the lens thickness $t = 7\,\mathrm{mm}$ ($1.4\lambda_{60GHz}$), with a focal distance $D = F/4$, and the level of discretization of the material parameters along the lens radial direction, which is determined after an optimization process with the maximum gain as a goal, being defined in a set of six concentric rings with a different relative permittivity ($\epsilon_r$) for each one, as it is depicted in Fig. 2.4. Once the design parameters have been established, the phase required at the output aperture plane of the lens is calculated using the condition that a plane wave incident upon the input aperture plane interferes constructively at the focal point of the lens.

Then, we start the design procedure by setting the dielectric constant of the outer ring of the lens to $\epsilon_r = 2.25$, which is a feasible value for the available commercial substrate materials. The relationship between the wavenumber ($k$) and the material parameters is given by [88],

$$k_1 = \frac{2\pi\sqrt{\epsilon_{r_1}}}{\lambda_0} \tag{2.2}$$

Next, we enforce

$$k_0 l_1 + k_1 t = k_0 l_6 + k_6 t \tag{2.3}$$

to realize the required phase behaviors associated with two different electrical path lengths that travel through the free-space and the media of the specific dielectric zone, as it is depicted in Fig. 2.3, where the lens functioning principle is shown. In Equation (2.3), $l_1$ and $l_6$ are the corresponding distances from the lens focal point $F$ to the center of rings 1 and 6, respectively, as it is also depicted in Fig. 2.3.

Then, the relative permittivity of the central ring is obtained by using

$$\epsilon_{r_1} = \left(\frac{l_6 - l_1 + \sqrt{\epsilon_{r_6}}t}{t}\right)^2 \tag{2.4}$$

**Table 2.1:** Inhomogeneous dielectric flat lens parameters.

| Ring | Ring width | $\epsilon_r$ |
|---|---|---|
| 1 | 1.14 mm | 6.05 |
| 2 | 2.27 mm | 5.77 |
| 4 | 2.27 mm | 5.06 |
| 1 | 2.27 mm | 4.13 |
| 5 | 2.27 mm | 3.16 |
| 6 | 2.27 mm | 2.25 |

in order to ensure that the maximum phase delay introduced by the lens zone is commensurate with the chosen focal length.

Therefore, the theoretical lens design has been modeled with a set of six concentric rings of different permittivity materials, in order to produce the desired phase delays required to obtain a plane wave behind the lens (i.e. at the output aperture plane), when the lens is illuminated with a source from its central focus position. In the same way, when the feeding position is moved along $y$-direction (see Fig. 2.3), the different permittivity values of the lens produce a linear phase slope that steers the beam, accordingly.

Moreover, we optimized the design considering the limitations in the subsequent fabrication process, and to lower the effective permittivity values required to avoid the considerable reflections that could occur between the radiating elements and the lens (due to the change of media). Then, the maximum permittivity value on the lens (center of the lens) is $\epsilon_r = 6$, decreasing continuously and smoothly to on the edges, creating the desired permittivity profile (see Fig. 2.3). Consequently, the characteristic parameters for the dielectric flat lens modeled with different permittivity materials are summarized in Table 2.1.

## 2.4 Multi-Dielectric Material Flat Lens Simulation Results

The inhomogeneous dielectric flat lens design modeled with different permittivity materials has been numerically simulated using Computer Simulation Technology (CST) Microwave Studio, which applies the finite-difference time-domain (FDTD) method, with a time-domain solver in order to test its focusing capabilities and complete response in a wide frequency band of interest (from 57 to 66 GHz). High Frequency Structure Simulator (HFSS), which applies the finite elements method (FEM) method instead, has also been used as a numerical tool only for comparison purposes, obtaining very similar results. However, in order to get the frequency response for an extended band (not only from 57 to 66 GHz, but also in the whole W band, up to 110 GHz), the CST solver performed faster than HFSS in the same setup conditions. Therefore, the CST Microwave Studio has been used to obtain all the numerical results reported in the present doctoral thesis.

A complete set of nine different simulations have been performed corresponding to different discrete positions of a radiating element (which could correspond to the positions of the antenna element in a switched-beam array) along the $x$-direction, going

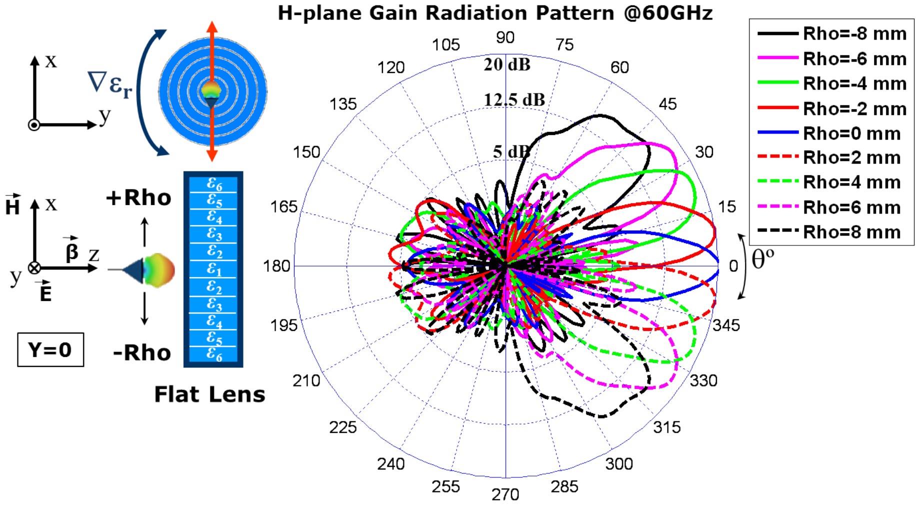

**Figure 2.5:** H-plane gain (dB) radiation pattern CST simulation results at 60 GHz for each *Rho* feeding position.

from $Rho = -8\,\text{mm}$ to $Rho = +8\,\text{mm}$ in steps of 2 mm (see Fig. 2.5), testing the gain performance and beam-steering capabilities of the lens. The radiating element used consists of a rectangular aperture, a WR-15 open-ended waveguide model, with the E-field linearly polarized along the $y$-direction, which provides an efficient illumination of the lens with around -14 dB edge taper in the H-plane. The WR-15 model is well-matched ($S_{11} < -10\,\text{dB}$) in the whole frequency band and for all the feeding positions. Then, for each *Rho* position of the feeding waveguide, the corresponding H-plane gain radiation patters are plotted at 60 GHz in Fig. 2.5. The simulation results at 60 GHz indicate that with the proposed design we are able to achieve up to 20.3 dB of broadside gain, beam-steering capabilities in both planes from -25º to +25º with around 18.8 dB gain, and up to ±45º with more than 16 dB gain, with low SLL, which are below -10 dB for all the cases. Note that given the lens symmetry identical E-plane radiation patterns are obtained when the lens is fed in the same way as for the H-plane, and therefore are not shown. Moreover, very good gain stability within the whole 60 GHz band is observed from the simulated bandwidth performance, plotted in Fig. 2.6. Furthermore, although the original lens has been designed at 60 GHz, the concept is not only scalable at higher frequencies, but also the original lens shows good performance at 79 and 94 GHz. In this sense, to demonstrate the broadband behavior of the proposed design, the lens has been also numerically tested at these two considered higher frequency bands, obtaining similar beam-steering capabilities, without pattern distortion, presenting very good gain stability. This remarkable behavior is also observed, in Fig. 2.6, in the simulated bandwidth performance, for both additionally considered frequency bands of interest, respectively. Note that for the 79 and 94 GHz bands, simulations have been realized replacing the WR15 open-ended waveguide for a WR-10 model, which is also well-matched over the whole W-band (75-110 GHz). From simulation results we also obtain total and radiation efficiencies around 90-95% for the lens fed with the corresponding rectangular apertures.

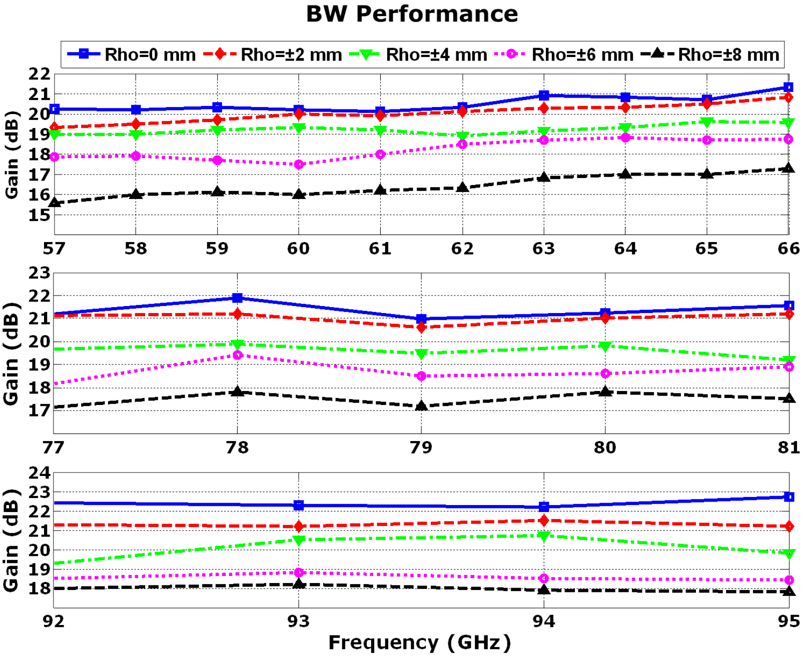

**Figure 2.6:** Simulated bandwidth performance: maximum gain (dB) for different focusing directions at 60 GHz WPAN band.

Practically, inhomogeneous lenses can be manufactured by assembling a finite number of concentric homogeneous dielectric shells [81, 82, 89]. This technology leads to a lens with uniform thickness, but the manufacturing complexity involved in precisely machining various materials into tight-fitting concentric rings makes this approach costly and not the best suitable, especially at high frequencies and, moreover, because air gaps can affect the efficiency of the lenses. Recently, a new technological process has been proposed to easily manufacture inhomogeneous Luneburg lenses, in which a foam material is pressed, to increase its concentration by releasing the trapped air, to achieve the different dielectric constants needed to follow the index law inside the lens [90]. However, this method provides a very limited range of permittivity values, since the initial permittivity of the foams is around 1.3, being able to offer permittivity values up to 2-2.5 after pressing, making this solution not appropriate in our case.

## 2.5 Perforated Dielectric Characterization

Because the difficulty in fabricating lenses through the fusion of different permittivity materials, alternative methods have to be contemplated. In this sense, the relative permittivity of a dielectric substrate material can be modified, modeled, and shaped by perforating the substrate [78, 79]. This perforations can be implemented as a uniform lattice of holes drilled through the substrate. If the diameter of the holes ($d$) and the separation between them ($s$) in this lattice are kept smaller compared to the wavelength

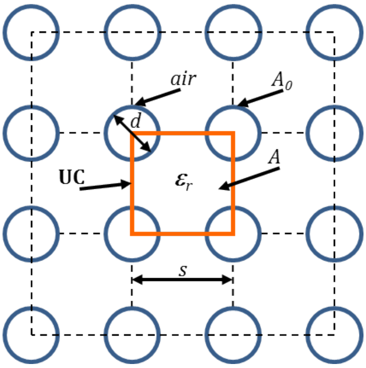

**Figure 2.7:** Perforated dielectric substrate modeling by square lattices.

of operation, the substrate will appear to have a uniform effective relative permittivity. This effective permittivity can be controlled by the diameter of the holes: the larger the hole diameter, the lower the effective permittivity for a given substrate material. The technique is well-known from many years ago [79], and more recently it was used to improve the radiation patterns and efficiencies of microstrip patch antennas [91, 92].

A perforated dielectric substrate with either square or triangular lattices considered to perform the perforations are shown in Fig. 2.7 and Fig. 2.8, respectively. They consist of a layer of dielectric material with a relative permittivity $\epsilon_r$, which is perforated by a set of holes of diameter $d$, arranged in uniform lattices, square or triangular. If the hole diameter and spacing remains less than a half-wavelength inside the dielectric material, it has been observed that the effective dielectric constant of the substrate will approximately be the volumetric average of the free-space holes and the remaining dielectric material [92]. This volumetric average model has been found to be insensitive to the exact hole geometry. This approach for lowering the dielectric constant of the substrate material has the advantage over using different substrate materials to create the same effect because it is monolithic in nature and can be realized using micro-machining techniques.

Moreover, using this technique there is considerable freedom in the range of lower effective dielectric constant values achievable by simple choice of the perforation geom-

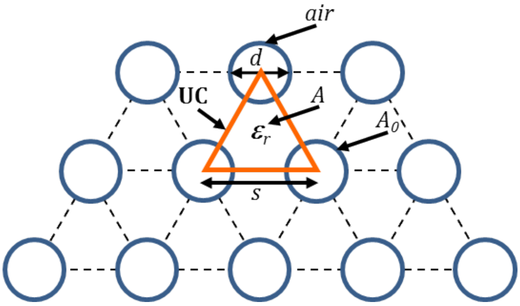

**Figure 2.8:** Perforated dielectric substrate modeling by triangular lattices.

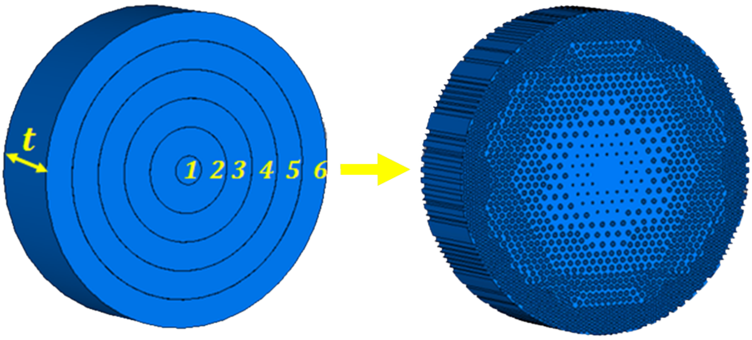

**Figure 2.9:** Modeling of the inhomogeneous dielectric flat lens by perforations.

etry, going from the highest permittivity value in the host material, to the air relative permittivity ($\epsilon_r$=1). Then, a static model is used to predict the value of the effective relative permittivity based on the area filling factor of the perforation lattice (fraction of area or volume of material removed from the substrate layer).

Therefore, the unit cell concept is adopted in order to derive the equations based on this model, considering the arrangement in uniform lattices as it is depicted in Fig. 2.7 and Fig. 2.8. In this sense, the effective relative permittivity $\epsilon_{eff}$ can be estimated using

$$\epsilon_{eff} = \epsilon_r(1-\alpha) + \alpha \tag{2.5}$$

where $\alpha$ is the filling factor given by

$$\alpha = \frac{A_0}{2A}, \qquad \text{for a triangular lattice} \tag{2.6}$$

$$\alpha = \frac{A_0}{A}, \qquad \text{for a square lattice} \tag{2.7}$$

where $A_0$ is the area of the perforated hole, and $A$ is the area of the corresponding unit cell. Thus, for the triangular lattice, this yields to:

$$\alpha = \frac{\pi d^2/4}{2(\sqrt{3}/4)s^2} = \frac{\pi}{2\sqrt{3}}\left(\frac{d}{s}\right)^2 \tag{2.8}$$

and for a square lattice:

$$\alpha = \frac{\pi d^2/4}{s^2} = \frac{\pi}{4}\left(\frac{d}{s}\right)^2 \tag{2.9}$$

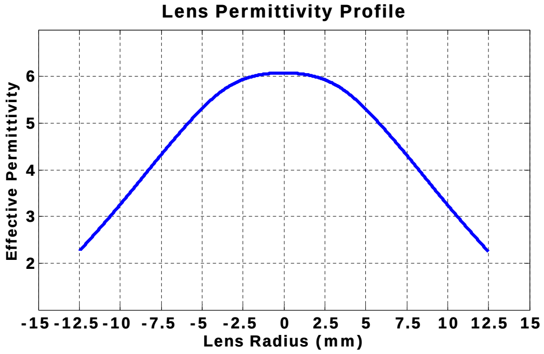

**Figure 2.10:** Permittivity profile required for the designed flat lens.

## 2.6 Perforated Dielectric Flat Lens Design

Following the derived expressions, and for the particular case of introduced the inhomogeneous dielectric flat lens modeled with different permittivity materials, the described method is applied to design the lens by means of perforating a single monolithic substrate material layer, as it is depicted in Fig. 2.9. Then, taking into account the range of permittivities needed to finally model the inhomogeneous flat lens (see Table 2.1), going from the maximum value ($\epsilon_r = 6$, center of the lens), decreasing continuously and smoothly to the lowest value ($\epsilon_r = 2.25$, on the lens edges), the permittivity profile of the final lens is plotted in Fig. 2.10.

The filling factor $\alpha$ is plotted as a function of the diameters of the perforate holes and the distance between them $(d/s)$, for both square and triangular lattice configurations in Fig. 2.11. As it is observed, a higher filling factor is achievable using the triangular lattice since the holes can be arranged closer together than for the corresponding square lattice, thus resulting in a more relaxed $(d/s)$ relationship and fabrication process for a fixed $\alpha$ needed. In practice, the maximum value of $(d/s)$ must be less than one, or else the material will no longer be self-supporting. Consequently, and because the maximum permittivity value on the lens is $\epsilon_r = 6$, we selected a commercial Rogers TMM6 dielectric substrate ($\epsilon_r = 6$, $\tan\delta = 0.0023$) with 7 mm of thickness, as a host material in order to model the perforated lens.

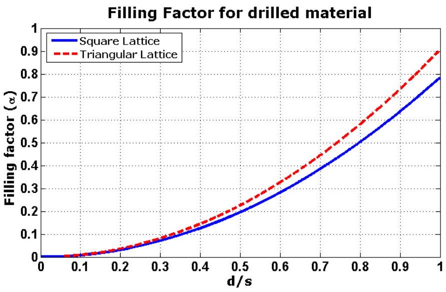

**Figure 2.11:** Filling factor versus $d/s$ relationship.

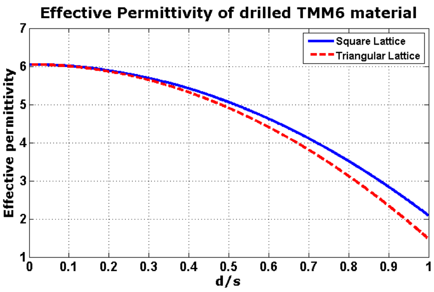

**Figure 2.12:** Theoretical effective permittiviity of the perforated TMM6 substrate.

**Table 2.2:** Perforated inhomogeneous dielectric flat lens characteristic parameters.

| **Ring** | **Ring width** | $\boldsymbol{\epsilon_r}$ | $\boldsymbol{\alpha}$ | $d$ | $s$ |
|---|---|---|---|---|---|
| 1 | 1.14 mm | 6.05 | - | - | - |
| 2 | 2.27 mm | 5.77 | 0.06 | 0.2 | 0.81 |
| 3 | 2.27 mm | 5.06 | 0.2 | 0.5 | 1.08 |
| 4 | 2.27 mm | 4.13 | 0.38 | 0.5 | 0.77 |
| 5 | 2.27 mm | 3.16 | 0.57 | 0.5 | 0.63 |
| 6 | 2.27 mm | 2.25 | 0.75 | 0.5 | 0.55 |

Following the curves of the characteristic parameters $(\epsilon_r, \alpha, d, ands)$ plotted in Fig. 2.12, the final lens model is designed. Triangular lattices are finally employed to model the design, as it has been mentioned before since, for a particular $\alpha$ needed, this results in a less restrictive $d/s$ relationship and subsequent fabrication process. The different perforated dielectric flat lens characteristic parameters of the final lens prototype, using triangular unit cells of holes, are also summarized in Table 2.2.

## 2.7 Perforated Dielectric Flat Lens Simulation Results

The perforated dielectric flat lens design has been simulated at whole 60, at 79, and at 94 GHz frequency bands using CST Microwave Studio with the time-domain solver in order to test its focusing capabilities. In the same way as it has been perofrmed for the different materials lens, for each frequency band, a total of 9 different simulations have been carried out corresponding to different discrete positions of a radiating element along the $x$-direction, going from $Rho = -8\,\text{mm}$ to $Rho = +8\,\text{mm}$ in steps of 2 mm (see Fig. 2.13). The radiating element used consists of a rectangular aperture (WR-15 waveguide for the 60 GHz setup and WR-10 waveguide for 79 GHz) with the E-field polarized in $y$-direction, which provides an efficient illumination of the lens with around -14 dB edge taper in the H-plane. Then, for each position of the feeding waveguide, the corresponding H-plane radiation patterns are plotted at 60 GHz, at 79 GHz, and at 94 GHz, in Fig. 2.13 (a), (b), and (c), respectively. The performance of the perforated dielectric flat lens design has been also compared to the original theoretical design of six rings with different permittivity materials. In Table 2.3, the different radiation pattern characteristic parameters (maximum gain for each focusing direction, steering angle, and -3 dB beamwidth) are summarized for both lens cases, at the three considered frequency bands of interest. As it is shown, the performances achieved with the Rogers TMM6 dielectric substrate perforated lens are comparable to the performances obtained with the original theoretical lens of six different permittivity materials, confirming the good approach achieved with the proposed modeling technique. The simulation results at 60 GHz indicate that with the proposed design we are able to obtain up to 19 dB of broadside gain, beam-steering capabilities in both planes from -20º to +20º with around 17.5 dB gain, and up to ±40º with more than 15 dB gain, with low SLL. Note, once again, that given the lens symmetry identical E-plane radiation patterns are obtained when the lens is fed in the same way as for the H-plane, and therefore are not shown. In some specific cases, the performance obtained with our numerical results in terms of maximum gain is even better with the perforated lens (e.g. for the broadside focusing direction at 94 GHz). This is a remarkable result, because for the different materials lens

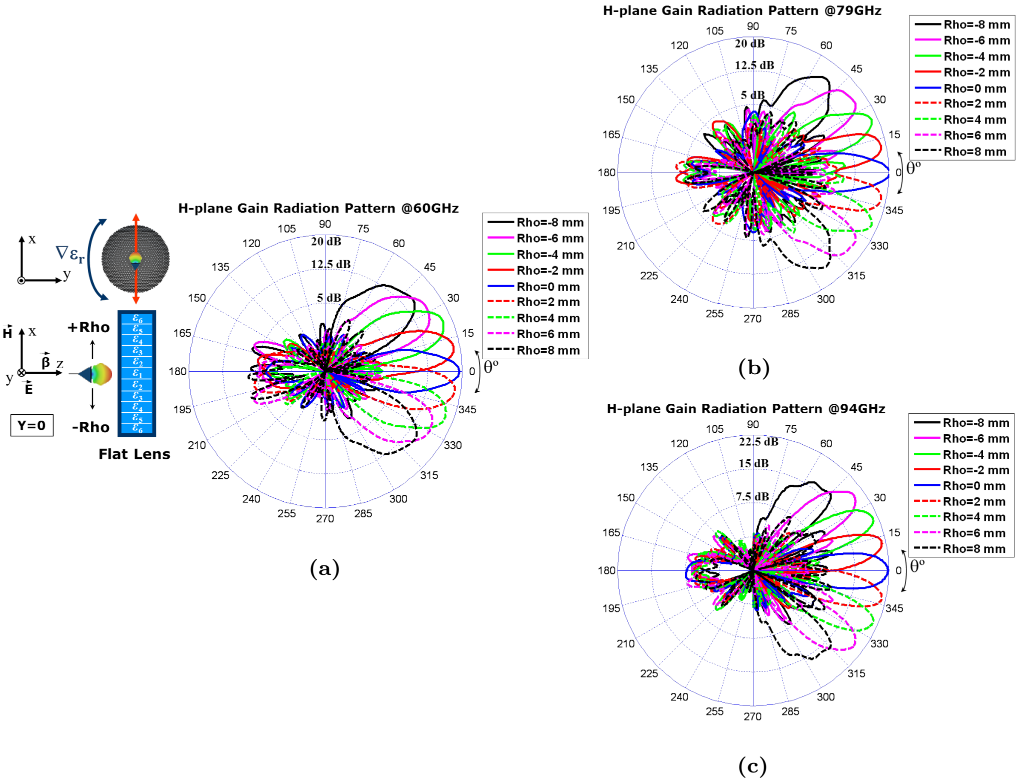

**(a)**

**(b)**

**(c)**

**Figure 2.13:** Perforated flat lens H-plane gain (dB) radiation pattern CST simulation results at 60 GHz (a), at 79 GHz (b), and at 94 GHz (c), for each *Rho* feeding position.

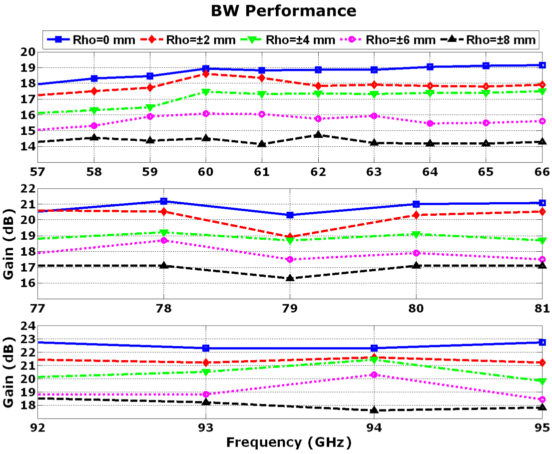

**Figure 2.14:** Simulated bandwidth performance: maximum gain (dB) for different focusing directions at 60 GHz, 79 GHz, and 94 GHz frequency bands for the perforated flat lens model.

**Table 2.3:** Performance comparison between different permittivity materials and perforated inhomogeneous flat lens at 60 GHz (a), 79 GHz (b), and 94 GHz (c).

**(a)**

| **Feeding Position (Rho)** | **Different materials lens** | | | **TMM6 material drilled lens** | | |
|---|---|---|---|---|---|---|
| | ***Gain*** | ***Steering angle($\theta^o$)*** | ***3-dB beamwidth*** | ***Gain*** | ***Steering angle($\theta^o$)*** | ***3-dB beamwidth*** |
| 0 mm | 20.3 dB | 0° | 10.5° | 18.9 dB | 0° | 13.1° |
| ±2 mm | 19.3 dB | 10° | 11.8° | 18.6 dB | 11° | 15° |
| ±4 mm | 18.4 dB | 19° | 13.5° | 17.5 dB | 20° | 19.2° |
| ±6 mm | 17.5 dB | 30° | 19.3° | 16.3 dB | 32° | 22.8° |
| ±8 mm | 16.2 dB | 40° | 22.3° | 14.9 dB | 41° | 27.3° |

**(b)**

| **Feeding Position (Rho)** | **Different materials lens** | | | **TMM6 material drilled lens** | | |
|---|---|---|---|---|---|---|
| | ***Gain*** | ***Steering angle($\theta^o$)*** | ***3-dB beamwidth*** | ***Gain*** | ***Steering angle($\theta^o$)*** | ***3-dB beamwidth*** |
| 0 mm | 21 dB | 0° | 10.3° | 20.3 dB | 0° | 10.9° |
| ±2 mm | 20.6 dB | 10° | 11.1° | 18.9 dB | 11° | 12.8° |
| ±4 mm | 19.5 dB | 22° | 13.2° | 18.7 dB | 24° | 12.9° |
| ±6 mm | 18.5 dB | 32° | 19.1° | 17.5 dB | 35° | 17.8° |
| ±8 mm | 17.2 dB | 50° | 22.5° | 16.3 dB | 52° | 21.6° |

**(c)**

| **Feeding Position (Rho)** | **Different materials lens** | | | **TMM6 material drilled lens** | | |
|---|---|---|---|---|---|---|
| | ***Gain*** | ***Steering angle($\theta^o$)*** | ***3-dB beamwidth*** | ***Gain*** | ***Steering angle($\theta^o$)*** | ***3-dB beamwidth*** |
| 0 mm | 22.2 dB | 0° | 11.7° | 22.3 dB | 0° | 11.7° |
| ±2 mm | 21.5 dB | 13° | 11.8° | 21.6 dB | 11° | 10.5° |
| ±4 mm | 20.7 dB | 26° | 13.5° | 21.4 dB | 24° | 10.8° |
| ±6 mm | 18.5 dB | 37° | 13.2° | 20.3 dB | 37° | 12.2° |
| ±8 mm | 17.9 dB | 45° | 20.1° | 16.6 dB | 45° | 18.5° |

CST simulation conditions, the different permittivities were set up considering a loss-less material (i.e. tg $\delta = 0$), and for the TMM6 perforated lens, the material was set with its respective losses (i.e. tg $\delta = 0.0023$), which unquestionably affect the maximum gain in any case. The explanation for this good behavior, even considering the material losses, is related to the fact that the permittivity curve achieved for the TMM6 drilled lens is very close to the theoretically needed (see Fig. 2.10), thus, in this sense, the permittivity curve is smoother than the curve for the different materials lens, which was stepped because the transitions between the concentric rings. Moreover, a remarkable broadband behavior is observed from the bandwidth performance simulation results, plotted in Fig. 2.14, with very good gain stability within the three whole frequency bands of interest, as it was previously indicated in the numerical analysis carried out for the multi-materials lens.

### 2.7.1 Back-Radiation Level - Need of a matching layer (ML)

It is important to note that, from the numerical results, there is always a certain amount of back-reflection level which is produced because of the transition between two mediums with different permittivity. Since the maximum relative permittivity of the dielectric material used to design the inhomogeneous lens is $\epsilon_r = 6$, multiple reflections of different significance are occurring. The magnitude of the power back-radiated is between 4 and 7 dB, depending on the scanning angle performed and the frequency of work. Hopefully, these undesirable effects can be reduced significantly using wave transformers, as matching layers (MLs). The chapter 3 of this PhD thesis is devoted specifically to evaluate and compare the performance of the original inhomogeneous lens with the performance of the lens with new inhomogeneous ML designs, in order to increase the maximum gain and impedance bandwidth, and reduce the mentioned back-radiation level.

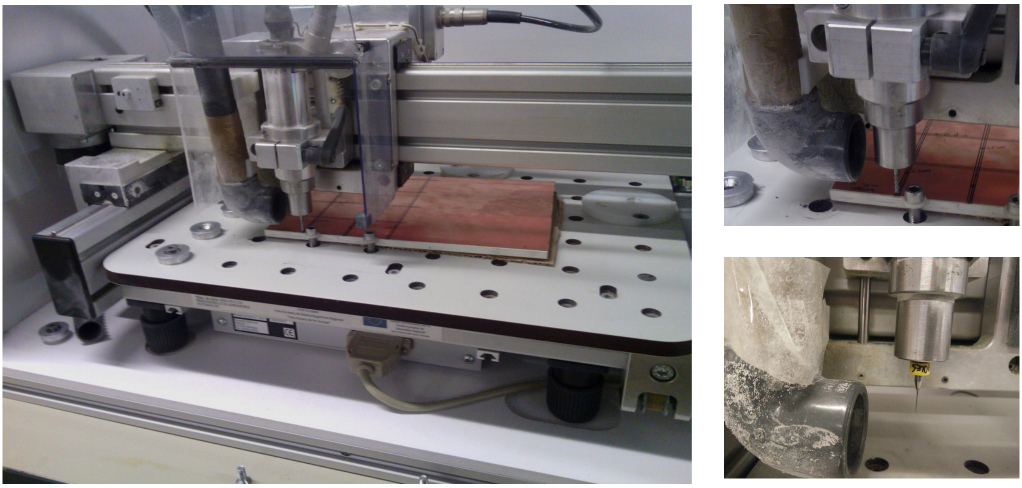

**Figure 2.15:** CNC machine used for the fabrication of the TMM6 lens prototype.

## 2.8 Fabrication of the Prototypes

Once the new introduced inhomogeneous gradient-index dielectric flat lens has been fully numerically tested, and promising simulation results have been obtained, a prototype of the lens has been fabricated at AntennaLab facilities of the Universitat Politècnica de Catalunya (UPC) using a computer numerical control (CNC) machine. A photograph of the CNC machine used is shown in Fig. 2.15.

Before starting with the lens fabrication process, we performed different tests with different material samples in order to confirm the expected behavior for the perforated substrate materials. Some issues related to the CNC machine (e.g. the machine is working in steps of imperial units, i.e. in a entire number of mills for each step) have been solved in order to previously perform the lens fabrication. A diamond-tipped drill bit is used for milling the lens outer circular contour. Carbide drill bits of 0.2 and 0.5 mm of diameter have been used to perform the holes. The drill bits need to be substituted after 150-200 holes for new ones in order to prevent them breaking out. A photograph of the fabrication process and different test samples performed with the CNC machine are shown in Fig. 2.16.

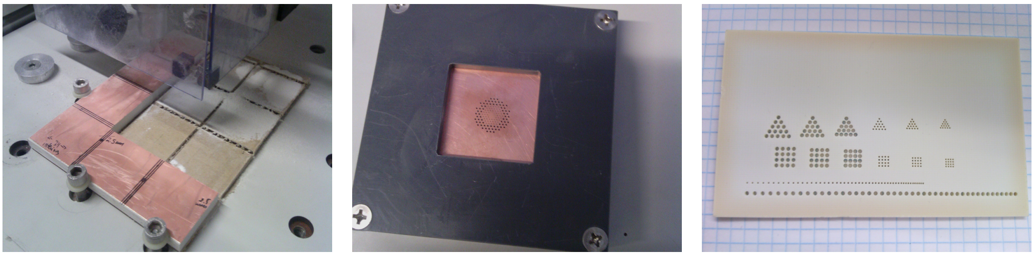

**Figure 2.16:** Lens fabrication process and different test samples.

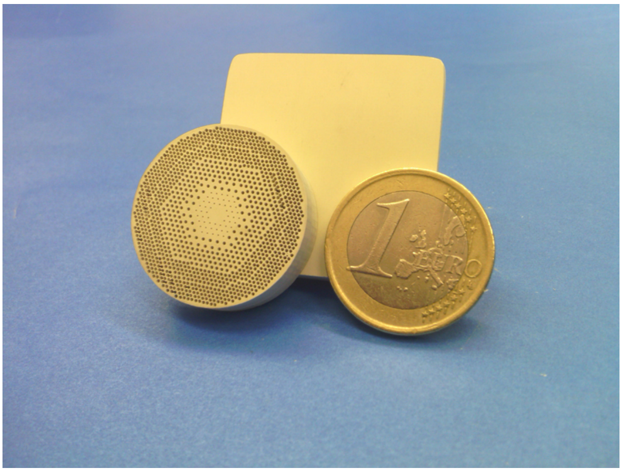

**Figure 2.17:** Photograph of the fabricated inhomogeneous dielectric flat lens prototype.

Then, after all the test needed to properly prepare the lens fabrication process, we performed a total of around 1200 holes on the TMM6 substrate with carbide drills of 0.2 and 0.5 mm of diameter to obtain the final lens prototype. A photograph of the inhomogeneous gradient-index dielectric flat lens is shown in Fig. 2.17. It has to be mentioned that the total time needed for the manufacture of one single lens prototype by drilling the hard dielectric substrate is around three hours.

## 2.9 Permittivity Profile Measurements and Validation

After fabricating some dielectric substrate samples with different hole densities, in order to validate the technique, the effective permittivity of these samples has been measured in free-space conditions at 60 GHz frequency band. The measurement setup is shown in Fig. 2.18. As it is show, the measurement setup consists of an Agilent N5247A vector network analyzer (VNA), two VNA extenders at millimeter-wave frequency band (one as a transmitter, the other as a receiver), two conical horn antennas performing narrow pencil beams, some absorbers are placed to avoid reflections, and a laptop to control the instrumentation.

### 2.9.1 Homogeneous Substrates Permittivity Measurements

In order to measure the permittivity and validate the technique, two different Rogers 4003C material substrates ($\epsilon_r = 3.38$, tg $\delta = 0.0027$), perforated with different uniform hole distribution (see Fig. 2.19), have been measured. The $S_{21}$ parameter is obtained with the VNA and, performing a phase comparison between the coefficient measured with the setup in free-space conditions, and placing the corresponding samples in the middle of the two conical horn antennas, the permittivity is obtained with the delay in the phase produced when the sample is introduced, taking into account the sample thicknesses.

First, a sample of a solid Rogers 4003C material has been measured, obtaining the expected permittivity around $\epsilon_r = 3.4$. Then, the two different drilled samples, with filling

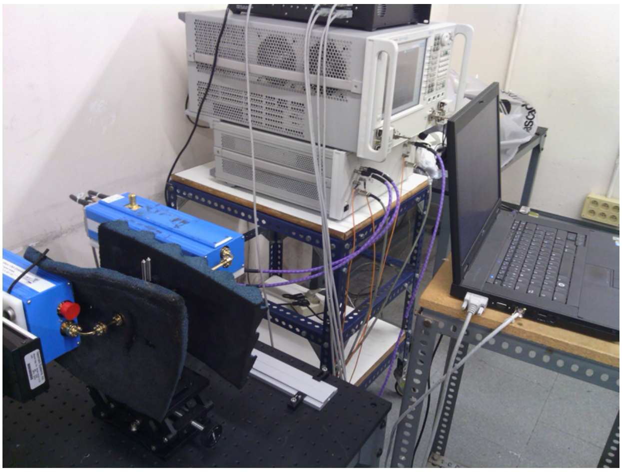

**Figure 2.18:** Effective permittivity measurement setup.

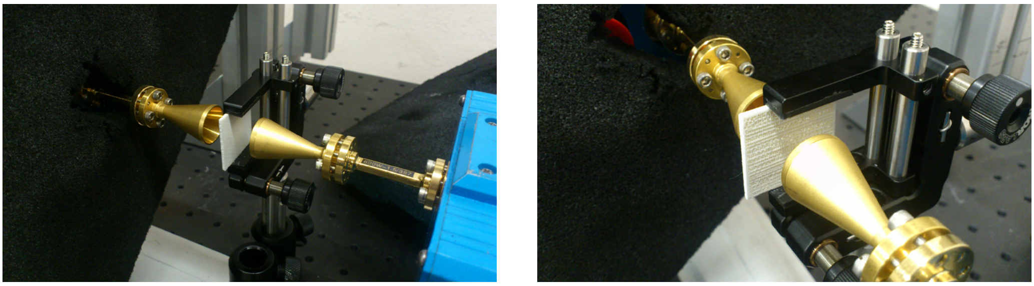

**Figure 2.19:** Measurement of two different density samples with uniform hole distribution.

factors equal to 0.2 and 0.8, which theoretically lead to permittivity values of $\epsilon_r = 3.25$ and $\epsilon_r = 1.55$, are placed in the setup performing the described measurements.

The corresponding permittivities obtained for the two samples after applying the phase comparison are plotted in Fig. 2.20. As it is shown, a stationary wave appears in the frequency response due to the interference between the outgoing and an incoming wave. Moreover, some additional reflections could occur in the transition between the free-space and the dielectric, and vice-versa, and the instrumentation. However, taking the mean value of the permittivity computed along the whole frequency band of measurement, the results confirm the expected behavior, with only a slight difference with the theoretically calculated permittivity values for the hole density performed in the substrates. Therefore, the expected behavior about the perforated substrates with homogeneous permittivity distribution, previously pointed out, is clearly confirmed.

### 2.9.2 Lens Permittivity Profile Measurements

Trying to characterize the permittivity profile of the fabricated TMM6 lens prototype, some difficulties have been found. The described method for the characterization of the permittivity of homogeneously distributed hole samples is not the best suitable to

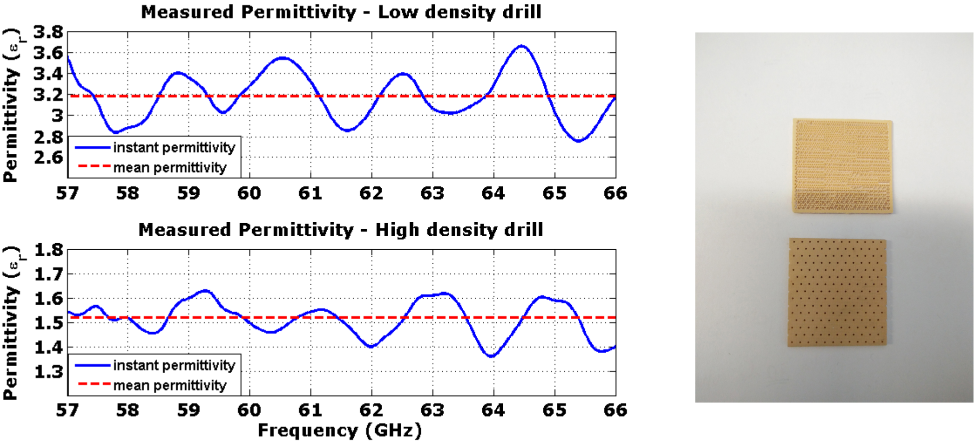

**Figure 2.20:** Measured permittivity results for the two different density hole samples.

characterize the lens profile (i.e. a sample with a gradient-index varying continuously in narrow zones). The technique is performing very well with homogeneous samples with an electrical size of some wavelengths, since the beamwidths of the conical horns are around 10º at -3 dB. For the purpose of measuring precisely the permittivity profile of a sample with radially varying its permittivity in small zones, a different approach is needed.

#### 2.9.2.1 Time-Domain Spectroscopy System

Before testing the performance of the dielectric flat lens in terms of radiation patterns, $S-parameters$, or efficiencies, it is very interesting and necessary to assert that the required permittivity profile has been achieved after fabrication. With this purpose, in order to precisely measure the permittivity profile of the fabricated prototype a time-domain spectroscopy (TDS) system has been used.

Our complete TDS measurement system is shown in Fig. 2.21. It consists of a femtosecond pulsed laser, which generates very short pulses that are sampled by using an optical delay stage. Once the complete pulse is retrieved, a discrete Fourier transform (DFT) is performed in order to obtain the spectrum, as it is usually realized in most of the TDS systems.

In this specific case, despite our TDS system is a THz-TDS system, which is able to measure up to 1-1.5 THz, it is also capable of measuring with a dynamic range (DR) above 30 dB around 60 GHz, and with a DR above 50 dB around 100 GHz. Taking advantage of the small beam spot generated by our TDS system, which is collimated with two focusing lenses placed after the photo-conductive receiver and transmitter antennas, as it is depicted in Fig. 2.21, we are able to precisely characterize the permittivity of different materials by using the delay produced introducing the sample in between, compared to the signal in free-space. The air humidity has to be the lower as possible to avoid the effect of the multiple water vapor absorption peaks in the spectrometer response. Then, the control of the atmosphere is achieved by purging with nitrogen gas the water vapor contained in the ambient air.

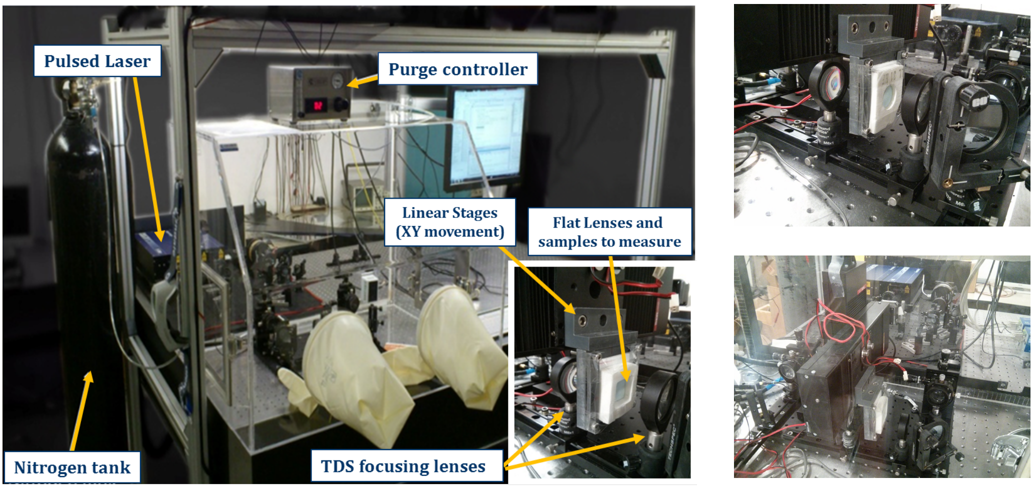

**Figure 2.21:** Time-domain spectroscopy TDS system used to characterize different materials in a wide frequency range.

#### 2.9.2.2 Lens Permittivity Time-Domain Spectroscopy System Measurements

First, solid samples of different substrate materials have been measured. Among them, a solid sample of 7-mm thickness Rogers TMM6 material, validating the maximum permittivity around 6, as it was expected, is plotted in Fig. 2.22. After that, some different samples with uniform hole distribution have also been tested, obtaining the expected results as well, confirming the anticipated behavior. Therefore, in order to measure the complete permittivity profile over the whole flat lens surface, the prototype is placed in between the two focusing lenses of the TDS system. With the help of two linear stages (to perform the specific movement needed in the X-Y axes) the TDS narrow radiation beam is scanned in steps of 1 mm ($\lambda_{0_{60GHz}}/5$) over the lens surface. Therefore, a 3-D representation of the measured permittivity profile for the inhomogeneous circular TMM6 lens is plotted in Fig. 2.23.

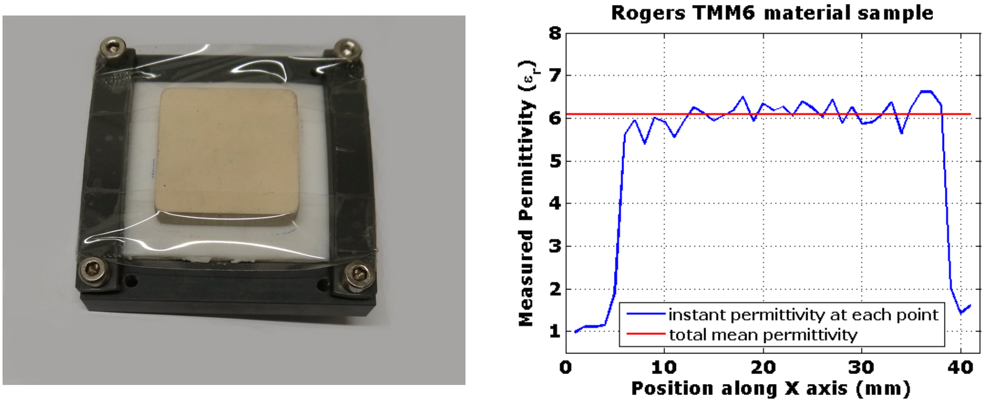

**Figure 2.22:** TMM6 sample of 7 mm thickness and its measured permittivity.

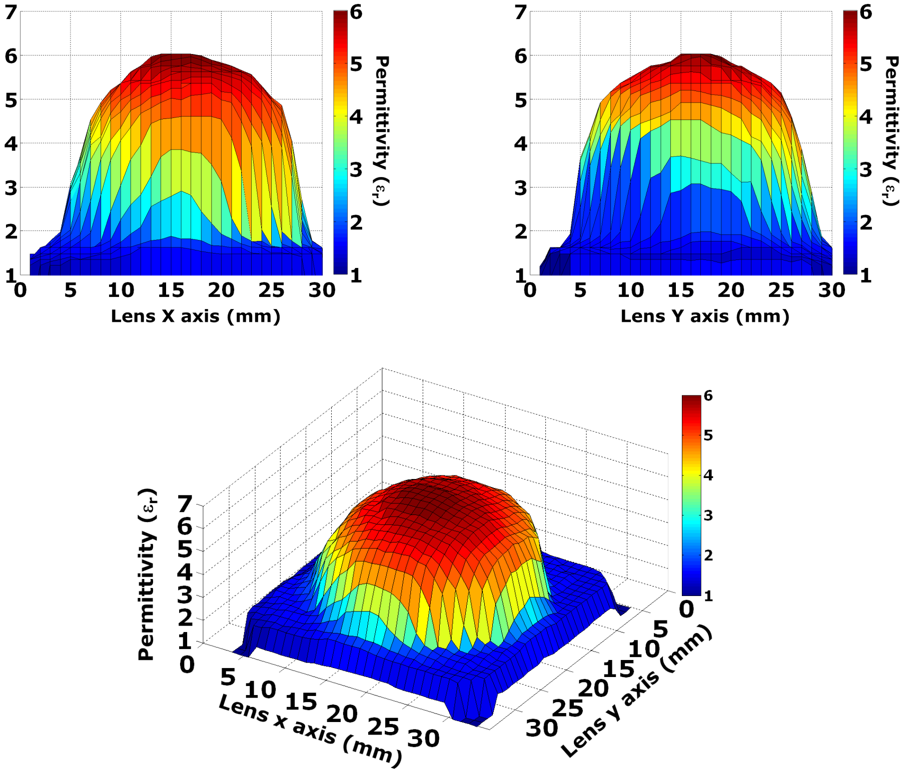

**Figure 2.23:** 3-D representations of the measured permittivity profile

As it is shown, despite the physical shape of the designed lens with an absolutely planar structure, the permittivity profile is very well defined in all lens dimensions (it is easy to identify the different permittivity zones), thus demonstrating the good fabrication results achieved with the proposed technique of perforating the TMM6 substrate. In Fig. 2.24, different cuts at every millimeter along $X$ and $Y$ dimensions are also plotted to clearly identify that the gradient-index is perfectly increasing and decreasing smoothly.

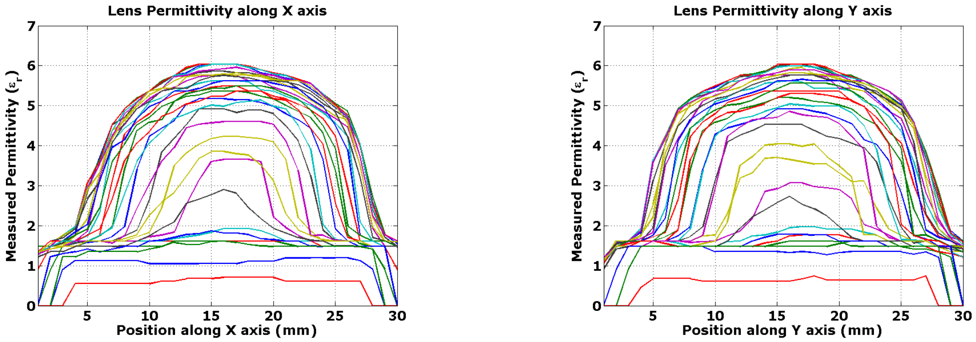

**Figure 2.24:** Permittivity profile sections of the inhomogeneous dielectric flat lens.

## 2.10 Dielectric Flat Lens Radiation Pattern Measurements

Once the permittivity profile of the new inhomogeneous lens design has been practically verified, in order to characterize the performance of the proposed solution, a complete set of electromagnetic measurements of the lens performance has been carried out at 60 GHz in the High Frequency Electronics Laboratory of the University of California at Irvine (UCI), and at W band, from 75 GHz to 110 GHz, in the AntennaLab facilities of Universitat Politècnica de Catalunya (UPC). The radiation pattern produced by the lens has been measured at 60 GHz directly in the far-field using the measurement system of UCI. Since the highest frequency of the far-field measurement setup of UCI is limited to 64 GHz, the E-Field radiated by the lens has been measured at 79 and 94 GHz in the Near-Field at AntennaLab facilities. Then, the Far-Field radiation pattern has been obtained at 79 GHz by using a Near-Field to Far-Field transformation [93].

### 2.10.1 Far-Field Radiation Pattern Measurement System at 60 GHz band

At the moment when the dielectric flat lens was fabricated, the instrumentation, components, and measurement setups available at Antennalab facilities of the UPC only allowed the measurement at certain frequency bands; unfortunately the 60 GHz WPAN band was not among these bands. Therefore, in order to measure the lens performance in terms of radiation patterns, we used the far-field measurement setup of the UCI. A photograph of the radiation pattern measurement setup is shown in Fig. 2.25. The system has a rotating arm which is able to perform a complete scanning of the upper/lower hemi-sphere, allowing to obtain the radiation pattern cut in a plane.

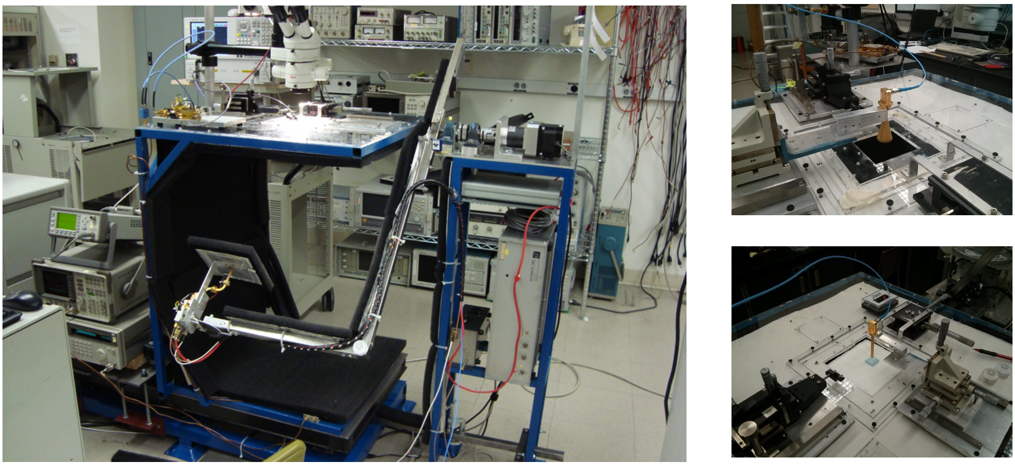

**Figure 2.25:** Far-field radiation pattern measurement setup of UCI.

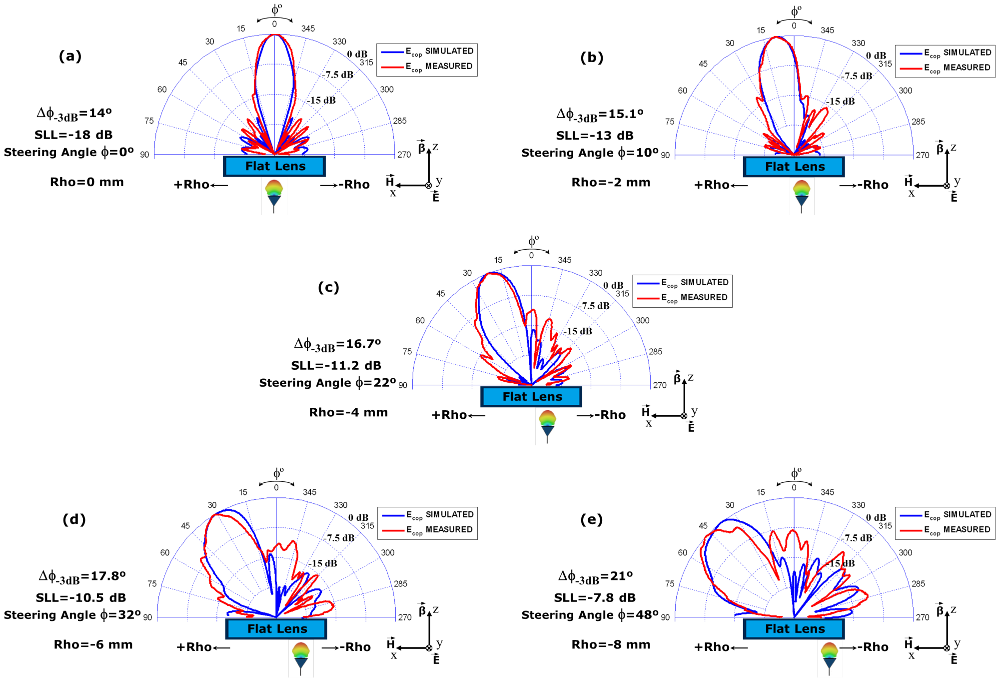

**Figure 2.26:** Comparison between simulated and measured Normalized H-Plane Radiation Patterns at 60 GHz for different *Rho* feeding positions: (a) $Rho = 0\,\text{mm}$, (b) $Rho = -2\,\text{mm}$, (c) $Rho = -4\,\text{mm}$, (d) $Rho = -6\,\text{mm}$, (e) $Rho = -8\,\text{mm}$. Symmetric patterns steered rightwards are obtained for the symmetric feeding positions

### 2.10.2 Far-Field Radiation Patterns at 60 GHz Communications Band

Then, as it has been carried out in the numerical simulations, a total of 9 measurements have been performed corresponding to different feeding positions of the transmitting WR-15 open-ended waveguide along the $x$-direction (going from $Rho = -8\,\text{mm}$ to $Rho = 8\,\text{mm}$) in steps of 2 mm. The WR-15 waveguide used during the measurements is well matched ($S_{11} < -10\,\text{dB}$) for all the *Rho* feeding positions in the whole frequency band of interest, as it is shown in Fig. 2.28. The corresponding normalized H-plane radiation pattern results are shown in Fig. 2.26, being at the same time compared to the simulation results. Given the lens structure, symmetric patterns are obtained for the corresponding symmetric feed positions with respect to the lens center, and therefore are not shown.

As it is observed in Fig. 2.26, as the *Rho* feeding position is moved rightwards, the high-gain radiation pattern produced by the dielectric flat lens is steered leftwards, accordingly. In general, very good agreement between radiation pattern simulation results and measurements at 60 GHz is observed.

In order to obtain the gain radiation pattern, we substitute the antenna under test (AUT) (i.e. the dielectric flat lens together with the feeding WR-15 waveguide) for a

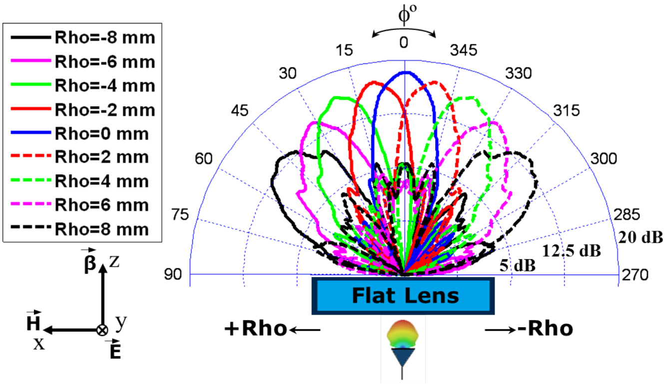

**Figure 2.27:** Complete set of measured H-Plane gain (dB) radiation patterns at 60 GHz for each *Rho* feeding position (from $Rho = -8$ mm to $Rho = 8$ mm) in steps of 2 mm.

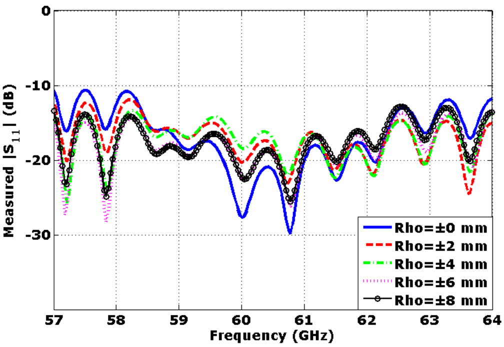

**Figure 2.28:** $S_{11}$-parameter of the WR-15 waveguide for each *Rho* feeding position.

well-known gain conical horn antenna (used as reference) to perform a received power level comparison. The complete set of gain radiation patterns for the 9 different Rho feeding positions is shown in Fig. 2.27. As it is observed, the measured gain values are very close to the simulation results (see Fig. 2.13).

In addition, very good gain stability within the 60 GHz WPAN band (from 57 to 64 GHz) is observed from the measured bandwidth performance in Fig. 2.29. The measured radiation pattern characteristic parameters at 60 GHz (maximum gain for each beam, scanning angles ($\theta^\circ_{scan}$), half-power beamwidth ($\Delta\theta_{-3\,\mathrm{dB}}$), and SLL) are summarized in Table 2.4. Finally, note that we cannot obtain the directivity or the efficiency with the radiation pattern measurement setup, since always there is a part of back-radiation level that cannot be measured, thus it is not possible to integrate the whole power for the complete radiation pattern. Therefore, we estimated the loss efficiency using the gain measurements and the CST simulation results of the directivity. The estimated loss efficiency is plotted in Fig. 2.30. As it is shown, very good loss efficiency values around 80% are obtained, since a low-loss substrate is used.

**Table 2.4:** Inhomogeneous dielectric flat lens measured characteristic parameters at 60 GHz.

| **Feeding Position** (*Rho*) | **Gain** | $\theta^{o}_{scan}$ | $\Delta\theta_{-3\,\mathrm{dB}}$ | **SLL** |
|---|---|---|---|---|
| 0 mm | 18.3 dB | 0º | 14º | -18 dB |
| ±2 mm | 17.2 dB | ±10º | 15.1º | -13 dB |
| ±4 mm | 16.6 dB | ±22º | 16.7º | -11.2 dB |
| ±6 mm | 14.7 dB | ±32º | 17.8º | -10.5 dB |
| ±8 mm | 13.7 dB | ±48º | 21º | -7.8 dB |

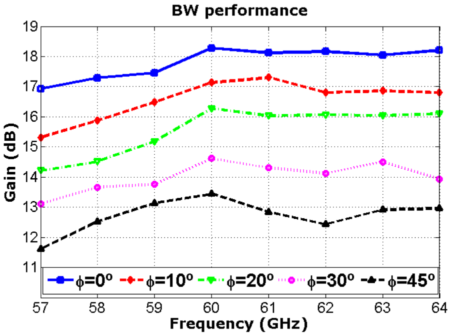

**Figure 2.29:** Measured maximum gain (dB) for different $\theta$ focusing directions.

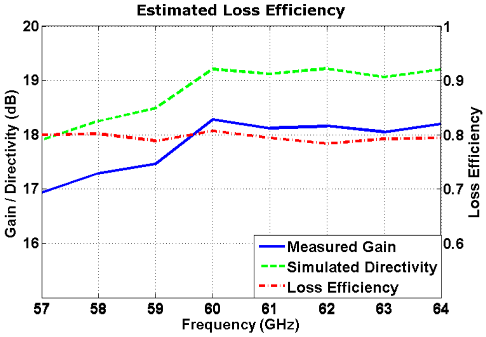

**Figure 2.30:** Estimated loss efficiency in the whole 60 GHz frequency band of interest.

### 2.10.3 Near-Field to Far-Field Radiation Pattern Measurement System at W-band (75 GHz and 110 GHz)

As it has been stated before, since the highest frequency of the Far-Field measurement setup of UCI is 64 GHz, the E-Field radiated by the lens has been measured at W-band in the Near-Field with the setup shown in Fig. 2.31 at AntennaLab facilities. Then, the Far-Field radiation pattern has been obtained at 79 GHz by using a Near-Field to Far-Field transformation [93]. The 2-D Near-Field measurement setup is composed of an Agilent N5247A VNA, two VNA extenders at W-band (one transmitter and one receiver), two precision linear stages to perform the 2-D scan ($X - Y$ movements), and two WR-10 open-ended waveguides (one to feed the lens and one as a probe). The WR-10 feeding waveguide used during the measurements is well matched ($S_{11} < -10\,\mathrm{dB}$) for all the *Rho* feeding positions in the whole frequency band of interest, as it is shown in Fig. 2.34. RF absorbers are also used to avoid reflections between the instrumentation. The flat lens prototype is placed between the WR-10 waveguides. The transmitting WR-10 feeds the lens at its focal point ($F$=6.25 mm), and the receiving WR-10 is placed at 40 mm behind the lens to perform the 2-D Near-Field measurement with the help of the two stages (see Fig. 2.31).

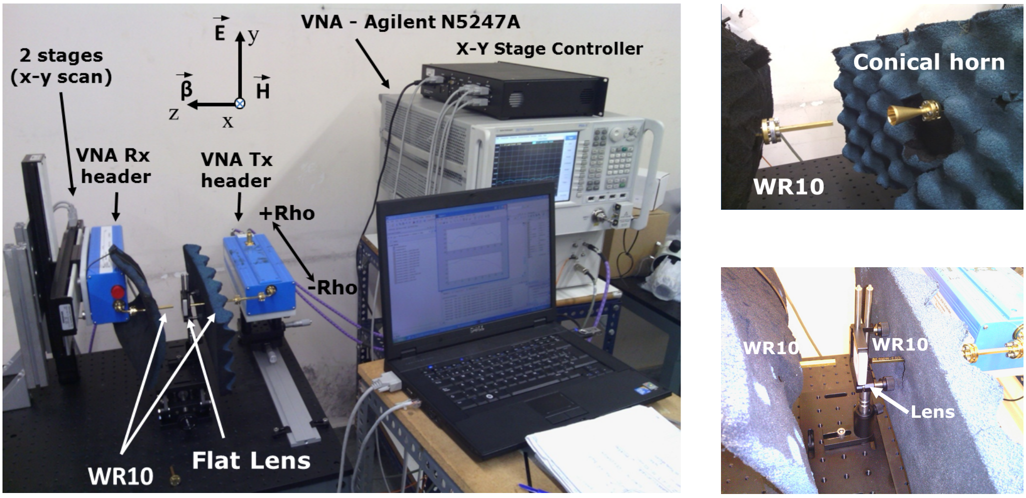

**Figure 2.31:** 2-D Near-Field to Far-Field radiation pattern measurement setup at W-band, and detailed images of the system.

### 2.10.4 Far-Field Radiation Pattern at 79 GHz Automotive Radar Band

A total of 9 measurements have also been performed corresponding to different feeding positions of the transmitting WR-10 along the $x$-direction. The corresponding normalized H-plane radiation pattern results have been obtained, and they are plotted in Fig. 2.32, togheter with the simulation results for comparison purposes. Given the lens structure, symmetric patterns are obtained for the corresponding symmetric feed positions with respect to the lens center, and therefore are not shown either in this case.

As it is observed in Fig. 2.32, as the *Rho* feeding position is moved leftwards, the high-gain radiation pattern produced by the dielectric flat lens is steered rightwards, accordingly. In general, good agreement between radiation pattern simulation results and measurements at 79 GHz is observed.

In addition, gain measurements have also been performed at 79 GHz; we also substitute the AUT for a well-known gain conical horn antenna at W-band to perform a received power level comparison, after the Near-Field to Far-Field transformation of the measurements [93]. The complete set of gain radiation patterns for the 9 different *Rho* feeding positions is shown in Fig. 2.33, and the radiation pattern characteristic parameters at 79 GHz are also summarized in Table 2.5. In the last case ($Rho = -8\,\mathrm{mm}$), the SLL is not much lower because of the diffraction on the lens edges and it could be considered not acceptable in some specific cases. Moreover, because we are using an open-ended wave-guide to illuminate the lens, there can be spurious radiations, which affect the SLL and the maximum achievable gain. In this sense, an optimum radiating element has to be designed for an optimum lens illumination for high steering angles. As at 60 GHz, good agreement between radiation pattern simulation results and measurements is also observed at 79 GHz (see Fig. 2.13 and Fig. 2.33).

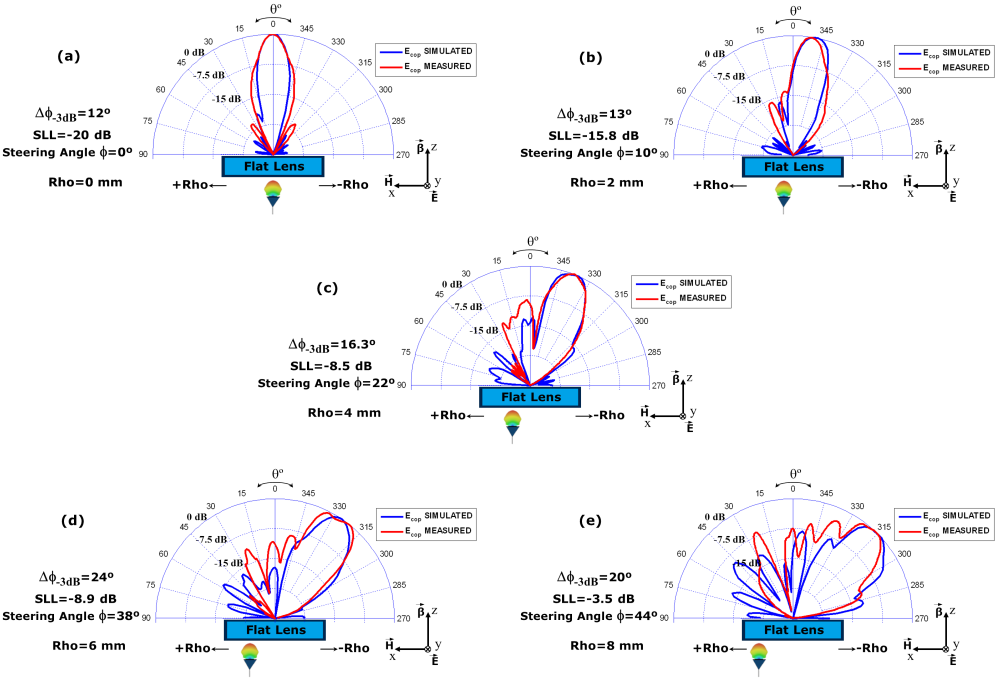

**Figure 2.32:** Comparison between simulated and measured Normalized H-Plane Radiation Patterns at 79 GHz for different *Rho* feeding positions: (a) $Rho = 0$ mm, (b) $Rho = -2$ mm, (c) $Rho = -4$ mm, (d) $Rho = -6$ mm, (e) $Rho = -8$ mm. Symmetric patterns steered rightwards are obtained for the symmetric feeding positions

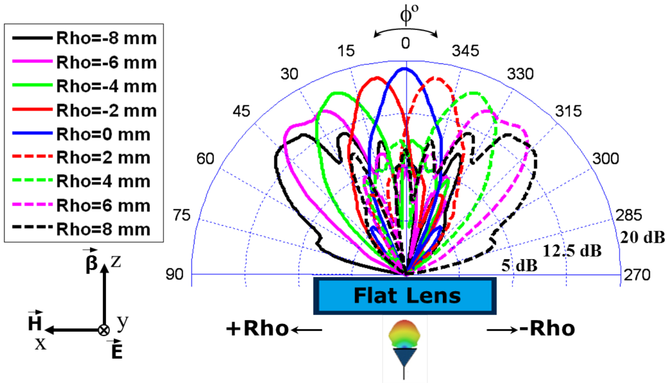

**Figure 2.33:** Complete set of measured H-Plane gain (dB) radiation patterns at 79 GHz for each *Rho* feeding position (from $Rho = -8$ mm to $Rho = 8$ mm) in steps of 2 mm.

Note that we also cannot obtain the directivity (or the efficiency) of the dielectric flat lens antenna with our 2-D Near-Field measurement setup since there is also a part of back radiation, due to the reflections on the lens, that cannot be measured. Therefore, we also

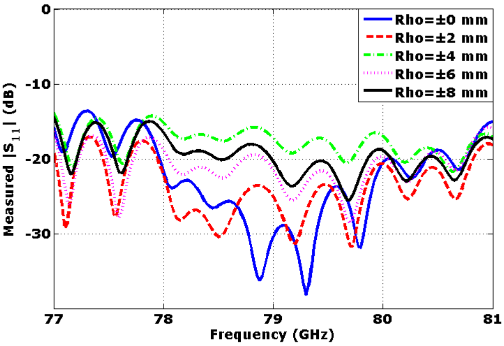

**Figure 2.34:** $S_{11}$-parameter of the WR-15 waveguide for each *Rho* feeding position.

**Table 2.5:** Inhomogeneous dielectric flat lens measured characteristic parameters at 60 GHz.

| **Feeding Position** (*Rho*) | **Gain** | $\theta^{\text{o}}_{scan}$ | $\Delta\theta_{-3\,\text{dB}}$ | **SLL** |
|---|---|---|---|---|
| 0 mm | 18.9 dB | 0º | 12º | -20 dB |
| ±2 mm | 17.8 dB | ±9.8º | 13.1º | -14 dB |
| ±4 mm | 17.3 dB | ±21.6º | 16.3º | -8.2 dB |
| ±6 mm | 16.5 dB | ±37.5º | 24º | -8.9 dB |
| ±8 mm | 15.4 dB | ±44.2º | 20º | -3.5 dB |

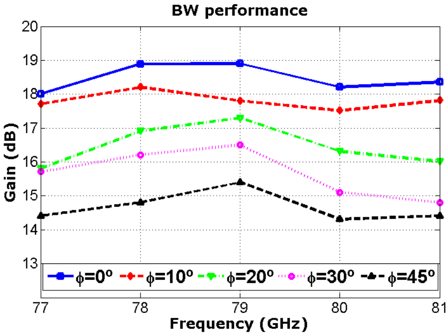

**Figure 2.35:** Measured maximum gain (dB) for different $\theta$ focusing directions.

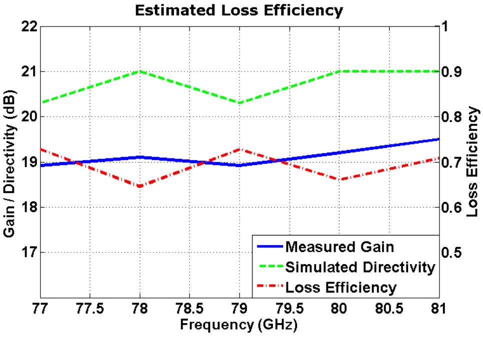

**Figure 2.36:** Estimated loss efficiency in the whole 79 GHz frequency band of interest.

estimated the loss efficiency using the gain measurements and CST simulation results of the directivity, obtaining very good values between 70% and 80%. Additionally, also very good gain stability within the 79 GHz band (from 77 to 81 GHz) is observed from the measured bandwidth performance plotted in Fig. 2.35.

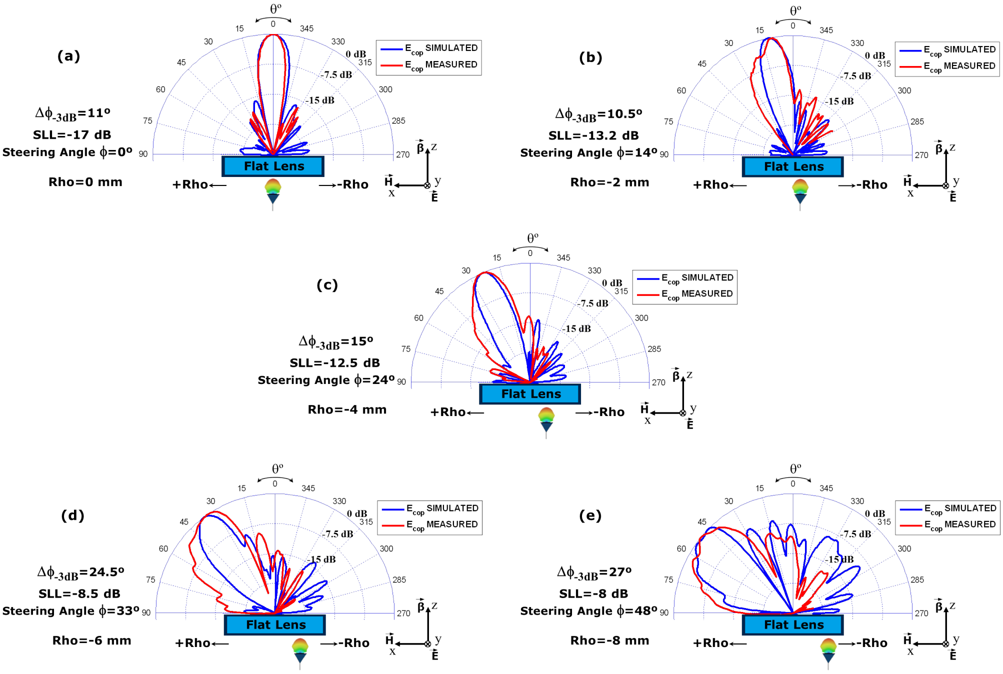

**Figure 2.37:** Comparison between simulated and measured Normalized H-Plane Radiation Patterns at 94 GHz for different *Rho* feeding positions: (a) $Rho = 0\,\text{mm}$, (b) $Rho = -2\,\text{mm}$, (c) $Rho = -4\,\text{mm}$, (d) $Rho = -6\,\text{mm}$, (e) $Rho = -8\,\text{mm}$. Symmetric patterns steered rightwards are obtained for the symmetric feeding positions

### 2.10.5 Far-Field Radiation Pattern at 94 GHz Passive Imaging Band

In the same way as it has been performed for the 79 GHz band, the complete set of measurements has been carried out at 94 GHz, from 92 to 95 GHz, with the same Near-Field to Far-Field radiation pattern measurement setup shown in Fig. 2.31. Again, a set of 9 measurements have also been performed corresponding to different feeding positions of the transmitting WR-10 along the x-direction. The normalized H-plane radiation pattern are plotted together with the simulation results, being compared beam by beam for each *Rho* feeding position, in Fig. 2.37.

As it is observed in Fig. 2.37, again, as the *Rho* feeding position is moved rightwards, the high-gain radiation pattern produced by the dielectric flat lens is steered leftwards, accordingly. In general, good agreement between radiation pattern simulation results and measurements at 94 GHz is observed. However, the measured beams are slightly wider, not for the broadside case, but for the different scanning angles. In this sense, it seems that the focal distance should be corrected, because the lens appears to be out of focus. The feeding aperture should be placed physically closer to the lens surface because in terms of wavelength it has been moved away since the frequency is higher.

Additionally, the gain calibration has been performed for the measured radiation pat-

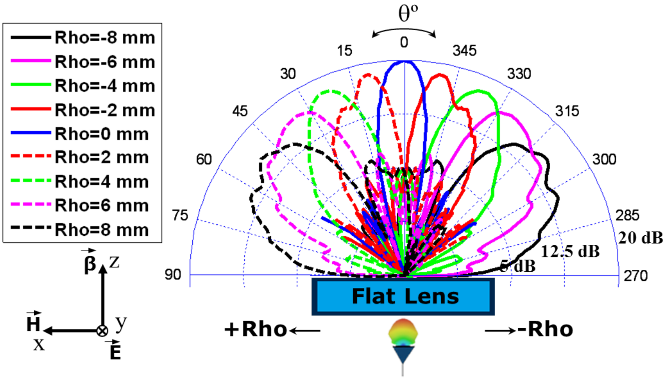

**Figure 2.38:** Complete set of measured H-Plane gain (dB) radiation patterns at 94 GHz for each *Rho* feeding position (from *Rho* = −8 mm to *Rho* = +8 mm) in steps of 2 mm.

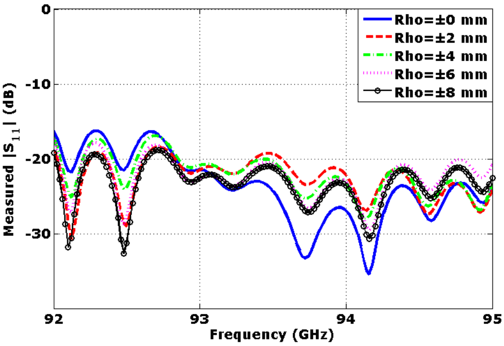

**Figure 2.39:** $S_{11}$-parameter of the WR-15 waveguide for each *Rho* feeding position.

terns at 94 GHz, after the same Near-Field to Far-Field transformation carried out before [93].

The complete set of gain radiation patterns for the 9 different *Rho* feeding positions is shown in Fig. 2.38, and the radiation pattern characteristic parameters at 94 GHz are also summarized in Table 2.6. In this case, the WR-10 feeding waveguide used during the measurements is also well matched for all the *Rho* feeding positions in the whole frequency band of interest, as it is shown in Fig. 2.39.

Moreover, the estimated loss efficiency using the gain measurements and CST simulation results of the directivity is still good considering the high frequency of operation, much higher than the frequency of design, with efficiency values between 60% and 70%. Additionally, also very good gain stability within the 94 GHz band (from 92 to 95 GHz) is observed from the measured bandwidth performance. Both bandwidth performance and estimated loss efficiency are plotted in Fig. 2.40 and Fig. 2.41, respectively. It has been demonstrated that, although the original inhomogeneous gradient-index lens is designed at 60 GHz, it is also performing very good in terms of gain, beam-steering capabilities, or efficiencies, at higher frequency bands such as the considered 79 and 94 GHz bands,

**Table 2.6:** Inhomogeneous dielectric flat lens measured characteristic parameters at 60 GHz.

| **Feeding Position** (*Rho*) | **Gain** | $\theta^{\text{º}}{}_{scan}$ | $\Delta\theta_{-3\,\text{dB}}$ | **SLL** |
|---|---|---|---|---|
| 0 mm | 20.0 dB | 0º | 11.0º | -17 dB |
| ±2 mm | 19.3 dB | ±14º | 10.5º | -13.2 dB |
| ±4 mm | 19.0 dB | ±24º | 15.0º | -12.5 dB |
| ±6 mm | 18.0 dB | ±33º | 24.5º | -8.5 dB |
| ±8 mm | 14.3 dB | ±48º | 27.0º | -8 dB |

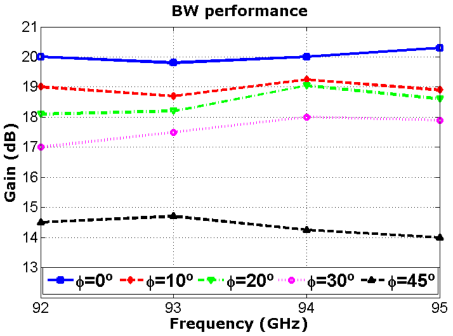

**Figure 2.40:** Measured maximum gain (dB) for different $\theta$ focusing directions.

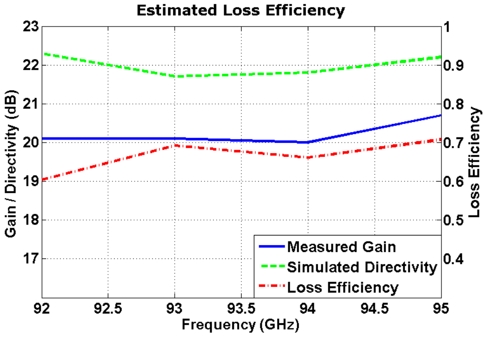

**Figure 2.41:** Estimated loss efficiency in the whole 94 GHz frequency band of interest.

thus showing a very good broadband behavior practically in the whole millimeter-wave frequency band. The measurements at three frequencies indicate that we can achieve up to around 20 dB of broadside gain, beam-steering capabilities in both planes from -30º to +30º with around 17-18 dB gain, with low side-lobe levels, and up to ±45º with around 15 dB gain. It has been practically demonstrated that this lens design could be used to develop a complete switched-beam array for millimeter-wave systems, including high-throughput communications at 60 GHz for WPAN applications for the future 5G systems, automotive radar systems at 77 GHz, or communications, radar and imaging applications at 94 GHz band, achieving beam scanning of high-gain radiation beams in both planes, broadband operation, and flat antenna profile. In the following subsections, the introduced lens design is used as a fundamental part of a switched-beam antenna (SWBA) array system.

## 2.11 Switched Beam Antenna Array - 5 x 5 Slot Antenna Array

As it has been stated at the beginning of this chapter, switched-beam arrays provide interesting alternatives because they have a set of multiple fixed beams that can be easily selected individually, and their implementation is much easier, cheaper, and less bulky than the solutions based on the phased-array antenna concept. Therefore, once the

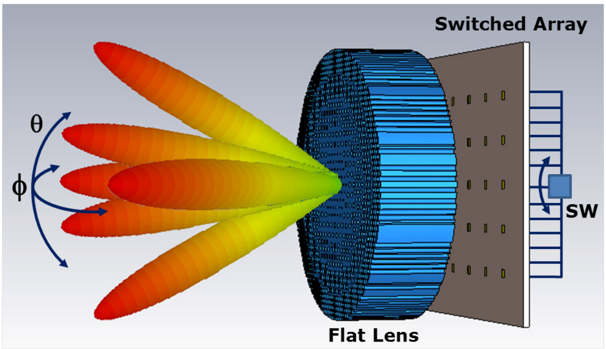

**Figure 2.42:** Complete SWBA scheme based on the introduced dielectric flat lens.

performance of the dielectric flat lens has been fully electromagnetically assessed, in this section we introduce the radiating part of the complete switched-beam antenna (SWBA) array system, and the performance evaluation of the complete structure.

### 2.11.1 Switched-Beam Antenna Array Principle

The SWBA array theoretical scheme is depicted in Fig. 2.42. As it is shown, a 2-D array is placed at the lens focal distance. Depending on which one of the radiating elements is selected, the low-gain radiation pattern produced for this single element will be steered and enhanced into a high-gain beam focusing the radiation to a particular direction of the space, in the same manner as the lens steered the beams when it has been fed with the corresponding open-ended waveguides. With this purpose, a planar array structure has to be carefully designed in order to provide an optimum lens illumination with each one of its single elements, with an edge taper of around -14 dB; similar lens illumination obtained when the lens is fed with the WR-10/15.

### 2.11.2 Slot Antenna Array Design

A five by five slot antenna array, in which each single element is selected individually for each operation mode while the rest of the elements are left in open circuit, is designed to feed the inhomogeneous dielectric flat lens in order to obtain 25 high-gain radiation patterns to scan in both theta and phi directions of the space. The following design is carried out specifically to operate at 60 GHz WPAN American frequency band, from 57 to 64 GHz. This is only to simply demonstrate the viability and test its performance for a particular case of application, but always keeping in mind and considering the higher frequency bands for the rest of considered applications taking into account the good broadband behavior of the lens, which already has been demonstrated.

The complete array structure is designed on a 25 x 25 mm Rogers 4350B dielectric substrate ($\epsilon_r = 3.48$, tan $\delta = 0.0037$) of 0.254 mm thickness. The slot elements in the array are spaced 4 mm center-to-center (note that this corresponds at the same $Rho = 4$ mm distance, in which the radiating WR-15 waveguide was spaced in the previous lens sections). The single element consists of a slot antenna fed by a co-planar waveguide (CPW) placed in the top layer of the substrate.

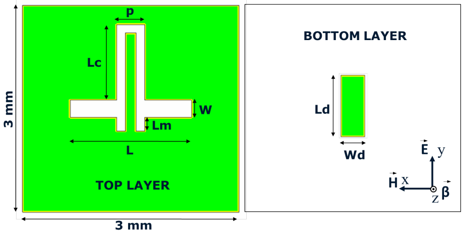

**Figure 2.43:** Geometry of a single element of the 5 by 5 antenna array.

Because an appropriate illumination of the lens is fundamental, the radiation pattern of the slot antenna has to be improved accordingly to feed the lens. Therefore, in the bottom layer of the substrate, a small copper patch acting as a director element is placed to increase the gain up to around 6.5 dB in the lens direction, achieving an efficient lens illumination. The geometry of the single element of the proposed array design is shown in Fig. 2.43. The feeding line is a 85Ω CPW (signal track width of 150$\mu$ m and gap of 120 $\mu$ m). The slot dimensions are $L = 1.68\,\text{mm}$ and $W = 0.25\,\text{mm}$, with a matching element length $L_m = 0.2\,\text{mm}$, and bottom patch director element dimensions of $L_d = 1.1\,\text{mm}$ and $W_d = 0.4\,\text{mm}$.

### 2.11.3 Slot Antenna Array Simulation Results

The CST Microwave Studio simulation results of the reflection coefficient ($S_{11}$-parameter) and radiation patterns for a single element of the array are plotted in Fig. 2.44 and Fig. 2.45, respectively. As it is shown, if we consider an impedance matching at -6 dB, as usual for mobile terminals, the proposed antenna is well-matched from 56.5 to 63 GHz, almost covering the whole band of interest. The simulated E and H-Plane radiation patterns show that around 6 dB of broadside gain are obtained, with a -3 dB beamwidth of around 60º, which leads to a good uniform lens illumination, despite at ±30º a decay in the gain is observed, which could cause a slight gain loss when feeding the lens when steering the beam.

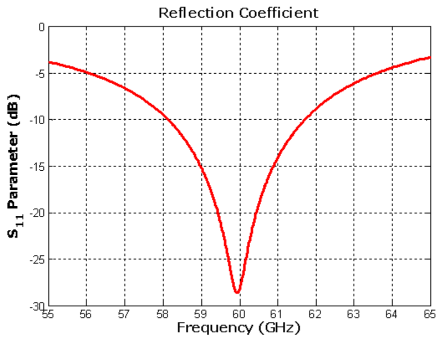

**Figure 2.44:** Simulated reflection coefficient for a single element of the array.

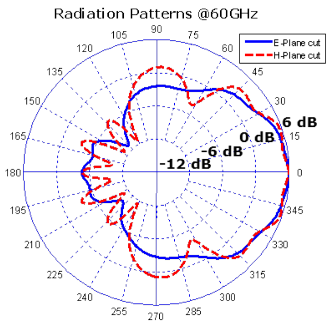

**Figure 2.45:** Simulated E and H-Plane radiation patterns at 60 GHz.

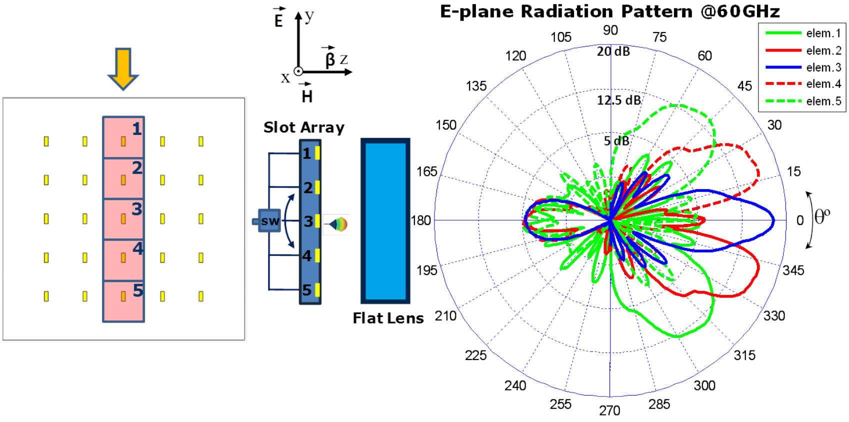

**Figure 2.46:** Complete set of H-plane gain radiation pattern simulation results at 60 GHz selecting each single radiating element of the 3rd column of the array.

## 2.11.4 Complete Switched-Beam Antenna Array Simulation Results

The proposed complete SWBA array has been finally designed based on the described five by five slot/patch antenna array together with the dielectric gradient-index flat lens to steer and enhance the radiation in a particular direction. The five by five slot/patch antenna array is placed parallel to the lens (along $x$-direction, see Fig. 2.46) at its focal distance $F = 6.25\,\text{mm}$. Then, the full structure has been simulated from 57 to 64 GHz. The complete set of 5 simulated H-Plane radiation patterns at 60 GHz, selecting individually each element of the 3rd column of the array (central column, along $x$, $y = 0$), are shown in Fig. 2.46. As it is shown, these results indicate that we can achieve up to 18.4 dB gain, and beam-steering capabilities from +30º to -30º with more than 15 dB gain, and up to ±45º with around 14 dB, with low SLL.

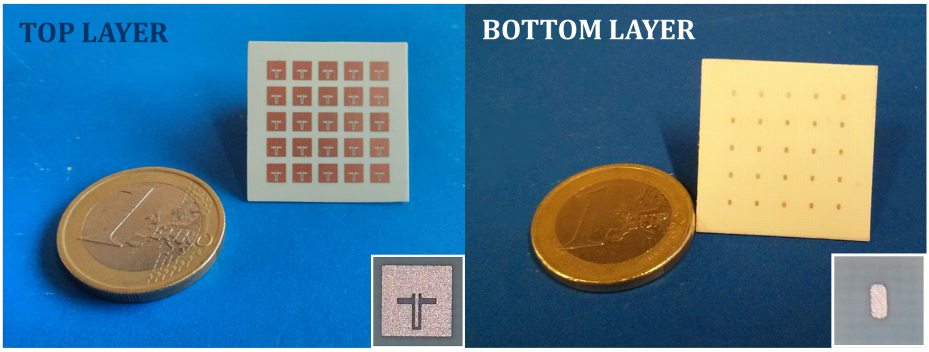

**Figure 2.47:** Photograph of the top and bottom layers of the slot/patch antenna array fabricated at UPC-AntennaLab facilities.

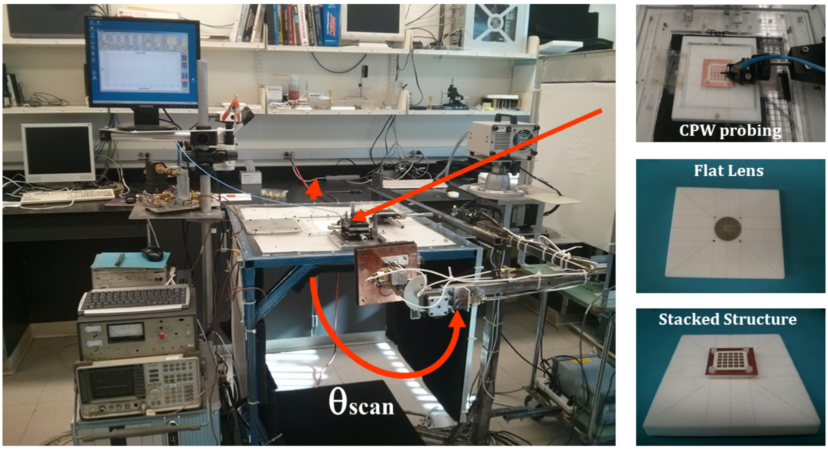

**Figure 2.48:** Far-field radiation pattern measurement setup of UCI in its probe station configuration.

### 2.11.5 Fabrication of the Array Prototypes

In order to practically evaluate the performance of the proposed antenna concept, a prototype of the five by five slot antenna array has been fabricated at UPC-AntennaLab facilities using standard photo-etching techniques. The fabrication process, described step by step, is explained in Appendix C, and a detailed scheme is plotted in C.1 at page 144. A photograph of the final fabricated prototype on a Rogers 4350B dielectric substrate is shown in Fig. 2.47, together with some detailed microscopic images plotted in the insets.

### 2.11.6 Complete Switched-Beam Antenna Array Measurements

For measuring the complete SWBA array performance in terms of radiation patterns, we also used the Far-Field measurement setup of the High Frequency Electronics laboratory of the UCI, in its probe station configuration to feed the CPW lines of each element of the 5 by 5 array. A 400$\mu$m pitch ground-signal-ground (GSG) probes are used for this purpose. A photograph of the radiation pattern measurement setup, together with a Rohacell foam structure, which is used to stack the dielectric lens with the array, and the probes feeding the array elements, is shown in Fig. 2.48. Then, a complete set of measurements of the slot/patch array, and of the SWBA array has been carried out at the 60 GHz band. The far-field co-polar and cross-polar radiation patterns produced by the lens when is illuminated for each single element of the array have been measured for a frequency sweep from 57 to 64 GHz in steps of 1 GHz.

#### 2.11.6.1 Radiation Pattern Results for a Single Element at 60 GHz Band

In order to test the radiating performance of a single antenna of the array, to evaluate the illumination of the lens, a single element of the five by five slot/patch array has been measured. We fed the CPW line of the central single element of the array ($3^{\text{rd}}$ column, $3^{\text{rd}}$ row) with the 400$\mu$m pitch probe. In Fig. 2.49 the H-plane normalized radiation patterns at 57, 60 and 64 GHz are shown. The observed ripples are caused by the scattering on the

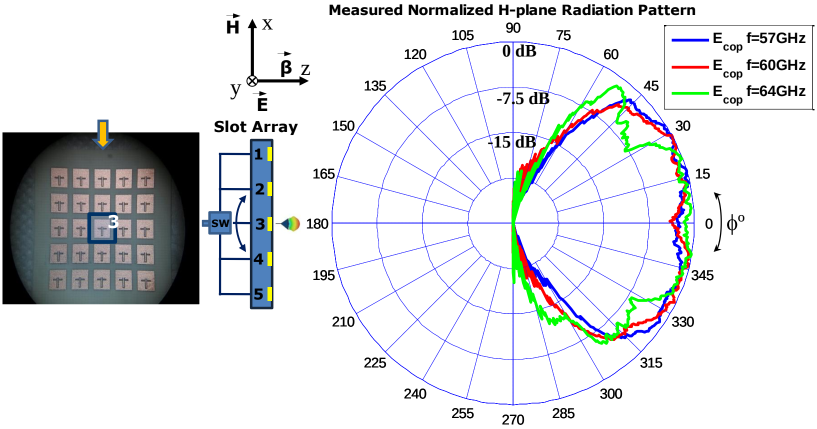

**Figure 2.49:** Measured normalized H-plane radiation pattern at 57, 60, and 64 GHz for the central element (3rd column, 3rd row) of the slot/patch antenna array (without the dielectric lens).

edges of the mechanical support structure. As in the previous cases, performing a power level comparison with the help of the conical horn antenna, we obtained a maximum broadside gain level of 6.5 dB, which is in good agreement with the simulation results, with a smaller decay at ±30º, which is even better than simulation results because its uniformity, providing an efficient lens illumination (-12 dB edge taper) to subsequently obtain the desired high-gain radiation patterns with the help of the lens.

### 2.11.6.2 Reflection Coefficient and Cross-Polarization Measurement Results

At the same time the radiation patterns were measured, we performed the reflection coefficient measurements of a single radiating element of the array, since it was already fed by the probes. The corresponding $S_{11}$-parameter meaured for the central element of the array is plotted in Fig. 2.50, after the calibration process, being compared to the

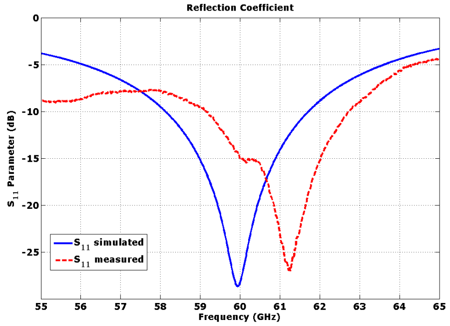

**Figure 2.50:** Measured reflection coefficient of the central element of the array.

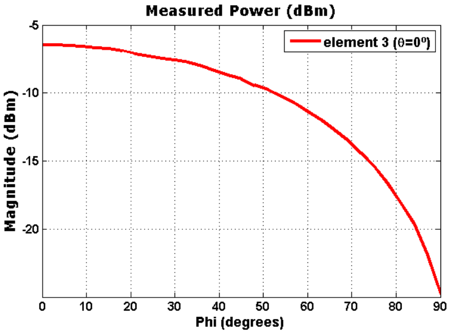

**Figure 2.51:** Measured cross-polarization level of the slot/patch antenna array.

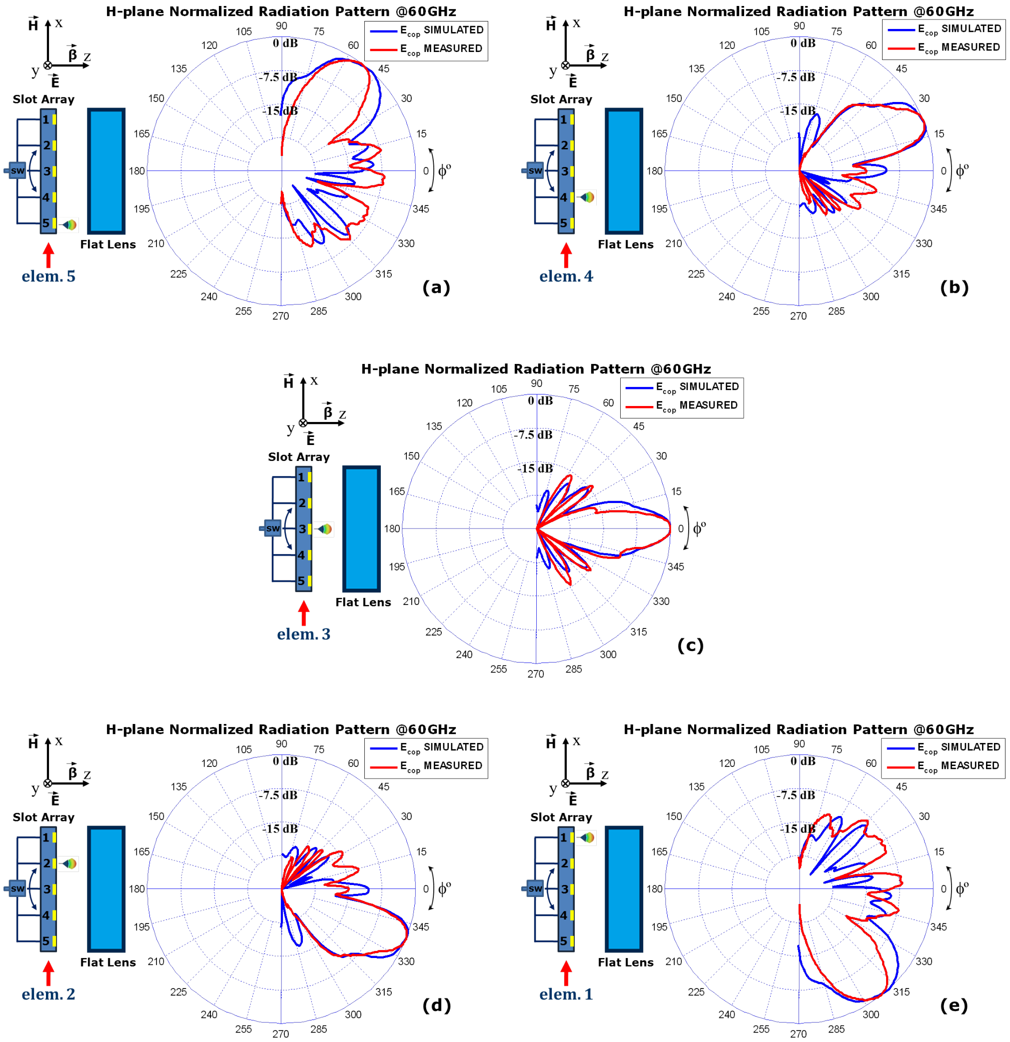

**Figure 2.52:** Comparison between simulated and measured H-plane radiation patterns at 60 GHz for the elements from 1 to 5 of the $3^{rd}$ row of the slot antenna array: (a) elem.5 (b) elem.4 (c) elem.3 (d) elem.2 (e) elem.1.

numerical result obtained with the CST. As it is shown, there is a slight shift of around 1 GHz in the frequency response, but the agreement, in general is good. The antenna is well-matched even in a wider frequency range compared to simulations, from 55 to 63.5 GHz at -10 dB, which practically represents the whole frequency band of interest. Moreover, the measured cross-polarization level is around 20 dB below the co-polarization level, as it is observed in the measurement results plotted in Fig. 2.51.

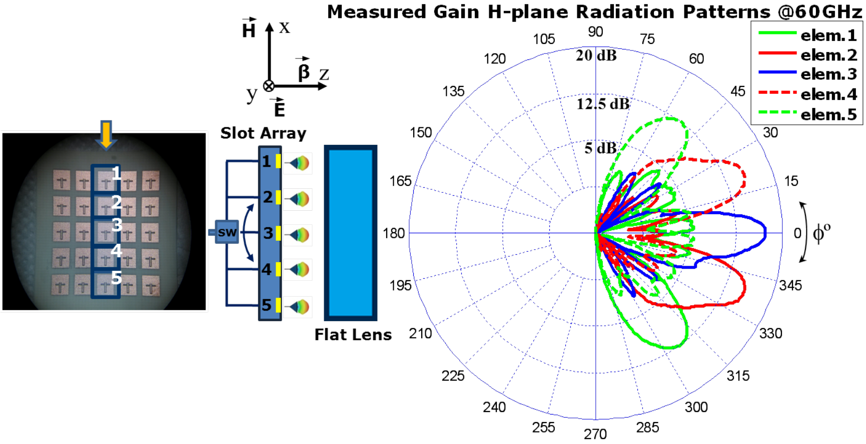

**Figure 2.53:** Complete set of H-plane gain radiation pattern measurement results at 60 GHz selecting each single radiating element of the 3$^{rd}$ column of the array.

### 2.11.6.3 Complete SWBA Array Radiation Pattern Measurement Results at 60 GHz Band

Finally, to evaluate the performance of the complete SWBA array, we measured the radiation patterns of the whole structure from 57 to 64 GHz in steps of 1 GHz. In order to obtain the complete set of beams in one single plane (e.g. H-plane), a total of 5 measurements have been performed at 60 GHz, again selecting and feeding individually all the elements of the 3$^{rd}$ row of the slot/patch antenna array. Therefore, the corresponding normalized H-plane Far-Field radiation patterns for the elements from 1 to 5 of the 3$^{rd}$ row are shown in Fig. 2.52. As it is observed, there is a very good agreement between CST simulation results and measurements performed at 60 GHz. Moreover, the measured cross-polarization level is also around -20 dB below the co-polarization component, since the lens is not affecting the performance of the array, plotted in Fig. 2.51, in this sense.

| Element Fed | Max. Gain | (θ°)scan | $\Delta\theta_{-3dB}$ | SLL |
|---|---|---|---|---|
| elem. 1 (*Rho*= +8 mm) | 12.82 dB | -52° | 19° | -7.2 dB |
| elem. 2 (*Rho*= +4 mm) | 15.45 dB | -20° | 16.4° | -12.3 dB |
| elem. 3 (*Rho*= 0 mm) | 17.25 dB | 0° | 12.7° | -14.3 dB |
| elem. 4 (*Rho*= -4 mm) | 15.45 dB | +20° | 16.4° | -12.3 dB |
| elem. 5 (*Rho*= -8 mm) | 12.82 dB | +52° | 19° | -7.2 dB |

**Table 2.7:** Summary of measured radiation pattern parameters of the SWBA array at 60 GHz selecting individually each one of the 5 elements of the central column.

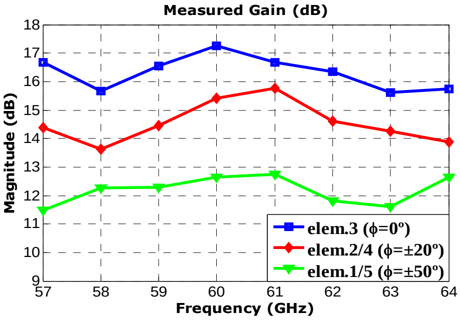

**Figure 2.54:** Measured bandwidth performance: maximum gain for each focusing direction.

In addition, gain measurements have also been performed at 60 GHz band. The complete set of 5 measured gain radiation pattern for the 3rd row of the array (i.e. H-plane) is shown Fig. 2.53, and the measured characteristic radiation pattern parameters at 60 GHz (maximum gain for each beam, scanning angles ($\theta°_{scan}$), half-power beamwidth ($\Delta\theta_{-3\,\mathrm{dB}}$), and SLL) are summarized in Table 2.7.

As it is observed, selecting the upper elements in the array, the high-gain radiation pattern produced by the dielectric flat lens is steered downwards. In the same way, selecting the lower elements, the high-gain radiation pattern is steered upwards, accordingly. Given the symmetry in the structure, selecting the elements on the left or on the right, the beams are steered rightwards or leftwards, respectively. Therefore, a total of 25 different high-gain beams can be obtained to scan in both theta and phi directions, selecting one single element of the array for each operation mode. Moreover, very good gain stability within the 60 GHz WPAN band (from 57 to 64 GHz) is also observed from the measured bandwidth performance shown in Fig. 2.54.

### 2.11.7 Switch Integration Issues

With the theoretical study, numerical simulations, modeling for a practical fabrication, manufacturing of the prototypes, and complete set of measurements, a total of 25 fixed high-gain beams can be selected individually to scan in both theta and phi directions. However, in order to individually select each one of the radiating elements of the 5 x 5 slot array, we need to address a complex integration of numerous switching elements, which represents a big technological challenge, and even more at millimeter-wave frequencies.

At this moment, to our best knowledge, different research groups are working in this sense to achieve fully integrated switching devices at 60 GHz frequency band. Some traditional solutions based on the complementary metal–oxide–semiconductor (CMOS) technology have been proposed, for example a single-pole double-throw (SPDT) transmit/recevie SW [94], or passive high electron-mobility transistor (HEMT) switches [95], which are very popular since they are easy to fabricate within integrated circuits on a single chip. However, both switching solutions proposed are very lossy, since the insertion losses vary between 3.6 and 4.5 dB, which represents a power drop unacceptable in order to achieve high data rate transmissions. More recently, other innovative solutions have been reported in the literature. micro-electromechanicals (MEMs) technology can enable switches with a superior performance than semiconductor switches in many aspects (e.g. low insertion losses, and almost zero power consumption). However, the reliability and robustness of RFMEM switches is nowadays still inferior to that of semiconductor switches [96]. Other innovative exotic solutions based on novel materials, such as graphene, have also been proposed in last years [97], but commercial implementations are still not available.

After all, the most common and reliable solution for switching at high frequencies is still based on the CMOS technology. In this sense, although recent results show better performance in terms of losses [98–100], these solutions allow only SPDT devices, when, in order to reduce considerably the number of SW needed to select individually each one of the 25 radiating elements of the proposed SWBA array, improved switching solutions with multiple throws were desirable (i.e. single-pole triple-throw (SP3T) or even single-pole quadruple-throw (SP4T), to an increased reduction of SW).

Therefore, alternative methods should be contemplated in order to avoid the issues related with the SW integration. In this sense, a novel alternative solution based on an inhomogeneous cylindrically distributed parameters dielectric flat lens and a linear FSSA array is introduced in Chapter 4 to realize not only a one-dimensional (1-D) beam-scanning, but a two-dimensional (2-D) beam scanning of high-gain radiation beams, representing an elegant solution applied from the antenna point of view to save the explained issues related to the integration of SW at millimeter-wave frequencies.

3

Chapter 3

# Inhomogeneous Matching Layer Design

*This chapter is specifically devoted to the design of a matching layer to increase the maximum achievable gain, reduce the back-radiation level, and enhance the bandwidth performance of a dielectric flat lens antenna for millimeter-wave applications. The performance of the original inhomogeneous gradient-index dielectric flat lens is compared to the performance of the lens with an inhomogeneous matching layer, and to the performance of the lens with a novel multiple-stacked inhomogeneous matching layer design.*

## 3.1 Introduction

As it has been pointed out in section 2.7.1, page 32, of the previous Chapter 2, from the numerical results obtained during the simulations of the inhomogeneous dielectric flat lens with the time-domain solver of the CST Microwave Studio, there is always a certain amount of back-reflection level which is produced because of the transition between two mediums with different permittivity (i.e. the transition between the free-space and the lens, and vice-versa, in the subsequent transition between the lens and the free-space again). Since the highest relative permittivity of the dielectric material used to design the inhomogeneous lens (center of the lens) is $\epsilon_r = 6$, multiple reflections of different significance are occurring. The magnitude of the power back-radiated is between 4 and 7 dB, which represents a front-to-back ratio (F/B) of around 12-15 dB, depending on the scanning angle performed and the frequency of operation, being in the best case around 2-3 dB of back-radiation, which leads to a F/B of 16-17 dB, as it is depicted in Fig. 3.1 from the CST simulation results for the complete SWBA array. This represents an additional loss factor that has to be considered in order to improve the maximum gain and the F/B.

## 3.2 Matching Layer Functioning Principles

The described undesirable effects can be reduced significantly using either corrugations fabricated on the lens surface [101,102], or wave transformers made of homogeneous [103], or artificial (metamaterial structures) dielectrics. Moreover, the influence of multiple ML upon the radiation characteristics of dielectric lenses has been studied in [104], especially in the perspective of wideband operation. However, to our best knowledge, the influence of single and multiple MLs has only been studied in detail for homogeneous shaped lenses (e.g. hemi-spherical lenses [104]), and they have never been studied before for inhomogeneous lenses, such as the presented in the first chapter of this PhD thesis. Therefore, an specific design should be proposed for inhomogenous lenses. In this sense, the main objectives to achieve for a new ML applied to inhomogeneous lenses are listed as follow:

- **Reduce the back-radiation level - Increase the F/B** To take advantage of the power which is being reflected.
- **Increase the maximum achievable gain** If the ML introduced is able to produce a smooth transition between the free-space and the lens, the reflected power will be optimally used to increase the gain in the boresight direction.
- **Improve the aperture efficiency** If the highest gain value is enhanced, the aperture efficiency is directly improved; the overall efficiency will be increased since the radiation performances will be better.
- **Reduce the SLL** Because of the spurious radiations of the lens feeding elements the SLL can be considerable, and the use of the ML can also help in their reduction.
- **Achieve a larger operational bandwidth** The lens broadband behavior has been already demonstrated with both numerical and experimental results. However, since the gain can be increased in a wider frequency band of interest, the bandwidth performance enhancement has also to be considered with the use of the ML.

With these objectives, the proposed ML structure is shown in Fig. 3.2.

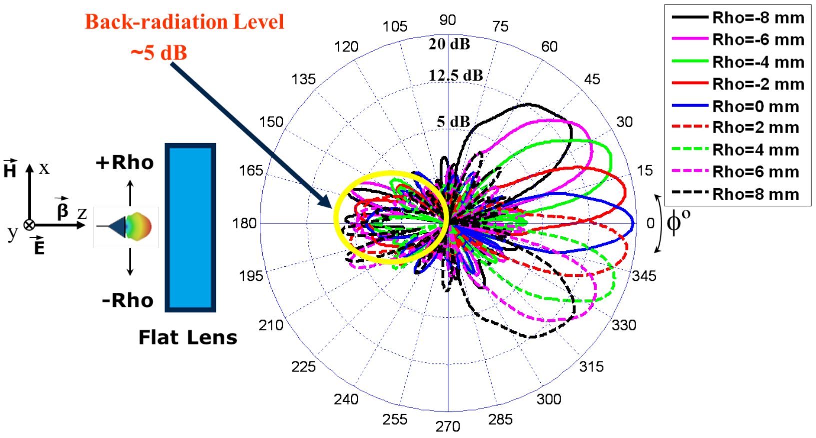

**Figure 3.1:** Simulation results of the back-radiation level of the dielectric flat lens.

## 3.3 Inhomogeneous Matching Layer Design Procedure

In order to reduce the described undesirable effects due to the reflections, the common quarter-wavelength matching technique is used to design the ML [88]. In this technique, a dielectric with a quarter-wavelength thickness is placed between two different dielectrics materials. If its intrinsic impedance is the geometric mean of those on the two sides, the ML will eliminate completely all the reflections [88]. In this sense, since our original flat lens design is an inhomogeneous gradient-index lens, an inhomogeneous gradient-index ML design (placed between a radiating element and the lens) is also required. Therefore, the novel iML design (same diameter as the lens, see Fig. 3.2) is initially also divided in six concentric rings with different permittivity values for each, in order to match the impedance for each lens permittivity zone. Thus, we determine the thickness and the effective permittivity of each iML ring by using:

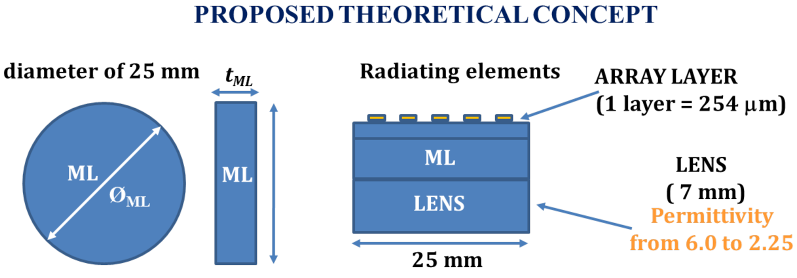

**Figure 3.2:** ML theoretical concept.

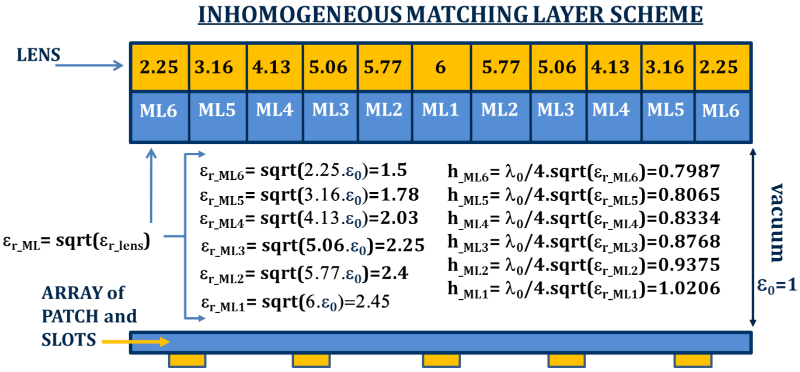

**Figure 3.3:** Single layer iML scheme.

$$h_{i_{ML}} = \frac{\lambda_0}{4\sqrt{\epsilon_{r_{i_{ML}}}}} \tag{3.1}$$

and,

$$\epsilon_{r_{i_{ML}}} = \sqrt{\epsilon_{r_{i_{Lens}}} \epsilon_0} \tag{3.2}$$

respectively, finally resulting in a stepped ML, as it is depicted in the schemes of Fig. 3.3 and Fig. 3.4. In the presented equations, $h_{i_{ML}}$ and and $\epsilon_{r_{i_{ML}}}$ are the thickness, and the permittivity of the i$^{\text{th}}$ zone of the dielectric iML, $\lambda_0$ is the free-pace wavelength, $\epsilon_{i_{Lens}}$ is the permittivity of the i$^{\text{th}}$ ring of the lens, and $\epsilon_0$ is the permittivity of the vacuum ($\epsilon_0 = 1$).

### 3.3.1 Single-Layer Matching Layer Design and Simulation Results (Narrowband Behavior)

The calculated values for each *i* zone of the inhomogeneous gradient-index ML are listed in Table 3.1. Then, the new introduced iML design has been numerically evaluated together with the dielectric flat lens in the same CST simulation setup used in the previous lens simulation sections at 60 GHz band.

The same set of simulations for each frequency using the same previously described CST simulation setup has been reproduced with the iML attached to the lens. Therefore, the H-Plane gain radiation patterns simulation results at 60 GHz for the cases of the lens with and without iML are compared and plotted in Fig. 3.5 for the same *Rho* feeding positions of the WR-15 open-ended waveguide, as in previous sections. Given the lens and ML structure, symmetric patterns are obtained for the negative *Rho* positions. As it is shown, the back-radiation reduction is remarkable, with a considerable enhancing in the maximum gain. Moreover, in some cases, the SLL are also reduced appreciably. To facilitate the reading, in Table 3.2 these values are summarized for the cases of the lens with and without the single ML.

**Table 3.2:** Radiation pattern characteristic parameters for the dielectric flat lens with and without the single layer iML.

| Feeding Position | No ML | | | Inhomogeneous ML | | |
|---|---|---|---|---|---|---|
| | Gmax | BR | SLL | Gmax | BR | SLL |
| Rho=0 mm | 18.9 dB | 4.9 dB | -23 dB | 20.1 dB | -3.7 dB | -28 dB |
| Rho=±2 mm | 18.6 dB | 5.1 dB | -21.9 dB | 19.2 dB | 0.8 dB | -22.7 dB |
| Rho=±4 mm | 17.4 dB | 5.1 dB | -14.1 dB | 18.7 dB | 1 dB | -21.6 dB |
| Rho=±6 mm | 16.2 dB | 6.5 dB | -13.4 dB | 17.5 dB | 1.3 dB | -12.5 dB |
| Rho=±8 mm | 14.8 dB | 6.7 dB | -13.8 dB | 16 dB | 5.4 dB | -12.5 dB |

It has been numerically demonstrated the improvement achieved with the proposed inhomogeneous ML (iML) design. The lens with the iML delivers a better performance in terms of maximum achievable gain, back-radiation reduction, and SLL. However, the simulation results reported until this moment has been obtained at a single frequency of 60 GHz (i.e. the frequency of design). In this sense, an accurate broadband analysis has also been performed. The numerical results obtained at frequencies below the frequency of design show that the lens with the novel introduced iML performs better in all the considered radiation pattern parameters. However, the results are not as good as the achieved at 60 GHz. Moreover, when the frequency of simulation is increased up to 64 GHz, the results show that the performance is even worse in terms of maximum back-radiation level. This behavior has been observed for all the frequencies above the frequency of design. The numercial results at these higher frequencies will be shown, after the following section, in which we will try to solve the narrowband behavior observed for this single iML. In this sense, the use of multiple stacked MLs to improve the results in a broad frequency band of interest is investigated in the next subsection for a particular case of the inhomogeneous dielectric flat lens.

### 3.3.2 Triple-Layer matching Layer Design and Simulation Results (Broadband behavior)

Since a certain narrowband behavior has been observed for the introduced inhomogeneous ML (iML), the use of stacked ML has been investigated in order to obtain a broadband

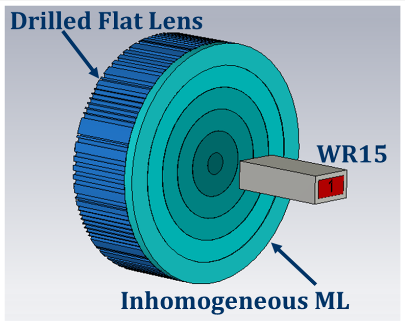

**Figure 3.4:** Single iML modeling.

**Table 3.1:** Calculated thicknesses and permittivity values for each zone of the single iML.

| FLAT LENS | | | MATCHING LAYER | |
|---|---|---|---|---|
| Ring | Ring width | $\varepsilon_{reff}$ | $\varepsilon_{reff\,ML}$ | $h_{ML}$ |
| 1 | 1.14 mm | 6.05 | 2.45 | 0.7987 mm |
| 2 | 2.27 mm | 5.77 | 2.40 | 0.8065 mm |
| 3 | 2.27 mm | 5.06 | 2.25 | 0.8334 mm |
| 4 | 2.27 mm | 4.13 | 2.03 | 0.8768 mm |
| 5 | 2.27 mm | 3.16 | 1.78 | 0.9375 mm |
| 6 | 2.27 mm | 2.25 | 1.5 | 1.0206 mm |

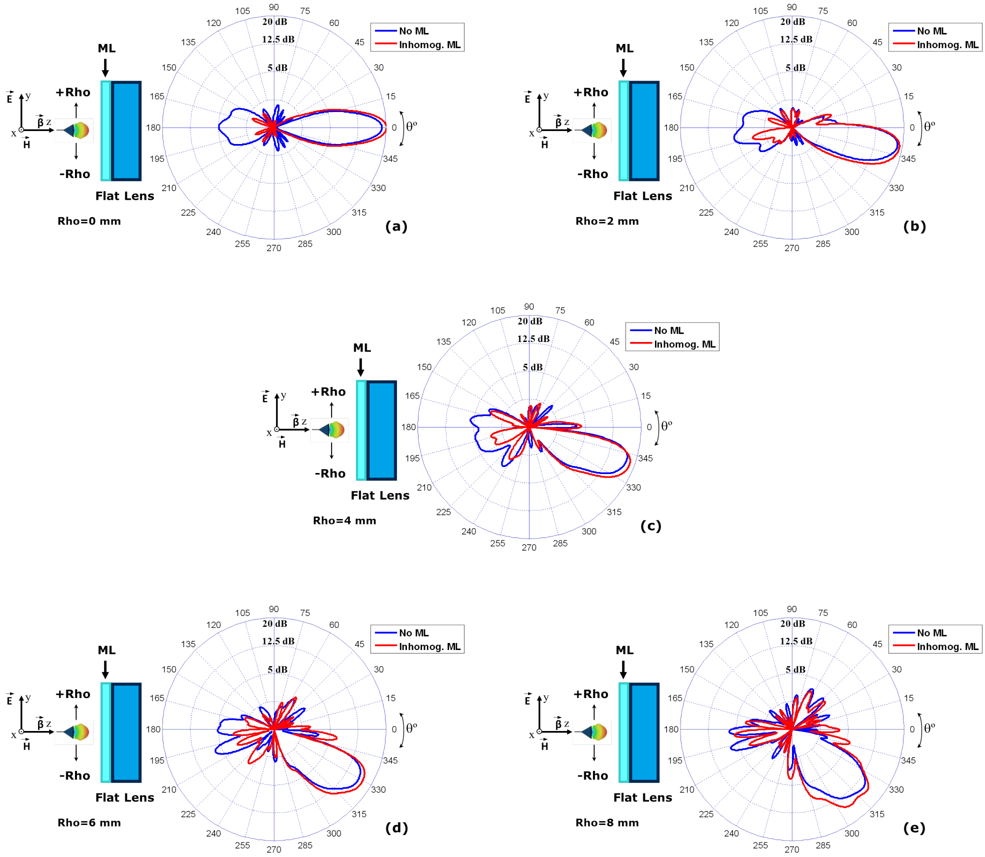

**Figure 3.5:** Comparison between simulated H-Plane radiation patterns at 60 GHz for the flat lens with and without single ML for different *Rho* feeding positions (a)$Rho = 0mm$ (b) $Rho = 2mm$ (c) $Rho = 4mm$ (d) $Rho = 6mm$ (e) $Rho = 8mm$. Given the lens and ML structure, symmetric patterns are obtained for the negative *Rho* positions.

operation solution. The design procedure for a triple-ML is the same as it is described for a single ML. Once the single ML is designed, and placed in between the two different medias that we want to match (i.e. the vacuum and the lens), we have to consider the new situation created, with a transition between the vacuum and one side of the single ML, and the transition between the other side of the single ML and the lens. Therefore, applying the aforementioned equations (3.1), and (3.2), two new ML are designed for the respective new transitions described (between the vacuum and the single ML, and the single ML and the lens). Then, three stacked ML are the final result of this complete process.

Once again, since the dielectric flat lens to match is homogeneous, and the first single ML applied is inhomogeneous as well, the resulting triple-ML has to be inhomogeneous in the same way, adapting each one of the individual zones of the lens. Then, with the described procedure, and applying the respective equations, the different thicknesses

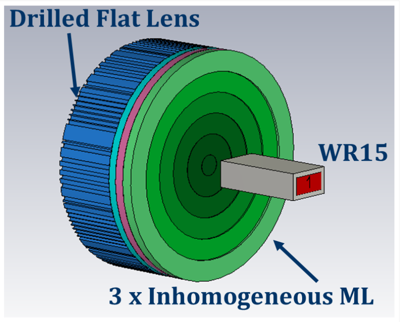

**Figure 3.6:** Triple-iML modeling.

**Table 3.3:** Calculated thicknesses and permittivity values for each zone of the triple-iML.

| | iML1 | | iML2 | | iML3 | |
|---|---|---|---|---|---|---|
| **Ring** | $\varepsilon_{\mathrm{reff\,ML}}$ | $h_{\mathrm{ML}}$ | $\varepsilon_{\mathrm{reff\,ML}}$ | $h_{\mathrm{ML}}$ | $\varepsilon_{\mathrm{reff\,ML}}$ | $h_{\mathrm{ML}}$ |
| 1 | 3.83 | 0.64 mm | 2.45 | 0.80 mm | 1.57 | 0.99 mm |
| 2 | 3.72 | 0.65 mm | 2.40 | 0.81 mm | 1.55 | 1.00 mm |
| 3 | 3.37 | 0.68 mm | 2.25 | 0.83 mm | 1.50 | 1.02 mm |
| 4 | 2.89 | 0.73 mm | 2.03 | 0.88 mm | 1.43 | 1.05 mm |
| 5 | 2.37 | 0.81 mm | 1.78 | 0.94 mm | 1.33 | 1.08 mm |
| 6 | 1.84 | 0.92 mm | 1.5 | 1.02 mm | 1.23 | 1.13 mm |

and permittivities of each one of new the three stacked iML designs are summarized in Table 3.3, and the triple-iML model attached to the dielectric flat lens is depicted in Fig. 3.6. Logically, the design parameters for the second layer (i.e. the one in the middle) of this triple-iML are the same as for the first single iML.

Then, the same set of simulations for each frequency using the same previously described CST simulation setup has been reproduced again with the triple-iML attached to the lens. Consequently, the H-Plane gain radiation patterns simulation results are obtained for all the frequency band of interest, from 57 to 66 GHz, and for the same *Rho* feeding positions of the WR-15 open-ended waveguide, as in previous sections. In this case, the H-Plane gain radiation patterns are plotted together for the broadside radiation (as a representative case) in Fig. 3.7, for the cases of the lens without ML, and using the single, and the triple-MLs designed, in order to perform a comparison in terms of back-radiation level, maximum achievable gain, and SLL, at the frequencies of 57, 60, and 64 GHz (low, middle, and upper frequencies inside the American WPAN band). To verify the aforementioned broadband behavior of the triple-iML, instead of plotting all the *Rho* feeding positions at a single frequency, or in a table, the bandwidth performance has been plotted in Fig. 3.8. Only the $Rho = 0mm, 4mm, and8mm$ are plotted in order to avoid cluttering the figure.

As it is observed, for the broadside direction, it is absolutely clear that at 60 GHz, which is the frequency of design, the back-radiation level is reduced considerably by using both iML; however, the reduction achieved with the single iML is obviously higher. At the lowest frequency of the band, 57 GHz, the single iML is decreasing the back-radiation level but, in any case, in the same magnitude as at 60 GHz. Nevertheless, the triple-iML design is clearly performing better, not only interms of back-radiation reduction, but also in terms of SLL and improved gain. The most important difference is observed at the highest frequency of the band, 64 GHz, in which the total amount of back-radiation power is reduced with the single iML, but the maximum level pointing to -180º is even worse than without using the iML. However, the use of the triple-iML at this frequency leads to a great result in all the considered radiation pattern parameters.

Moreover, from the bandwidth performance plotted in Fig. 3.8, the gain improvement along the whole frequency band of interest for different scanning angles of the lens, is unquestionably better using the triple-iML proposed in this section.

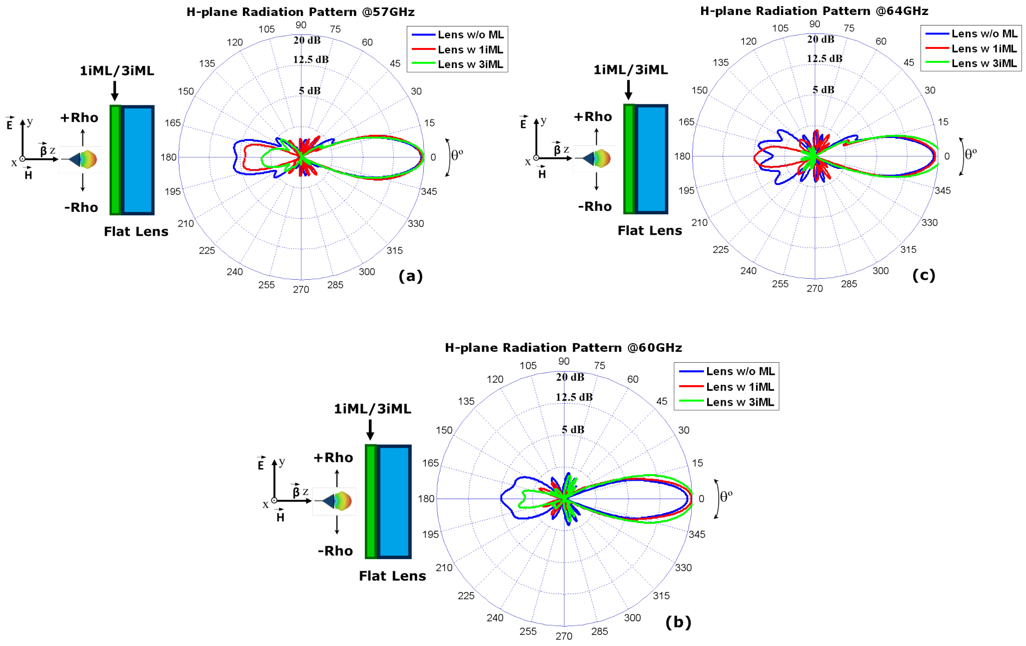

**Figure 3.7:** Simulated H-Plane gain radiation patterns produced by the dielectric flat lens, with and without the considered MLs, at the frequencies of (a) 57 GHz, (b) 60 GHz, and (c) 64 GHz.

### 3.3.3 Final Comments on the inhomogeneous ML (iML) design

In this section, two different inhomogeneous ML (iML) designs have been evaluated to improve the performance of a dielectric flat lens for millimeter-wave applications. Our numerical results indicate that compared to the original flat lens design without ML, the lens with the single inhomogeneous ML delivers a better performance in terms of maximum achievable gain, back-radiation reduction, and SLL at 60 GHz. However, its use in an extended frequency band, such as the whole 60 GHz WPAN band, is not recommended. In this sense, it has been demonstrated that the use of multiple stacked iML is able to improve the performance for a broad frequency range.

The observed behavior is the commonly obtained in most of the broadband systems; there exist a trade-off between the maximum performance in a desired particular single frequency, or in an extended range, paying the price of a lower performance.

Most probably a broadband system is not improving the performance of a particular full custom design at an specific frequency but, on the contrary, is performing very well in a wide frequency range, in which an specific design is even able to deteriorate the overall performance due to its narrowband behavior.

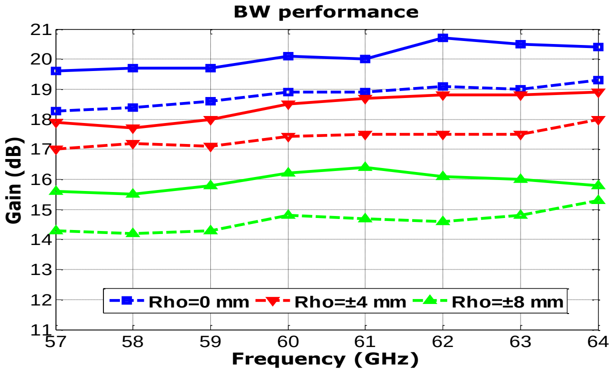

**Figure 3.8:** Bandwidth performance for the lens with and without the novel triple-iML. Solid lines identify the use of the lens with triple-iML, whereas a dashed line identifies the lens without it.

Finally, as it is shown, the range of permittivity values obtained for the different iML designs proposed in this chapter vary from $\epsilon_r = 1.23$ to $\epsilon_r = 3.83$. In this sense, novel alternatives in the manufacturing of materials have to be considered, since with the proposed method of drilling a substrate to reduce its effective dielectric constant, in practice, the minimum achievable permittivity depends on the density of holes performed, thus a severe limitation exists in order to preserve the substrate material to be self-supporting despite the drills. For this reason, permittivity values around 1.2 seem to be hardly achievable with the described technique. However, as it has been mentioned before, novel techniques such as the recently introduced in [90], propose a technological process in which a foam material is pressed to increase its concentration by releasing the trapped air, thus increasing the final dielectric constant of the resulting material. Since the initial permittivity of the foams is around 1.3, being able to offer permittivity values up to 2-2.5 after pressing [90], makes this solution interesting from our point of view to manufacture the introduced novel iMLs.

# 4

## Chapter 4

# Cylindrically Distributed Parameters Dielectric Flat Lens Design

*THIS chapter is intended to give an alternative solution, specifically applying the knowledge from the antenna architecture point of view, to reduce the number of switching elements needed to perform a full 2-D beam-scanning of high gain radiation beams. A new switched-beam antenna array concept based on an inhomogeneous dielectric flat lens with a cylindrical effective parameter distribution is introduced. With this cylindrical parameters distribution, the beam-scanning can be performed in one plane by moving (or selecting) the position of a radiating single element along the gradient-index axis, whereas the beam can be maintained invariant in the other direction, despite changing the radiating element position. In this way, the beam-scanning can be achieved in the constant-index axis of the lens by means of a different technique, a frequency-scanned slot antenna array, which it is also introduced in next Chapter 5, in order to reduce the switching elements needed in the proposed complete switched-beam antenna array structure, to finally perform the scan of the high-gain radiation beam in both theta and phi dimensions of the space.*

## 4.1 Introduction

With the work presented in Chapter 2, a total of 25 fixed high-gain beams can be selected individually to scan in both theta and phi directions. However, in order to individually select each one of the radiating elements of the 5 × 5 slot array, we need to address a complex integration of numerous switching elements, which represents a big technological challenge, and even more at millimeter-wave frequencies.

Then, as it has been explained in section 2.11.7, page 56, alternative methods should be contemplated in order to avoid the issues related with the SW integration. In this sense, a novel antenna architecture alternative solution based on an inhomogeneous cylindrically distributed parameters dielectric flat lens, and a linear frequency-scanned slot antenna (FSSA) array (Chapter 5), is introduced to realize not only a one dimensional (1-D) beam-scanning, but a two-dimensional (2-D) beam scanning of high gain radiation beams, representing an elegant solution applied from the antenna point of view to save the explained issues related to the integration of SW at millimeter-wave frequencies.

## 4.2 Cylindrically Distributed Parameters Dielectric Flat Lens: Design and Simulation Results

In order to avoid the switch integration issues we introduce a new interesting antenna solution based on a novel design of inhomogeneous dielectric flat lens with an effective gradient-index in one axis, while a constant-index is maintained along the other one (see Fig. 4.1). With this cylindrical effective parameter distribution, the beam-scanning can be performed in one plane by moving (or selecting) the position of a single radiating element along the gradient-index axis, whereas the beam can be kept invariant in the other direction, in which the effective parameters are maintained constant, despite changing the radiating element position in this particular axis.

In this way, the beam-scanning can be achieved in the constant-index axis of the lens by means of a different technique, a frequency-scanned slot antenna array (e.g. [105]), which it is also presented in next Chapter 5, thus reducing the number of switch elements needed in the proposed complete switched-beam antenna array structure, to finally perform a 2-D scanning of high-gain radiation pencil beams.

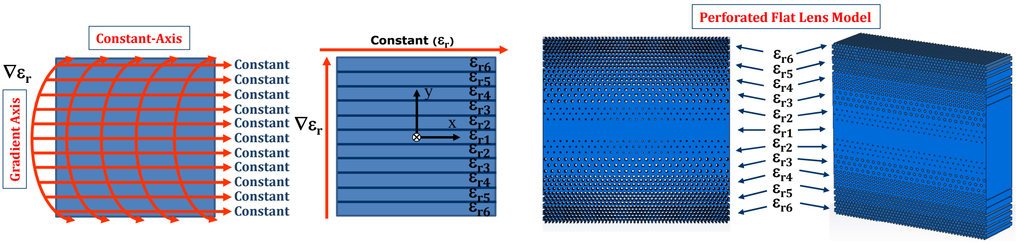

**Figure 4.1:** Cylindrically distributed parameters flat lens theoretical design (left) and modeling by using triangular unit cells of perforations (bottom).

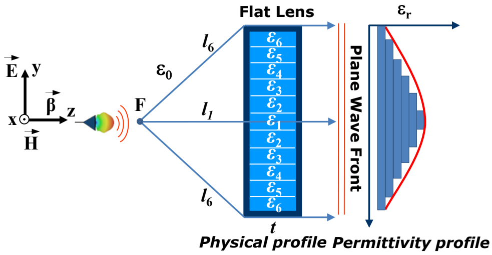

| Section | Section dimensions | $\varepsilon_{reff}$ | $\alpha$ | $d$ | $s$ |
|---|---|---|---|---|---|
| $\varepsilon_{r1}$ | 25 x 2.27 $mm^2$ | 7.1 | - | - | - |
| $\varepsilon_{r2}$ | 25 x 2.27 $mm^2$ | 6.79 | 0.051 | 0.2 mm | 0.845 mm |
| $\varepsilon_{r3}$ | 25 x 2.27 $mm^2$ | 6.01 | 0.179 | 0.4 mm | 0.901 mm |
| $\varepsilon_{r4}$ | 25 x 2.27 $mm^2$ | 4.99 | 0.346 | 0.4 mm | 0.648 mm |
| $\varepsilon_{r5}$ | 25 x 2.27 $mm^2$ | 3.92 | 0.521 | 0.4 mm | 0.528 mm |
| $\varepsilon_{r6}$ | 25 x 2.27 $mm^2$ | 2.9 | 0.639 | 0.4 mm | 0.476 mm |

**Figure 4.2:** Cylindrically distributed parameters dielectric flat lens functioning principle along its gradient-index axis (left); the permittivity profile values are constant along $x$-axis. Table with perforated dielectric flat lens characteristic parameters (right).

### 4.2.1 Concept Description

The inhomogeneous cylindrically distributed parameters flat lens functioning principle, along gradient-index axis, is shown in Fig. 4.2. As it is shown, in this specific axis, the needed behavior is the same as for any axis of the circular lens introduced in the previous Chapter 2, therefore, the same concepts can be applied. The theoretical lens design consists in a set of eleven rectangular sections of different permittivity ($\epsilon_r$) materials, in order to produce the desired phase delays required to obtain a plane wave behind the lens, when the lens is illuminated from its central focus position. In the same way, when the feeding position is moved along y-direction (see Fig. 4.2), the different permittivity values of the lens produce a linear phase slope, which steers the beam only along the gradient-index axis (i.e. along $y$-direction), accordingly. As a result of the lens cylindrical parameters distribution, if the position of the feeding element is moved along the constant-index axis (i.e. along $x$-direction), the beam is maintained invariant, because the phase is not being corrected in this specific dimension. Therefore, the theoretical concept for the described behavior of the flat lens in front of a linear array of antennas distributed along the constant-index axis, which is able to scan its beam in this dimension by sweeping the frequency, is shown in Fig. 4.3. Although the described innovative antenna concept can be applied and scaled for all the aforementioned millimeter-wave applications, the main part of following sections are devoted specifically for future 5G communication systems at 60 GHz frequency band, since the lens is designed to operate at this frequency; this is only to simply demonstrate the viability and test its performance for a particular case of application, but always keeping in mind and considering the higher frequency bands along this paper due to the good broadband behavior of the lens, which will be demonstrated.

### 4.2.2 Practical Dielectric Flat Lens Design

After an optimization process, with a trade-off between maximum achievable gain and aperture dimensions (again, a value around 20 dB gain is estimated as sufficient for typical WPAN communication systems [87]), the theoretical lens total dimensions are fixed in 25 mm x 25 mm (5 $\lambda_{0_{60GHz}}$ x 5 $\lambda_{0_{60GHz}}$), with 7 mm thickness (1.4 $\lambda_{0_{60GHz}}$), and a focal length of $F = 6.25$ mm (1.25 $\lambda_{0_{60GHz}}$). The lens geometry, which possesses axial symmetry, is divided in eleven equal dimension sections (see Fig. 4.1 and Fig. 4.2), with six different permittivity materials, symmetrically distributed from the center, as it is depicted.

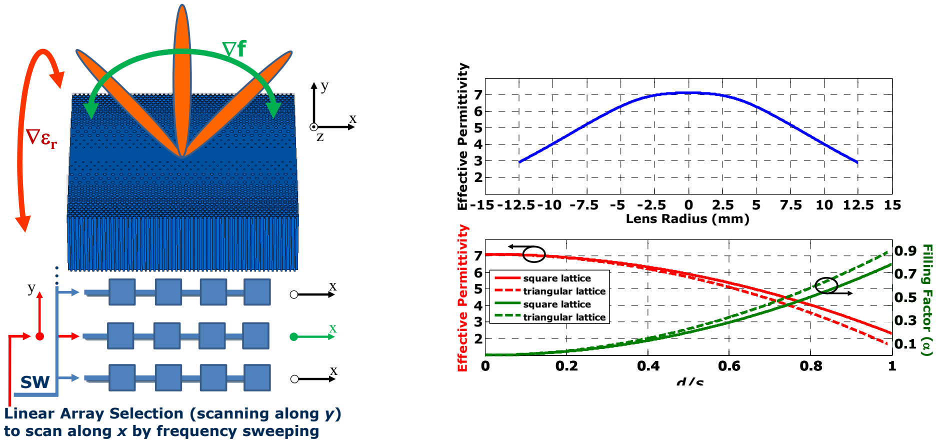

**Figure 4.3:** New SWBA array concept (left) with cylindrically distributed parameters flat lens and frequency-scanned array to perform beam-scanning in theta and phi, by frequency sweeping or selecting a specific linear array. Flat lens permittivity profile along gradient-index axis (right, top), and characteristic parameters for the drilled LTCC Dupont 9k7 (right, bottom): effective permittivity needed to fabricate the lens versus d/s relationship (left axis, red curves), and filling factor also as a function of d/s (right axis, green curves).

We start the design procedure, in the same way as it has been described for the previous inhomogeneous circular lens design, by setting the permittivity value of the outer sections of the lens, and then, the rest of the permittivity values for the different sections are obtained in order to produce the desired phase delays required to equal the different electrical path lengths that travel, from the lens focal point to the lens rear, through free space and each dielectric section of the lens. The set of six permittivity values needed for the eleven different zones of the lens are summarized in the Table of Fig. 4.2. Consequently, we selected the DuPont 9k7 ($\epsilon_r = 7.1$, $\tan\delta = 0.0009$) dielectric substrate in order to model, simulate, and fabricate the final lens prototype. This dielectric material has also been selected because in this PhD thesis we also explore new fabrication techniques for dielectric flat lenses. In this sense, the proposed cylindrically distributed parameters flat lens will be fabricated using low-temperature co-fired ceramics (LTCC) technology which, essentially, consists in building a multi-layered substrate structure with the capability of printing different metallization individually in each single dielectric glass/ceramic sheet (called green-tape). The complete fabrication process, described in detail, is explained in next Chapter 6, at page 91.

Therefore, as it has been described in previous section 2.5, at page 26, because of the difficulty of fabricating lenses through the fusion of different materials, we modeled again the cylindrically distributed parameters lens in order to build a prototype by means of perforating a single layer of dielectric substrate, applying the introduced equations.

Hence, the flat lens permittivity profile curve needed along the gradient-index of the lens, and the curves of characteristic parameters ($\epsilon_{r_{eff}}$, $\alpha$, $d$, and $s$) required to construct this smooth profile by drilling the substrate using triangular or square unit cells of holes are plotted in Fig. 4.2, where again, the filling factor ($\alpha$) is the fraction of material

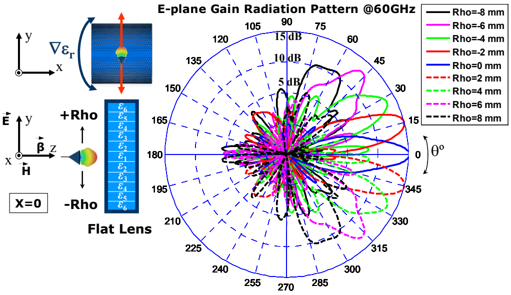

**Figure 4.4:** E-Plane Gain Radiation Pattern simulation results at 60 GHz for each *Rho* feeding position of the WR-15 waveguide along gradient-axis of the lens.

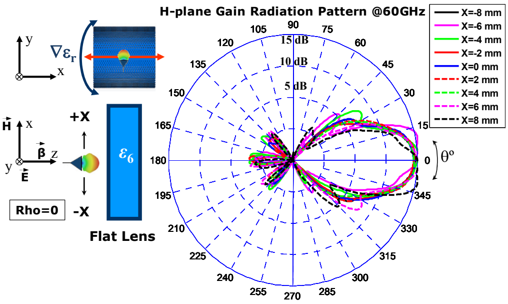

**Figure 4.5:** H-Plane Gain Radiation Pattern simulation results at 60 GHz for each Rho feeding position of the WR-15 waveguide along gradient-axis of the lens

removed by perforations. Triangular lattices are finally selected as well to model the design since, for a fixed $\alpha$ needed, this results in a more relaxed $d/s$ relationship and fabrication process. The characteristic parameters of the final prototype modeled by perforations, using triangular unit cells of holes, are also included in the Table of Fig. 4.1.

### 4.2.3 Dielectric Flat Lens Simulation Results

The perforated flat lens model has been simulated at 60 GHz band, from 57 to 66 GHz, using the time-domain solver of the CST Microwave Studio in order to test its focusing capabilities in the whole European WPAN frequency band. A complete set of nine different simulations have been performed corresponding to different discrete positions of a radiating element (which could correspond to the positions of the antenna element in a switched-beam array) along the gradient-index axis (i.e. $y$-direction in Fig. 4.2), going from $Rho = -8$ mm to $Rho = +8mm$, in steps of 2 mm, testing the beam-steering capabilities of the lens. Another set of nine different simulations have also been performed moving the radiating element along the constant-index axis (i.e. $x$-direction), to test that the beam produced by the lens remains almost invariant despite the position of the feeding antenna in this specific dimension.

In both sets of simulations, the radiating element used is aslo a rectangular aperture model, a WR-15 open-ended waveguide ($S_{11} < -10$ dB in the whole frequency band of interest), which provides an efficient lens illumination with around -12 dB edge taper in the E-Plane. Then, for each position of the radiating waveguide, the corresponding E and H-plane radiation patterns are plotted at 60 GHz in Fig. 4.4 and Fig. 4.5, for the gradient-index and constant-index cases, respectively.

As it is shown, the expected behavior of the lens is obtained for both described cases: a radiation beam with around 15 dB of gain can be steered ±15º in the gradient-axis, and up to ±60º with more than 10 dB gain, while a radiation beam with around 15 dB gain is practically maintained invariant pointing to the broadside direction despite the feeding aperture is being moved along the constant-index axis, allowing us to perform the beam-scanning in this direction by using a different technique.

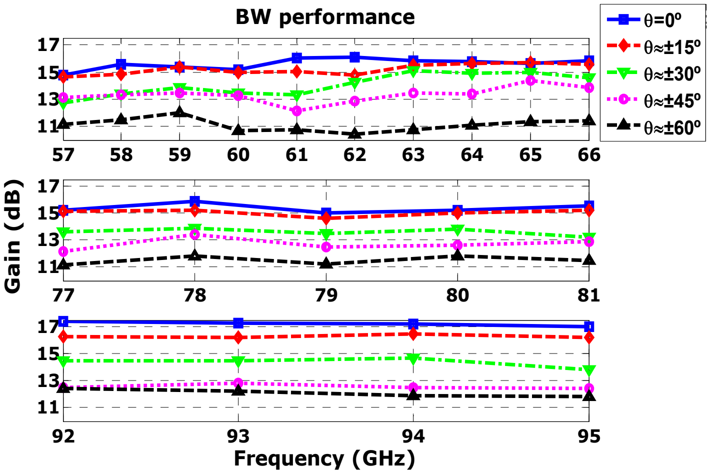

**Figure 4.6:** Simulated bandwith performance: gain for different *Rho* positions of feeding WR15/10 along lens gradient-axis at frequency bands of interest.

The maximum gain obtained in our numerical results is slightly lower compared to the gain achieved with the inhomogeneous circular lens presented in 2, because in this case the cylindrically distributed parameters flat lens is performing the phase correction only in one single dimension instead of two. For this reason, the radiation beam obtained is a fan-beam type pattern (i.e. a beam with a narrow beamwidth in one dimension, broader in the orthogonal), which could be also very interesting for some particular applications such as radar and imaging systems and, more specifically, for high-speed indoor communication systems at 60 GHz [106], in which this kind of pattern has been successfully evaluated operating in the 60 GHz band, recommending its utilization in certain situation at access points (APs) or portable stations (PSs), for example, due to its good immunity to azimuth pointing deviation [106].

However, sometimes it is not easy to obtain a fan-beam shape with good beam-scanning capabilities without paying the price of a complex and bulky antenna configuration. The introduced novel lens achieves the described fan-beam behavior at the same time it preserves a planar antenna structure, very interesting for all the aforementioned reasons related to APs and PSs. Furthermore, although the original lens has been designed at 60 GHz, the concept is not only scalable at higher frequencies, but also the original lens shows good performance at 79 and 94 GHz. In this sense, to demonstrate the broadband behavior of the proposed design, the lens has been also numerically tested at these two considered higher frequency bands, obtaining similar beam-steering capabilities in the gradient-axis, without pattern distortion, presenting very good gain stability. This remarkable behavior is observed, in Fig. 4.6, from the simulated bandwidth performance, for the three considered frequency bands of interest. Note that for the 79 and 94 GHz bands, the simulations have been realized replacing the WR-15 open-ended waveguide for a WR-10 model, which is also well-matched over the whole W-band (from 75 to 110 GHz). It is also remarkable that from simulation results we obtain total and radiation efficiencies between 90 and 95% for the lens fed with the corresponding rectangular apertures, since a low-loss LTCC substrate is used.

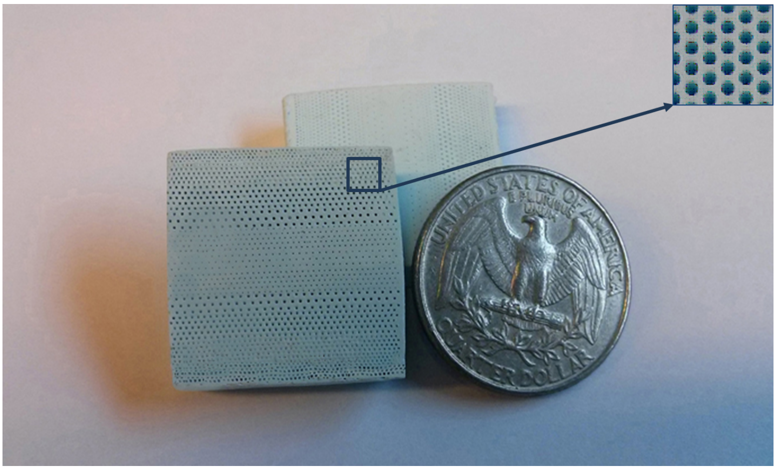

**Figure 4.7:** LTCC dielectric flat lens prototype with the effective parameters cylindrically distributed. A microscopic image of a high hole density zone is shown in the inset of the upper-right corner.

## 4.3 Fabrication of the prototypes

Once the new designed inhomogeneous cylindrically distributed parameters dielectric flat lens has been numerically characterized, and promising simulation results were obtained, different prototypes have been fabricated at the facilities of the Universitat Politècnica de València (UPV) in low-temperature co-fired ceramics (LTCC) technology, as it is completely described in Chapter 6, at page 91, in order to characterize its performance with a complete set of measurements. It is remarkable that the proposed fabrication method reduces considerably the final fabrication time compared to the fabrication time needed for manufacturing the TMM6 lens introduced in Chapter 2, which was huge using carbide drills on a hard substrate, because the LTCC process allows to perform around 1000 holes per minute on each soft substrate layer.

Then, we performed at each one of the 31 layers needed to built the lens a total of around 1500 holes of 0.2 and 0.4 mm in diameter, with a via punching process machine following the curves previously specified in Fig. 4.2, to finally achieve the desired gradient-index permittivity profile in one axis, while a constant-index profile is achieved in the orthogonal one. A photograph of the final lens prototype is shown in Fig. 4.7, where a detailed microscopic image of a high hole density zone is additionally provided.

## 4.4 Cylindrically Distributed Parameters Dielectric Flat Lens: Measurements

A complete set of measurements have been carried out at UPC facilities in order to assess the performance of the proposed cylindrically distributed paramters dielectric flat lens for millimeter-wave applications.

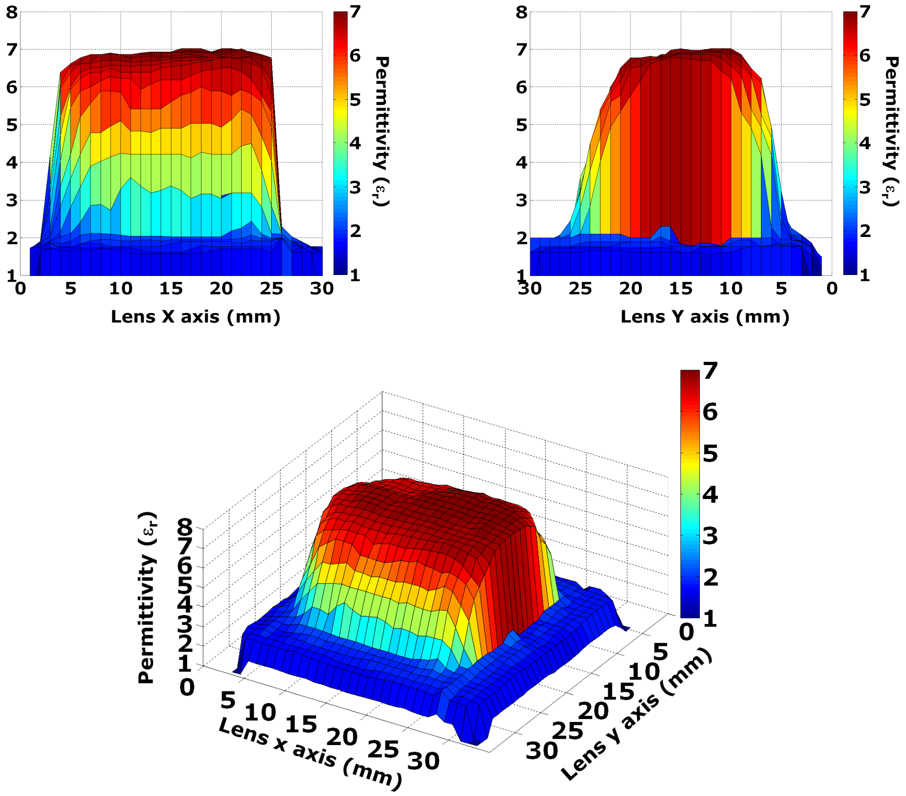

**Figure 4.8:** 3-D representations of the measured permittivity profile.

## 4.4.1 LTCC Lens Permittivity Profile Measurements

Once again, before testing the performance of the *cylindrical* dielectric flat lens in terms of radiation patterns parameters, $S$-parameters, or efficiencies, it is fundamental to assert that the required permittivity profiles have been achieved after the LTCC fabrication process. With the described purpose, to precisely measure the permittivity profile of the fabricated prototype, the same time-domain spectroscopy (TDS) system shown in Fig. 2.21, applying the same methodology described in section 2.9.2.1, 36, of the previous chapter 2 has been used. Then, the 3-D representation of the measured permittivity profile for the LTCC dielectric flat lens with the effective parameters cylindrically distributed is plotted in Fig. 4.8. As it is shown, the gradient-index axis is perfectly defined, while the constant-index dimension is also well described (it is easy to identify the different permittivity zones), despite the physical shape of the designed lens with an absolutely planar structure, thus demonstrating the good fabrication results achieved, and confirming the viability in the LTCC fabrication process for integrated lens antennas. In Fig. 4.9, different cuts at every millimeter along $X$ and $Y$ dimensions are also plotted to clearly identify the gradient-index and the constant-index are perfectly defined.

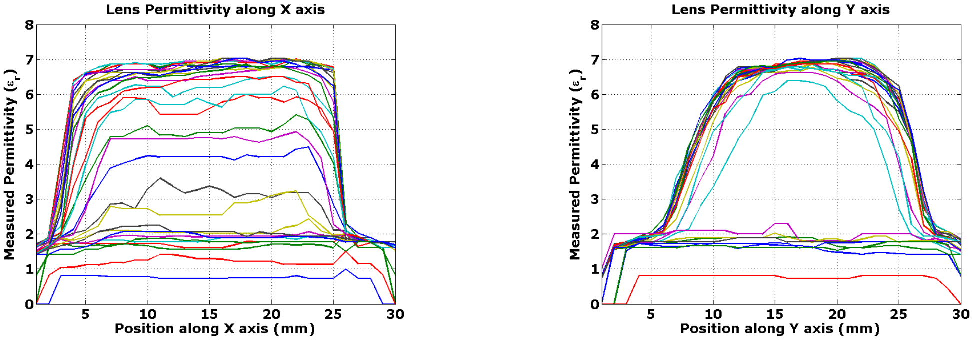

**Figure 4.9:** Permittivity profile sections of the inhomogeneous *cylindrical* dielectric flat lens.

### 4.4.2 LTCC Lens Radiation Pattern Measurements

A complete set of measurements of the lens performance has been carried out at 60 GHz band in the AntennaLab facilities of the UPC. In the previous sections we described that in order to measure the far-field radiation patterns produced by the lens, we used the measurement setup of the UCI, since at that moment the instrumentation and components available at AntennaLab facilities only allowed the measurement at different frequency bands but not at 60 GHz. Fortunately, the new far-field measurement setup is currently available and already allows the measurement of the far-field radiation patterns in a plane. Therefore, the far-field radiation patterns produced by the lens fed with a WR-15 open-ended waveguide have been measured from 57 to 66 GHz using the new UPC's measurement setup depicted Fig. 4.10. It is composed of an Agilent N5247A vector

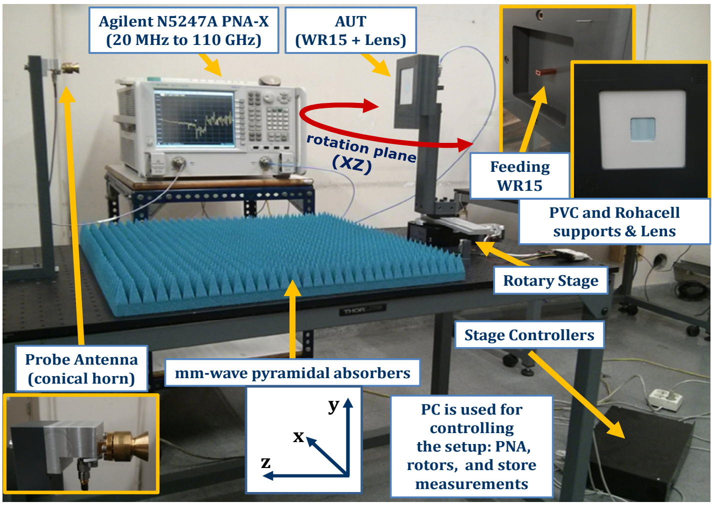

**Figure 4.10:** New UPC Far-Field radiation pattern measurement setup at 60 GHz band. Detailed images of the WR-15 waveguide and lens on PVC supports are shown in the insets.

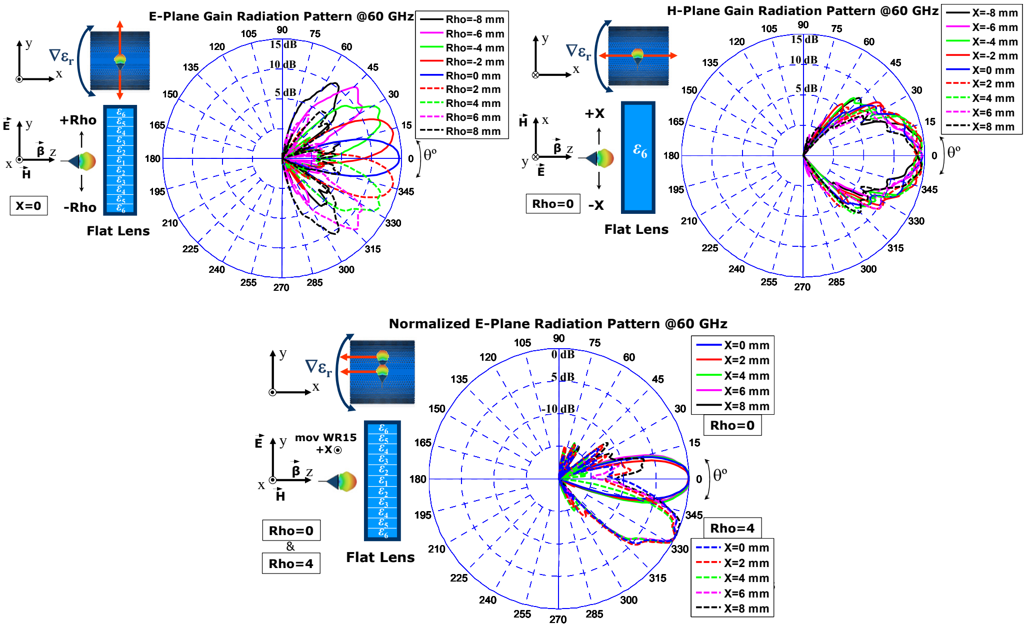

**Figure 4.11:** Measured E-Plane, H-Plane gain radiation patterns at 60 GHz for each *Rho* feeding position of the WR-15 waveguide along gradient-axis of the lens, and measured normalized E-Plane radiation patterns at 60 GHz (cut along gradient-index axis) moving the WR-15 in the constant-axis of the lens (along $X$) for $Rho = 0\,\text{mm}$ and $Rho = 4\,\text{mm}$ feeding positions.

network analyzer, a precision rotary stage to perform the scanning of the antenna under tests (AUTs) in the $XZ$ plane (see Fig. 4.10), stage controllers, a WR-15 waveguide to feed the lens, a conical horn antenna used as a probe, some RF absorbers in order to avoid undesired reflections between the instrumentation, and a computer for controlling the automatization of the complete setup. It is remarkable to note that, in order to validate the setup, the same measurements performed at UCI were reproduced at UPC with this new equipment, obtaining exactly the same results.

A total of nine measurements have been performed for different *Rho* feeding positions of the transmitting WR-15 along the gradient-index axis of the lens (going from $Rho = -8\,\text{mm}$ to $Rho = +8\,\text{mm}$) in steps of 2 mm. Once the radiation patterns are measured, in order to obtain the gain radiation patterns, the AUT (WR-15 with the lens) is replaced for a well-known gain conical horn (used as a reference) to perform a power level comparison. Therefore, the corresponding E-Plane gain radiation pattern results are plotted in Fig. 4.11 at 60 GHz (WR-15 with the electric field y-direction polarized, as it is depicted in the scheme of the figure). As it is observed, as the *Rho* feeding position is moved upwards, the high-gain radiation pattern produced by the lens is steered downwards (and vice versa), accordingly. Compared to the simulation results (see Fig. 4.4),

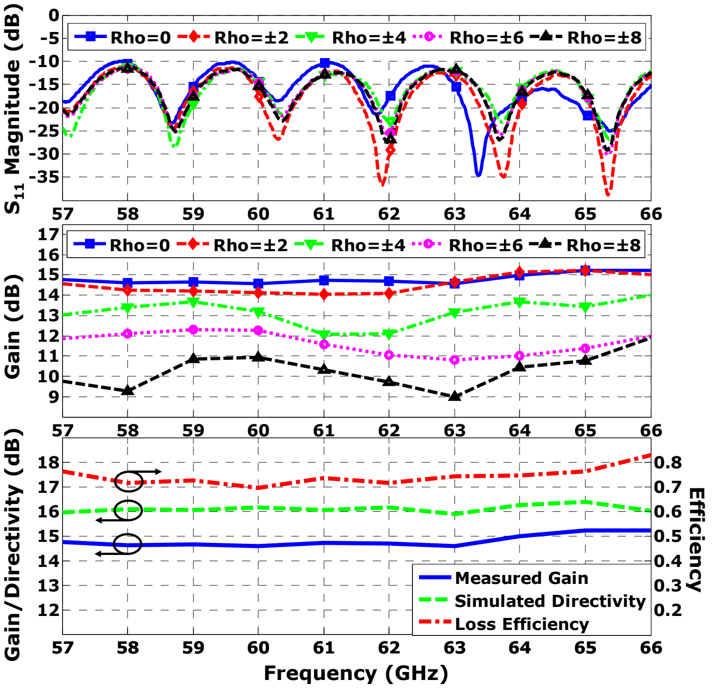

**Figure 4.12:** Measured $S_{11}$ (top) and bandwidth performance (middle) for different positions of the feeding WR-15 along the gradient-index axis of the lens, and estimated loss efficiency (bottom) in the whole frequency band of interest.

in general there is a very good agreement. Up to 14.6 dB gain in the broadside direction is achieved, with around 13 dB at ±25º, and more than 10 dB when the beam is scanned ±55º. In addition, the corresponding nine H-Plane gain radiation patterns for nine different positions of the WR-15 waveguide along the constant-index axis of the lens (i.e. $x$-direction), maintaining the *Rho* position centered to the lens ($Rho = 0mm$), are plotted in the same Fig. 4.11. As it is shown, despite moving the feeding aperture, the beams are maintained almost invariant in this specific dimension, as it was expected. Moreover, going one step further in this sense, the E-Plane radiation patterns corresponding at different $X$ feeding positions of the WR-15 along the constant-index axis of the lens, keeping invariant the *Rho* position, are plotted also in Fig. 4.11. Only the $Rho = 0$ mm ($X = 0...8$ mm) and $Rho = 4$ mm ($X = 0...8$ mm) feeding positions are plotted in order to avoid cluttering the figure, but it is enough to observe and confirm the previously described behavior, which is also obtained for the rest of the feeding positions. As it is noticed, although the WR-15 is moved in the $x$-dimension, the E-Plane (vertical cut, $y$-direction in Fig. 4.11, see the related scheme which depicts the movements performed), is maintained practically invariant for all $X$ positions of the open-ended waveguide.

The WR-15 waveguide used during the measurements is well matched for all the *Rho* feeding positions in the whole frequency band of interest, as it is shown in the measured $S_{11}$-parameter in Fig. 4.12. Additionally, very good gain stability within the 60 GHz WPAN band is observed from the bandwidth performance, plotted in Fig. 4.12 (middle).

**Table 4.1:** Summary of the most important measured radiation pattern parameters of the new LTCC dielectric flat lens with its effective parameters cylindrically distributed.

| ***Rho*** | **E-PLANE (along gradient axis)** | | | | **H-PLANE (along constant axis)** | | | |
|---|---|---|---|---|---|---|---|---|
| | **Gain** | **($\theta^{o}$)scan** | **$\Delta\theta_{-3dB}$** | **SLL** | **Gain** | **($\theta^{o}$)scan** | **$\Delta\theta_{-3dB}$** | **SLL** |
| 0 mm | 14.6 dB | 0° | 19° | -17.7 dB | 14.6 dB | 0° | 48° | -17.5 dB |
| ±2 mm | 14.1 dB | ±13° | 21° | -12 dB | 14.4 dB | 0° | 44° | -8.9 dB |
| ±4 mm | 13.2 dB | ±27° | 20° | -11.5 dB | 14.3 dB | 0° | 46° | -9.6 dB |
| ±6 mm | 12.3 dB | ±43° | 21° | -8.9 dB | 14.6 dB | 0° | 35° | -10.6 dB |
| ±8 mm | 10.9 dB | ±54° | 17° | - 5.5 dB | 14.5 dB | 0° | 35° | -14 dB |

Note that we cannot obtain the directivity or the efficiency with our radiation pattern measurement setup, since always there is a part of back-radiation level that cannot be measured. Therefore, we estimated the loss efficiency using the gain measurements and CST simulation results of the directivity. The estimated loss efficiency is plotted in Fig. 4.12 (bottom). As it is shown, very good loss efficiency values between 70% and 82% are obtained.

Finally, the most important radiation pattern parameters measured at 60 GHz for the introduced novel inhomogeneous gradient-index dielectric flat lens with the effective parameters cylindrically distributed are summarized in Table 4.1, in order to concisely compact all the interesting and most relevant results, showing the good experimental performance achieved, preserving a planar antenna structure.

It has been demonstrated that with this cylindrical parameters distribution, the beam-scanning can be performed in one plane by moving (or selecting) the position of the radiating WR-15 along the gradient-index axis, whereas the beam can be maintained invariant in the other direction, despite changing the radiating element position. Therefore, the beam-scanning can be achieved in the constant-index axis of the lens by means of a frequency-scanned slot antenna array, which it is introduced in next Chapter 5, in order to reduce the switching elements needed in the proposed complete switched-beam antenna array structure, to finally perform the scan of the high-gain radiation beam in both theta and phi dimensions of the space.

# 5

# Chapter 5

# Frequency-Scanned Stripline-Fed Transverse Slot Antenna Array

*THE design of a frequency-scanned stripline-fed transverse slot antenna array is the central topic of this section. Taking advantage of the huge amount of bandwidth allocated at 60* GHz *frequency band for communication applications, a novel linear array of transverse slot antennas fed by a meandering stripline structure is designed to achieve beam-steering in one single plane by sweeping the carrier frequency, in order to be placed together with the presented cylindrically distributed parameters dielectric flat lens to obtain a full 2-D scanning capability.*

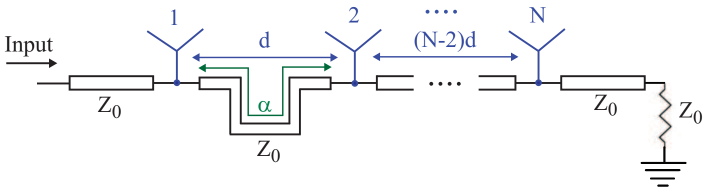

**Figure 5.1:** Theoretical concept of an N-element frequency-scanned antenna array fed by a transmission line.

## 5.1 Introduction

Considering that a broadside invariant radiation pattern is obtained along the constant-index axis of the cylindrically distributed parameters dielectric flat lens introduced in the previous Chapter 4, despite a feeding aperture is being moved along this axis, a linear frequency-scanned stripline-fed transverse slot antenna array with a particular novel structure has been designed to achieve beam-scanning in one single plane by sweeping the carrier frequency, taking advantage of the huge amount of available bandwidth for communication applications around the 60 GHz WPAN band.

## 5.2 FSSA Array: Functioning Principle

The frequency-scanned slot antenna (FSSA) array schematic is shown conceptually in Fig. 5.1. In this kind of arrays (e.g. [105]), the beam-steering capability is obtained controlling the relative phase shift between the array elements by sweeping the operating frequency [107], instead of introducing phase delays by means of bulky and complex phase-shifters, as it is common in traditional phased-arrays. When the input signal frequency is varied, the relative phase between elements changes and as a results, the radiation beam is steered [107]. The phase of each element is determined by the length of the feed line section placed between the different elements, as well as the mutual coupling. As it is depicted in Fig. 5.1, the array is fed by a transmission line of physical length $\alpha$ between elements and propagation constant $\beta$, with element spacing of $d$ in air. For a steering angle $\theta_m$, being $m$ an integer, the following can be written:

$$\beta_0 d \sin\theta_m = \beta\alpha - 2m\pi, \tag{5.1}$$

Then, the phase equation can be written as:

$$\sin\theta_m = \frac{\alpha\lambda_0}{d\lambda_g} - \frac{m\lambda_0}{d} \tag{5.2}$$

where $\lambda_0$ is the free-space wavelength and $\lambda_g$ is the guided wavelegth in the feed. It is clear that a longer feeding line section leads to a wider beam-scanning with frequency [107].

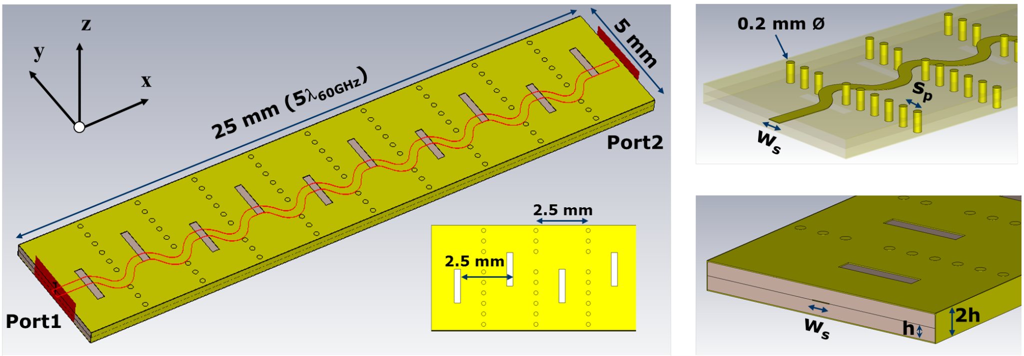

**Figure 5.2:** Frequency-scanned stripline-fed transverse slot antenna array geometry: whole structure (left), and detailed images of the meandering stripline and the pin curtains (rigth, top) and two layer structure geometry dimensions (right, bottom).

## 5.3 FSSA Array: Design

Based on the described theoretical concept, the proposed novel linear array geometry is shown in Fig. 5.2. It consists of a set of ten transverse slots fed by a meandering stripline, which provides the required phase delay between slot elements in order to steer the beam when the frequency is conveniently changed. The signal is propagating through the stripline and it is coupling energy to each one of the slots, which in turn, is radiating the coupled energy to the free-space. In this way, the slots which are closer to the stripline feeding point need to be less coupled than the slots which are far away from this point, because the signal is stronger at the beginning and tends to be smoothly weakened because it is being radiated at every consecutive slot it finds during its propagation. The stripline is terminated with a matched load in order to absorb the remaining power which is not being radiated after the last of the slots, thus avoiding undesired reflections. This array is a non-resonant structure, in which traveling-waves are used for the excitation of the slots, opposed to resonant or standing wave-arrays, in which a short circuit is placed at the end, instead of a matched-load [107].

The total dimensions of this novel stripline-fed slot antenna array are only 25 mm × 5 mm ($5\lambda_{0_{60GHz}} \times 1\lambda_{0_{60GHz}}$), with 508 $\mu m$ thickness. It is designed from two different Rogers Duroid 5880 ($\epsilon_r = 2.2$ ; tan $(\delta) = 0.004$ at 60 GHz [108]) substrate layers of 254 $\mu m$ thickness. This substrate was chosen for its low losses and low permittivity values, which facilitate the radiation and improve the overall antenna efficiency. The slot geometry plane is printed on the top substrate layer (35 $\mu m$ copper thickness), while the meandering stripline and the ground-plane are printed on the bottom layer; thus the feeding line is placed in between top and bottom planes. The slot dimensions are all the same (1.6 × 0.3 mm). The meandering stripline is designed in 370 $\mu m$ width, in order to ensure 50 Ω at the feeding port. This stripline structure is chosen to isolate the feeding line from the outer parts, avoiding undesired radiations because it is enclosed, and ensuring its dimensions despite the material that could be placed attached on the top of the array. This is an interesting point from our perspective because in this approach of the complete design, there is a vacuum space between the array and the cylindrically distributed parameters flat lens, but in a further step, the inhomogeneous ML (iML) described in Chapter 3,

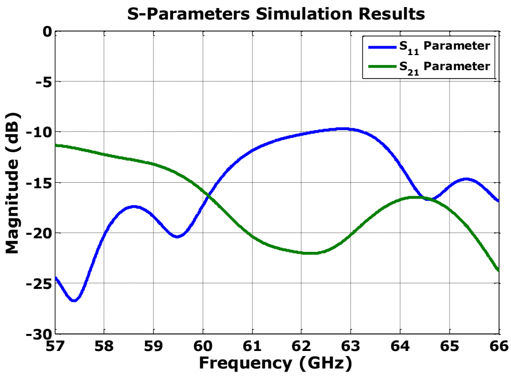

**Figure 5.3:** $S$-Parameters ($S_{11}$ and $S_{21}$) simulation results for the FSSA array in the whole band of interest.

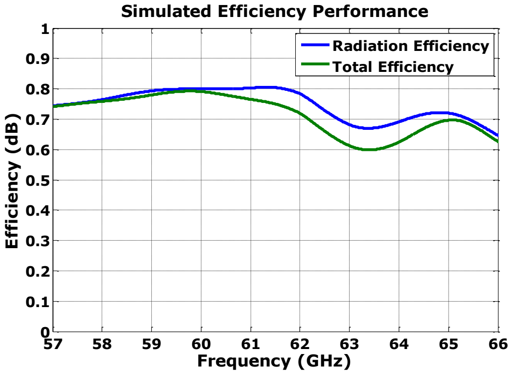

**Figure 5.4:** Total and radiation efficiencies simulation results for the FSSA array in the whole band of interest.

page 59, could be placed in between, filling the empty space and touching the top of the array. In this sense, the feeding line dimensions could be completely altered by the iML introduced. With the proposed structure, only slot dimensions would need an easy and small adaptation to a new model; even if a higher frequency design is required, for example, at 79 or 94 GHz. As it is shown in Fig. 5.2, the ten slots are placed transversal to the feeding stripline, leaving a physical distance of $\lambda_{0_{60GHz}}/2$ between them. The meandering stripline length is around $\lambda_{g_{60GHz}}/2$ (a wavelength inside the substrate media) and guarantees the needed phase delay to perform the desired beam-steering with the frequency sweeping from 57 to 66 GHz.

Initially, all the ten slots are placed -0.4/+0.4 mm (odd/even slots, respectively) with respect to the array center along the $y$-direction (i.e. the slot feeding position, see Fig. 5.2), thus providing the same coupling level to all of them. After an iterative optimization process, by using the CST's trust region algorithm, defining a trade-off between maximum achievable gain and a fixed value of side-lobe levels (SLL) below -10 dB, considering the whole frequency band from 57 to 66 GHz, the final position along $y$-direction for each individual slot is determined. A transversal pin curtains (see Fig. 5.2) are placed between slot elements in order to isolate each one from each other to avoid the coupling, and suppressing the surface wave propagation between the parallel plates of the array. It is important to stress that point because due to the excitation of surface waves, the design was not able to perform as we desired. Several studies (e.g. [109, 110] ) have been carried out in this sense in order to suppress the parallel-plate modes introducing conducting vias.

## 5.4 FSSA Array: Simulation Results

Therefore, the final frequency-scanned slot array design has been simulated using CST Microwave Studio with the time-domain solver from 57 to 66 GHz. In Fig. 5.3 and Fig. 5.3, the simulation results of the S-parameters, and radiation and total efficiencies for the FSSA array, are plotted, respectively. As it is shown, the structure is well-matched since the reflection coefficient ($S11$) is below -10 dB over the whole frequency band.

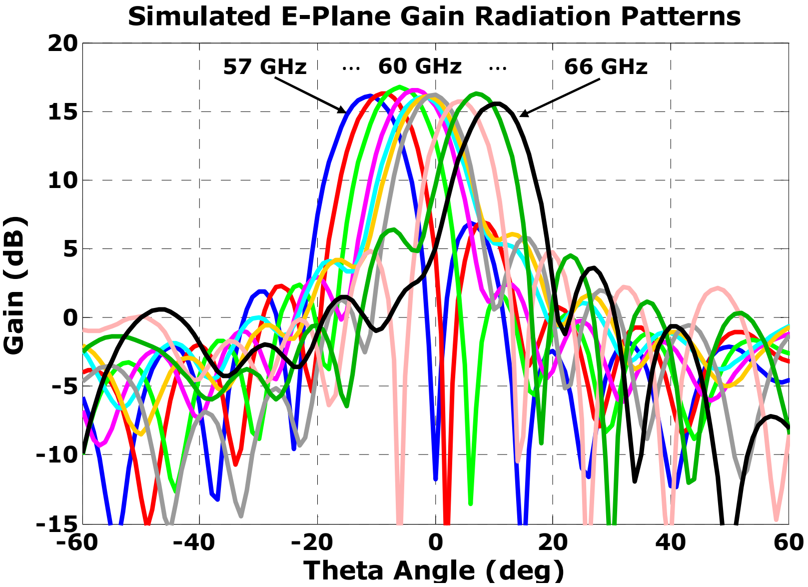

**Figure 5.5:** Simulated E-Plane Gain Radiation Patterns obtained sweeping the frequency of the linear slot array, in steps of 1 GHz, from 57 to 66 GHz.

The simulated transmission coefficient ($S_{21}$) is also below -10 dB, which means that most part of the input power is being transferred to the antenna from the feeding stripline, and then, radiated to the free-space; likewise it is supposed that the power is not being trapped into the array structure. Moreover, in this sense, the simulated total and radiation efficiencies are showing values around 70-80%, strengthening the hypothesis. Note that $S_{22}$ and $S_{12}$ parameters are not plotted due to the symmetry and reciprocity of the design.

The E-Plane gain radiation pattern at each frequency, in steps of 1 GHz, is plotted in Fig. 5.5. As it is shown, with the proposed design we are able to scan the maximum of the beam from -12º to +12º, with almost constant gain values around 16 dB, and up to 16.7 dB gain. From -15º to +14º we are able to obtain beam-scanning with more than 15 dB gain, and from -20º to +18º we still have 10 dB. SLL are below -10 dB for all the radiation beams and below -14 dB in most of the cases, with -3 dB beamwidths around 12º.

Because of the linear distribution of the slots along $x$-direction, the frequency-scanned array is also generating a fan-beam radiation pattern having a narrow beamwidth in this specific dimension, while the typical broader beamwidth of a single slot antenna is obtained along the orthogonal $y$-axis, as it is expected, from the properties of the Fourier transform of a linear distribution. A three-dimensional representation of the fan-beam radiation pattern obtained with the numerical results of the performed simulations is plotted in Fig. 5.6. Note that since the linear array is modeled with a set of slot antennas individually linearly polarized in $x$-direction, the whole array structure is performing a linearly $x$-direction polarized radiation pattern as well. The overall performance of the proposed slot array in simulation is comparable to the obtained with similar designs [111], having even better gain values while using a smaller fractional bandwidth fractional

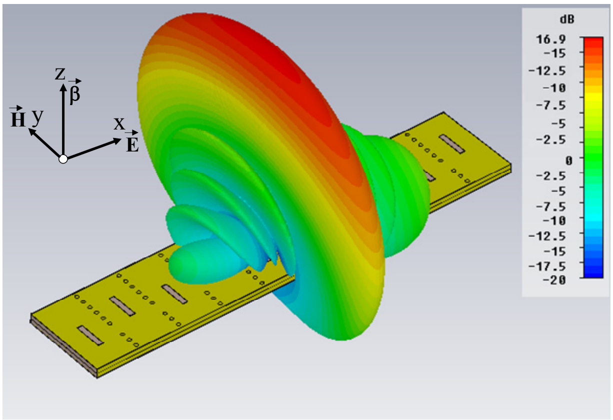

**Figure 5.6:** 3-D representation of the fan-beam obtained in simulation with the frequency-scanned stripline-fed transverse slot antenna array at 60 GHz.

bandwidth (FBW) to perform the frequency sweep. Moreover, its singular novel stripline-fed transverse structure, with the feeding line isolated from outer parts, allows for a better control of the radiated fields in order to optimally illuminate the cylindrically distributed parameters flat lens, also facilitating an easier adaptation of the design if there is a change in the boundaries, or a redesign for higher frequencies is needed.

### 5.4.1 Fabrication of the Array Prototypes

A prototype of the FSSA array has been fabricated at UPC facilities using standard photo-etching techniques on two Rogers Duroid 5880 substrate layers of 254 $\mu$m thickness. All the FSSA array dimensions are specified in the previous section 5.3. The fabrication process, described step by step, is explained in Appendix C, and a detailed scheme is plotted in C.1 at page 144. A photograph of the fabricated prototype, mounted over a PVC support to facilitate its electromagnetic characterization with our measurement setup, is shown in Fig. 5.7. A low insertion loss 1.85 mm flange jack connector is mated to each signal pin of the FSSA array. The transversal pin curtains are made from 0.2 mm diameter brass rivets, which are separated 0.5 mm center to center; they are arranged in line, as it is depicted in Fig. 5.2, in two different groups of six and three pins, leaving a central space between them to allow the meandering stripline pass-through. The pins are soldered interconnecting the top plane, in which the slots are printed, to the bottom ground plane, going through the two substrates.

## 5.5 FSSA Array Measurements

A complete set of measurements of the lens performance has been carried out at 60 GHz band in the AntennaLab facilities of the UPC using the same far-field measurement setup described in previous section 4.4.2, at page 77, and shown in the following Fig. 5.10, in which the fabricated prototype of the FSSA array is conveniently placed.

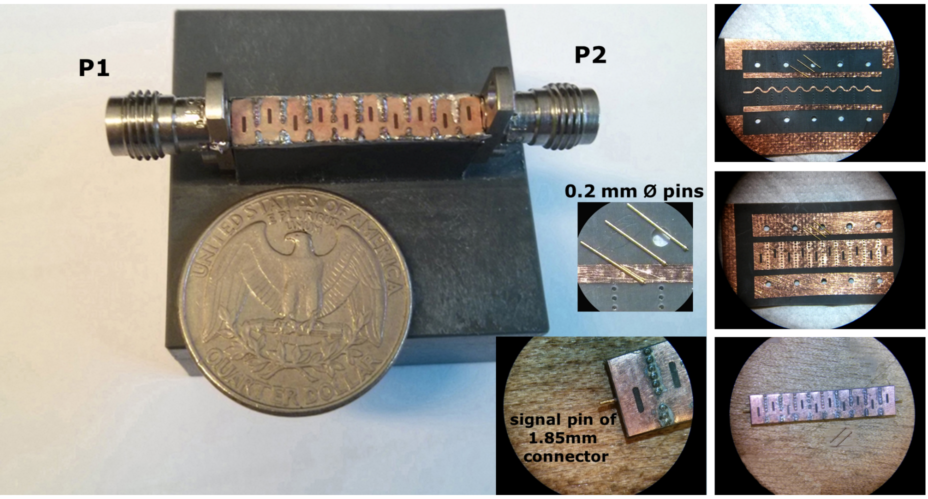

**Figure 5.7:** Fabricated FSSA antenna array connectorized and mounted over a PVC support. Some microscopic images of the bottom layer before being stacked (with the meandering stripline), complete design before connectorization, top layer (with the slots), and detailed image of the signal pin together with the first two slots and the first pin curtain, are shown in the insets.

## 5.6 FSSA Radiation Pattern Measurements

In the same way as it has been previously realized for the corresponding cylindrically distributed parameters lens, the radiation pattern measurements for the FSSA array have been carried out. The measured E-Plane gain (after the respective calibration with a well-known gain conical horn) radiation patterns obtained from 57 to 66 GHz, in steps of 1 GHz, are plotted in Fig. 5.11. Note that, as it is shown in the upper-rigth inset of the Fig. 5.10, a broadband 1.85 mm 50 Ω RF load is placed at port 2 of the FSSA array.

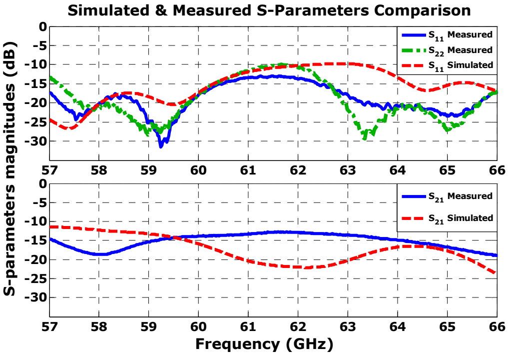

**Figure 5.8:** Simulated and mesured *S*-Parameters comparison for the FSSA array in the whole frequency band of interest.

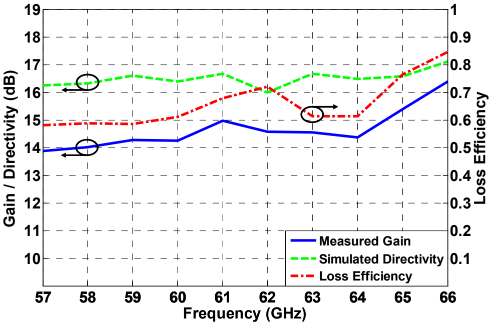

**Figure 5.9:** Computed loss efficiency by using measured gain and CST simulated directivity results of the FSSA array in the whole frequency band of interest.

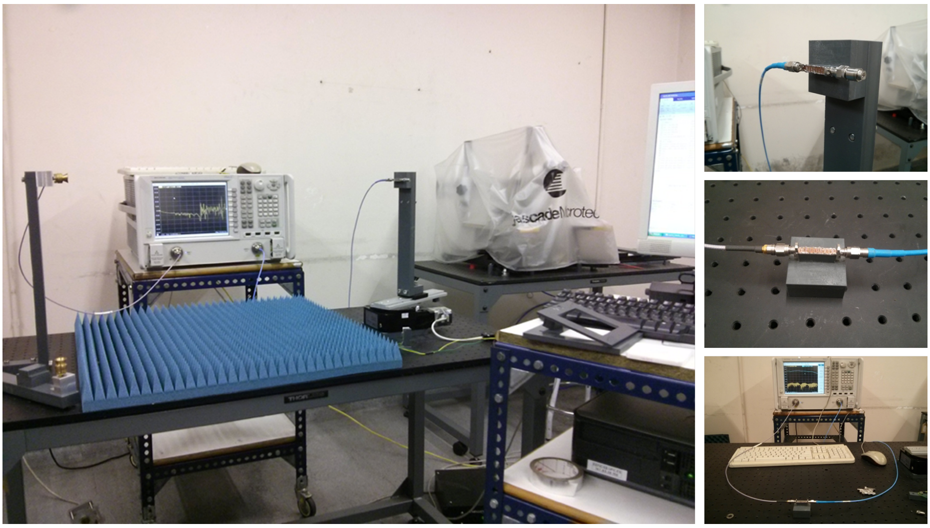

**Figure 5.10:** Far-field radiation pattern measurement setup at 60 GHz band. Detailed images of the FSSA placed on a PVC support mounted on the rotor, and the $S_{11}$ measurement process, are shown in the insets.

As it is observed, with the fabricated prototype we are able to scan the maximum of the beam from -10º to +9º, with remarkable gain values above 14 dB for all scanning angles, with a maximum of 16.4 dB at 66 GHz, with 10º of beam-steering. Moreover, we are able to scan the radiation beam from -18º to +16º with at least 10 dB gain. SLL are below -10 dB in most of the cases and around -8.5 dB in the worst case, at 59 GHz, with -3 dB beamwidths between 11º and 13º. The measured H-Plane gain radiation pattern, which is the typical broad radiation pattern obtained for a single slot antenna, as it was expected, is also plotted (dashed line) in Fig. 5.11, for a frequency of 61 GHz, in which the beam is pointing at 0º in elevation, thus allowing the measurement in the $XZ$ plane (horizontal cut) with our setup. Additionally, the measured cross-polarization level of the FSSA array is around -20 dB below co-polarization level, as it is plotted in Fig. 5.12.

The measured $S$-parameters of the FSSA array, after applying a full 2-port short-open-load-thru (SOLT) calibration in the Agilent N5247A VNA (see the calibration process performed in Fig. 5.11, are plotted in Fig. 5.8 for the whole frequency band of interest, being compared to simulation results. As it is shown, there is a very good agreement between simulation and measurement results; the FSSA is well-matched and, since the measured transmission coefficient ($S_{21}$ / $S_{12}$) is below -10 dB, it is supposed that most part of the power is being radiated from the slots to the freespace, as we previously pointed out.

Going further in this sense, the estimated loss efficiency is plotted in Fig. 5.9, also computed from CST simulation results of the directivity, and measured gain values in the whole WPAN frequency band. The efficiency values, above 60%, and up to 80%, confirm the hypothesis that most part of the power is being correctly radiated. Also note that the measured $S_{11}$ and $S_{22}$ parameters are not identical because of small imperfections in the FSSA array fabrication process, which is very hard at these high frequencies.

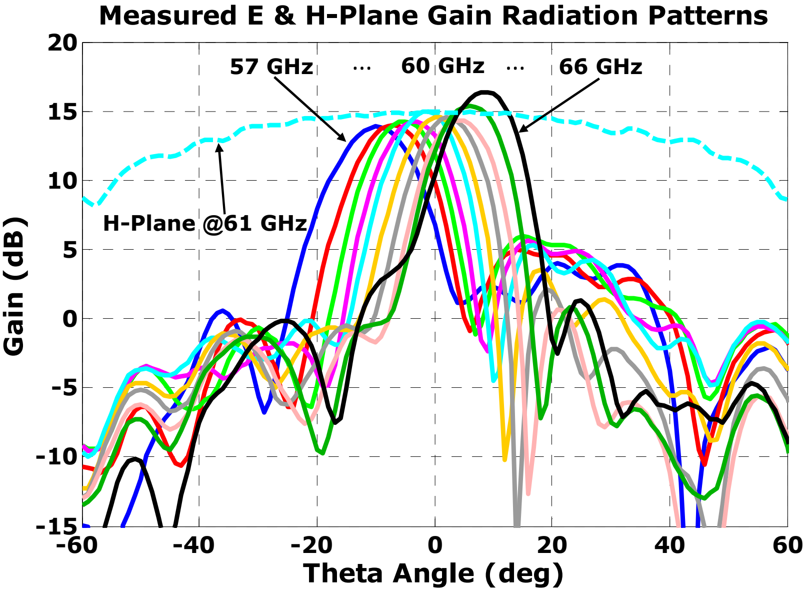

**Figure 5.11:** Measured E-Plane (solid lines) and H-Plane (dashed) radiation patterns of the FSSA sweeping the frequency, from 57 to 66 GHz, in steps of 1 GHz.

Finally, the most important radiation pattern parameters measured from 57 to 66 GHz, in steps of 1 GHz, are also summarized in Table 5.1, in order co concisely compact all the most relevant results, showing the good performance achieved with the introduced FSSA antenna to scan the beam in one single plane by sweeping the frequency, taking advantage of the 9 GHz of bandwidth available at 60 GHz WPAN band.

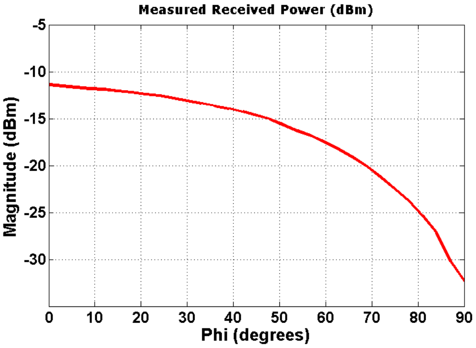

**Figure 5.12:** Measured cross-polarization level obtained for the FSSA array.

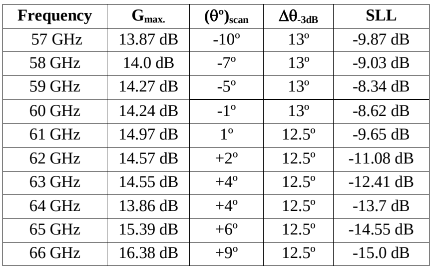

| Frequency | $G_{max.}$ | $(\theta^{o})_{scan}$ | $\Delta\theta_{-3dB}$ | SLL |
|---|---|---|---|---|
| 57 GHz | 13.87 dB | -10° | 13° | -9.87 dB |
| 58 GHz | 14.0 dB | -7° | 13° | -9.03 dB |
| 59 GHz | 14.27 dB | -5° | 13° | -8.34 dB |
| 60 GHz | 14.24 dB | -1° | 13° | -8.62 dB |
| 61 GHz | 14.97 dB | 1° | 12.5° | -9.65 dB |
| 62 GHz | 14.57 dB | +2° | 12.5° | -11.08 dB |
| 63 GHz | 14.55 dB | +4° | 12.5° | -12.41 dB |
| 64 GHz | 13.86 dB | +4° | 12.5° | -13.7 dB |
| 65 GHz | 15.39 dB | +6° | 12.5° | -14.55 dB |
| 66 GHz | 16.38 dB | +9° | 12.5° | -15.0 dB |

**Table 5.1:** Summary of the most important measured radiation pattern parameters for the introduced FSSA array prototype.

# 6

# Chapter 6

# Low-Temperature Co-fired Ceramics (LTCC) Technology Inhomogeneous Lens Integration

*This chapter is devoted to study the potential fabrication of the designed inhomogeneous perforated flat lenses in low-temperature co-fired ceramics (LTCC) technology. This technology allows processing different layers separately, preserving a planar profile, thus making possible the integration of the dielectric flat lenses together with the designed arrays in different substrate layers, which are later stacked together, laminated, and co-fired (sintering process), in order to build a single monolithic structure.*

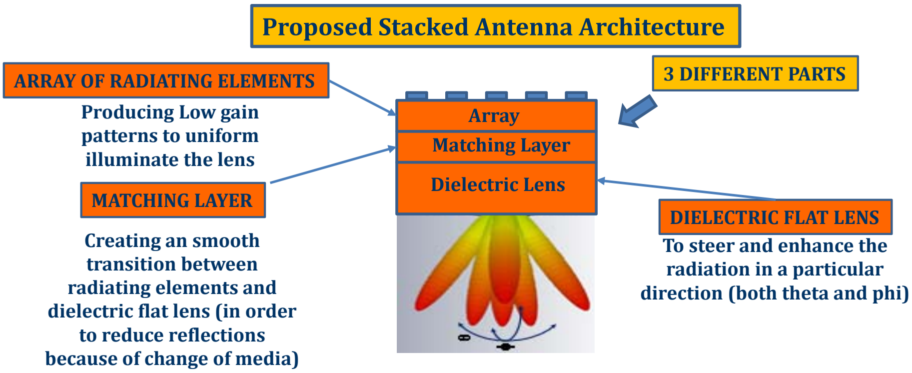

**Figure 6.1:** Proposed antenna architecture to implement using LTCC technology.

## 6.1 LTCC Technology Description

LTCC is a mature technology which was developed around 30 years ago. LTCC has been used from that time for the fabrication of different multi-layer substrates, more recently with ceramic packages, with integrated electronic components, for commercial electronics, industry, and military applications. Different material manufacturers, such as DuPont, Heraeus, NEC, CeramTec, or Ferro, provide Green Tape materials with excellent dielectric properties, with a good range of permittivities and, in general, low losses at millimeter-wave frequencies. The technology allows processing different layers separately, thus making possible the integration of different RF components and metallization designs at each different layer, which are later stacked together, laminated, and co-fired (sintering process), in order to build a single monolithic structure. LTCC shows less complexity, faster fabrication time, reduce the fabrication costs, and allows mass production in its industrial process.

## 6.2 Proposed Antenna Architecture using LTCC Technology

Since LTCC allows the integration, in a single monolithic structure, of different dielectric substrate material layers, processed separately, it is perfect for the development of the antenna architecture proposed in Fig. 6.1, based on both circular and cylindrically distributed parameters inhomogeneous dielectric flat lenses, inhomogeneous matching layers, and square or linear arrays introduced in previous Chapters 2, 3, 4, and 5, respectively. Therefore, in the next sections we contribute to describe the technological process performed in order to achieve the integration of the proposed antenna architecture as a innovative solution to the needs of the applications at millimeter-wave frequencies.

### 6.2.1 LTCC Technology Fabrication Process Description

Fig. 6.2 illustrates the process flow of the complete LTCC process, with some specific characteristics for the DuPont 9k7 dielectric material, which is the used to fabricate our prototypes.

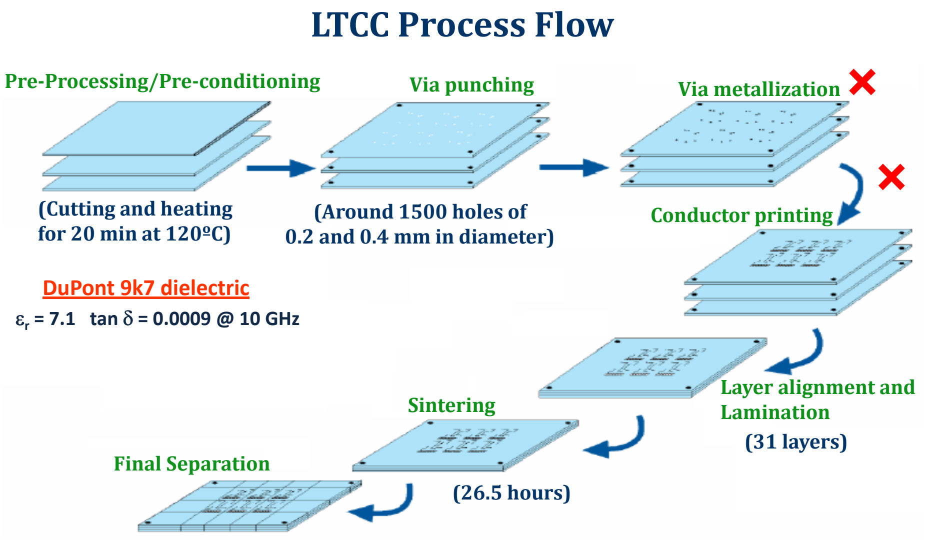

**Figure 6.2:** LTCC technology fabrication process flow.

As it is shown, consists of different parts that may or not be performed, depending on the individual design needed at each layer. Each step of the complete process can be briefly explained and summarized as follows:

- **Pre-conditioning Process:** The smooth dielectric glass/ceramic sheets of material (called green-tape) are cut depending on the design size, and then, preconditioned by heating up in the oven each single layer. The heating time and temperature depends on the material and each manufacturer provides the specifications for it.
- **Via Punching Process:** Punching is usually used to create through-holes (vias) for electrical connection, thermal transport, and/or registration. Vias are punched using conventional mechanical punching techniques. Minimum via diameter depends on tape thickness; typically a 1 to 1 aspect ratio should be maintained. Via spacing is recommended by the substrate manufacturers to be a minimum of 20 mils (i.e. 0.508 mm).
- **Via metallization:** The metallization of the performed vias provides electrical routing and serves also as thermal via in LTCC technology. Vias can be filled using conventional screen printing. Material should be printed through a stainless steel stencil. Vacuum through a porous stone is used to secure the tape during printing.
- **Conductor Printing:** Ground planes can be printed with conventional screen printers. Routing conductor traces are printed using conventional printing techniques done by using a 290 to 400 mesh screen. Vacuum through a porous stone is used to secure the tapes during printing. Solid ground planes are recommended. Top conductors can be printed with the routing conductor silver for non-soldered areas. For areas requiring soldered connections, a solderable top conductor should be used. Lead free solder has been found to yield optimal results for aged adhesion. Each manufacturer also provides the specifications.

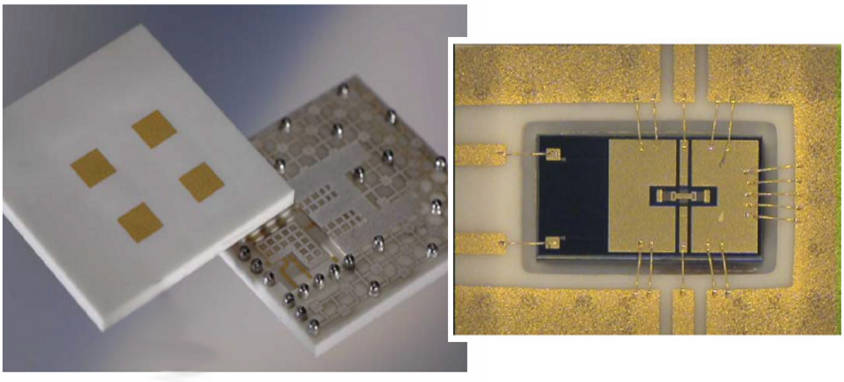

**Figure 6.3:** Two different examples of antenna designs fabricated in LTCC: Patch antenna array (left), and a MEM switch integrated in a LTCC package.

- **Layer Alignment:** Alignment of tape layers can be facilitated by the use of a backing plate with registration pins. Registration holes are punched in the tape during punching process.
- **Lamination Process:** Isostatic lamination is the most recommended. Care must be taken to completely evacuate bag prior to lamination, and registration pins need to be removed to minimize the possibility of bag leakage or blistering. Sometimes a pre-lamination process is recommended. Lamination conditions vary depending on the material. Usually huge pressures are applied (around 2000 $psi$, which is around 140 $kg/cm^2$.
- **Sintering Process:** The co-firing process should be done in a box furnace, applying a recommended firing profile. Each material possess its own profile. Firing must be done on a flat, low contact area setter, such as porous or honey comb. The tape will conform to the setter material.
- **Final Separation:** Singulation or separation can be accomplished in either green or fired state. For green ceramic, the laminate should be heated to 80°C and the razor edge should be heated to 70°C. For fired ceramic, singulation is accomplished by dicing with a diamond saw after firing.

As example, two different designs fabricated in LTCC are shown in Fig. 6.3. In any case, if further information about the LTCC technology were needed, a good detailed description of the complete fabrication process can be found in [112].

## 6.3 LTCC Dielectric Flat Lens Fabrication Process

Then, once the principal steps of the LTCC technology has been presented, the new introduced antenna solutions has been numerically analyzed, and promising simulation results were obtained, different prototypes have been fabricated at Universitat Politècnica de València (UPV) facilities in order to practically evaluate their performance. The UPV LTCC facilities are shown in Fig. 6.5. Different prototypes of the new inhomogeneous dielectric flat lens with the effective parameters cylindrically distributed, and one new

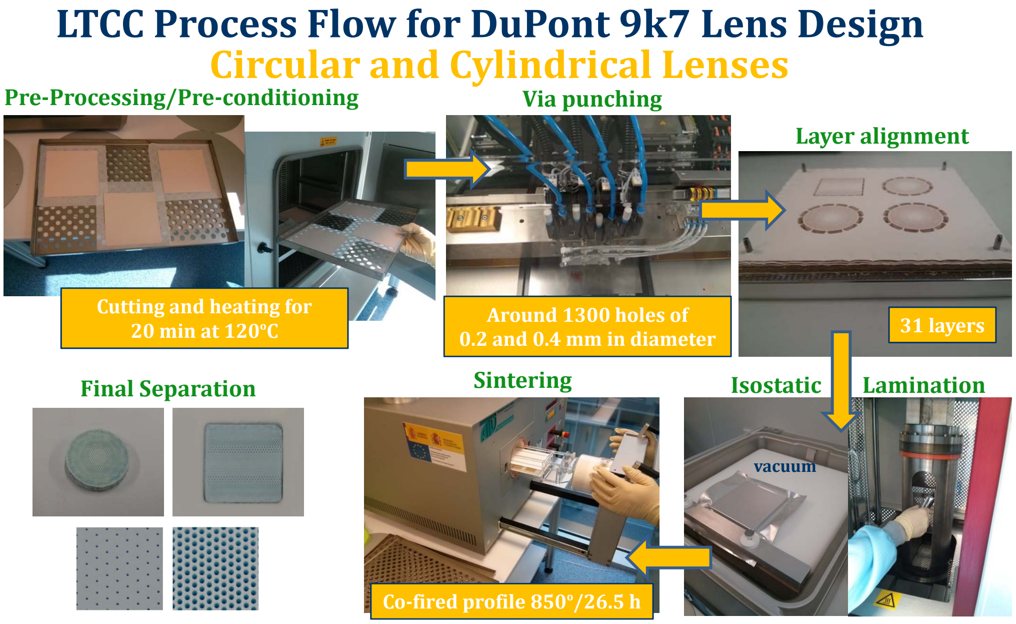

**Figure 6.4:** Process flow followed for the fabrication of the inhomogeneous LTCC lenses.

circular design with its effective parameters radially distributed, have been fabricated in the facilities of the UPV using LTCC technology. The new circular flat lens, is designed exactly with the same procedure and behavior of the previously introduced TMM6 flat lens in Chapter 2, at page 19, but taking into account that the dielectric material used for the LTCC process has a permittivity of $\epsilon_r = 7.1$, instead of the permittivity of the TMM6 material, which is $\epsilon_r = 6$. In any case, the complete description of the new circular LTCC lens, with its numerical analysis, and measurements, is reported in next Chapter 8, at page 111, in which all the introduced lenses are evaluated experimentally in a real scenario.

Once all the 31 layers needed to build each one of the lenses are processed in parallel, separately, they are stacked, laminated together at high pressure of around 3000 *psi* (around 210 $kg/cm^2$) in an isostatic process and co-fired (sintering process) at a temperature of 850ºC during 26.5 hours, following the curve plotted in Fig. 6.6.

The specific LTCC process flow followed for fabricating the inhomogeneous lenses is plotted in Fig. 6.4. After a pre-conditioning process, in which each sheet of smooth green-tape dielectric substrate is heated up to 120ºC during 20 minutes, we perform at each layer a total of around 1500 holes with a via punching process machine following the curves previously specified in Fig. 4.3, of Chapter 4, at page 72, to finally achieve the desired gradient-index permittivity profile in one axis, while a constant-index profile is achieved in the orthogonal one, in the case of the cylindrically distributed parameters lens, and a gradient-index axis in any direction, for the new circular inhomogeneous lens. These holes, of 0.4 mm and 0.2 mm in diameter, are performed on the soft 254 $\mu$m thickness DuPont GreenTape 9k7 dielectric substrate at a rate of around 1000 holes per minute,

**Figure 6.5:** LTCC facilities of the Universitat Politècnica de València (UPV).

reducing considerably the final fabrication time compared to the fabrication time needed for manufacturing the TMM6 lens introduced in 2, which was huge using carbide drills on a hard substrate.

After the punching process (see also Fig. 6.4), the 31 layers needed to finally build the lenses are stacked together, laminated, and sintered in order to obtain a single monolithic structure of 7 mm thickness. During the lamination and sintering LTCC processes, the DuPont 9k7 material is shrinking 11.8% in $Z$-direction and 9.1% in $X$-$Y$-direction and, therefore, we previously considered this shrinkage of the substrate material before manufacturing the final lens design to achieve the characteristic parameters explained in previous sections of Chapter 2 (lens thickness, via-hole dimensions, and separation between holes).

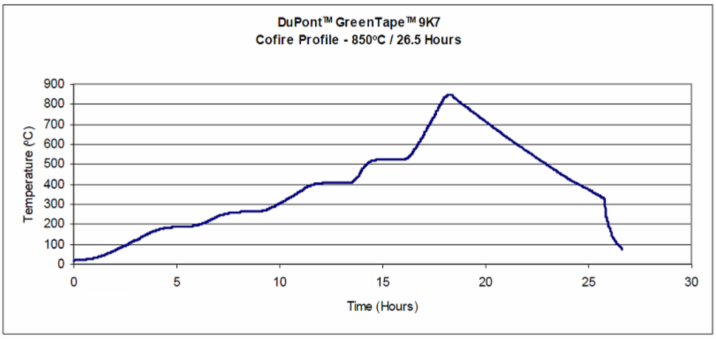

**Figure 6.6:** DuPont Green Tape 9k7 co-fire profile.

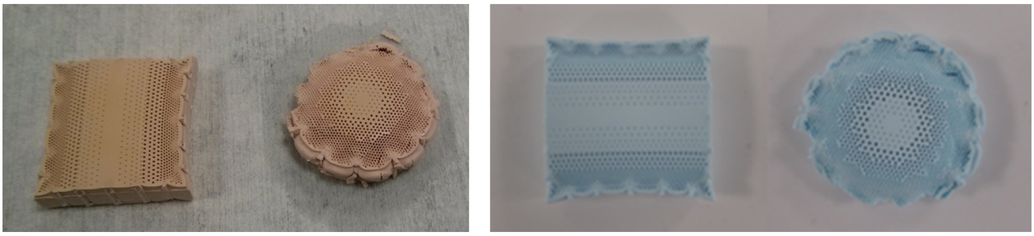

**Figure 6.7:** LTCC flat lenses fabrication results after the first attempt.

## 6.3.1 Dielectric Flat Lens Prototype Fabrication: First Attempt

After a first fabrication attempt, the obtained results were not the expected.

### 6.3.1.1 Problems Encountered

During the lamination process, because of the huge isostatic pressure applied to the 31 stacked layers of material (3000 *psi* during 10 min at 70ºC), the zones with higher density of holes collapsed and completely broken. A photograph of the described result is shown in Fig. 6.7, where the lenses after the lamination process (left), and after the sintering process (right) are plotted.

## 6.3.2 Dielectric flat lens prototype fabrication: Second attempt

After the second at attempt, the finally prototypes were successfully fabricated.

### 6.3.2.1 Solutions Adopted

Different solutions were contemplated in order to avoid the bad fabrication results obtained because of the weak structure in the high hole density zones. Complex solutions such as the misalignment of the odd/even layers, the use of fugitive/sacrificial hole filling materials (e.g. carbon, waxes, polymeric materials, etc.), the study of the deformations obtained in order to take advantage of them for a new design, or the lamination in sets of 5-6 layers, were contemplated. However, the straightforward solution applied was to modify the lamination process, in which the problems were encountered.

The first option adopted was the introduction of cutting channels surrounding the lens models, separating individually the high hole zones from the rest of the substrate material, as it is shown in Fig. 6.8, where all the layers are stacked together. Then, an specific aluminum tool was designed with two different planes, each one at one side of the first/last layer to laminate, in order to obtain an axial lamination, instead of the standard isostatic lamination obtained with the laminating machine (see Fig. 6.4), which contributed on the hole breaking. Moreover, different tests with pressures under the recommended by the manufacturer were carried out, as it is shwon in Fig. 6.9. In this sense, the 3000 *psi* were reduced up to 1000 *psi*, still obtaining a perfect lamination of all the layers. It is also remarkable that we performed some test using pressures around 300 *psi* (10 times below the recommended by the material manufacturer), obtaining good results (i.e. the perforated prototype was perfectly laminated). Probably, the huge pressure

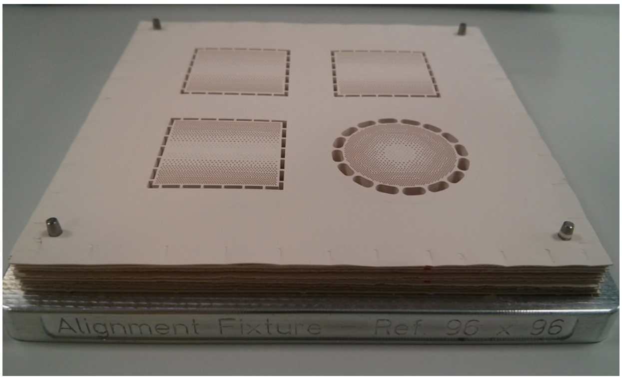

**Figure 6.8:** LTCC dielectric flat lens prototypes fabrication: 31 DuPont 9k7 layers aligned and stacked together before the lamination process.

recommended by the manufacturer is taking into account the metallization printed in the layers. Therefore, and because in our case any layer has any metallization, the pressure applied can be much lower than the recommended.

Finally, after multiple tests, a photograph of the final lens prototypes, of both cylindrically and radially distributed parameters lenses, achieved after the second attempt of fabrication, is shown in Fig. 6.10, where a microscopic image of one of the high hole density zones is also included.

## 6.4 LTCC Lens Fabrication Process Validation

As it has been described in section 4.3, page 75, of the Chapter 4, it is fundamental and very interesting to assert that the required permittivity profiles have been achieved after the LTCC fabrication process. With the described purpose, to precisely measure the permittivity profile of the fabricated prototypes a time-domain spectroscopy (TDS) system has been used. The complete description of the permittivity profile measuring process can be found in section 4.4.1, page 76, where the 3-D representations of the measured permittivity profile for the LTCC fabricated lenses are plotted.

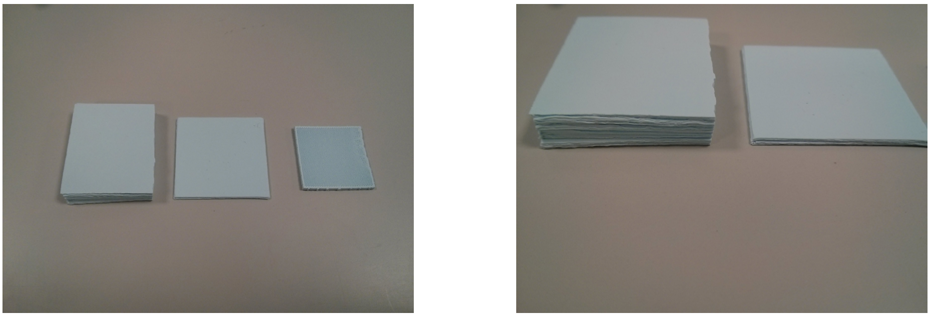

**Figure 6.9:** LTCC samples fabricated with different laminating pressures.

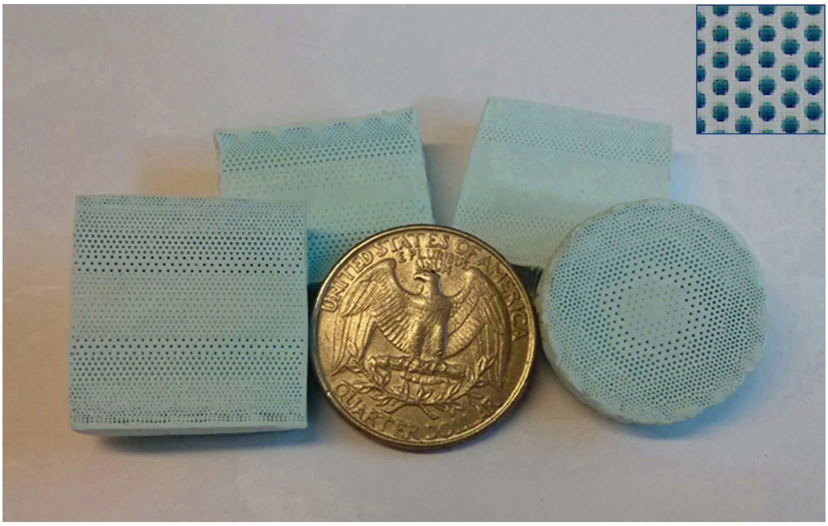

**Figure 6.10:** Final LTCC-based inhomogeneous dielectric flat lens prototypes.

Additionally, in Fig. 6.11 some microscopic images taken with the equipment of the LTCC facilities of the UPV are plotted, showing in detail the good fabrication obtained. As it is shown, despite the physical shape of the designed lenses, with an absolutely planar structure, the permittivity profile is very well defined in all the cases for all the considered lenses, thus demonstrating the good fabrication results achieved, confirming the viability in the LTCC fabrication process for the proposed antenna architecture at millimeter-wave frequencies.

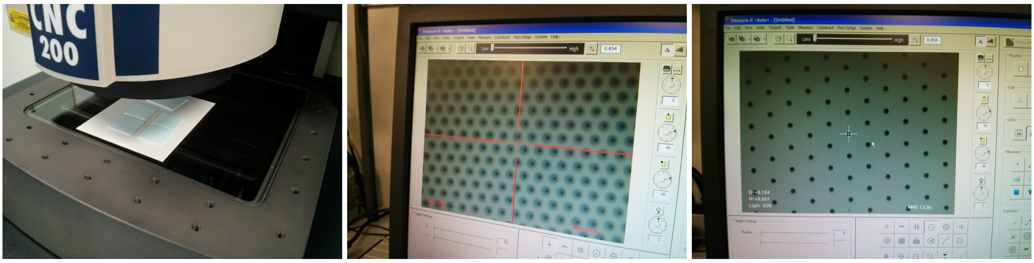

**Figure 6.11:** Different microscopic images of the LTCC fabricated prototypes.

# 7

## Chapter 7

# Complete Switched-Beam Antenna Array for Millimeter-Wave Systems

---

*This chapter is intended to describe the final design, numerical simulation, practical fabrication, and experimental evaluation of the complete switched-beam antenna (SWBA) array structure performance based on both presented inhomogeneous dielectric flat lens with its effective parameters cylindrically distributed and frequency-scanned slot antenna (FSSA) array. The full SWBA array architecture is finally introduced to realize not only a one-dimensional (1-D) beam scanning, but a two-dimensional (2-D) beam scanning of high-gain radiation beams, reducing the switching elements needed in a compact millimeter-wave antenna solution, preserving a planar antenna profile, easy to integrate in a single monolithic structure with LTCC technology.*

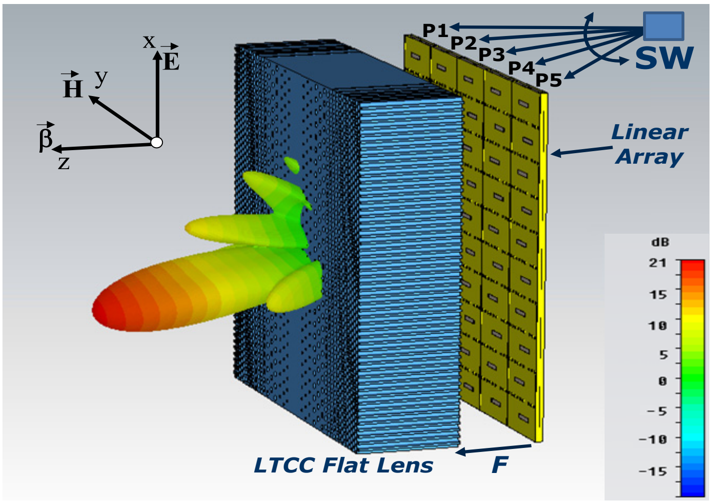

**Figure 7.1:** Complete novel SWBA array architecture for the future high data rate 5G wireless communication applications and 3-D representation of the high-gain pencil beam obtained in CST numerical simulations.

## 7.1 Introduction

The following sections are devoted to numerically evaluate the performance of the complete SWBA array structure based on both presented flat lens and frequency-scanned array. After the numerical simulations, the array prototype fabrication is described. Finally, the performance of the complete architecture is full experimentally evaluated.

## 7.2 Concept Description and Final Geometry

As it has been demonstrated before, in Chapter 4, with the help of the cylindrically distributed parameters flat lens it is possible to correct the phase in one single plane in order to focus the radiation beam. Since the frequency-scanned slot antenna (FSSA) array provides a fan-beam radiation pattern, which is easy to steer along its linear structure by sweeping the frequency, if we correctly place this linear array orthogonally to the gradient-index axis of the lens, the final result will lead to a two-dimensionally focused radiation beam, which in turn will allow the beam-scanning easily in 2-D. Therefore, the linear frequency-scanned array model (see section 5.4.1), at page 86, has been replied five times along the gradient-index of the flat lens, placed orthogonally at its focal distance, as it is depicted in Fig. 7.1.

Since the overall dimensions of a single linear array are 5 mm $x$ 25 mm, and because it is replied five times along $y$-axis (see Fig. 7.1), the final array planar dimensions are 25 mm $x$ 25 mm, exactly the same square dimensions of the flat lens. The final structure is modeled with five input ports (P1–P5, Fig. 7.1), and five matched ports (50 Ω) at the end of each linear array. In this way, the number of switching elements needed if we want to individually select one single port among the five available is significantly reduced, thus in turn decreasing considerably the losses introduced and the complexity of the integration of this kind of electronic components at millimeter-wave frequencies.

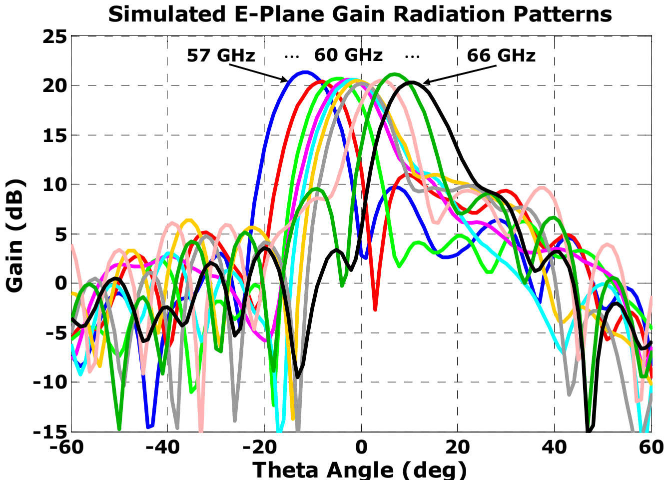

**Figure 7.2:** Simulated E-Plane Gain Radiation Patterns obtained sweeping the frequency of Port3 of the SWBA array, in steps of 1 GHz, from 57 to 66 GHz.

## 7.3 Complete SWBA Array Simulation Results

The complete switched-beam antenna array structure has been numerically simulated with CST Microwave Studio in the 60 GHz band, from 57 to 66 GHz, to evaluate the final performance of the proposed novel antenna solution. The corresponding E-Plane gain radiation patterns obtained by sweeping the frequency from 57 to 66 GHz, in steps of 1 GHz, are plotted in Fig. 7.2, for the case of selecting the 3rd port (i.e. the central linear array among the five).

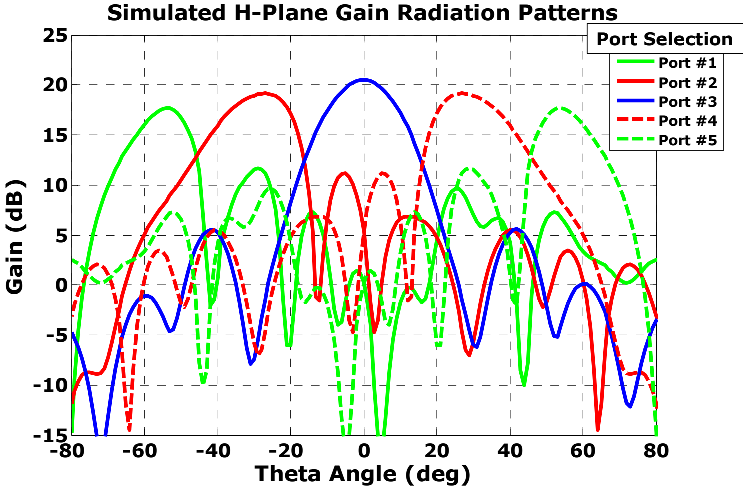

**Figure 7.3:** Simulated H-Plane gain radiation patterns at 61 GHz obtained selecting individually each one of the five ports of the SWBA array.

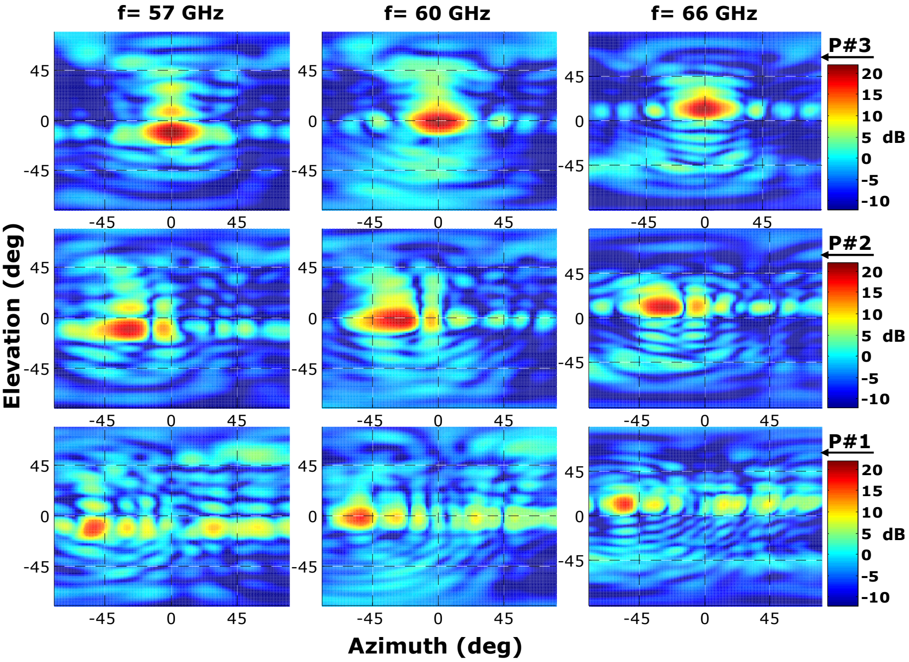

**Figure 7.4:** 3-D representation of the simulated gain patterns obtained with the SWBA selecting individually ports #3 (1st row of the plot), #2 (2nd row), and #1 (3rd row) at single frequencies of 57, 60, and 66 GHz (columns 1, 2, and 3).

As it is shown, with the proposed solution we are theoretically able to increase the maximum achievable gain up to 21.5 dB, with constant gain level over 20 dB, and beam scanning capabilities along the vertical dimension from -12º to +12º by sweeping the frequency from 57 to 66 GHz. SLL are below -10 dB for all the beams, with narrow -3 dB beamwidths around 11-12 degrees.

The fan-beam radiation pattern generated by the FSSA array is modified by the gradient-axis of the lens producing a high-gain pencil-beam radiation pattern. A three-dimensional representation of the pencil-beam radiation pattern obtained with the numerical results of the performed simulations, together with the SWBA array structure, is plotted in Fig. 7.1. Theoretically, an infinite number of high-gain pencil beams can be obtained to scan in the vertical direction, while in the horizontal dimension we can pick one of the five different sets of beams, depending on which one of the five ports of the array is selected, as it is plotted in Fig. 7.3 where the radiation patterns in the H-Plane are shown at a frequency of 61 GHz (in which the beams are pointing at 0º in elevation), to finally cover the scanning in both azimuth and elevation.

In this sense, and in order to show the complete scanning capabilities of the SWBA array, a 3-D representation of the simulated gain radiation patterns obtained selecting individually ports #3, #2, and #1, and changing the frequency at each port to 57, 60, and 66 GHz (low, mid, and high band frequencies, respectively) are plotted in Fig. 7.4. Given the SWBA array symmetric structure, symmetric radiation patterns pointing rightwards

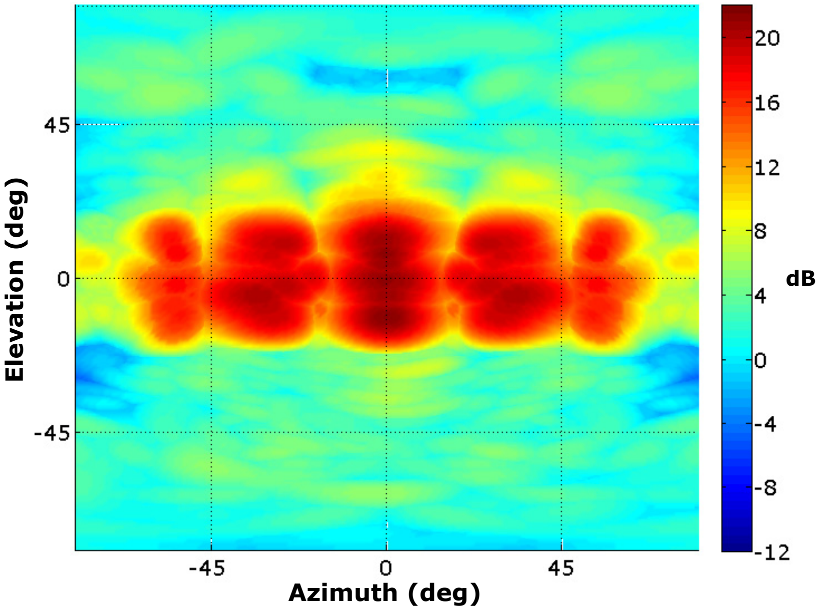

**Figure 7.5:** 3-D joint representation of the complete set of simulated gain radiation patterns obtained with the SWBA selecting each one of the five ports (to scan over azimuth), and sweeping the frequency from 57 to 66 GHz in steps of 1 GHz at each port (to scan over elevation).

in azimuth are obtained selecting ports #4 and #5 instead of ports #1 and #2, and therefore are not shown. Alternatively, the complete set of radiation patterns obtained selecting individually each one of the five ports, and sweeping the frequency from 57 to 66 GHz, in steps of 1 GHz (10 patterns) at each port, are jointly plotted in Fig. 7.5.

As it is observed in Fig. 7.4 and Fig. 7.5, our numerical results indicate that we are able to scan a high gain radiation pencil-beam (up to 21–21.5 dB in the broadside direction) from around -55º to +55º in azimuth, by selecting one single port of the five available, and from around -20º to +20º in elevation, by sweeping the frequency from 57 to 66 GHz (the maximum of the beams in elevation is going from -12º to +12º as it is clearly shown in Fig. 7.2, but at ±20º we still achieve up to 15 dB gain.

The simulation results also indicate that the whole structure is well-matched for the entire frequency band ($S_{11} < -10\,\text{dB}$), as it was expected, obtaining the same simulation results as the previously reported for the single FSSA array alone in Chapter 5 at page 81 (thus are not plotted here), because the lens, which is placed at $F = 6.25\,\text{mm}$ (focal distance) from the slot array, is not altering or modifying the FSSA array behavior in this sense. Likewise, simulated total and radiation efficiencies results are also quite similar to the previously reported for the FSSA array evaluated individually, since a low-loss substrate is used to model the lens, and therefore are not shown either.

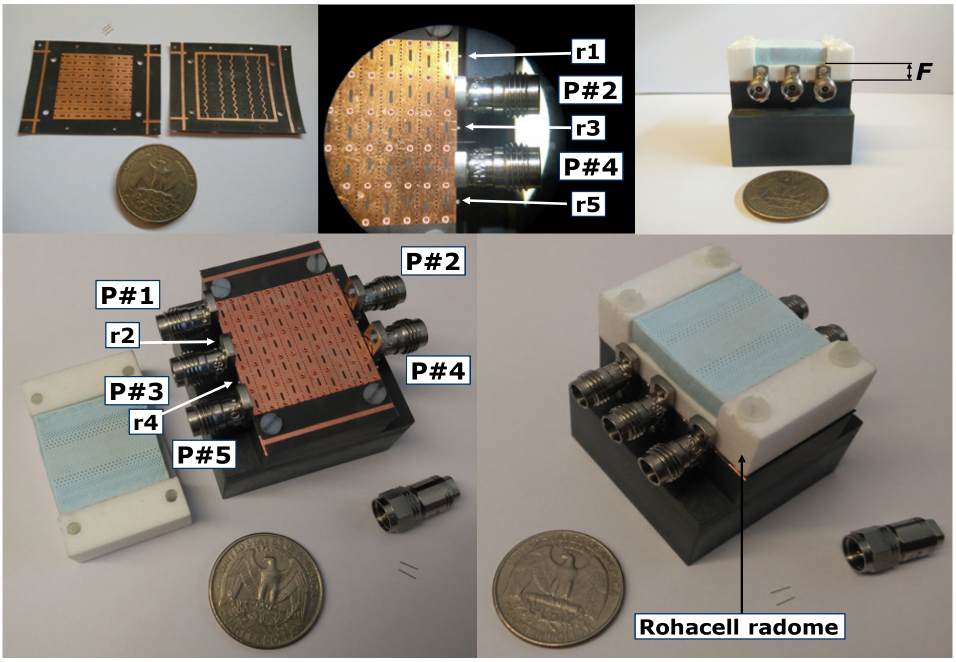

**Figure 7.6:** Complete 5-input port SWBA array for 60 GHz WPAN applications, able to perform 2-D scanning of high-gain beams, mounted on a PVC support. Images of the 5-input port FSSA array are also included.

## 7.4 Complete SWBA Array Fabrication

Once the new introduced antenna solution has been numerically tested and promising simulation results were obtained, different prototypes have been fabricated at Universitat Politècnica de Catalunya (UPC) and Universitat Politècnica de València (UPV) facilities in order to practically evaluate their performance. A prototype of the new inhomogeneous dielectric flat lens with the effective parameters cylindrically distributed has been fabricated in the facilities of the UPV using LTCC technology, as it is completely described in Chapter 4, at page 69. A prototype of the single FSSA array has been fabricated at UPC facilities using standard photo-etching techniques on two Rogers Duroid 5880 substrate layers of 254 $\mu$m thickness. All the FSSA array dimensions and have been specified in the previous Chapter 5, at page 81, where a photograph of the single array configuration is shown. Finally, the FSSA structure for the complete SBWA array, in which the single array is five times replied along its short dimension, has also been fabricated. A photograph of the prototype also mounted on a PVC support is shown in Fig. 7.6.

Therefore, the complete SWBA array structure, and the different parts of the final design (e.g. the 5 input ports connectorized, with their corresponding matched resistors (r1-r5) welded at the end of each meandering line) are identified, together with the cylindrically distributed permittivity lens placed over the array at its focal distance $F$ with the help of a Rohacell foam structure is also shown in Fig. 7.6.

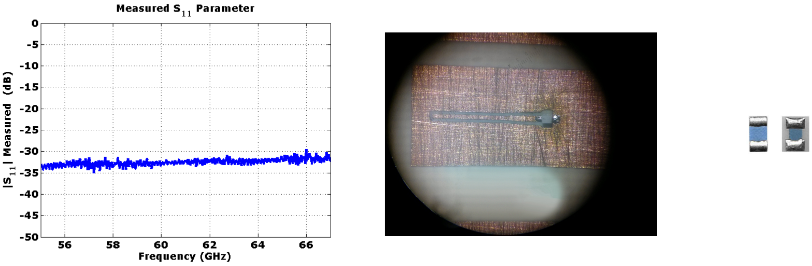

**Figure 7.7:** SMD Vishay Sfernice resistors used in the fabricated prototype of the SWBA array, and measured performance at 60 GHz band.

As it is shown in Fig. 7.6, for this SWBA array compact design, five high frequency surface mount device (SMD) integrated thin film chip resistors, which are welded at the end of each linear array stripline, have been used, instead of the bulky 1.85 mm resistor used in the single FSSA array measurements performed in Chapter 5, at page 81. Because the availability of this kind of devices at millimeter-wave frequencies is limited, and commercial resistors at 60 GHz band have not been found, a broadband Vishay Sfrenice resistor model has been used. From the specifications of the manufacturer, this specific model is theoretically able to operate up to 50 GHz. Therefore, we fabricated a test board in order to measure the performance of this resistor model in the 60 GHz band. In Fig. 7.7, the measured $S_{11}$-parameter for the resistor is plotted from 55 to 67 GHz, together with a microscopic image of the evaluation board with the resistor fed by a CPW. We performed the measurements with a probe station and a 250 $\mu$m pitch ground-signal-ground (GSG) probes to feed the CPW. As it is observed, the reflection coefficient obtained is very low in the whole frequency band of interest (around -30 dB) thus the resistor is well-matched despite the frequency of operation is higher compared to the recommended by the manufactured. Therefore, we confirm that this resistor can be used for our purposes to match the impedance at the end of each linear array.

## 7.5 Complete SWBA Array Measurements

The electromagnetic characterization of the complete SWBA array structure, based on the previously presented and evaluated dielectric flat lens and FSSA array in its complete 5-input port configuration, has also been carried out at AntennaLab facilities of the UPC. A photograph of the final SWBA array prototype mounted on a PVC-Rohacell support to facilitate the measurements is shown Fig. 7.6.

### 7.5.1 Far-Field Radiation Pattern Measurements

Similarly as in previous sections, the gain radiation patterns of the SWBA array have been measured for different antenna configurations, from 57 to 66 GHz, in steps of 1 GHz, with the same setup of the AntennaLab, shown in previous Fig. 4.10, 77. The E-Plane gain radiation patterns obtained selecting the 3rd port (central linear array of the five available), and sweeping the frequency are plotted in Fig. 7.8. The H-Plane gain radiation patterns obtained selecting each one of the five ports separately, at a fixed frequency of 61 GHz, in which the beams are pointing $0^{\text{o}}$ in elevation, thus having their maximums in the $XZ$ plane, are plotted Fig. 7.9.

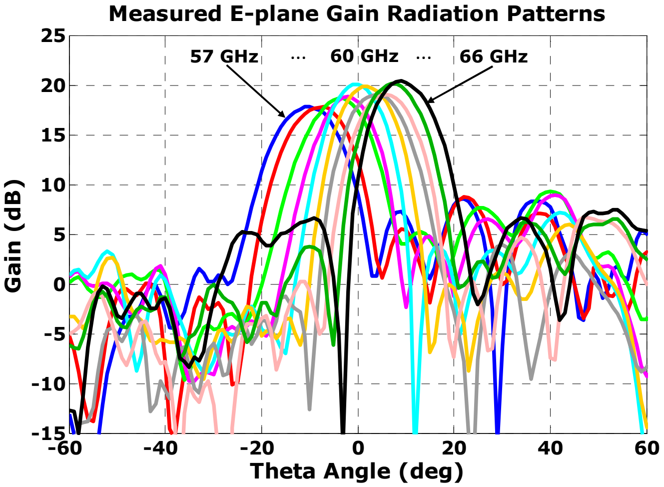

**Figure 7.8:** Measured E-Plane gain radiation patterns obtained sweeping the frequency, from 57 to 66 GHz, in steps of 1 GHz, selecting the third port (central linear array) of the SWBA array.

As it is observed in Fig. 7.8, by sweeping the frequency, with the fabricated SWBA array prototype we are able to scan the maximum of the beam from -10º to +9º in the E-plane, with high gain values around 18 dB and above for all the scanning angles, and up to 20.4 dB at 66 GHz, when the beam is steered at +9º. It is also remarkable that for wider scanning angles, from -21º to +20º, we still have at least 10 dB gain. SLL are, at least, below -9.25 dB in the worst case, and below -12 dB in general, with -3 dB beamwidths between 11.5º and 13º, in the E-plane. To facilitate the reading, the measured radiation pattern parameters of the SWBA array (maximum gain for each beam ($Gmax$), scanning angles ($\theta°_{scan}$), half-power beamwidths ($\Delta\theta_{-3\,\mathrm{dB}}$), and SLL) are summarized in Table 7.1, for the E-plane, and in Table 7.2, for the H-plane, respectively. Additionally, the measured cross-polarization level is around -20 dB below co-polarization level, as in the case of the FSSA array alone (see Fig. 5.12, page 89, because the lens is not affecting in this sense the performance of the combination, and therefore is not shown here.

As it is also observed from Fig. 7.9, selecting each one of the five ports, we are able to scan a high-gain radiation beam from -54º to +54º in the azimuth plane, obtaining more than 16.5 dB for this wide scanning angle, and still having 10 dB gain at ±65º. In the broadside direction we achieve a considerable value over 20 dB gain. Therefore, five different sets of high-gain radiation beams can be selected to scan in the azimuth plane from -54º to +54º, while at the same time an infinite number of beams can be generated in the elevation plane to scan from -10º to +9º with around 18-20 dB gain. In general, very good agreement is observed between the obtained radiation pattern measurement results in both planes and the estimated in advance from numerical simulations. Thus, despite we are not able to measure the complete 3-D gain radiation patterns for the SWBA array, the 3-D representation of the complete set of simulated gain radiation patterns plotted in previous Fig. 7.4 and Fig. 7.5, seems to be an accurate estimation, since the observed agreement between measurements and simulations in the E and H-Planes is very good.

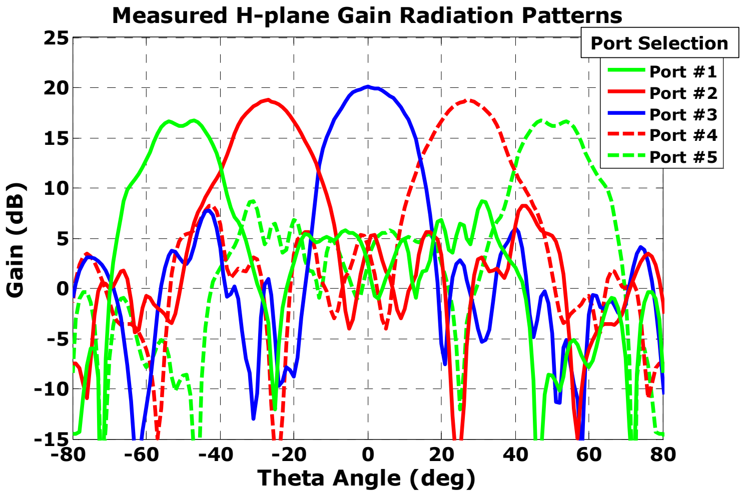

**Figure 7.9:** Measured H-Plane gain radiation patterns obtained at a frequency of 61 GHz, selecting individually each one of the five ports of the SWBA array.

**Table 7.1:** Summary of SWBA array performance at 60 GHz band selecting port #3 (central port) of the array.

| Frequency | $G_{max.}$ | $(\theta^o)_{scan}$ | $\Delta\theta_{-3dB}$ | SLL |
|---|---|---|---|---|
| 57 GHz | 17.8 dB | -10º | 13º | -9.3 dB |
| 58 GHz | 17.79 dB | -7º | 12.5º | -9.25 dB |
| 59 GHz | 18.7 dB | -4º | 12º | -9.4 dB |
| 60 GHz | 18.81 dB | -2º | 11.5º | -9.9 dB |
| 61 GHz | 20.05 dB | 0º | 11.5º | -12.95 dB |
| 62 GHz | 19.87 dB | +2º | 11.5º | -14 dB |
| 63 GHz | 19.03 dB | +4º | 11.5º | -15.1 dB |
| 64 GHz | 19.02 dB | +6º | 11.5º | -12.3 dB |
| 65 GHz | 20.14 dB | +7º | 11.5º | -13.9 dB |
| 66 GHz | 20.4 dB | +9º | 11.5º | -13 dB |

**Table 7.2:** Summary of SWBA array performance at 61 GHz selecting individually each one of the five ports available.

| | Frequency= 61 GHz | | | |
|---|---|---|---|---|
| PORT # | $G_{max.}$ | $(\theta^o)_{scan}$ | $\Delta\theta_{-3dB}$ | SLL |
| #1 | 16.72 dB | -54º | 17 | -8 dB |
| #2 | 18.77 dB | -27º | 19º | -10.6 dB |
| #3 | 20.05 dB | 0º | 19º | -12.3 dB |
| #4 | 18.77 dB | 27º | 19º | -10.6 |
| #5 | 16.72 dB | 54º | 17º | -8 dB |

### 7.5.2 Reflection Coefficients and Computed Loss Efficiency

The reflection coefficients ($S_{11}$, $S_{22}$, $S_{33}$, $S_{44}$, and $S_{55}$) of the SWBA array for the 5 input ports have also been measured after a short-open-load-thru (SOLT) calibration, obtaining approximately the same measurement results as for the $S_{11}$ of the FSSA array plotted in Fig. 5.8, at page 87, because the lens placed at focal distance is not affecting the performance in this sense, and therefore are not shown here.

Finally, the estimated loss efficiency of the SWBA array is also reported in Fig. 7.10, computed again from CST simulation results of the directivity and measured gain values, since with our measurement setup we are not able to measure the complete 3-D radiation patters in order to integrate the whole power to obtain directly the directivity or the efficiency.

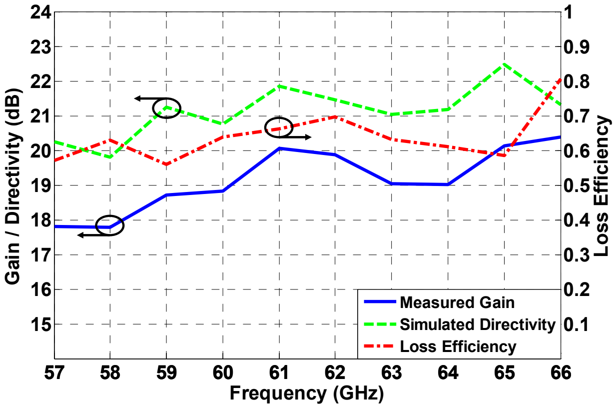

**Figure 7.10:** Computed loss efficiency by using measured gain and simulated directivity results of the SWBA array in the whole frequency band of interest.

As it is observed, good values between 60 and 70%, and above, are estimated in the whole frequency band of interest, also confirming the previously obtained simulation results. Moreover, very good bandwidth performance is also observed in Fig. 7.10, with gain slightly increasing in frequency, thus also validating the previously reported numerical results.

8

Chapter 8

# Assessment of LTCC-based Dielectric Flat Lens Antennas in a Real Indoor Millimeter-Wave Communications System

---

*In this chapter, the performance of three inhomogeneous perforated lenses is experimentally evaluated and compared to a single omni-directional antenna and to a 10-element uniform linear array (ULA) of omni-directional antennas in real 60 GHz WPAN indoor line-of-sight (LOS) and obstructed-LOS environments, obtaining interesting and promising remarkable results in terms of measured received power and root mean square (RMS) delay spread, confirming the potential applicability of the proposed antenna solution for future 5G wireless millimeter-wave communication systems.*

| Section/Ring | Ring thickness | $\varepsilon_{\text{reff}}$ | $\alpha$ | *d* | *s* |
|---|---|---|---|---|---|
| 1 | 2.27 mm | 7.1 | - | - | - |
| 2 | 2.27 mm | 6.79 | 0.051 | 0.2 mm | 0.845 mm |
| 3 | 2.27 mm | 6.01 | 0.179 | 0.4 mm | 0.901 mm |
| 4 | 2.27 mm | 4.99 | 0.346 | 0.4 mm | 0.648 mm |
| 5 | 2.27 mm | 3.92 | 0.521 | 0.4 mm | 0.528 mm |
| 6 | 2.27 mm | 2.9 | 0.639 | 0.4 mm | 0.476 mm |

**Table 8.1:** Summary of the design parameters for the new perforated LTCC-based circular flat lens.

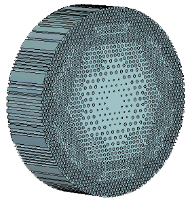

**Figure 8.1:** LTCC-based circular lens modeled by perforations.

# 8.1 Introduction

The novel inhomogeneous dielectric flat lenses introduced during this PhD thesis are finally evaluated in a real millimeter-wave scenario for communication systems. For the following experimental study, we considered the circular TMM6 flat lens, presented in Chapter 2, at page 19, the new LTCC-based flat lens with its effective parameters cylindrically distributed, and a new circular flat lens, which as already mentioned during the LTCC fabrication process described in 6, at page 91. This new circular lens, designed applying the same functioning principle and process described for the TMM6 lens, has still not been presented and characterized numerically in previously; therefore, in the following section it is briefly analyzed.

After this section, the main radiation pattern parameters for the three considered flat lenses are summarized to concisely compact the most relevant results, which will be interesting for the next sections, to finally experimentally evaluate the performance of the three lenses, being compared to a single omni-directional antenna and to a 10-element uniform linear array (ULA) of omni-directional antennas in real 60 GHz WPAN indoor line-of-sight (LOS) and obstructed-LOS environments, to study their potential applicability for future 5G indoor wireless millimeter-wave communication systems.

# 8.2 LTCC-based New Circular Dielectric Flat Lens

As it has been described in section 6.3, of the Chapter 6, at page 94, during the LTCC fabrication process, a new circular inhomogeneous lens has been fabricated at the same time in which the cylindrically distributed parameters lens has been fabricated. A photograph on this new circular lens can bee seen in Fig. 6.10, at page 99.

## 8.2.1 LTCC-based Circular Lens Design

Using the same design process as it has been described for the circular TMM6 lens, considering that now the maximum permittivity of the LTCC substrate is $\epsilon_r = 7.1$, this new lens is designed in order to obtain a plane wave behind the lens when it is illuminated from its central focus position. Then, it is also modeled by using the same technique of perforating the substrate material, with the characteristic parameters summarized in Table 8.1, and the lens model is depicted in Fig. 8.1.

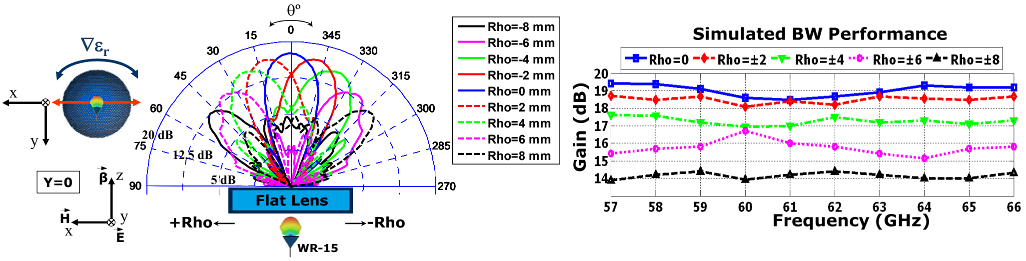

**Figure 8.2:** H-Plane (left) and bandwidth performance (right) simulation results at 60 GHz for the LTCC-based circular lens.

## 8.2.2 LTCC-based Circular Lens Simulation Results

The new lens has been numerically simulated by using CST Microwave Studio with the same simulation setup previously considered for all the introduced lenses. The H-Plane gain radiation pattern, and bandwidth performance from 57 to 66 GHz simulation results for this lens are plotted in Fig. 8.2. As it is shown, the obtained results are very similar as the achieved with the circular TMM6 lens, with around 19 dB gain for the broadside direction, and beam-steering capabilities from -45º to +45º with around 14 dB gain.

## 8.2.3 LTCC-based Circular Lens Measurements

After the LTCC fabrication process, described for this lens in section 6.3 , at page 94, of the Chapter 6, the lens performance has been evaluated in terms of radiation patterns, bandwidth performance, computed loss efficiency, and reflection coefficient. Moreover, the LTCC fabrication process for this lens has also been tested with the time-domain spectroscopy (TDS) system in order to obtain the achieved permittivity profile of the circular LTCC lens.

### 8.2.3.1 LTCC-based Circular Lens Permittivity Profile Measurements

As it has been carried out for the rest of the previously introduced lenses, the permittivity profile of this new LTCC-based lens has also been measured with our TDS system to assert that the measured profile is in agreement with the designed. The measurement results are plotted in Fig. 8.3 from different points of view, and two cuts along $X$ and $Y$ axes are plotted in Fig. 8.4. As it is observed, the measured permittivity profile is very well defined as in the previous cases, with the maximum around $\epsilon_r = 7$, decreasing smoothly to around 3 on the edges, despite the planar physical profile, confirming the viability of the LTCC technology for the integration of inhomogeneous lenses.

### 8.2.3.2 LTCC-based Circular Lens Radiation Pattern Measurements

The radiation patterns produced by the LTCC-based circular lens when is fed with a WR-15 aperture have been measured with the UPC's measurement setup at 60 GHz band, from 57 to 66 GHz. The corresponding H-Plane gain radiation pattern measurement results are plotted in Fig. 8.5, after performing the gain calibration with a conical horn.

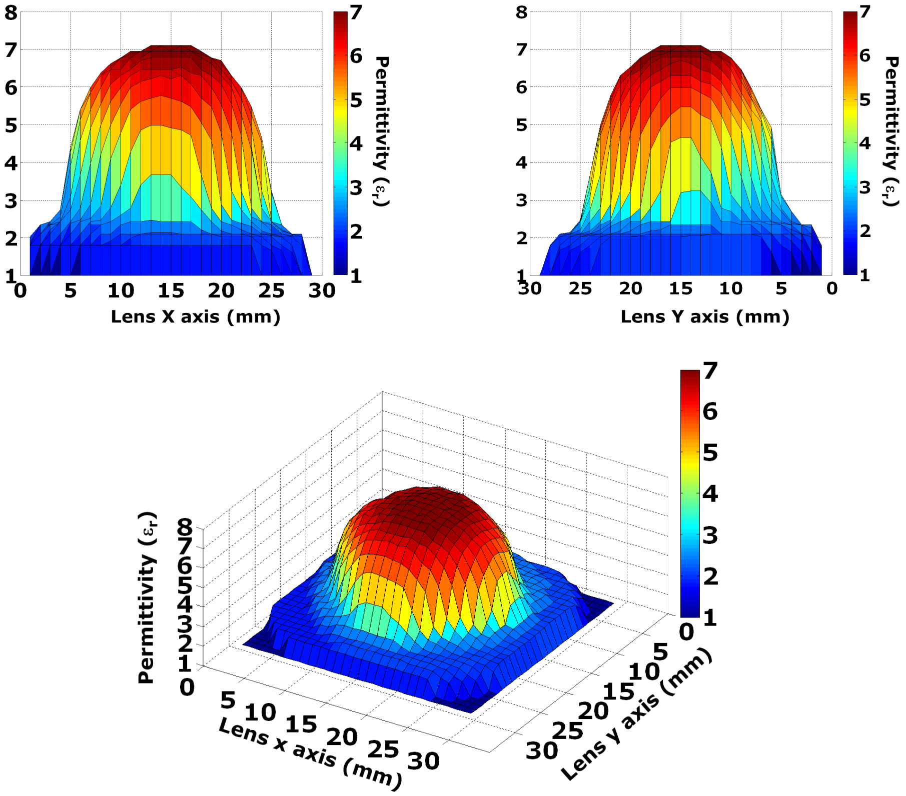

**Figure 8.3:** 3-D representations of the measured permittivity profile for the LTCC-based circular lens.

In the same way, the bandwidth performance, and the reflection coefficient of the WR-15 feeding waveguide are also obtained, being plotted together with the measurement results for the introduced circular TMM6 and cylindrically distributed parameters lenses, in Fig. 8.6, and Fig. 8.7, respectively, for comparison purposes.

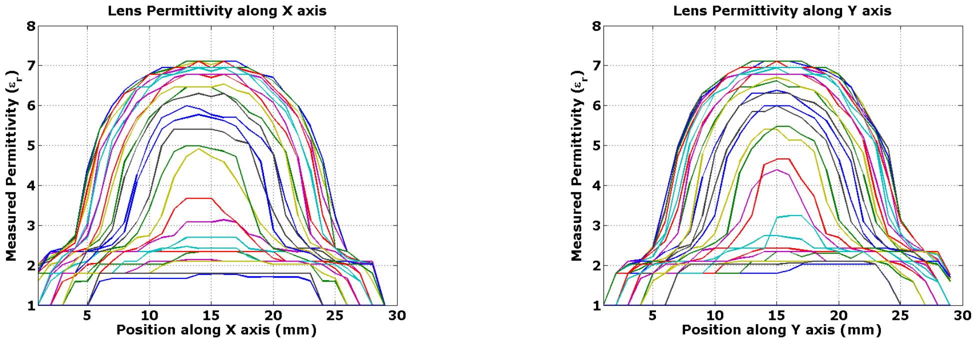

**Figure 8.4:** Measured permittivity profile sections of the LTCC-based circular lens.

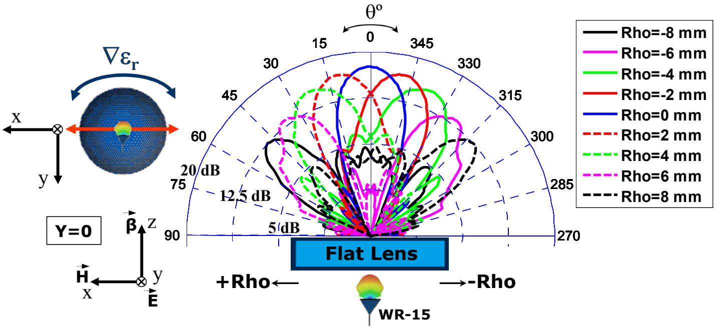

**Figure 8.5:** Complete set of measured H-Plane gain radiation patterns at 60 GHz for each *Rho* feeding position of the WR-15, for the LTCC-based circular lens.

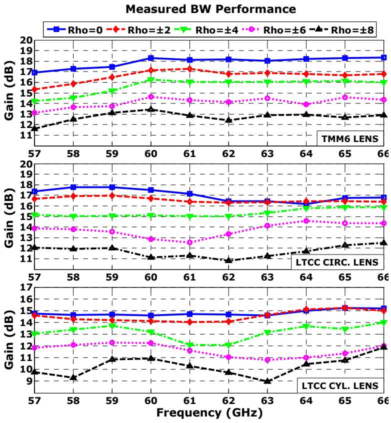

**Figure 8.6:** Measured bandwidth performance comparison for the 3 considered inhomogeneous lenses: TMM6, LTCC-based circular and cylindrically distributed parameters.

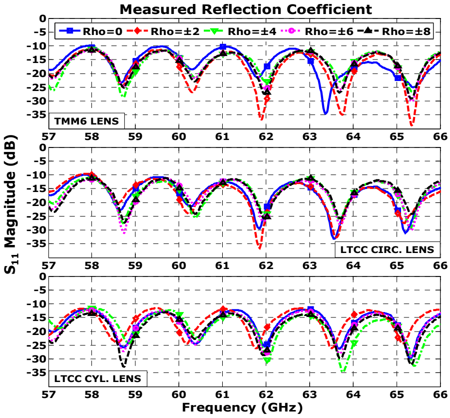

**Figure 8.7:** Measured reflection coefficient comparison for the 3 considered inhomogeneous lenses: TMM6, LTCC-based circular and cylindrically distributed parameters.

As it is observed, the performance of the LTCC-based circular flat lens in terms of radiation pattern parameters, efficiency, and broadband operation is comparable to the achieved with the circular TMM6 lens, confirming again the viability of the LTCC technology for the integration of this kind of inhomogeneous lenses, also enabling the capability of printing the radiating elements together with the lenses.

## 8.3 Summary of Inhomogeneous Lens Performance

The three considered gradient-index inhomogeneous flat lenses are assessed in the following section for a real case of application. The three lenses provide very good scanning-capabilities, despite their planar profile implementation, as it has been demonstrated with a complete set of measurements, of high gain radiation beams. Two of them, the circu-

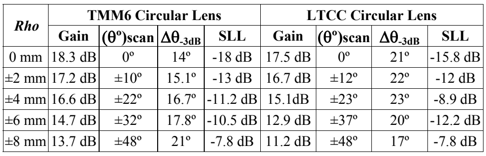

| *Rho* | TMM6 Circular Lens | | | | LTCC Circular Lens | | | |
|---|---|---|---|---|---|---|---|---|
| | Gain | (θ°)scan | Δθ$_{-3dB}$ | SLL | Gain | (θ°)scan | Δθ$_{-3dB}$ | SLL |
| 0 mm | 18.3 dB | 0° | 14° | -18 dB | 17.5 dB | 0° | 21° | -15.8 dB |
| ±2 mm | 17.2 dB | ±10° | 15.1° | -13 dB | 16.7 dB | ±12° | 22° | -12 dB |
| ±4 mm | 16.6 dB | ±22° | 16.7° | -11.2 dB | 15.1dB | ±23° | 23° | -8.9 dB |
| ±6 mm | 14.7 dB | ±32° | 17.8° | -10.5 dB | 12.9 dB | ±37° | 20° | -12.2 dB |
| ±8 mm | 13.7 dB | ±48° | 21° | -7.8 dB | 11.2 dB | ±48° | 17° | -7.8 dB |

**Table 8.2:** Summary of TMM6 and LTCC-based circular lenses performance at 60 GHz.

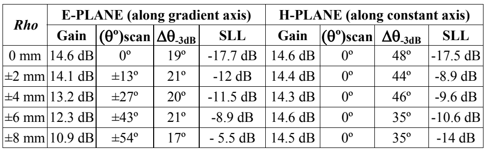

| *Rho* | E-PLANE (along gradient axis) | | | | H-PLANE (along constant axis) | | | |
|---|---|---|---|---|---|---|---|---|
| | Gain | (θ°)scan | Δθ$_{-3dB}$ | SLL | Gain | (θ°)scan | Δθ$_{-3dB}$ | SLL |
| 0 mm | 14.6 dB | 0° | 19° | -17.7 dB | 14.6 dB | 0° | 48° | -17.5 dB |
| ±2 mm | 14.1 dB | ±13° | 21° | -12 dB | 14.4 dB | 0° | 44° | -8.9 dB |
| ±4 mm | 13.2 dB | ±27° | 20° | -11.5 dB | 14.3 dB | 0° | 46° | -9.6 dB |
| ±6 mm | 12.3 dB | ±43° | 21° | -8.9 dB | 14.6 dB | 0° | 35° | -10.6 dB |
| ±8 mm | 10.9 dB | ±54° | 17° | - 5.5 dB | 14.5 dB | 0° | 35° | -14 dB |

**Table 8.3:** Summary of LTCC-based cylindrically distributed parameters lens performance at 60 GHz.

lar TMM6 and LTCC-based lenses, provide high gain pencil-beam radiation patterns, whereas the lens with its effective parameters cylindrically distributed produce a high gain fan-beam. This type of radiation pattern radiation pattern, which have a narrow beamwidth in one dimension, broader in the orthogonal, could be very useful for many applications and communication environments. More specifically, a fan-beam radiation pattern has been successfully evaluated for high-speed indoor wireless communication systems operating in the 60 GHz band [106], recommending its use in certain situation at access points (APs) or portable stations (PSs), for example, due to its good immunity to azimuth pointing deviation.

Therefore, the following experimental analysis is very interesting also to compare the performance of the lenses from the different type of radiation pattern which they provide. The summary of the measured performance in terms of the most important radiation pattern parameters for the three lenses is reported in Table 8.2, and Table 8.3, for the circular and cylindrically distributed parameters lenses, respectively.

## 8.4 Experimental Investigations in a 60 GHz Indoor Environment

Once the three considered dielectric flat lenses have been fully electromagnetically characterized and remarkable good measurement results have been obtained, their performance is experimentally evaluated and compared to a single commercial omni-directional antenna, as well as their use as smart antennas is compared to a traditional uniform linear array (ULA) in a real 60 GHz WPAN communications environment, in an experimental analysis conducted by researchers of the Universidad Politécnica de Cartagena (UPCT).

### 8.4.1 Introduction

For this experimental part, we have considered an indoor scenario in the facilities of the UPCT varying the position of the receiver (Rx) antenna. Three different positions for the Rx antenna have been measured forming an angle of 0°, 22.5°, and 45° with respect to the transmitting (Tx) antenna, which is placed in a fixed position. The receiver antenna is, in all the cases, a single commercial Q-par QOM55-65 VRA 55 to 65 GHz omni-directional V-type antenna. The gain of this antenna varies from 4.3 to 5.2 dB within the considered 57 to 64 GHz frequency band, and the typical 3 dB elevation beamwidth ranges from 24° to 33°, while being omni-directional in the horizontal plane.

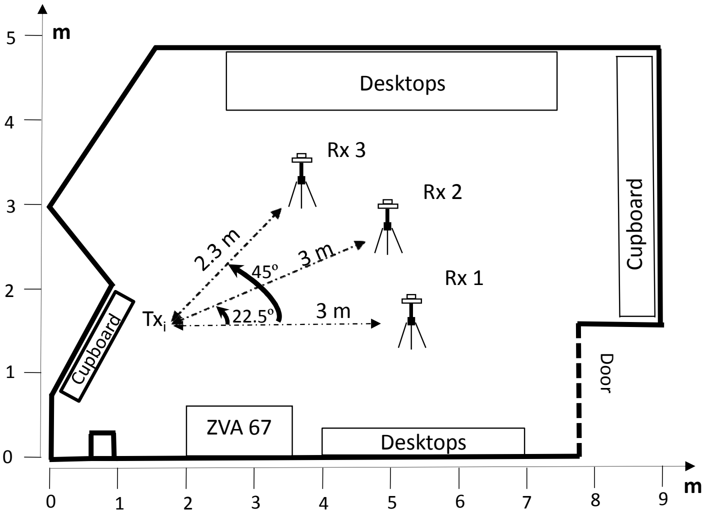

**Figure 8.8:** Indoor scenario and experimental measurement setup arrangement.

In this study, the considered Tx antennas are the three presented lenses fed by the same rectangular aperture WR-15 waveguide used during the previous sections, the same commercial omni-directional antenna used in the Rx part, and a virtual ULA modeled with 10 positions of this same omni-directional antenna. The performance test with the considered Tx antennas is carried out in direct LOS conditions for all the angles between Tx and Rx, and also in obstructed- LOS (OLOS) conditions for the 0º case. In the following subsections all the important considerations about the experimental scenario, channel sounder, and methodology are conveniently described before to proceed with the analysis of the measurement results.

### 8.4.2 Experimental Scenario

The scenario for this experimental study is a laboratory of the UPCT. The laboratory is an almost rectangular room of about 5 x 9 meters furnished with several closets, desktops, and shelves. The laboratory scheme with the measurement setup arrangement is depicted in Fig. 8.8, and a picture of the real scenario setup for the 0º case between Tx and Rx in OLOS conditions is shown in Fig. 8.10. As it is shown in Fig. 8.8, the three different considered Tx-Rx situations are established as follow: 3 meters between Tx and Rx forming an angle of 0º (1st position), 3 meters between Tx and Rx forming an angle of 22.5º (2nd position), and at 2.3 meters between Tx and Rx forming an angle of 45º (3rd position).

### 8.4.3 Channel Sounder

The channel sounder employed in this work is based on a vector network analyzer (VNA), Rohde & Schwarz ZVA67. The VNA is used to measure the transmission ($S_{21}$) parameter in order to obtain in the frequency domain the complex transfer function of a wireless

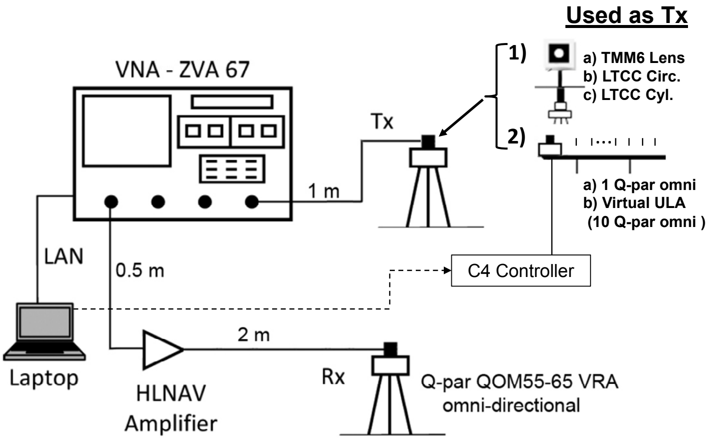

**Figure 8.9:** Scheme of the measurement setup (channel sounder).

system. As it is plotted in the scheme of Fig. 8.9, the transmitting antenna is directly connected to one port of the VNA through a 1 m coaxial cable, while the receiving antenna is connected to a second port of the VNA through 2 m coaxial cable section, in which a 25 dB gain amplifier is placed in order the amplify the received signal. The reference of the amplifier used is HXI HLNA-465. The virtual ULA is created by moving the Tx omni-directional antenna, with the help of a linear positioner and a C4 controller [113] connected to a laptop, in 10 positions separated by 2 mm ($< \lambda_{0_{60GHz}}/2$). The insertion losses of the coaxial cable are around 5 dB/m at 62 GHz. In any case, a detailed description of the channel sounder used in this work can be found in [114]. The channel can be considered stationary, because during the measurements nobody was inside the measuring environment.

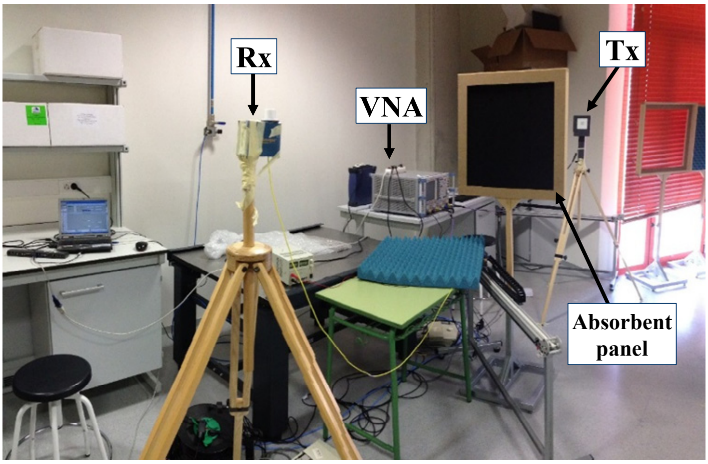

**Figure 8.10:** Photograph of the real scenario for the first position in OLOS situation.

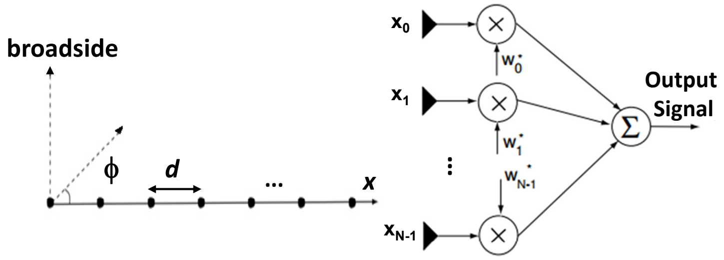

**Figure 8.11:** Scheme of the uniform linear array (left) and generalized beamforming on receive (right).

### 8.4.4 Methodology

The frequency domain function measured H(f) is acquired. Then, the relative received power ($P$) is computed. Next, the time domain function $h(t)$ is obtained by using the inverse fast Fourier transform (iFFT). Lastly, the power delay profile (PDP) and the root mean square (RMS) delay spread ($\sigma_\tau$) are calculated.

In order to do so, the relative received power is defined as the ratio between the transmitted power and the received power, which describes the attenuation of the transmitted signal in the radio link, and can be expressed as [115]

$$P = -10\log_{10}\frac{1}{N_f}\sum_{f=1}^{N_f}|H(f)|^2 \tag{8.1}$$

The power delay profile, which gives the power repartition as a function of the delay, and is computed by averaging, spatially or temporally, the channel impulse response over a local area, is defined as

$$PDP = \overline{|h(d,\tau)|^2} \quad , \tag{8.2}$$

while the RMS delay spread, which shows the dispersion in the delay domain and represents the standard deviation of the PDP, is calculated for each measured PDP as

$$\sigma_\tau = \sqrt{\frac{\sum_k PDP(\tau_k)\tau_k^2}{\sum_k PDP(\tau_k)} - \left(\frac{\sum_k PDP(\tau_k)\tau_k}{\sum_k PDP(\tau_k)}\right)^2} \tag{8.3}$$

In order to minimize the effect of noise, a threshold placed 30 dB below the maximum value of the PDP is used in the calculations.

For the virtual ULA, a beamforming technique (i.e. spatial filtering) has been used to obtain the response taking into account the angles of the transmitted or received signals. Therefore, as it is depicted in Fig. 8.11 (left), we dispose of a linear array model of equidistant elements, which are practically spaced a distance $d = 2\,\text{mm}$ ($< \lambda/2$). Then, a non-adaptive processing, which is the traditional approach to array processing, is used. The scheme of the beamforming technique applied is also plotted in Fig. 8.11 (right).

In this sense, any beam-former adds the signal at the $N$ antenna elements weighted by scalars. Considering the array structure shown in Fig. 8.11, the output signal $(y)$ is given by [116]

$$y = \frac{1}{\sqrt{N}} \sum_{n=0}^{N-1} w_n^* x_n \tag{8.4}$$

where the signal xn at each element of the array is multiplied with a complex conjugate weight being w the length-N vector of weights. Then, taking into account our specific case:

$$H_{beamforming} = \frac{1}{\sqrt{N}} \sum_{i=1}^{F} \sum_{\varphi=-\frac{\pi}{2}}^{\frac{\pi}{2}} w_{i,\varphi}^* H_{i,\varphi} \qquad \text{and then,} \tag{8.5}$$

$$H_{beamforming} = \frac{1}{\sqrt{N}} \sum_{n=1}^{N} \sum_{i=1}^{F} \sum_{\varphi=-\frac{\pi}{2}}^{\frac{\pi}{2}} H_{i,\varphi}^* e^{-j2\pi D \sin(\varphi_t)(n-1)} \tag{8.6}$$

where $N$ is the number of elements ($N = 10$ in our case), $D = \frac{d}{\lambda}$, being $\lambda = \frac{c}{f_i}$, $d$ the inter-element distance (2 mm in our case, as it has been stated before), $i$ represents the frequencies vector [1:2048], and $\varphi_r$ denotes the angles between [-90:90] in steps of 5º.

Additionally, the single-input single-output (SISO) transmission situation, where only the considered omni-directional antenna is used in both receiver and transmitter points, has also been considered. In this case, the time domain function $h(t)$ is calculated as the iFFT of the average of all elements of the frequency domain function $H(f)$.

### 8.4.5 Experimental Results

In the following subsections the experimental results obtained for the three considered positions are reported and compared for the three dielectric flat lenses, and for the ULA and SISO cases.

### 8.4.6 First Position Measurements

As it is depicted in Fig. 8.8, in the first position situation the Tx and the Rx antennas are separated 3 meters forming an angle of 0º between them. A photograph of the real scenario situation is shown in Fig. 8.10, for the OLOS condition. For the LOS condition, the absorbent panel placed in between the Tx and Rx is removed. Then, the detailed methodology is applied obtaining the following results for all the considered antennas. For the LOS situation, the relative received power in function of the angle and the PDP are plotted for each different transmitting antenna in Fig. 17 and Fig. 18, respectively.

As it is observed in Fig. 8.12, the highest relative received power is achieved using the circular TMM6 as a transmitting antenna, as it was expected from the measured radiation pattern parameter results obtained in previous sections (see Table 8.2 and Table 8.3). In any case, with all the designed lenses the relative received power is better compared to

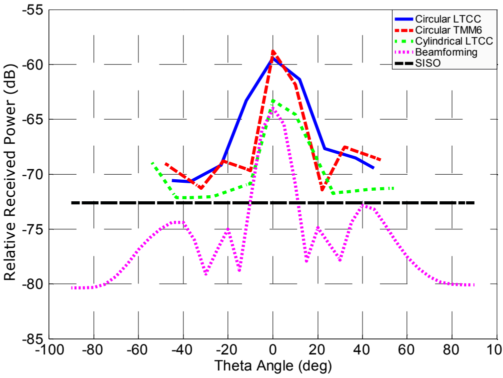

**Figure 8.12:** Relative received power at 1st position ($\theta = 0^{\circ}$) in LOS conditions.

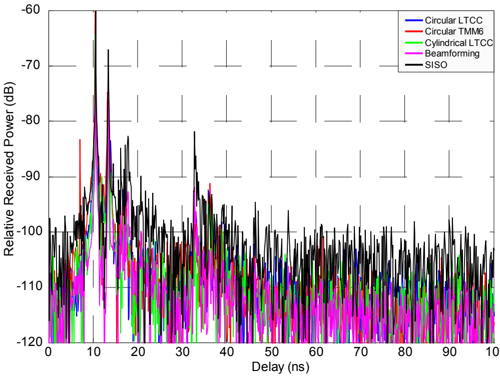

**Figure 8.13:** Power delay profile at 1st position ($\theta = 0^{\circ}$) in LOS conditions.

**Table 8.4:** Relative received power and RMS delay spread values for 1st position in LOS conditions.

| | **Relative Received Power** | **RMS Delay Spread** |
|---|---|---|
| Circular LTCC | -59.45 dB | 0.68 ns |
| Circular TMM6 | -58.79 dB | 0.66 ns |
| Cylindrical LTCC | -63.30 dB | 0.64 ns |
| 10-elem. ULA | -63.96 dB | 1.21 ns |
| SISO | -72.56 dB | 4.47 ns |

using a beamforming technique applied to the 10-element ULA. In Fig. 8.13, the measured PDP shows that for all cases, the direct ray with highest power (LOS component) is received at 10.5 ns. The rest of the components arrive attenuated in the next moments due to the multipath propagation. It is worthwhile mention that the shape obtained for all the PDPs is almost identical, which means that the situation of the antennas has been the same during the whole process of the measurements campaign, fact that is very difficult in this kind of measurements at these frequencies. In the Table 8.4, the relative received power and the RMS delay spread calculated from the PDP for each evaluated transmitting antenna are summarized. As it is observed in Table 8.4, the highest relative received power is achieved with the circular TMM6 lens, which it has been stated before.

Additionally, the power difference among the rest is according to the measured gain values (see Table 8.2 and Table 8.3). For example, the measured gain difference obtained in previous sections between the circular TMM6 lens and the circular LTCC-based is around 0.8 dB, which is almost the same relative received power difference obtained for this first measured position in LOS conditions. Similar results are also obtained comparing the TMM6 lens and the cylindrical LTCC lens: a measured gain difference of 3.7 dB between the two lenses, and a relative received power difference of 4.5 dB. Moreover, a remarkable result is that the measured relative received power for the 10-element acULA is lower than the measured for all the designed lenses, being the SISO case the worst, and constant, independently of the angle, as it is shown in Fig. 8.12, since a single omni-directional antenna is used.

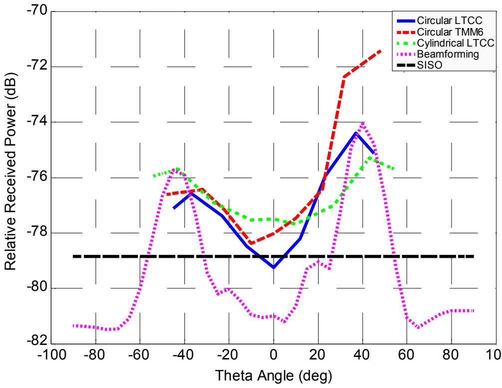

**Figure 8.14:** Relative received power at 1st position ($\theta = 0^{\circ}$) in OLOS conditions.

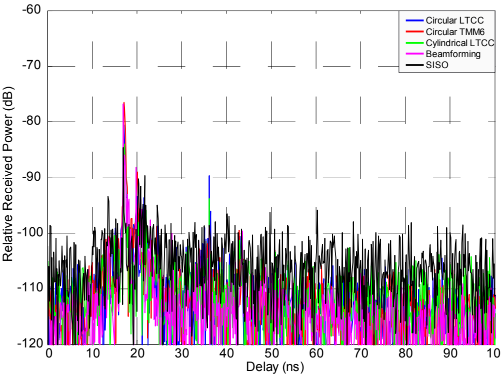

**Figure 8.15:** Power delay profile at 1st position ($\theta = 0^{\circ}$) in OLOS conditions.

**Table 8.5:** Relative received power and RMS delay spread values for 1st position in OLOS conditions.

| | **Relative Received Power** | **RMS Delay Spread** |
|---|---|---|
| Circular LTCC | -74.38 dB | 18.81 ns |
| Circular TMM6 | -71.42 dB | 5.77 ns |
| Cylindrical LTCC | -75.29 dB | 36.01 ns |
| 10-elem. ULA | -74.05 dB | 42.78 ns |
| SISO | -78.83 dB | 33.18 ns |

Regarding the RMS delay spread, the computed values from measurements are very low for all the considered antennas due to the LOS situation, in which the signal is propagating without facing any obstacle. For the lens antennas the results are very similar, below 1 ns, being for the cylindrical LTCC lens the lowest. However, for the ULA case the RMS delay spread is the double due to the diversity, and for the SISO is even higher because the use of the omni-directional antenna, which has a wider -3 dB beamwidth radiation pattern.

For the same setup of the first measured position, we placed an absorbent panel in the middle of the Tx and Rx antennas, which exactly corresponds to the OLOS situation shown in Fig. 8.10. Therefore, in this case the direct ray is obstructed by the obstacle. In the same way as in the previous situation, the relative received power in function of the angle and the PDP are plotted for each transmitting antenna in Fig. 8.14 and Fig. 8.15, respectively. As it is shown in Fig. 8.15, the direct ray is cancelled and a component with lower power than the previous one is received at 17.1 ns. In Fig. 8.14, it is observed that at 0º, the received power is really low because this path is being obstructed for the absorbent panel. However, thanks to multipath propagation, around 40º we are receiving a certain amount of power. For this angle, the TMM6 lens is still performing better than the rest of transmitting antennas, despite the ULA is steering the beam to the direction of maximum propagation, but it is clearly receiving less power.

Table 8.5 shows a summary of the computed values for the relative received power and RMS delay spread for this OLOS situation in the first measurement position. Due

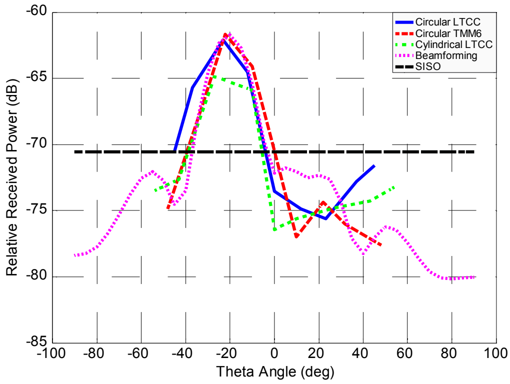

**Figure 8.16:** Relative received power at $2^{\text{nd}}$ position ($\theta = 22.5^{o}$) in LOS conditions.

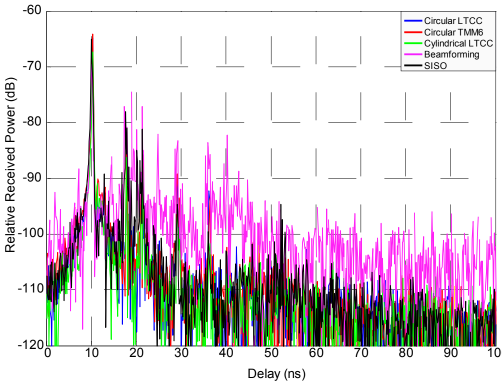

**Figure 8.17:** Power delay profile at $2^{\text{nd}}$ position ($\theta = 22.5^{o}$) in LOS conditions.

**Table 8.6:** Relative received power and RMS delay spread values for $2^{\text{nd}}$ position in LOS conditions.

| | **Relative Received Power** | **RMS Delay Spread** |
|---|---|---|
| Circular LTCC | -62.11 dB | 1.84 ns |
| Circular TMM6 | -61.67 dB | 1.86 ns |
| Cylindrical LTCC | -64.87 dB | 1.38 ns |
| 10-elem. ULA | -61.75 dB | 12.37 ns |
| SISO | -70.54 dB | 4.11 ns |

to the obstacle, the received power decreases, while the RMS delay spread increases, as it was expected. It is observed that the lowest delay spread is also achieved with the TMM6 lens.

### 8.4.7 Second Position Measurements

As it is depicted in Fig. 8.8, in the second position situation the Tx and the Rx antennas are separated 3 meters forming an angle of $22.5^{o}$ between them in a LOS condition. In the same way as it has been previously described, the measurements are carried out. Therefore, the relative received power in function of the angle and the PDP are plotted for each different transmitting antenna in Fig. 8.16 and Fig. 8.17, respectively, and in the Table 8.6, the computed relative received power and the RMS delay spread are also summarized.

As it is shown in Fig. 8.17, the strongest component is received at 10.1 ns, a similar time delay as for the first position in LOS situation, but the received power is slightly lower because the antennas are forming $22.5^{o}$ between them. In this case, the highest received power value is obtained using the TMM6 lens, and the lowest RMS delay spread is achieved with the cylindrically distributed parameters LTCC lens. The power received with the 10-element ULA is almost the same as with the TMM6 lens, however the RMS delay spread is considerably higher, nearly 7 times higher in comparison to TMM6 lens, and up to 9 times compared to the value obtained using the *cylindrical* LTCC lens, which

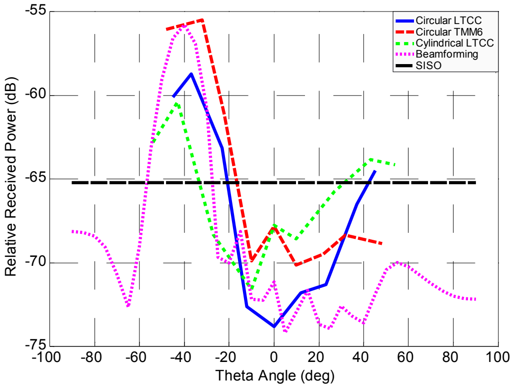

**Figure 8.18:** Relative received power at 3$^{rd}$ position ($\theta = 45^{o}$) in LOS conditions.

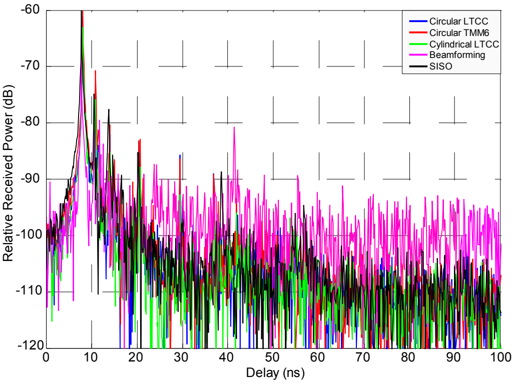

**Figure 8.19:** Power delay profile at 3$^{rd}$ position ($\theta = 45^{o}$) in LOS conditions.

**Table 8.7:** Relative received power and RMS delay spread values for 3$^{rd}$ position in LOS conditions.

| | Relative Received Power | RMS Delay Spread |
|---|---|---|
| Circular LTCC | -58.75 dB | 1.80 ns |
| Circular TMM6 | -55.51 dB | 1.27 ns |
| Cylindrical LTCC | -60.37 dB | 1.20 ns |
| 10-elem. ULA | -55.80 dB | 18.16 ns |
| SISO | -65.21 dB | 2.92 ns |

is a remarkable result because directly affects the coherence bandwidth, which in turn limits the capacity in a wireless transmission system.

## 8.4.8 Third Position Measurements

The third position considered in this experimental study is also depicted in Fig. 8.8, defining a distance of 2.3 meters separating the Tx and Rx antennas and forming an angle of 45º between them in LOS conditions. For this particular wide-angle case, the measured relative power, and the computed PDP are plotted in Fig. 8.18 and Fig. 8.19, respectively. In addition, the maximum relative received power and the RMS delay spread values are summarized in Table 8.7 for each evaluated Tx antenna. As it is observed, the direct ray with the strongest component (LOS condition) is received at 7.7 ns for all the considered antennas. The rest of the components arrive delayed due to the multipath propagation, all of them with different levels of attenuation depending on which antenna is used. The maximum received power is centered around 40º, as it is shown in Fig. 8.18. Once again, the highest received power is achieved with the circular TMM6 lens, despite the wide steering angle in which the Rx antenna is placed with respect to the Tx. Regarding the RMS delay spread, the results confirm the obtained in previous situations, being the cylindrical LTCC lens the best option in order to obtain the lowest value, with a RMS delay spread of 1.2 ns, 15 times lower than the obtained with the 10-element ULA.

## 8.5 Experimental Measurements Conclusions

The performance of the considered lens antennas has been experimentally evaluated and compared to a 10-element ULA of omni-directional antennas applying a beamforming technique, and to a single omni-directional antenna in real 60 GHz WPAN indoor environment under LOS and OLOS conditions, obtaining remarkable results in terms of measured received power and RMS delay spread. It has been practically demonstrated that in a real millimeter-wave communication scenario the best results in terms of relative received power are achieved in all the considered cases, despite the wide steering angle in which Rx antenna is placed respect to the Tx, with the TMM6 flat lens, closely followed by the circular LTCC-based lens, and in any case improving the results obtained with the 10-element ULA.

Moreover, the experimental analysis also indicate that in terms of RMS delay spread, the best results are obtained with the LTCC-based flat lens with the effective parameters cylindrically distributed, which provides a steerable fan-beam radiation pattern, a remarkable result because enhances the coherence bandwidth to improve the capacity in a wireless transmission system. In this sense, the measured RMS delay spread can be up to 15 times smaller using the proposed *cylindrical* LTCC flat lens compared to the RMS delay spread obtained with the virtual ULA, when, in a LOS situation, a wide angle between Tx and Rx is established.

Additionally, the complexity in the implementation of the proposed LTCC-based lens antenna solution, which is considerably lower compared to the difficulty in the implementation of beam-forming techniques for phased-array antennas, has also to be taken into account as an important point. It has been experimentally demonstrated their practical application as smart antenna solution for high data rate 5G millimeter-wave commercial systems, not only for mobile devices, but also as a possible solution for access points, or even for outdoor base stations, due to their planar antenna configuration and 2-D scanning capability of high-gain radiation beams.

9

## Chapter 9

# Conclusions

*As a conclusion of the present doctoral thesis, this chapter summarizes the main ideas that have been developed through the 4-year research study, with the intent of wrapping them up into solid concepts for future research and applications.*

## 9.1 Main Conclusions

This doctoral thesis has contributed to the study, development, and assessment of the performance of innovative antenna solutions in order to improve the existing architectures at millimeter-wave frequencies, conveniently solving the problems related specifically to short-range high data rate communication systems at 60 GHz WPAN band (including future 5G millimeter-wave systems), automotive radar sensors at 79 GHz band, and communications, radar, and imaging systems at 94 GHz. The specific goals pursued in this work, focused on defining an alternative antenna architecture able to achieve a full reconfigurable 2-D beam-scanning of high gain radiation beams at millimeter-wave frequencies, has been fulfilled. In this sense, this thesis has been mainly devoted to study in depth and practically develop the fundamental part of an innovative switched-beam antenna array concept: novel inhomogeneous gradient-index dielectric flat lenses, which, despite their planar antenna profile configurations, allow full 2-D beam-scanning of high gain radiation beams. A transversal study, going from theoretical investigations, passing by numerical analysis, new fabrication strategies, performance evaluation, and to full experimental assessment of the new antenna architectures in real application environment has been successfully carried out.

The main and original contributions and conclusions can be summarized as follows:

- A new antenna architecture, based on the switched-beam antenna array concept, which provides an interesting alternative to the traditional solutions because it has a set of multiple fixed beams that can be easily selected individually, with a much easier implementation, has been introduced. We initially presented the theoretical design and functioning principle of the flat lens-based switched-beam antenna array concept. In this novel antenna concept, the flat lens steers and enhances the radiation in a particular direction of the space. Only one radiating element of the array is selected for each operation mode. It has been demonstrated that the focusing direction depends on the position of this single element of the array, which is selected and activated, allowing us to scan the high-gain radiation beam in both theta and phi directions of the space.
- A specific inhomogeneous gradient-index dielectric flat lens model has been presented for millimeter-wave applications. This model has been theoretically described, numerically simulated, practically fabricated on TMM6 dielectric substrate by means of perforations, and fully electromagnetically tested at 60 GHz WPAN frequency band, at 77 GHz, and at 94 GHz. The measurements at these three frequency bands indicate that we can achieve up to around 20 dB of broadside gain, beam-steering capabilities in both planes from -30º to +30º with around 17-18 dB gain, with low side-lobe levels, and up to ±45º with around 15 dB gain. It has been practically demonstrated that this lens design could be used to develop a complete switched-beam array for millimeter-wave systems, including high throughput communications at 60 GHz for WPAN applications for the future 5G systems, automotive radar systems at 77 GHz, or communications, radar and imaging applications at 94 GHz band, achieving full 2-D beam-scanning capabilities of high-gain radiation beams, broadband operation, and flat antenna profile.
- The theoretical study and design of two new alternatives of inhomogeneous ML (iML) to increase the maximum achievable gain, reduce the back-radiation level

and the SLLs, and enhance the bandwidth performance of the original dielectric flat lens have been presented. Our numerical results indicate that compared to the original flat lens design without iML, the lens with the single inhomogeneous iML delivers a better performance in terms of maximum achievable gain, back-radiation reduction, and SLL at a particular frequency of 60 GHz. However, its use in an extended frequency band, such as the whole 60 GHz WPAN band, from 57 to 66 GHz, is not recommended. In this sense, it has been demonstrated that the use of multiple stacked iML (e.g. a triple-iML is able to improve the performance for a broad frequency range.

- In order to build the complete switched-beam array for the considered millimeter-wave applications, the radiating part of the structure has been also studied, designed, fabricated, and experimentally tested. In this case, we proposed a five by five planar array of slot and patch antennas to facilitate the integration in a low-profile antenna configuration for compact mobile devices. A total of 25 fixed high-gain beams can be selected, one by one, to scan in both theta and phi directions. However, the integration of the corresponding switching elements to individually select each one of the radiating elements of the array has been demonstrated as one of the biggest and more difficult technological challenges at millimeter-wave frequencies. These switch integration issues still have to be solved by the specific scientific community; therefore, an alternative solution has been contemplated, studied and presented, to solve the problem directly from the antenna point of view: a switched-beam antenna array based on dielectric flat lenses with cylindrically distributed effective parameters. In consequence, a complete study of this innovative proposed antenna concept has been carried out. A novel dielectric flat lens with its effective parameters cylindrically distributed has been introduced, studied, numerically simulated, fabricated and fully electromagnetic characterized at millimeter-wave frequencies.
- Because of the cylindrically effective parameters distribution of this new lens (i.e. effective gradient-index in one axis, constant-index in the other one), it has been demonstrated that the beam-scanning can be performed by moving (or selecting) the position of the radiating element along the gradient-index axis, whereas the beam can be maintained invariant in the other direction, in which the effective parameters are maintained constant, despite changing the radiating element position in this particular axis. In this way, the beam-scanning can be achieved in the constant-index axis by means of a different technique, thus reducing considerably the switch elements needed, to finally perform a full 2-D scan in all the directions of the space.
- A traveling-wave frequency-scanned stripline-fed transverse slot antenna array has been designed in order to achieve beam-scanning in one single plane by sweeping the frequency taking advantage of the huge amount of bandwidth available at millimeter-wave frequencies.
- A new switched beam antenna array concept based on the innovative LTCC-based dielectric flat lens with the permittivity cylindrically distributed and on the frequency-scanned slot antenna array has been introduced, numerically investigated, fabricated, and successfully practically assessed for millimeter-wave applications. The dielectric flat lens and the frequency-scanned array have been exhaustively tested, first separately, and after that together as the complete SWBA array, showing in

all cases very good performance in terms of radiation pattern parameters, beam-steering capabilities in both theta an phi planes, measured gain values, efficiencies, impedance matching, and broadband behavior in the whole frequency band of interest (57-66 GHz).

- It has been demonstrated the feasibility of fabricating perforated flat lenses in LTCC technology, which to our best knowledge has never been proved before, and even less stacking up to 31 green tape layers of dielectric material in order to create a desired permittivity profile. Moreover, the LTCC lens manufacturing process performance has also been evaluated in terms of the permittivity profile achieved, being this one measured with a pulsed time-domain spectroscopy system, obtaining very good results to confirm the viability of the process.
- The potential integration of the proposed complete antenna solution in a single monolithic structure has been demonstrated. This technology is suitable and allows mass production for a flat antenna structure such as the proposed in this work, which is very interesting in order to integrate the solution in compact millimeter-wave wireless mobile devices.
- The two new LTCC dielectric flat lens antennas have been exhaustively evaluated and compared to a previously introduced TMM6 material flat lens, showing in all cases very good performance in terms of radiation pattern parameters: maximum measured gain (between 15 and 18 dB), beam-steering capabilities in both planes (between approximately -50º and +50º), low SLL (below -10 dB in most of the cases, and below -15 dB and -17.5 dB for the broadside direction); estimated efficiencies (over 70-80%), impedance matching, and broadband behavior in the whole frequency band of interest ($57 - 66$ GHz).
- In contrast to other antenna alternatives, with the proposed solution we are able to scan high-gain radiation beams in both azimuth and elevation planes, necessary for supporting high data rate transmissions ( 1.5 Gbps) as it is recommended in the IEEE 802.15.3c standard, and additionally avoiding the need of high number of integrated RF switches to perform such full 2-D radiation pattern reconfiguration.
- Although the final models have been designed specifically at 60 GHz for high data rate 5G communication systems, due to their the good broadband behavior observed along this PhD thesis, the antenna concept is not only scalable at higher frequencies, but also the prototypes could even perform well directly at higher bands (e.g. 77 and 94 GHz bands, taking advantage of the huge amount of bandwidth available) exactly for the observed broadband operation of the introduced antenna solution.
- The performance of the considered lenses has also been experimentally evaluated and compared to a 10-element ULA of omni-directional antennas applying a beam-forming technique, and to a single omni-directional antenna in real 60 GHz WPAN indoor environment under LOS and OLOS conditions, obtaining remarkable results in terms of measured received power and RMS delay spread. It has been practically demonstrated that in a real millimeter-wave communication scenario the best results in terms of relative received power are achieved in all the considered cases, despite the wide steering angle in which Rx antenna is placed respect to the Tx, with the TMM6 flat lens, closely followed by the circular LTCC lens, and in any case improving the results obtained with the 10-element ULA.

- Moreover, the experimental analysis also indicate that in terms of RMS delay spread, the best results are obtained with the cylindrically distributed parameters flat lens, which provides a steerable fan-beam radiation pattern, a remarkable result because enhances the coherence bandwidth to improve the capacity in a wireless transmission system. In this sense, the measured RMS delay spread can be up to 15 times smaller using the proposed cylindrical LTCC flat lens compared to the RMS delay spread obtained with the virtual ULA, when, in a LOS situation, a wide angle between Tx and Rx is stablished.
- Additionally, the complexity in the implementation of the proposed LTCC-based lens antenna solution, which is considerably lower compared to the difficulty in the implementation of beam-forming techniques for phased-array antennas, has also to be taken into account as an important point. It has been experimentally demonstrated their practical application as smart antenna solution for high data rate 5G millimeter-wave commercial systems, not only for mobile devices, but also as a possible solution for access points, or even for outdoor base stations, due to their planar antenna configuration and full 2-D scanning capability of high-gain radiation beams.

## 9.2 Future Research Lines

During this doctoral research several open points have been identified as well as opportunities for further investigations, and are highlighted as follows:

- **Complete SWBA array integration using LTCC technology** The inhomogeneous lens integration in a flat antenna profile with LTCC process has been demonstrated; in the same way, the fabrication of arrays of radiating elements is very common in this technology. However, it is necessary to develop the complete SWBA array integration in LTCC technology, layer by layer, from the radiating elements layer, passing by the iML layers, and finally to the inhomogeneous lens layers, to built a single monolithic structure, as it is depicted in Fig. 6.1, at page 92.
- **Extend the experimental studies carried out in a real 60** GHz **indoor environment** The assessment of the performance of the introduced flat lenses has been carried out at 60 GHz WPAN band for indoor communication systems in a real case scenario. It would be very interesting to perform similar experimental studies, not only in indoor environments, but also in outdoors, as well as at different frequency bands, such as the new promising bands for future 5G systems, and for the considered automotive radar applications at 79 GHz, and for the imaging, radar, and communication systems at 94 GHz. In this sense, the facilities of the UPCT will allow the measurement in indoor communication scenarios at 94 GHz in a short time.

A

Appendix A

# Additional Contributions

*THIS appendix presents a summary and a brief description of some additional contributions carried out in collaboration with researchers of other institutions during this doctoral thesis.*

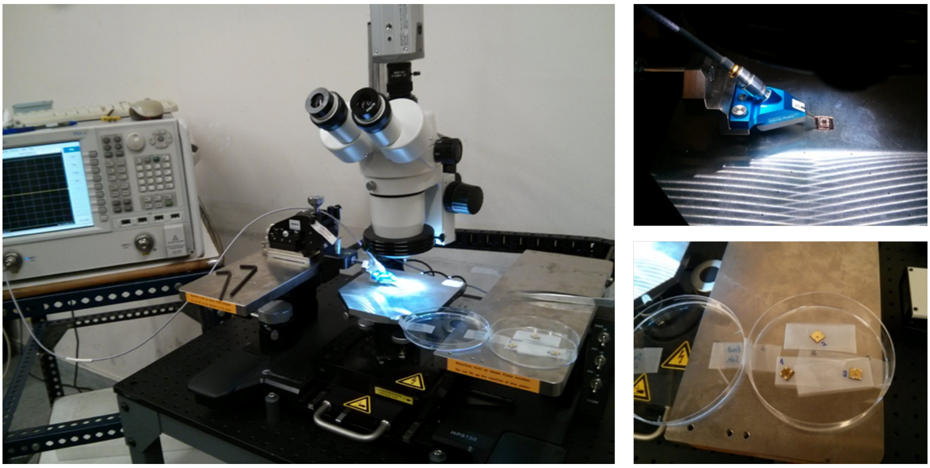

**Figure A.1:** Measurement setup for the characterization of the micro-fabricated patch antenna. Details of the GSG probes with the fabricated antennas are shown in the right insets.

## A.1 Three-Dimensional Microfabricated Broadband Patch Antenna for WiGig Applications

In collaboration with researchers from Utah State University, we have also contributed in part to a publication of a three-dimensional microfabricated broadband patch antenna for WiGig Applications [JA4], [CA7], specifically in the antenna characterization section.

In this collaboration, we presented the design, microfabrication, and characterization of a broadband patch antenna capable of covering the entire IEEE 802.11ad (WiGig) frequency band (57-66 GHz). A conductor-backed (CB) coplanar waveguide (CPW)-fed loop slot couples the energy to the patch antenna, resulting in a broad bandwidth. The feed circuitry along with the loop is formed on a quartz substrate ($\epsilon_r = 3.9$, $\tan \delta = 0.0002$ at 60 GHz), on top of which an SU-8-based three-dimensional (3-D) structure with air cavities is microfabricated. The patch metallization is deposited on top of this 3-D structure. While the main role of the structure made out of SU-8 material is to provide a mechanical support for the patch metallization, the antenna takes advantage of the air cavities underneath, thus resulting in an antenna substrate with a very low loss. This, in turn, improves the overall antenna performances. The simulated and measured impedance characteristics agree well, showing $\approx 15\%$ bandwidth. Also, the radiation pattern results demonstrate the integrity of radiation pattern with reasonably constant gain values (average dB) in the broadside direction over the entire WiGig band.

In Fig. A.2 the 3-D structure for the microfabricated patch is shown. Additionally, in Fig. A.1, a photograph of the AntennaLab facilities of the UPC with the probe station setup used to characterize the introduced patch antenna is also shown, together with GSG probes used and the fabricated prototypes, and in Fig. A.3 the measured reflection coefficient is plotted compared to the simulation results for the microfabricated patch antenna.

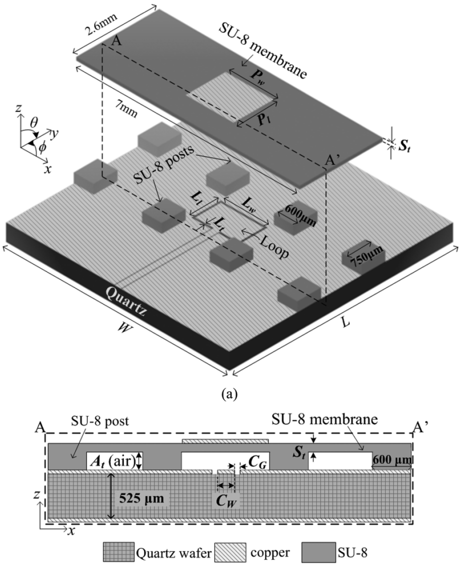

**Figure A.2:** Schematic depicting (a) 3-D (for the sake of illustration, the SU-8 membrane is suspended on top of the CPW metallization and (b) cross-sectional drawings of the antenna.

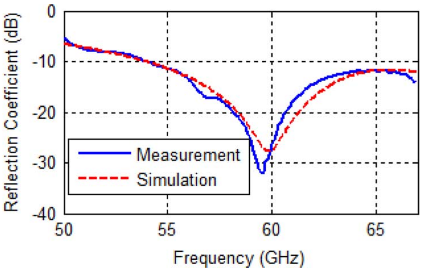

**Figure A.3:** $S_{11}$-parameter comparison between simulations and measurements.

In a subsequent evolution of the presented microfabricated patch antenna, a study to achieve reconfiguration capabilities has been carried out. In the present doctoral research we contributed in the characterization of the new proposed solutions. A detailed images of the new designs implemented to achieve certain beam-steering capabilities are shown in Fig. A.4

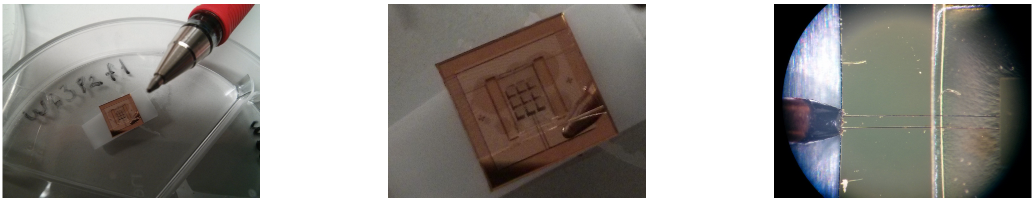

**Figure A.4:** Different photographs of the microfabricated prototypes and CPW feeding.

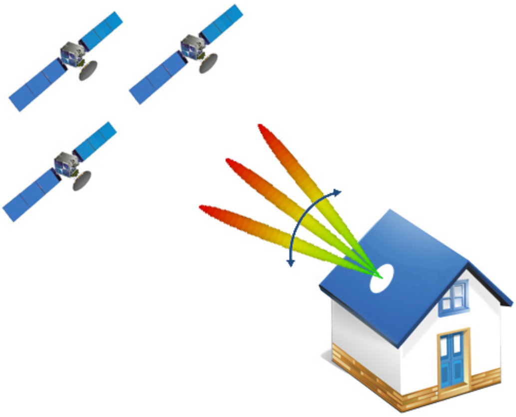

**Figure A.5:** Principle of application of the proposed flat lens structure on the roof top.

## A.2 Ku-band flat lens design for satellite TV applications

In this additional contribution in collaboration with researchers of the University of California at Irvine (UCI) [CA7], following the same design principles described for the flat lens introduced in 2, at page 19, the design of a dielectric flat lens to operate in the Ku-band for satellite communications is presented. Modern dishes intended for home television are generally bulky and heavy. Moreover, the costs of installation and alignment with the desired satellite are high. Satellite television providers are therefore looking for alternatives to the traditional dishes that could provide narrow beamwidths (5º max.), high gains, low side-lobe levels and beam steering capabilities. To satisfy the aforementioned requirements, we proposed a dielectric flat lens to steer and enhance the radiation of the feed in a particular direction.

Our simulation results indicate that we can achieve up to 31 dB of gain with 2.3º beamwidth, and beam-steering capabilities from +15º to -15º in both azimuth and elevation with more than 28 dB of gain with around 4º beamwidth, with low side-lobe levels, in the entire frequency band of interest (from 11.7 to 12.2 GHz). Moreover, the proposed design leads to a low-profile antenna configuration, easy to manufacture and low-cost in order to be successfully installed on the roof surface of homes, or even in the walls, conveniently focusing the beam to peak the right satellite.

**Table A.1:** Summary of the permittivity values for each ring of the flat lens.

| Ring | Ring width | $\varepsilon_{reff}$ | Ring | Ring width | $\varepsilon_{reff}$ |
|---|---|---|---|---|---|
| 1 | 24.8 mm | 8.15 | 7 | 49.6 mm | 5.09 |
| 2 | 49.6 mm | 8.03 | 8 | 49.6 mm | 4.31 |
| 3 | 49.6 mm | 7.71 | 9 | 49.6 mm | 3.56 |
| 4 | 49.6 mm | 7.21 | 10 | 49.6 mm | 2.85 |
| 5 | 49.6 mm | 6.57 | 11 | 49.6 mm | 2.2 |
| 6 | 49.6 mm | 5.85 | | | |

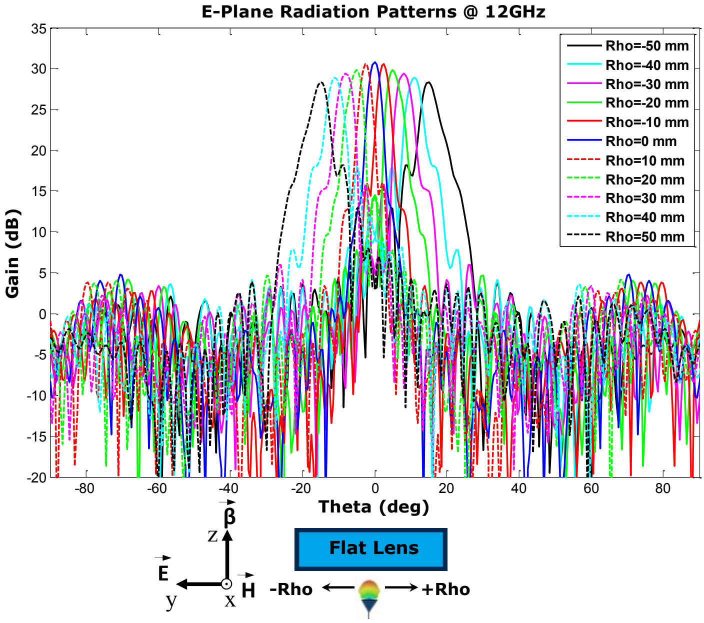

**Figure A.6:** Complete set of E-Plane gain radiation patterns obtained with CST for different *Rho* feeding positions of the circular aperture.

This functioning principle is shown in Fig. A.5 By changing the feed position the beam pointing direction can be steered in both theta and phi directions with minimal distortion of the radiation pattern, keeping the side lobes at a low level. The feed motion can be performed by simple mechanical gimbals. When the optimum location is found, the feed can be properly locked. The final lens design consists of a set of eleven concentric permittivity material rings, summarized in Table A.1 with a total diameter of $D = 52\,\text{cm}$ ($20.8\lambda_{12GHz}$), much less than conventional parabolic reflectors used in satellite TV applications, with a focal length of $F = D/4$, and a thickness of $t = 10\,\text{cm}$ ($4\lambda_{12GHz}$).

Then, the corresponding E-Plane gain radiation pattern CST simulation results for this lens were obtained, and are plotted in Fig. A.6, for a different *Rho* feeding positions of a circular aperture with the E-field polarized in the $y$-direction (see Fig. A.6).

# B

## Appendix B

# Additional Measurements

*This appendix presents some additional results obtained for the introduced flat lens and array designs carried out during this doctoral research.*

## B.1 Additional Flat Lens Measurements

This section is devoted to collect some additional measurement results obtained for the presented inhomogeneous dielectric flat lenses.

### B.1.1 Circular TMM6 lens

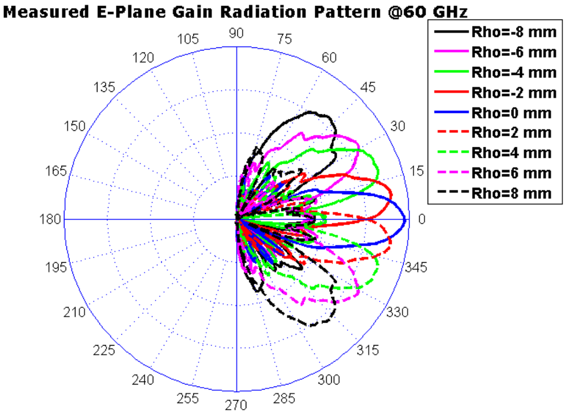

**Figure B.1:** Complete set of measured E-Plane gain (dB) radiation patterns at 60 GHz for each *Rho* feeding position (from *Rho* $= -8$ mm to *Rho* $= 8$ mm in steps of 2 mm.

### B.1.2 WR-15 Radiation Pattern Measurements

During all the flat lens radiation pattern measurements, the WR-15 waveguide used to feed the lenses presented the following E and H-Plane gain radiation patterns at 60 GHz.

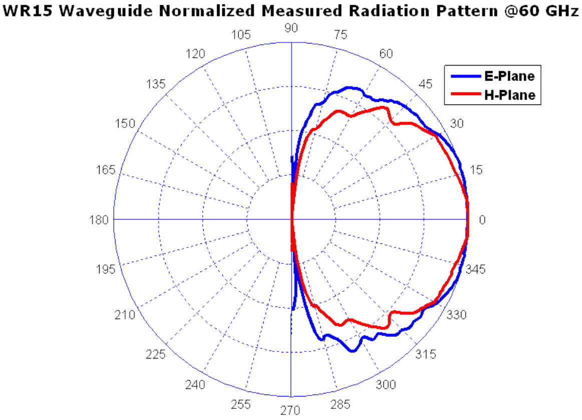

**Figure B.2:** Measured normalized E and H-Plane radiation patterns for the WR-15 waveguide used during the measurements to fed the lenses.

### B.1.3 Flat Lens with Effective Parameters Cylindrically Distributed

This section is devoted to collect some additional measurement results obtained for the lens with the effective parameters cylindrically distributed.

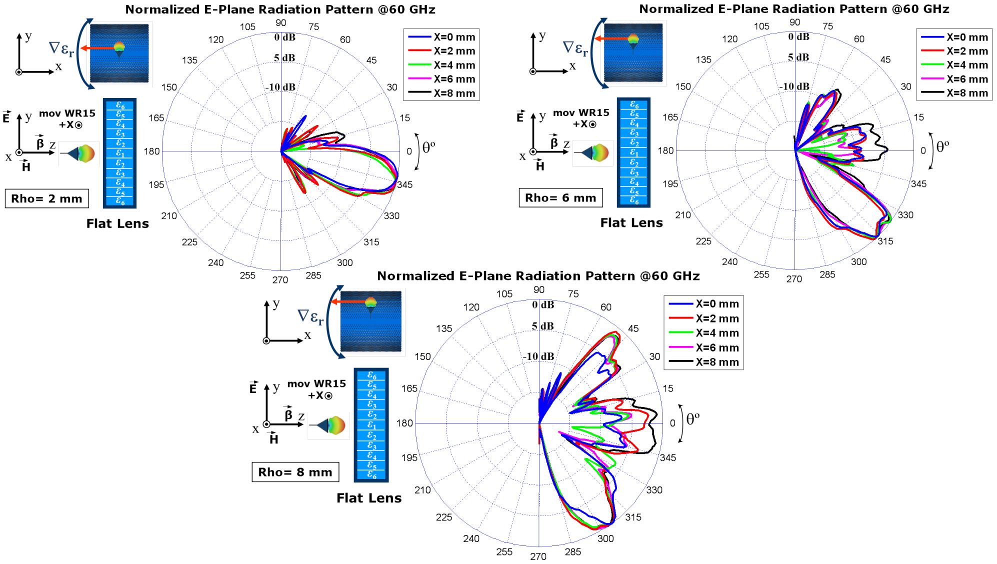

**Figure B.3:** Measured normalized E-Plane radiation patterns at 60 GHz (cut along gradient-index axis) moving the WR-15 in the constant-axis of the lens (along $X$) for $Rho = 2\,\text{mm}$, $Rho = 6\,\text{mm}$, and $Rho = 8\,\text{mm}$ feeding positions.

## B.2 Additional Array Measurements

This section is devoted to collect some additional measurement results obtained for the introduced 5 by 5 planar array and FSSA array.

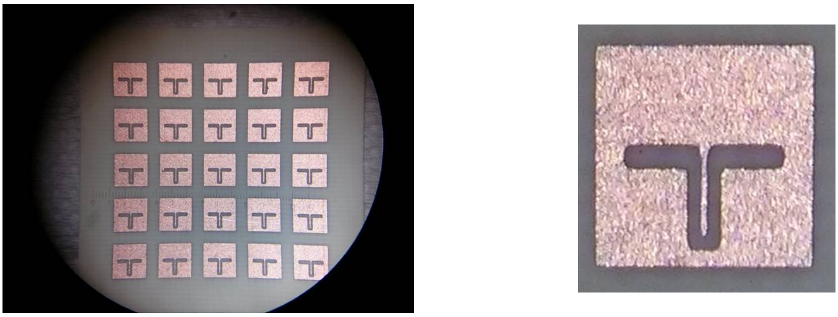

**Figure B.4:** Additionally designed slot/patch antenna array based on the original slot design but without the inductive impedance matching element.

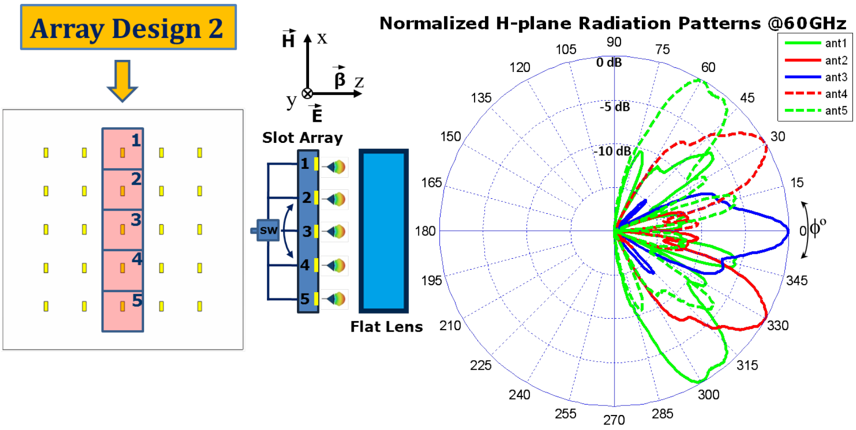

**Figure B.5:** Measured normalized H-Plane radiation patterns for the second planar array design feeding the TMM6 flat lens.

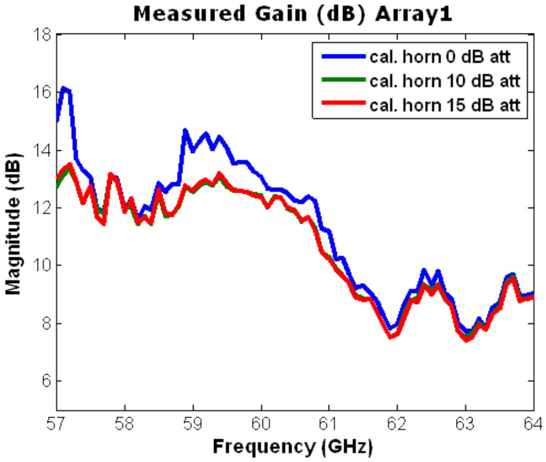

**Figure B.6:** Measured gain calibration of the radiation patterns for the second planar array design feeding the TMM6 flat lens.

C

Appendix C

# Fabrication Techniques

*This chapter is intended to give a general overview and additional consideration about the fabrication techniques used during this doctoral thesis. The standard photo-etching process, in which the introduced 5 by 5 slot/patch array, and the FSSA array have been fabricated, is described in detail. Moreover, some additional photographs of the LTCC fabrication process are provided.*

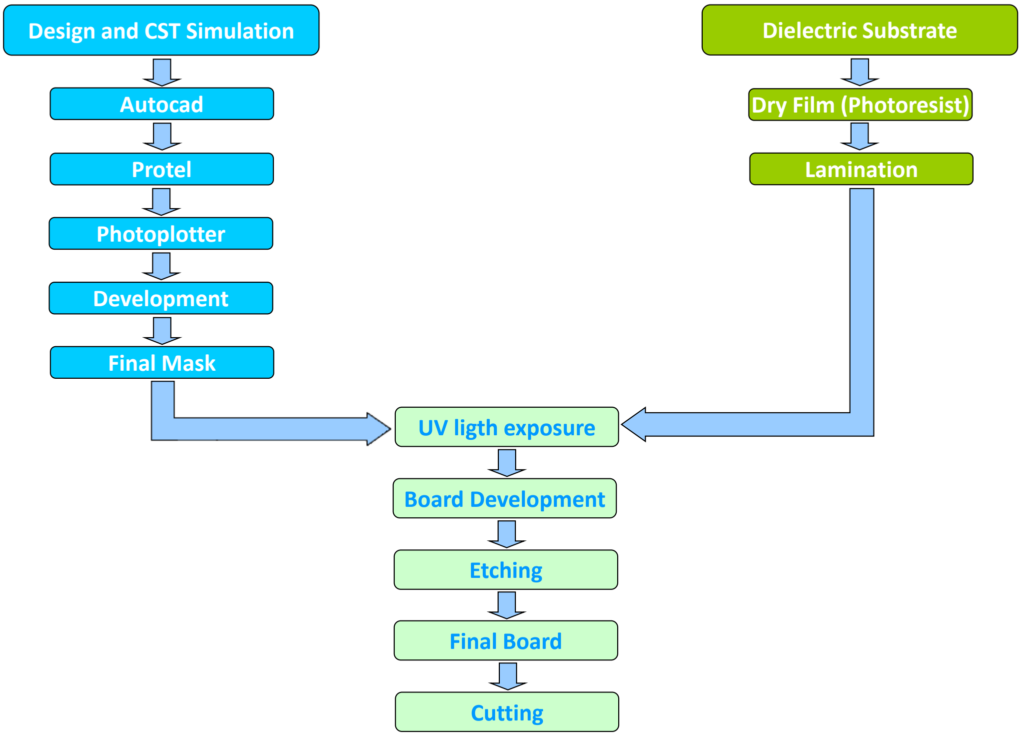

**Figure C.1:** Scheme of the standard photo-etching techniques, described step-by-step.

In Fig. C.1, the general scheme description of the standard fabrication process for printed circuit boards (PCBs), particularized for antennas design, is depicted. As it is shown, the process is divided in two parts, which finally converge in the step in which the substrate with the laminated photo-resist material is exposed to ultra violet radiation.

After designing our antenna with CST Microwave Studio, we obtain the final layout. This draw is exported to a Autocad .dxf file. This new Autocad file is then saved as a gerber file, which is imported to the photo-plotter to print the mask in a high-contrast monochromatic black-and-white photographic transparent film. Once the desired draw is printed on the film, the media is processed in a processor using a developer solution, along with fixing, washing, and drying, to finally obtain our mask.

On the other hand, the dielectric substrate is laminated together with a photo-resist material. If our design has top and bottom layers, we have to laminate both sides of our substrate in order to fix the photo-resist 8dry film). Once the material is laminated on the substrate, then, the mask with our antenna design is placed over the substrate, and it is exposed to ultra-violet light for only 30 seconds, in order to fix the draw on the substrate. Then, the whole board is developed using a standard photographic process, with a sodium hydroxide solution.

After this step, the photo-resist material will be removed from the parts exposed to the ultra violet light, and the parts which were covered by the photo-plotter mask, will be preserved. Then, we obtain a board in which our antenna design is exactly printed with a photo-resist material on our substrate. This photo-resist material will protect the copper layer of the substrate material from the chemical reaction when the board is placed inside an acid solution. Usually, the etchant is a ferric chloride solution, which is very polluting. However, in the AntennaLab facilities of the UPC, protecting the environment, we use a solution, which is much less polluting, based on a 50% of Hydrogen peroxide, 25% of distilled water, and 25% of hydrochloric acid (HCl) at 37%, plus the fabrication results are even better. When finished the etching process, a stripper solution is used to remove the photo-resist material which is still attached to the substrate protecting the copper. With the described technique, we are able to fabricate prototypes with air gaps and tracks of around 80 $\mu$m width.

In the next pages, some photographs of the photo-etching process followed to fabricate the introduced antenna designs along this PhD thesis, are shown. Moreover, some additional photographs with other fabricated prototypes and further tools fabricated for the measurement processes are also plotted.

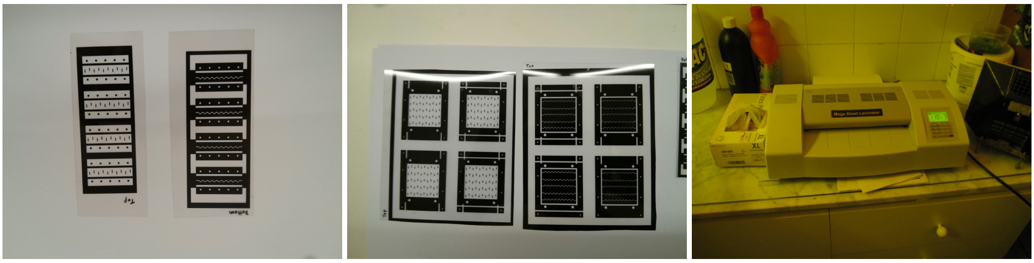

**Figure C.2:** Different images of the photo-etching technique: photo-plotter masks of the single FSSA (left), complete 5-port FSSA (middle), and laminating machine to fix the photo-resist on the substrate (right).

**Figure C.3:** Different images of the photo-etching technique: UV-exposure system (left), development of the array substrates (middle), and etching process (right), carried out at UPC facilities.

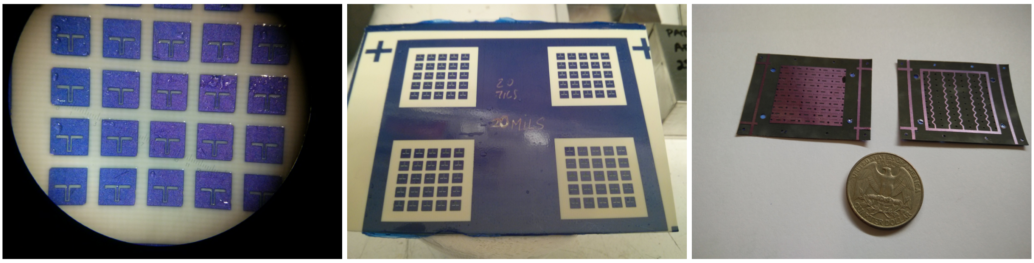

**Figure C.4:** Three images of the substrates for the fabrication of the arrays with the photo-resist already developed.

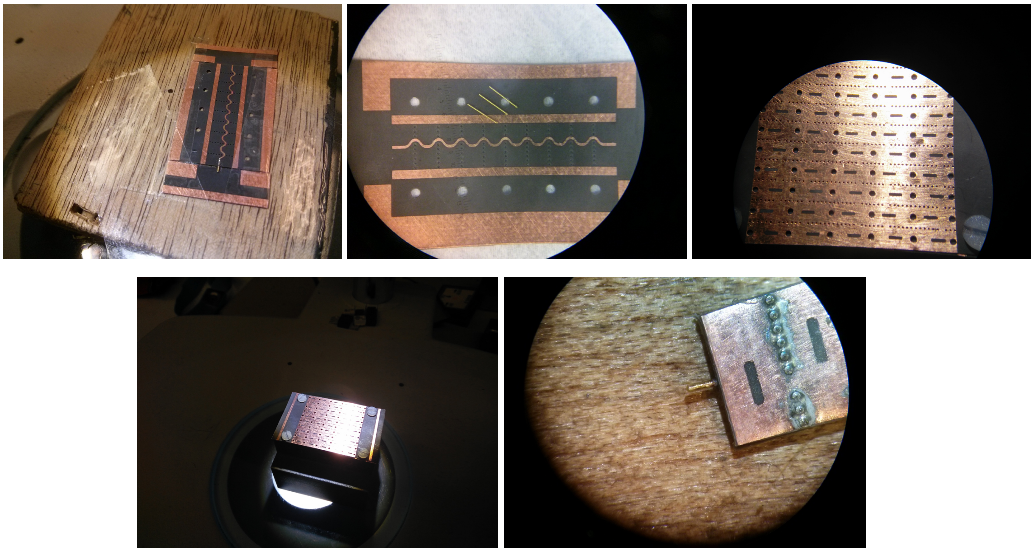

**Figure C.5:** Images from the final fabrication process of the FSSA.

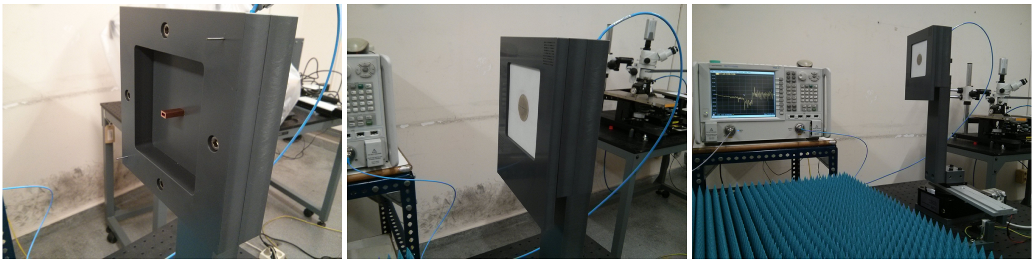

**Figure C.6:** PVC support fabricated to perform the radiation pattern measurements of the presented lenses with the UCP's far-field setup.

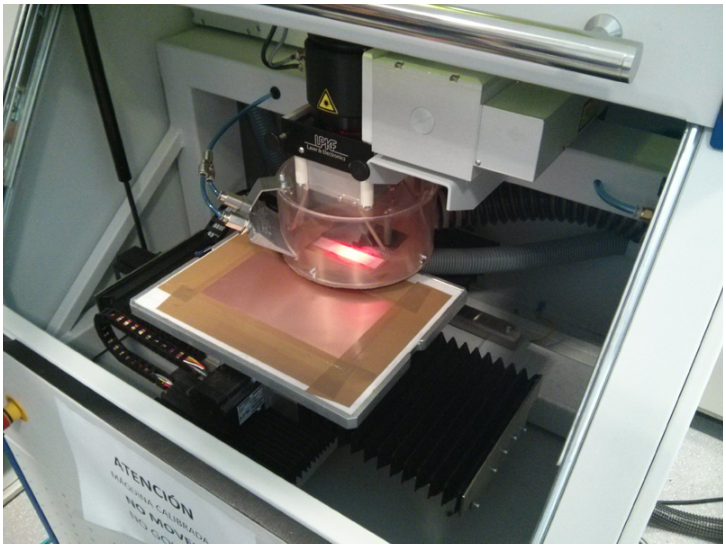

**Figure C.7:** Laser machine at the facilities of UPC in Castelldefels used to fabricate some patch and linear array of patch antennas at 60GHz during the work supervised in this Master Thesis [MA1].

**Figure C.8:** Machines used during the LTCC process: punching machine (left), laminating machine (middle), and box furnace (right).

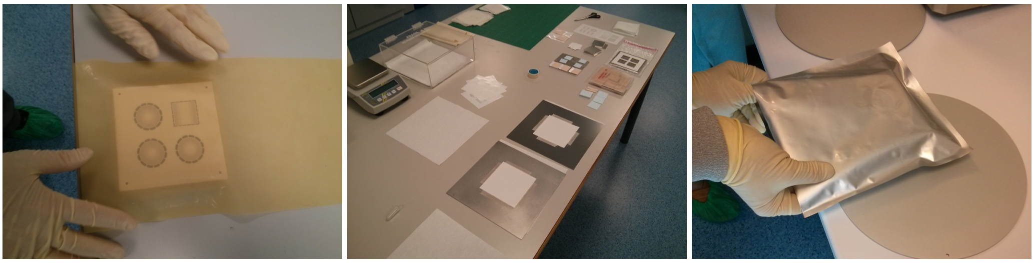

**Figure C.9:** Some parts of the LTCC process: hermetically sealed of the stacked layers (left and right photographs), and work space at the facilities of the UPV.

# Acronyms

**ACC** adaptive cruise control

**AiP** antenna-in-package

**ALG** autonomous landing guidance

**AoC** antenna-on-chip

**AP** access point

**AUT** antenna under test

**BAN** body area networks

**CMOS** complementary metal–oxide–semiconductor

**CNC** computer numerical control

**CPW** co-planar waveguide

**CST** Computer Simulation Technology

**DFT** discrete Fourier transform

**DR** dynamic range

**DRA** dielectric resonator antenna

**ECMA** European computer manufacturers association

**EHF** Extremely High Frequency

**EIRP** equivalent isotropic radiated power

**ETSI** European Telecommunications Standards Institute

**F/B** front-to-back ratio

**FBW** fractional bandwidth

**FCC** Federal Communications Commission

**FDTD** finite-difference time-domain

**FEM** finite elements method

**FFT** Fast Fourier Transform

**FM** frequency modulation

**FSSA** frequency-scanned slot antenna

**FT** field transformation
**GSG** ground-signal-ground
**HEMT** high electron-mobility transistor
**HFSS** High Frequency Structure Simulator
**IEEE** Institute of Electrical and Electronics Engineers
**iFFT** inverse fast Fourier transform
**iML** inhomogeneous ML
**ISM** industrial scientific and medical
**ITU** International Telecommunications Union
**LCP** liquid crystal polymer
**LOS** line-of-sight
**LTCC** low-temperature co-fired ceramics
**MEM** micro-electromechanical
**ML** matching layer
**MMIC** Monolithic Microwave Integrated Circuit
**NLOS** non-line-of-sight
**OLOS** obstructed-line-of-sight
**PCB** printed circuit board
**PDP** power delay profile
**PS** portable station
**RF** radio-frequency
**RMS** root mean square
**Rx** receiver
**SISO** single-input single-output
**SIW** substrate integrated waveguide
**SLL** side-lobe levels
**SMD** surface mount device
**SOLT** short-open-load-thru
**SP3T** single-pole triple-throw
**SP4T** single-pole quadruple-throw
**SPDT** single-pole double-throw
**SW** switch
**SWBA** switched-beam antenna
**TDS** time-domain spectroscopy
**TO** transformation optics

**Tx** transmitter
**UCI** University of California at Irvine
**ULA** uniform linear array
**UPC** Universitat Politècnica de Catalunya
**UPCT** Universidad Politécnica de Cartagena
**UPV** Universitat Politècnica de València
**UWB** ultra-wide-band
**VHT** very high throughput
**VNA** vector network analyzer
**Wi-Fi** wireless fidelity
**WLAN** wireless local area network
**WPAN** wireless personal area network

# List of Figures

# List of Tables

# Bibliography

[1] *Radio Regulations, Section 5.138 and 5.150.*, International Telecommunications Union-Radiocommunications (ITU-R) Std. (Cited on pages 2 and 4.)

[2] *Revision of Part 15 of the Commission's Rules Regarding Ultra-Wideband Transmission Systems, ET Docket 98-153, First Report and Order.*, Federal Communications Comission 02-48. Adopted February 14, 2002. Released: April 22, 2002. Std. (Cited on page 2.)

[3] *Characteristics of Ultra-Wideband technology, SM. 1755.*, ITU-R Recommendation, Geneva, Switzerland. Feb. 2002. Std. (Cited on page 2.)

[4] *Impact of devices using Ultra-Widebandide technology on systems operating within radiocommunication services, SM.1757.*, ITU-R Recommendation, Geneva, Switzerland. May 2006. Std. (Cited on page 2.)

[5] J. C. Wiltse, "History of millimeter and submillimeter waves," *Microwave Theory and Techniques, IEEE Transactions on*, vol. 32, no. 9, pp. 1118–1127, Sep 1984. (Cited on page 3.)

[6] *Code of Federal Regulation, Title 47 Telecommunication, Chapter 1, part 15.255*, Federal Communications Comision (FCC). October 2004. Std. (Cited on page 4.)

[7] R. Fisher, "60 ghz wpan standardization within ieee 802.15.3c," in *Signals, Systems and Electronics, 2007. ISSSE '07. International Symposium on*, July 2007, pp. 103–105. (Cited on pages 4 and 8.)

[8] *Multiple Gigabit Wireless Systems in frequencies around 60 GHz, Report M.2227 (Question ITU-R 212/5)*, ITU-R, Geneva, Switzerland, November 2011. Std. (Cited on pages 5 and 153.)

[9] *IEEE standard for information technology - Telecommunications and information exchange between systems - Local and metropolitan area networks - specific requirements. Part 15.3: Wireless medium access control (MAC) and physical layer (PHY) specifications for high rate wireless personal area networks (WPANs) Amendment 2: Millimeter-Wave-based alternative physical layer extension*, IEEE Std 802.15.3c. 2009 (Amendment to IEEE Std 802.15.3-2003), pp. 1-187, Oct. 2009. Std. (Cited on pages 6 and 8.)

[10] *IEEE Draft Standard for Local and Metropolitan Area Networks - Specific Requirements - Part 11: Wireless LAN Medium Access Control (MAC) and Physical Layer (PHY) Specifications - Amendment 3: Enhancements for Very High Throughput in*

*the 60 GHz Band*, IEEE P802.11ad/D8.0, May 2012 (Draft Amendment based on IEEE 802.11-2012), vol., no., pp.1-667, June 5, 2012. Std. (Cited on page 6.)

[11] *WiGig White Paper: Defining the Future of Multi-Gigabit Wireless Communications*, Wireless Gigabit Alliance (WiGig Alliance), July 2010. Std. (Cited on page 6.)

[12] *WirelessHD Specification Version 1.1 Overview*, WirelessHD Consortium. May, 2010. Std. (Cited on page 6.)

[13] *High Rate 60 GHz Phy, MAC and HDMI PAL, Standard ECMA-387, 2nd Edition*, ECMA International, December, 2010. Std. (Cited on page 6.)

[14] T. S. Rappaport, G. R. MacCartney, M. K. Samimi, and S. Sun, "Wideband millimeter-wave propagation measurements and channel models for future wireless communication system design," *IEEE Transactions on Communications*, vol. 63, no. 9, pp. 3029–3056, Sept 2015. (Cited on page 6.)

[15] T. S. Rappaport, S. Sun, R. Mayzus, H. Zhao, Y. Azar, K. Wang, G. N. Wong, J. K. Schulz, M. Samimi, and F. Gutierrez, "Millimeter wave mobile communications for 5g cellular: It will work!" *IEEE Access*, vol. 1, pp. 335–349, 2013. (Cited on page 6.)

[16] J. G. Andrews, S. Buzzi, W. Choi, S. V. Hanly, A. Lozano, A. C. K. Soong, and J. C. Zhang, "What will 5g be?" *IEEE Journal on Selected Areas in Communications*, vol. 32, no. 6, pp. 1065–1082, June 2014. (Cited on page 6.)

[17] K. Chandra, R. V. Prasad, B. Quang, and I. G. M. M. Niemegeers, "Cogcell: cognitive interplay between 60 ghz picocells and 2.4/5 ghz hotspots in the 5g era," *IEEE Communications Magazine*, vol. 53, no. 7, pp. 118–125, July 2015. (Cited on page 6.)

[18] European Telecommunications Standards Institute, "Electromagnetic compatibility and radio spectrum." ETSI, EN 302 264-1 V1.1.1, November 2009. (Cited on page 6.)

[19] *The 79 GHz Project. [Online].Available: http://www.79ghz.eu, accessed May. 2016.* (Cited on page 6.)

[20] K. van Caekenberghe, K. F. Brakora, and K. Sarabandi, "A 94 ghz ofdm frequency scanning radar for autonomous landing guidance," in *2007 IEEE Radar Conference*, April 2007, pp. 248–253. (Cited on pages 7 and 153.)

[21] Federal Communication Commission, "Allocation and service rules for the 71-76 ghz, 81-86 ghz, and 92-95 ghz bands," FCC, 03-248, November 2003. (Cited on pages 7 and 13.)

[22] G. C. Giakos, M. Pastorino, F. Russo, S. Chowdhury, N. Shah, and W. Davros, "Noninvasive imaging for the new century," *IEEE Instrumentation Measurement Magazine*, vol. 2, no. 2, pp. 32–35, 49, Jun 1999. (Cited on page 7.)

[23] D. M. Sheen, D. L. McMakin, and T. E. Hall, "Three-dimensional millimeter-wave imaging for concealed weapon detection," *IEEE Transactions on Microwave Theory and Techniques*, vol. 49, no. 9, pp. 1581–1592, Sep 2001. (Cited on page 7.)

[24] E. J. Bond, X. Li, S. C. Hagness, and B. D. V. Veen, "Microwave imaging via space-time beamforming for early detection of breast cancer," *IEEE Transactions on Antennas and Propagation*, vol. 51, no. 8, pp. 1690–1705, Aug 2003. (Cited on page 7.)

[25] A. Brizzi, A. Pellegrini, L. Zhang, and Y. Hao, "Statistical path-loss model for on-body communications at 94 ghz," *IEEE Transactions on Antennas and Propagation*,

vol. 61, no. 11, pp. 5744–5753, Nov 2013. (Cited on page 8.)

[26] L. Q. Bui, Y. Alon, and T. Morton, “94 ghz fmcw radar for low visibility aircraft landing system,” in *Microwave Symposium Digest, 1991., IEEE MTT-S International*, July 1991, pp. 1147–1150 vol.3. (Cited on page 8.)

[27] E. Moldovan, S. O. Tatu, T. Gaman, K. Wu, and R. G. Bosisio, “A new 94-ghz six-port collision-avoidance radar sensor,” *IEEE Transactions on Microwave Theory and Techniques*, vol. 52, no. 3, pp. 751–759, March 2004. (Cited on page 8.)

[28] S. Collonge, G. Zaharia, and G. Zein, “Influence of the human activity on wide-band characteristics of the 60 ghz indoor radio channel,” *IEEE Transactions on Wireless Communications*, vol. 3, no. 6, pp. 2396–2406, Nov 2004. (Cited on page 8.)

[29] R. Daniels, J. Murdock, T. Rappaport, and R. Heath, “60 ghz wireless: Up close and personal,” *Microwave Magazine, IEEE*, vol. 11, no. 7, pp. 44–50, Dec 2010. (Cited on pages 8 and 10.)

[30] T. Rappaport, J. Murdock, and F. Gutierrez, “State of the art in 60-ghz integrated circuits and systems for wireless communications,” *Proceedings of the IEEE*, vol. 99, no. 8, pp. 1390–1436, Aug 2011. (Cited on pages 8, 9, 10, 11, and 20.)

[31] Y. Zhang, M. Sun, and L. Guo, “On-chip antennas for 60-ghz radios in silicon technology,” *Electron Devices, IEEE Transactions on*, vol. 52, no. 7, pp. 1664–1668, July 2005. (Cited on pages 9, 11, and 153.)

[32] I.-S. Chen, H.-K. Chiou, and N.-W. Chen, “V-band on-chip dipole-based antenna,” *IEEE Transactions on Antennas and Propagation*, vol. 57, no. 10, pp. 2853–2861, Oct 2009. (Cited on page 9.)

[33] S. S. Hsu, K. C. Wei, C. Y. Hsu, and H. Ru-Chuang, “A 60-ghz millimeter-wave cpw-fed yagi antenna fabricated by using 0.18-um cmos technology,” *IEEE Electron Device Letters*, vol. 29, no. 6, pp. 625–627, June 2008. (Cited on page 9.)

[34] C. C. Lin, S. S. Hsu, C. Y. Hsu, and H. R. Chuang, “A 60-ghz millimeter-wave cmos rfic-on-chip triangular monopole antenna for wpan applications,” in *2007 IEEE Antennas and Propagation Society International Symposium*, June 2007, pp. 2522–2525. (Cited on page 9.)

[35] P. V. Bijumon, Y. M. M. Antar, A. P. Freundorfer, and M. Sayer, “Dielectric resonator antenna on silicon substrate for system on-chip applications,” *IEEE Transactions on Antennas and Propagation*, vol. 56, no. 11, pp. 3404–3410, Nov 2008. (Cited on pages 9 and 10.)

[36] F. Gutierrez, S. Agarwal, K. Parrish, and T. S. Rappaport, “On-chip integrated antenna structures in cmos for 60 ghz wpan systems,” *IEEE Journal on Selected Areas in Communications*, vol. 27, no. 8, pp. 1367–1378, October 2009. (Cited on page 9.)

[37] J. A. Z. Luna, L. Dussopt, and A. Siligaris, “Hybrid on-chip/in-package integrated antennas for millimeter-wave short-range communications,” *IEEE Transactions on Antennas and Propagation*, vol. 61, no. 11, pp. 5377–5384, Nov 2013. (Cited on page 9.)

[38] L. Ragan, A. Hassibi, T. S. Rappaport, and C. L. Christianson, “Novel on-chip

antenna structures and frequency selective surface (fss) approaches for millimeter wave devices," in *2007 IEEE 66th Vehicular Technology Conference*, Sept 2007, pp. 2051–2055. (Cited on page 9.)

[39] A. Babakhani, D. B. Rutledge, and A. Hajimiri, "mm-wave phased arrays in silicon with integrated antennas," in *2007 IEEE Antennas and Propagation Society International Symposium*, June 2007, pp. 4369–4372. (Cited on page 10.)

[40] P. H. Park and S. S. Wong, "An on-chip dipole antenna for millimeter-wave transmitters," in *2008 IEEE Radio Frequency Integrated Circuits Symposium*, June 2008, pp. 629–632. (Cited on page 10.)

[41] D. G. Kam, D. Liu, A. Natarajan, S. Reynolds, and B. Floyd, "Low-cost antenna-in-package solutions for 60-ghz phased-array systems," in *Electrical Performance of Electronic Packaging and Systems (EPEPS), 2010 IEEE 19th Conference on*, Oct 2010, pp. 93–96. (Cited on page 10.)

[42] Y. Zhang and D. Liu, "Antenna-on-chip and antenna-in-package solutions to highly integrated millimeter-wave devices for wireless communications," *IEEE Transactions on Antennas and Propagation*, vol. 57, no. 10, pp. 2830–2841, Oct 2009. (Cited on page 10.)

[43] L. Wai, K. Chua, A. Lu, Y. Zhang, and M. Sun, "Ultra compact ltcc based aip for 60 ghz applications," in *Electronics Packaging Technology Conference, 2007. EPTC 2007. 9th*, Dec 2007, pp. 595–599. (Cited on page 10.)

[44] M. Sun, Y. Zhang, K. Chua, L. Wai, D. Liu, and B. Gaucher, "Integration of yagi antenna in ltcc package for differential 60-ghz radio," *IEEE Transactions on Antennas and Propagation*, vol. 56, no. 8, pp. 2780–2783, Aug 2008. (Cited on pages 10, 11, and 153.)

[45] M. F. Karim, Y. X. Guo, M. Sun, J. Brinkhoff, L. C. Ong, K. Kang, and F. Lin, "Integration of sip-based 60-ghz 4 x 4 antenna array with cmos ook transmitter and lna," *IEEE Transactions on Microwave Theory and Techniques*, vol. 59, no. 7, pp. 1869–1878, July 2011. (Cited on page 10.)

[46] S. Brebels, K. Mohammadpour-Aghdam, W. De Raedt, and G. Vandenbosch, "3d system-in-package integration of 60 ghz aperture-coupled micromachined microstrip antennas," in *Microwave Symposium Digest (MTT), 2010 IEEE MTT-S International*, May 2010, pp. 1028–1031. (Cited on page 10.)

[47] D. G. Kam, D. Liu, A. Natarajan, S. Reynolds, H. C. Chen, and B. A. Floyd, "Ltcc packages with embedded phased-array antennas for 60 ghz communications," *IEEE Microwave and Wireless Components Letters*, vol. 21, no. 3, pp. 142–144, March 2011. (Cited on page 10.)

[48] T. Zwick, D. Liu, and B. Gaucher, "Broadband planar superstrate antenna for integrated millimeterwave transceivers," *IEEE Transactions on Antennas and Propagation*, vol. 54, no. 10, pp. 2790–2796, Oct 2006. (Cited on page 10.)

[49] W. Menzel and A. Moebius, "Antenna concepts for millimeter-wave automotive radar sensors," *Proceedings of the IEEE*, vol. 100, no. 7, pp. 2372–2379, July 2012. (Cited on pages 11, 12, 13, and 153.)

[50] T. Binzer, M. Klar, and V. Gross, "Development of 77 ghz radar lens antennas for

automotive applications based on given requirements," in *Antennas, 2007. INICA '07. 2nd International ITG Conference on*, March 2007, pp. 205–209. (Cited on page 12.)

[51] I. Gresham, N. Jain, T. Budka, A. Alexanian, N. Kinayman, B. Ziegner, S. Brown, and P. Staecker, "A compact manufacturable 76-77-ghz radar module for commercial acc applications," *Microwave Theory and Techniques, IEEE Transactions on*, vol. 49, no. 1, pp. 44–58, Jan 2001. (Cited on pages 12 and 13.)

[52] Millitech Corporation, "Crach avoidance flr sensors," *Microwave Journal*, vol. 37, no. 12, pp. 122–126, 1994. (Cited on page 12.)

[53] W. Menzel, D. Pilz, and M. Al-Tikriti, "Millimeter-wave folded reflector antennas with high gain, low loss, and low profile," *Antennas and Propagation Magazine, IEEE*, vol. 44, no. 3, pp. 24–29, Jun 2002. (Cited on page 12.)

[54] J. R. James, P. S. Hall, and C. Wood, *Microstrip Antenna Theory and Design.* Peregrinus, London, U.K., 1981. (Cited on page 12.)

[55] K.-F. Lee and K.-F. Tong, "Microstrip patch antennas - basic characteristics and some recent advances," *Proceedings of the IEEE*, vol. 100, no. 7, pp. 2169–2180, July 2002. (Cited on page 12.)

[56] I. Gresham, A. Jenkins, R. Egri, C. Eswarappa, N. Kinayman, N. Jain, R. Anderson, F. Kolak, R. Wohlert, S. Bawell, J. Bennett, and J.-P. Lanteri, "Ultra-wideband radar sensors for short-range vehicular applications," *Microwave Theory and Techniques, IEEE Transactions on*, vol. 52, no. 9, pp. 2105–2122, Sept 2004. (Cited on page 12.)

[57] V. Winkler, R. Feger, and L. Maurer, "79ghz automotive short range radar sensor based on single-chip sige-transceivers," in *Radar Conference, 2008. EuRAD 2008. European*, Oct 2008, pp. 459–462. (Cited on pages 12 and 13.)

[58] M. Russell, A. Crain, A. Curran, R. Campbell, C. Drubin, and W. Miccioli, "Millimeter-wave radar sensor for automotive intelligent cruise control (icc)," *Microwave Theory and Techniques, IEEE Transactions on*, vol. 45, no. 12, pp. 2444–2453, Dec 1997. (Cited on page 12.)

[59] S. Tokoro, K. Kuroda, A. Kawakubo, K. Fujita, and H. Fujinami, "Electronically scanned millimeter-wave radar for pre-crash safety and adaptive cruise control system," in *Intelligent Vehicles Symposium, 2003. Proceedings. IEEE*, June 2003, pp. 304–309. (Cited on page 12.)

[60] K. Sakakibara, A. Mizutani, N. Kikuma, and H. Hirayama, "Design of narrow-wall slotted hollow waveguide array for arbitrarily linear polarization in the millimeter-wave band," in *Antennas and Propagation Society International Symposium 2006, IEEE*, July 2006, pp. 3141–3144. (Cited on page 12.)

[61] J. Hirokawa and M. Ando, "76 ghz post-wall waveguide fed parallel plate slot arrays for car-radar applications," in *Antennas and Propagation Society International Symposium, 2000. IEEE*, vol. 1, July 2000, pp. 98–101 vol.1. (Cited on page 12.)

[62] J. Xu, W. Hong, P. Chen, and K. Wu, "Design and implementation of low sidelobe substrate integrated waveguide longitudinal slot array antennas," *Microwaves, Antennas Propagation, IET*, vol. 3, no. 5, pp. 790–797, August 2009. (Cited on page 12.)

[63] Y. Asano, S. Ohshima, T. Harada, M. Ogawa, and K. Nishikawa, "Proposal of

millimeter-wave holographic radar with antenna switching," in *Microwave Symposium Digest, 2001 IEEE MTT-S International*, vol. 2, May 2001, pp. 1111–1114 vol.2. (Cited on page 13.)

[64] A. Stelzer, R. Feger, and M. Jahn, "Highly-integrated multi-channel radar sensors in sige technology for automotive frequencies and beyond," in *ICECom, 2010 Conference Proceedings*, Sept 2010, pp. 1–11. (Cited on page 13.)

[65] W. Hu, M. Arrebola, R. Cahill, J. A. Encinar, V. Fusco, H. S. Gamble, Y. Alvarez, and F. Las-Heras, "94 ghz dual-reflector antenna with reflectarray subreflector," *IEEE Transactions on Antennas and Propagation*, vol. 57, no. 10, pp. 3043–3050, Oct 2009. (Cited on pages 13 and 14.)

[66] K. B. Cooper, R. J. Dengler, N. Llombart, B. Thomas, G. Chattopadhyay, and P. H. Siegel, "Thz imaging radar for standoff personnel screening," *IEEE Transactions on Terahertz Science and Technology*, vol. 1, no. 1, pp. 169–182, Sept 2011. (Cited on page 14.)

[67] X. Gu, A. Valdes-Garcia, A. Natarajan, B. Sadhu, D. Liu, and S. K. Reynolds, "W-band scalable phased arrays for imaging and communications," *IEEE Communications Magazine*, vol. 53, no. 4, pp. 196–204, April 2015. (Cited on page 14.)

[68] Z. Chen, Y. P. Zhang, A. Bisognin, D. Titz, F. Ferrero, and C. Luxey, "An ltcc microstrip grid array antenna for 94-ghz applications," *IEEE Antennas and Wireless Propagation Letters*, vol. 14, pp. 1279–1281, 2015. (Cited on page 14.)

[69] A. Lamminen and J. Saily, "Wideband stacked patch antenna array on ltcc for w-band," in *Proceedings of the 5th European Conference on Antennas and Propagation (EUCAP)*, April 2011, pp. 2962–2966. (Cited on page 14.)

[70] N. Ghassemi, K. Wu, S. Claude, X. Zhang, and J. Bornemann, "Low-cost and high-efficient w-band substrate integrated waveguide antenna array made of printed circuit board process," *IEEE Transactions on Antennas and Propagation*, vol. 60, no. 3, pp. 1648–1653, March 2012. (Cited on pages 14 and 153.)

[71] N. Ghassemi and K. Wu, "Planar high-gain dielectric-loaded antipodal linearly tapered slot antenna for e- and w-band gigabyte point-to-point wireless services," *IEEE Transactions on Antennas and Propagation*, vol. 61, no. 4, pp. 1747–1755, April 2013. (Cited on page 14.)

[72] Z. Chen, Y. P. Zhang, A. Bisognin, D. Titz, F. Ferrero, and C. Luxey, "A 94-ghz dual-polarized microstrip mesh array antenna in ltcc technology," *IEEE Antennas and Wireless Propagation Letters*, vol. 15, pp. 634–637, 2016. (Cited on page 14.)

[73] *IEEE Standard for Definitions of Terms for Antennas*, IEEE Std 145-2013 (Revision of IEEE Std 145-1993) Std., March 2014. (Cited on page 21.)

[74] C. Hua, N. Yang, X. Wu, and W. Wu, "Millimeter-wave fan-beam antenna based on step-index cylindrical homogeneous lens," *IEEE Antennas and Wireless Propagation Letters*, vol. 11, pp. 1512–1516, 2012. (Cited on page 21.)

[75] B. Chantraine-Bares and R. Sauleau, "Electrically-small shaped integrated lens antennas: A study of feasibility in q -band," *IEEE Transactions on Antennas and Propagation*, vol. 55, no. 4, pp. 1038–1044, April 2007. (Cited on page 21.)

[76] J. R. Costa, E. B. Lima, and C. A. Fernandes, "Compact beam-steerable lens antenna for 60-ghz wireless communications," *IEEE Transactions on Antennas and Propagation*, vol. 57, no. 10, pp. 2926–2933, Oct 2009. (Cited on pages 21 and 22.)

[77] A. D. Greenwood and J.-M. Jin, "A field picture of wave propagation in inhomogeneous dielectric lenses," *IEEE Antennas and Propagation Magazine*, vol. 41, no. 5, pp. 9–18, Oct 1999. (Cited on page 21.)

[78] A. Petosa and A. Ittipiboon, "Design and performance of a perforated dielectric fresnel lens," *Microwaves, Antennas and Propagation, IEE Proceedings*, vol. 150, no. 5, pp. 309–314, Oct 2003. (Cited on pages 21 and 26.)

[79] G. Peeler and H. Coleman, "Microwave stepped-index luneberg lenses," *Antennas and Propagation, IRE Transactions on*, vol. 6, no. 2, pp. 202–207, April 1958. (Cited on pages 21, 26, and 27.)

[80] B. Zhou, Y. Yang, H. Li, and T. J. Cui, "Beam-steering vivaldi antenna based on partial luneburg lens constructed with composite materials," *Journal of Applied Physics*, vol. 110, no. 8, pp. –, 2011. (Cited on page 21.)

[81] B. Fuchs, O. Lafond, S. Palud, L. Le Coq, M. Himdi, M. Buck, and S. Rondineau, "Comparative design and analysis of luneburg and half maxwell fish-eye lens antennas," *IEEE Transactions on Antennas and Propagation*, vol. 56, no. 9, pp. 3058–3062, Sept 2008. (Cited on pages 21 and 26.)

[82] B. Fuchs, O. Lafond, S. Rondineau, and M. Himdi, "Design and characterization of half maxwell fish-eye lens antennas in millimeter waves," *IEEE Transactions on Microwave Theory and Techniques*, vol. 54, no. 6, pp. 2292–2300, June 2006. (Cited on pages 21 and 26.)

[83] J. Eaton, "On spherically symmetric lenses," *Transactions of the IRE Professional Group on Antennas and Propagation*, vol. PGAP-4, pp. 66–71, December 1952. (Cited on page 21.)

[84] Y. Nomura and K. Takaku, "On the propagation of the electromagnetic waves in an inhomogeneous atmosphere," *Science Report of Tohoku University*, vol. 7, pp. 107–148, 1955. (Cited on page 21.)

[85] T. McManus, R. Mittra, and C. Pelletti, "A comparative study of flat and profiled lenses," in *Antennas and Propagation Society International Symposium (APSURSI), 2012 IEEE*, July 2012, pp. 1–2. (Cited on page 21.)

[86] S. Jain, M. Abdel-Mageed, and R. Mittra, "Flat-lens design using field transformation and its comparison with those based on transformation optics and ray optics," *IEEE Antennas and Wireless Propagation Letters*, vol. 12, pp. 777–780, 2013. (Cited on pages 21 and 22.)

[87] A. Artemenko, A. Maltsev, A. Mozharovskiy, A. Sevastyanov, V. Ssorin, and R. Maslennikov, "Millimeter-wave electronically steerable integrated lens antennas for wlan/wpan applications," *IEEE Transactions on Antennas and Propagation*, vol. 61, no. 4, pp. 1665–1671, April 2013. (Cited on pages 22 and 71.)

[88] C. A. Balanis, *Advanced Engineering Electromagnetics.* John Wiley & Sons, 2012. (Cited on pages 23 and 61.)

[89] H. Mosallaei and Y. Rahmat-Samii, “Nonuniform luneburg and two-shell lens antennas: radiation characteristics and design optimization,” *IEEE Transactions on Antennas and Propagation*, vol. 49, no. 1, pp. 60–69, Jan 2001. (Cited on page 26.)

[90] J. Bor, O. Lafond, H. Merlet, P. L. Bars, and M. Himdi, “Foam based luneburg lens antenna at 60 ghz,” *Progress In Electromagnetics Research Letters*, vol. 44, pp. 1–7, 2014. (Cited on pages 26 and 67.)

[91] M. J. Vaughan, K. Y. Hur, and R. C. Compton, “Improvement of microstrip patch antenna radiation patterns,” *IEEE Transactions on Antennas and Propagation*, vol. 42, no. 6, pp. 882–885, Jun 1994. (Cited on page 27.)

[92] J. S. Colburn and Y. Rahmat-Samii, “Patch antennas on externally perforated high dielectric constant substrates,” *IEEE Transactions on Antennas and Propagation*, vol. 47, no. 12, pp. 1785–1794, Dec 1999. (Cited on page 27.)

[93] A. Yaghjian, “An overview of near-field antenna measurements,” *IEEE Transactions on Antennas and Propagation*, vol. 34, no. 1, pp. 30–45, Jan 1986. (Cited on pages 39, 42, 43, and 47.)

[94] C. M. Ta, E. Skafidas, and R. J. Evans, “A 60-ghz cmos transmit/receive switch,” in *2007 IEEE Radio Frequency Integrated Circuits (RFIC) Symposium*, June 2007, pp. 725–728. (Cited on page 56.)

[95] K. Y. Lin, W.-H. Tu, P.-Y. Chen, H.-Y. Chang, H. Wang, and R.-B. Wu, “Millimeter-wave mmic passive hemt switches using traveling-wave concept,” *IEEE Transactions on Microwave Theory and Techniques*, vol. 52, no. 8, pp. 1798–1808, Aug 2004. (Cited on page 56.)

[96] G. M. Rebeiz, C. D. Patel, S. K. Han, C. H. Ko, and K. M. J. Ho, “The search for a reliable mems switch,” *IEEE Microwave Magazine*, vol. 14, no. 1, pp. 57–67, Jan 2013. (Cited on page 56.)

[97] P. Sharma, J. Perruisseau-Carrier, C. Moldovan, and A. M. Ionescu, “Electromagnetic performance of rf nems graphene capacitive switches,” *IEEE Transactions on Nanotechnology*, vol. 13, no. 1, pp. 70–79, Jan 2014. (Cited on page 56.)

[98] C. W. Byeon and C. S. Park, “Design and analysis of the millimeter-wave spdt switch for tdd applications,” *IEEE Transactions on Microwave Theory and Techniques*, vol. 61, no. 8, pp. 2858–2864, Aug 2013. (Cited on page 56.)

[99] M. Uzunkol and G. Rebeiz, “A low-loss 50-70 ghz spdt switch in 90 nm cmos,” *IEEE Journal of Solid-State Circuits*, vol. 45, no. 10, pp. 2003–2007, Oct 2010. (Cited on page 56.)

[100] J. He, Y. Z. Xiong, and Y. P. Zhang, “Analysis and design of 60-ghz spdt switch in 130-nm cmos,” *IEEE Transactions on Microwave Theory and Techniques*, vol. 60, no. 10, pp. 3113–3119, Oct 2012. (Cited on page 56.)

[101] T. Morita and S. Cohn, “Correction to ”microwave lens matching by simulated quarter wave transformers”,” *IEEE Transactions on Antennas and Propagation*, vol. 21, no. 6, pp. 919–919, November 1973. (Cited on page 60.)

[102] A. Kezuka and Y. Yamada, “Roles of matching layers for a shaped beam lens horn antenna,” in *Antennas and Propagation Society International Symposium, 2004.*

*IEEE*, vol. 2, June 2004, pp. 1543–1546 Vol.2. (Cited on page 60.)

[103] M. J. M. van der Vorst, P. J. I. de Maagt, A. Neto, A. L. Reynolds, R. M. Heeres, W. Luinge, and M. H. A. J. Herben, "Effect of internal reflections on the radiation properties and input impedance of integrated lens antennas-comparison between theory and measurements," *IEEE Transactions on Microwave Theory and Techniques*, vol. 49, no. 6, pp. 1118–1125, Jun 2001. (Cited on page 60.)

[104] N. T. Nguyen, R. Sauleau, and C. J. M. Perez, "Very broadband extended hemispherical lenses: Role of matching layers for bandwidth enlargement," *IEEE Transactions on Antennas and Propagation*, vol. 57, no. 7, pp. 1907–1913, July 2009. (Cited on page 60.)

[105] M. Danielsen and R. Jorgensen, "Frequency scanning microstrip antennas," *IEEE Transactions on Antennas and Propagation*, vol. 27, no. 2, pp. 146–150, Mar 1979. (Cited on pages 70 and 82.)

[106] J. George, P. F. M. Smulders, and M. H. A. J. Herben, "Application of fan-beam antennas for 60 ghz indoor wireless communication," *Electronics Letters*, vol. 37, no. 2, pp. 73–74, Jan 2001. (Cited on pages 74 and 116.)

[107] R. Hansen, *Phased Array Antennas.* Wiley-Interscience, New York, 1998. (Cited on pages 82 and 83.)

[108] W. Moulder, W. Khalil, and J. Volakis, "60-ghz two-dimensionally scanning array employing wideband planar switched beam network," *Antennas and Wireless Propagation Letters, IEEE*, vol. 9, pp. 818–821, 2010. (Cited on page 83.)

[109] A. Bhattacharyya, O. Fordham, and Y. Liu, "Analysis of stripline-fed slot-coupled patch antennas with vias for parallel-plate mode suppression," *IEEE Transactions on Antennas and Propagation*, vol. 46, no. 4, pp. 538–545, Apr 1998. (Cited on page 84.)

[110] R. Shavit and R. Elliott, "Design of transverse slot arrays fed by a boxed stripline," *IEEE Transactions on Antennas and Propagation*, vol. 31, no. 4, pp. 545–552, Jul 1983. (Cited on page 84.)

[111] L. Ranzani, N. Ehsan, and Z. Popovic, "G-band frequency-scanned antenna arrays," in *Antennas and Propagation Society International Symposium (APSURSI), 2010 IEEE*, July 2010, pp. 1–4. (Cited on page 85.)

[112] C. Scrantom and J. Lawson, "Ltcc technology: where we are and where we're going. ii," in *Technologies for Wireless Applications, 1999. Digest. 1999 IEEE MTT-S Symposium on*, Feb 1999, pp. 193–200. (Cited on page 94.)

[113] *C4/M2D stepper motor system user guide, Arrick Robotics, Texas, USA*. (Cited on page 118.)

[114] M. T. Martinez-Ingles, D. P. Gaillot, J. Pascual-Garcia, J. M. Molina-Garcia-Pardo, M. Lienard, and J. V. Rodriguez, "Deterministic and experimental indoor mmw channel modeling," *IEEE Antennas and Wireless Propagation Letters*, vol. 13, pp. 1047–1050, 2014. (Cited on page 118.)

[115] J. M. Molina-Garcia-Pardo, J. V. Rodriguez, and L. Juan-Llacer, "Wide-band measurements and characterization at 2.1 ghz while entering in a small tunnel," *IEEE Transactions on Vehicular Technology*, vol. 53, no. 6, pp. 1794–1799, Nov 2004. (Cited

on page 119.)

[116] T. S. Rappaport, *Smart Antennas: Adaptive Arrays, Algorithms, & Wire-less Position Location.* Piscataway, NJ: IEEE Press, 1998. (Cited on page 120.)

# List of Publications

## Journal Articles

[JA1] **M. Imbert**, J. Romeu, M. Baquero, and L. Jofre, "Switched-beam antenna based on LTCC dielectric flat lenses and frequency-scanned arrays for future 5G millimeter-wave communications," submitted for publication in *Transactions on Antennas and Propagation*, 2016.

[JA2] **M. Imbert**, J. Romeu, M. Baquero, M.-T. Martinez-Ingles, J.-M. Molina-Garcia-Pardo, and L. Jofre, "Assessment of LTCC-based dielectric flat lens antennas for future 5G indoor millimeter-wave communication systems," submitted for publication in *Transactions on Antennas and Propagation*, 2016.

[JA3] **M. Imbert**, A. Papió, F. De Flaviis, L. Jofre, and J. Romeu, "Design and performance evaluation of a dielectric flat lens antenna for millimeter-wave applications," *IEEE Antennas and Wireless Propagation Letters*, vol. 14, pp. 342–345, 2015.

[JA4] H. Mopidevi, H. V. Hunerli, E. Cagatay, N. Biyikli, **M. Imbert**, J. Romeu, L. Jofre, and B. A. Cetiner, "Three-dimensional microfabricated broadband patch antenna for wigig applications," *IEEE Antennas and Wireless Propagation Letters*, vol. 13, pp. 828–831, 2014.

[JA5] **M. Imbert**, P. J. Ferrer, J. M. Gonzalez-Arbesu, and J. Romeu, "Assessment of the performance of a metamaterial spacer in a closely spaced multiple-antenna system," *IEEE Antennas and Wireless Propagation Letters*, vol. 11, pp. 720–723, 2012.

## Conference Articles

[CA1] **M. Imbert**, S. Blanch, M. Baquero, L. Jofre, and J. Romeu, "LTCC-based dielectric flat lens performance evaluation at 94 GHz," in *Antennas and Propagation Society International Symposium (APSURSI), 2016 IEEE*, Fajardo, Puerto Rico, July 2016, pp. 1–2.

[CA2] **M. Imbert**, L. Jofre, and J. Romeu, "Dielectric flat lenses with cylindrically distributed parameters for millimeter-wave applications," in *Antennas and Prop-*

*agation (EuCAP), 2016 10th European Conference on*, Davos, Switzerland, Apr 2016, pp. 1–5.

[CA3] **M. Imbert**, J. Romeu, and L. Jofre, “Matching layer design to improve the performance of an inhomogeneous dielectric flat lens at millimeter-wave frequencies,” in *Antennas and Propagation Society International Symposium (APSURSI), 2015 IEEE*, Vancouver, BC, Canada, July 2015, pp. 2069–2070.

[CA4] H. V. Hunerli, H. Mopidevi, E. Cagatay, **M. Imbert**, J. Romeu, L. Jofre, B. A. Cetiner, and N. Biyikli, “Three dimensional microfabricated broadband patch and multifunction reconfigurable antennae for 60 GHz applications,” in *Antennas and Propagation (EuCAP), 2015 9th European Conference on*, Lisboa, Portugal, April 2015, pp. 1–5.

[CA5] **M. Imbert**, A. Papió, F. De Flaviis, L. Jofre, and J. Romeu, “Design and performance evaluation of a switched-beam antenna array for 60 GHz WPAN applications,” in *Antennas and Propagation (EuCAP), 2015 9th European Conference on*, Lisboa, Portugal, April 2015, pp. 1–5.

[CA6] **M. Imbert**, M. Baquero, L. Jofre, and J. Romeu, “LTCC-based dielectric flat lens antenna at millimeter-wave frequencies,” in *XXIX Simposium Nacional de la Unión Científica Internacional de Radio (URSI)*, València, Spain, September 2014.

[CA7] **M. Imbert**, J. Romeu, L. Jofre, A. Papió, and F. De Flaviis, “Ku-band flat lens design for satellite TV applications,” in *Antennas and Propagation Society International Symposium (APSURSI), 2014 IEEE*, Memphis, TN, USA, July 2014, pp. 1453–1454.

[CA8] **M. Imbert**, J. Romeu, L. Jofre, A. Papió, and F. De Flaviis , “Switched-beam antenna array for 60 GHz WPAN applications,” in *Antennas and Propagation Society International Symposium (APSURSI), 2014 IEEE*, Memphis, TN, USA, July 2014, pp. 1672–1673.

[CA9] **M. Imbert**, A. Papió, F. De Flaviis, L. Jofre, and J. Romeu, “Design and performance evaluation of a dielectric flat lens for millimeter-wave applications,” in *Antennas and Propagation (EuCAP), 2014 8th European Conference on*, The Hague, The Netherlands, April 2014, pp. 3193–3196.

[CA10] **M. Imbert**, J. Romeu, and L. Jofre, “Design of a dielectric flat lens antenna for 60 GHz WPAN applications,” in *Antennas and Propagation Society International Symposium (APSURSI), 2013 IEEE*, Orlando, FL, USA, July 2013, pp. 1164–1165.

# Master Thesis Supervised

[MA1] R. Z. Syeda, “Design and performance analysis of switched beam series-fed patch antenna array for 60GHz WPAN applications,” Master’s thesis, Universitat Politecnica de Catalunya (UPC), July 2014.

# Book Chapters

[BC1] **M. Imbert** and J. Romeu, “Introduction to 60 GHz wireless communication systems,” in *60 GHz Wireless Communication Systems*, F. De Flaviis, Ed., Irvine, CA, 2016, ch. 1, pp. 1–30, in Edition.

# Awards and Mentions

Part of the work developed during this PhD thesis has lead to the following mentions at international conferences:

- Finalist at the Best Paper Award in Antenna Applications at the *European Conference on Antennas and Propagation (EuCAP) 2014*, held in The Hague, The Netherlands, in April 2014 for the paper “Design and Performance Evaluation of a Dielectric Flat Lens for Millimeter-Wave Applications” [CA9].

# Participation in R&D Projects

**FPI Fellowship** Supported by the Formación de Personal Investigador (FPI) Fellowship Program from the Spanish Ministerio de Economía y Competitividad (MinEco).

**CICYT TEC2013-47360-C3-1-P** Supported by the Spanish Interministerial Comission on Science and Technology (CICYT) under project TEC2013-47360-C3-1-P entitled “Sistemas radiantes en milimétricas y submilimétricas para radar, comunicaciones e imagenes”.

**CICYT TEC2010-20841-C04-02** Supported by the Spanish Interministerial Comission on Science and Technology (CICYT) under project TEC2010-20841-C04-02 entitled “Design, Simulation and Measurement of Millimeter-Wave Antennas for Communications and Imaging”.

**CONSOLIDER CSD2008-00068** Project CSD2008-00068 entitled “Terahertz Technology for Electromagnetic and Sensing Applications (TERASENSE)” supported by the Spanish Government.